PROMINENCES AND MAGNETIC ACTIVITY ON YOUNG SINGLE AND BINARY STARS
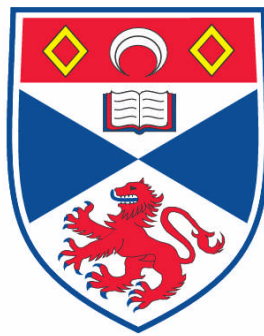
Nicholas J. Dunstone

A Thesis Submitted for the Degree of PhD
at the
University of St. Andrews

2008

THE UNIVERSITY OF ST. ANDREWS
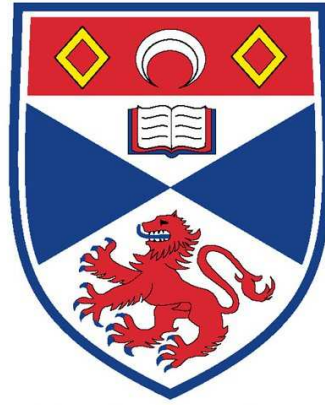
Prominences and magnetic activity on young single and binary stars

Nicholas J. Dunstone

Submitted for the degree of Ph.D.

21 March 2008

DECLARATION

I, Nicholas Dunstone, hereby certify that this thesis, which is approximately 50,000 words in length, has been written by me, that it is the record of work carried out by me and that it has not been submitted in any previous application for a higher degree.

I was admitted as a research student in October 2004 and as a candidate for the degree of PhD in October 2004; the higher study for which this is a record was carried out in the University of St Andrews between 2004 and 2008.

Date: Signature of Candidate:

I hereby certify that the candidate has fulfilled the conditions of the Resolution and Regulations appropriate for the degree of PhD in the University of St Andrews and that the candidate is qualified to submit this thesis in application for that degree.

Date: Signature of Supervisor:

The following is an agreed request by candidate and supervisor regarding the electronic publication of this thesis:

Access to printed copy and electronic publication of thesis through the University of St Andrews.

Date: Signature of Candidate:

Date: Signature of Supervisor:

Acknowledgements

Firstly I would like to thank my supervisor, Andrew Cameron, for his excellent advice and for always making himself available when I needed words of wisdom. Also, many thanks for sending me to Australia three times!

Many thanks must go Gaitee Hussain and John Barnes, without whose help and enthusiasm I would not have got this far. In particular, I really appreciate the time Gaitee devoted to helping me with the HD 155555 project, right from the telescope proposal, through the DoTS code modifications, to publication. Thanks to John for all his help, especially at the start of my PhD, for taking me out to Australia and most importantly, for driving as we passed very slowly through the Hunter Valley!

I would like to say a big thank you to Moira Jardine, you have always been so enthusiastic about my research and so patient when listening to all my daft ideas. I would also like to thank Jean-Francois Donati for both providing his excellent data reduction software and for very helpful discussions in the final stages of my PhD. I have also benefited greatly from scientific conversations with Eric Stempels, Leslie Hebb, Keith Horne, Volkmar Holzwarth, Ettore Pedretti, Kenny Wood and Ron Hilditch.

Thanks to Meir Semel for providing his SemelPol instrument for my research. Many thanks also to Julio Ramirez for taking time out of his final year of PhD studies to travel out to Australia and set-up SemelPol (in record time). Thanks also to Stephen Marsden for much help during that observing run, including extracting SemelPol from Australian customs and getting it delivered to the telescope on time - I doubt I'll ever again be so glad to see a wooden crate in my life! Similarly, I cannot praise the staff at the Anglo-Australian Telescope enough - there is surely no friendlier nor more supportive observatory in the world.

I would like to thank my office mates over the years, Ed, John and Eric for putting up with me! Thanks to everyone in the astronomy department, especially old friends: Neil, Tom, Katharine and Rowan. A special thanks to my housemate, Alexis, for making me laugh during the dark days of finishing up - your friendship is greatly valued. Noé, thanks for the titanic battles on the tennis court - keep working on that forehand!

Thanks also to Jeremy Pollard for encouraging me to pursue my interest in astron-

omy all those years ago. Thanks to Jackie of the Whey Pat, my Mondays simply won't be the same again without your wonderful bacon and brie sandwiches!

Finally, and by far the most important, I would like to dedicate this thesis to my parents. Your continual love and support has been such a great source of encouragement throughout my education. Thank you.

Preface

This thesis is based on all the first author papers listed below.

[1] Dunstone, N.J., Hussain, G.A.J., Collier Cameron, A., Marsden, S.C., Jardine, M., Barnes, J.R., Ramirez Vlez, J.C., Donati, J.-F.

2008, in press, accepted for publication in MNRAS, astro-ph/0804.2491

[2] Dunstone, N.J., Hussain, G.A.J., Collier Cameron, A., Marsden, S.C., Jardine, M., Stempels, H.C., Ramirez Vlez, J.C., Donati, J.-F.

2008, in press, accepted for publication in MNRAS, astro-ph/0803.0837

[3] Dunstone, N.J., Collier Cameron, A., Barnes, J.R., Jardine, M.

2006, MNRAS, 373, 1308

[4] Dunstone, N.J., Barnes, J.R., Collier Cameron, A., Jardine, M.

2006, MNRAS, 365, 530

THE UNIVERSITY OF ST. ANDREWS

Prominences and magnetic activity on young single and binary stars

Submitted for the degree of Ph.D.

21 March 2008

Nicholas J. Dunstone

ABSTRACT

In this thesis I study the magnetic activity of young stars via observations of stellar prominences on single stars and by applying the Zeeman Doppler imaging (ZDI) technique to map the magnetic fields and measure differential rotation of a young binary system.

Stellar prominences can be observed as absorption transients in the rotationally broadened chromospheric lines of rapidly rotating stars. Observations of Speedy Mic (K3V) reveal a densely packed prominence system at heights far above the stellar co-rotation radius. Further observations were used to estimate prominence column densities and masses. From very high signal-to-noise observations, loops of emission are found that trace the path of prominences seen transiting the stellar disc. I also present what appears to be the first observation of an erupting stellar prominence on AB Doradus (K0V).

I modify an existing ZDI code so that it can recover the magnetic maps of a binary system. The new code is applied to observations of the pre-main sequence binary system HD 155555 (G5IV+K0IV). The radial magnetic maps reveal a complex surface magnetic topology with mixed polarities at all latitudes and rings of azimuthal field present on both stars. The evolution of the relative field strengths between observations in 2004 and 2007 could be indicative of a magnetic activity cycle. I adapt the sheared image technique for measuring differential rotation parameters to the binary case. Both stellar components of HD 155555 are found to have rates of differential rotation similar to those of the same spectral type main sequence single stars. This is in apparent conflict with previous work on evolved binary systems where low rates of differential rotation were found, leading to the suggestion of suppression by binary tidal forces. I find that the depth of convection zone alone can likely explain the differential rotation results without invoking tidal forces.

CONTENTS

LIST OF FIGURES

LIST OF TABLES

CHAPTER 1

Introduction

Our nearest star, the Sun, seen rising over Warrumbungle National Park, Australia

With the possible exception of harbouring 'intelligent' life, the Sun is a rather ordinary star. It is a single star approximately halfway through its life on the hydrogen burning main sequence phase of stellar evolution. The Sun is our nearest star and as such the energy it provides has a profound influence on all life on Earth. However, the Sun is not simply a constant energy source in space. On human timescales solar activity can affect everything from satellite communications to changes in the Earth's climate (such as the Maunder minimum in the late 17th century). The young Sun will have affected the formation of the planets and the evolution of life on Earth. Similarly, the future evolution of the Sun as it exhausts its supply of hydrogen will doubtless have profound implications

for the then inhabitants of our planet.

The aim of this thesis is essentially to further our understanding of magnetic activity on other stars. I will study both young single stars and a binary system. The solar-stellar connection works in both directions. Firstly, the detailed observation of solar magnetic phenomena provide us with a framework in which to understand the activity we observe on other stars. Given that astronomers are very limited by the large distances to even nearby stars, if we had to understand stellar activity without reference to the Sun then progress would be extremely slow. Secondly, observations of solar-like activity on other stars are often outwith the range of parameters seen on the Sun (e.g. temperatures, energies and timescales) and so test our understanding of mechanisms thought to generate the solar behaviour. If we were to study the Sun in isolation then we would be severely restricting the conditions under which we could test the underlying physical processes that occur on the Sun in the past, present and future.

1.1 Solar and stellar activity

By observing the behaviour of other stars we can hope to learn how their magnetic activity relates to their fundamental properties; such as mass and rotation rate. First though we should examine the magnetic activity of the Sun and our current understanding of the processes that cause it.

1.1.1 The Sun

We know dark spots on the Sun (sunspots) have been observed since the time of ancient Chinese astronomers in the first century BC. Very large sunspot groups can be seen on the solar surface by the naked eye when the light from the Sun is sufficiently attenuated by the Earth's atmosphere during sunrise or sunset (particularly when the atmosphere contains a greater than average amount of dust). Detailed and regular sunspot observations would have to wait until the invention of the telescope when sunspots were subsequently observed by Harriot, Fabricius, Scheiner and Galileo in the early decades of the 17th century. By tracking the sunspots from day to day they produced the first estimate of the solar rotational period (approximately 25 days).

DAILY SUNSPOT AREA AVERAGED OVER INDIVIDUAL SOLAR ROTATIONS
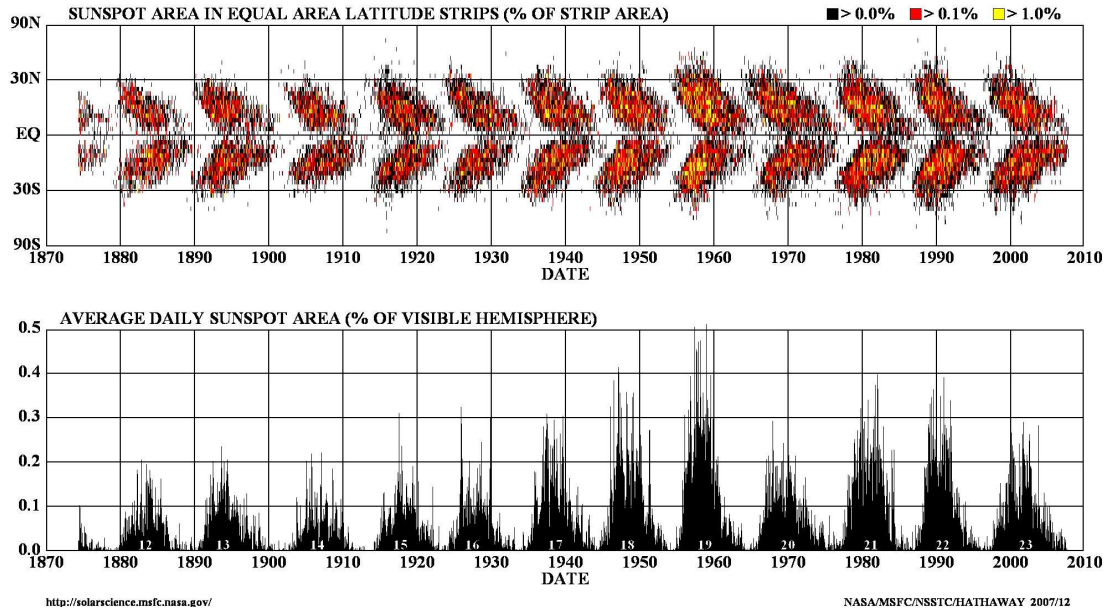
Figure 1.1: The sunspot butterfly diagram. Plot created by David Hathaway, NASA Marshall Space Flight Center.

Some 250 years later Carrington discovered that spots observed near the solar equator had a shorter rotational period than those at higher latitudes (Carrington 1860). This marked the discovery of solar differential rotation; where we now know the equator laps the pole approximately every 120 days. Carrington also gave his name to the numbering of solar activity cycles which were first observed by Schwabe in 1843. As can be seen in Fig. 1.1, at the time of writing we are currently in solar minimum at the transition between Carrington cycles 23 and 24. The first sunspot with a reversed polarity was seen on 2008 January 4, indicating the start of the new cycle.

Sunspots are caused by magnetic flux tubes erupting through the solar surface. These act to insulate a region of the photosphere by inhibiting convective motions and therefore causing the observed cool spots with temperatures that are over 1000 K lower than the surrounding photosphere. Sunspots are not the only observable manifestation of the solar magnetic field: prominences, flares, active plage regions and the solar corona are all a direct consequence of the solar magnetic field. All of these solar activity phenomena are strongly modulated by the solar magnetic cycle.
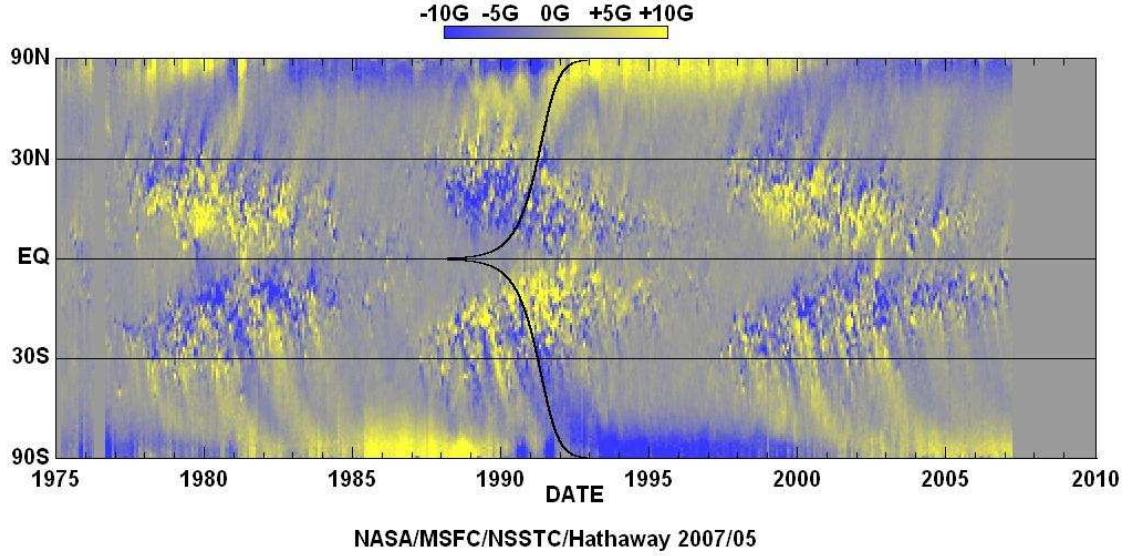
Figure 1.2: The solar radial magnetic field is plotted. The "butterfly" diagram (Fig. 1.1) is clearly present. Note the magnetic polarity switching at the poles during the middle of each solar cycle. Plot created by David Hathaway, NASA Marshall Space Flight Center.

The 11 year sunspot cycle (Fig. 1.1) is a consequence of the solar activity cycle, during which the polarity of the global solar magnetic field is observed to reverse. Hence the full activity cycle is really 22 years in duration in order for each solar pole to return to the same magnetic polarity. Fig. 1.2 shows how the radial component of the solar magnetic field changes over the solar activity cycle. At the start of the solar cycle, at solar minimum (e.g. 1997, Fig. 1.2), we observe a 'quiet' Sun with very few sunspots, plage, prominences or flares. At this time the global solar field resembles that of a simple dipole with both poles composed of single (and opposite) polarities. This simple field structure is revealed in the white light corona during total solar eclipses occurring at solar minimum. Then, as the cycle progresses, sunspots are first seen at higher latitudes ($\approx 40°$) and then at progressively lower latitudes. They are a product of the strong toroidal field produced by differential rotation. Sunspots decay on a typical timescale of days to weeks, releasing magnetic flux into the photosphere. This is then transported by large-scale solar flows towards the poles and eventually results in the field reversal at solar maximum (again, see Fig. 1.2).

The driving mechanism behind the solar activity cycles shown in Figs. 1.1 & 1.2 is the magnetic field generated by the solar dynamo deep in the solar interior. The currently favoured solar dynamo model is that of the *interface dynamo* operating at the base of the convection zone as suggested by Parker (1993). This replaces the previous 'distributed dynamo' model where the dynamo was thought to act in the majority of the convection zone but which predicted the rise of strong magnetic flux tubes in too short a period (Montesinos et al. 2001). Both models are based on the $\alpha\omega$-effect (Parker 1955), which explains the generation and maintenance of the solar magnetic field. The toroidal field is amplified by the presence of differential rotation (the ω-effect), while the poloidal field is produced by helical turbulence (the α-effect). These two processes are thought to occur in adjacent layers near the base of the convection zone which are coupled by diffusion. In the interface dynamo the ω effect is thought to occur in the so called 'overshoot' layer just below the convection zone. The α effect operates on this toroidal field as it diffuses into the lower layers of the convection zone.

In the last two decades, helioseismic measurements have explored the interior rotation rate of the Sun. In particular, such measurements have shown that rotation is primarily latitudinal with angular velocity at the solar surface persisting throughout the bulk of the convective envelope (e.g. Schou 1998). This was counter to the prediction of many early dynamo models that predicted rotation to be constant along cylinders parallel to the rotation axis. Helioseimology has recently provided observational evidence for a thin layer of strong differential rotation (named the tachocline) between the nearly rigidly rotating radiative core and the convective envelope (e.g. Charbonneau et al. 1999). This provides direct support for the overshoot region required by the interface dynamo model.

As a young star, the Sun would have had a deeper convection zone and would have rotated faster. In order study what effect these physical changes would have had on the solar magnetic activity we now turn to observations of stars other than our Sun.

1.1.2 Stellar rotation

There are three main mechanisms that are thought to contribute to the rotational evolution of a star. Chronologically, the first of these is *disc braking*. This is when the stellar magnetosphere couples to a circumstellar disc. Due to the fact that such discs rotate at Keplerian velocities, the field lines connecting the star and the disc prevent the star from

spinning up. The tendency for the star to spin-up results from the second mechanism of *contraction*. Once a proto-stellar disc has dispersed the star is then free to spin-up as it contracts, conserving angular momentum. When a star has reached the zero-age main-sequence, and so stopped significant contraction, then *magnetic winds* driven by dynamo action will act to spin-down the star as they carry away mass and so angular momentum.

Most of our knowledge about the evolution of rotation stems from studies of open clusters. This is due to the fact that all stars can be assumed to be approximately the same age and so the distribution and mass dependence of rotation can be studied alone. A large spread in the distribution of stellar rotation rates was first discovered in the young clusters α Persei and the Pleiades (ages of approximately 50 and 100 Myr respectively) by Stauffer et al. (1989) and Stauffer & Hartmann (1987) respectively. Some of the stars were found to have stellar $v \sin i$ in excess of 100 km s^{-1}. The range of observed rotational velocities is thought to be a result of the different durations each star spent coupled with its circumstellar disc. The initial conditions of star formation are such that some stars become classical T Tauri stars (cTTs) with large discs (exhibiting considerable infra-red excesses) and show the characteristics of stellar accretion (e.g. large H$_\alpha$ emission). Other stars appear to possess a very small disc (or none at all) and are thus referred to as Weak-lined T Tauri Stars (wTTs). These wTTs are observed to have faster rotation rates than cTTS and are therefore thought to experience less or no braking from a disc (see Herbst et al. 2007 for a recent review). Such stars are then free to "spin-up" as they contract while evolving onto the main-sequence.

Comparisons of the α Persei and Pleiades clusters (e.g. Soderblom & Stauffer 1991) showed that the younger α Persei had a higher number of rapidly rotating early G dwarfs than the older Pleiades cluster. Further comparison with the much older Hyades cluster (age 600 Myr) showed that, in addition to the G dwarfs, the K dwarfs had also spun-down by this age (Radick et al. 1987). This is due to the onset of rotational braking, via magnetic winds, which occurs once a star has reached the main sequence. In G dwarfs (solar type stars) this mechanism is highly efficient and can be described by the Skumanich law (Skumanich 1972), which predicts that the rotational period will increase as the square root of time ($P \propto \sqrt{t}$). In reality the efficiency of wind-braking is related to the rotation rate of the star. Rapidly rotating stars have more efficient dynamos (discussed in the next section) and so are more active than slower rotators leading to higher mass loss through stellar winds. As a consequence of this feedback mechanism, stars with a range of initial
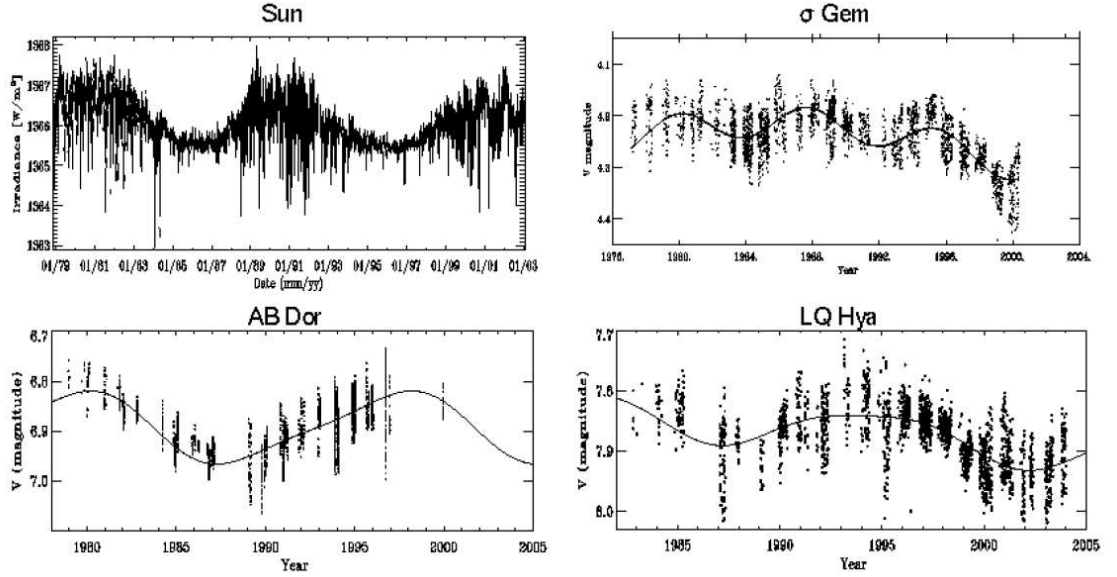
Figure 1.3: The activity cycles from brightness variations of the Sun, the binary star σ Gem and the two rapidly rotating single stars AB Dor and LQ Hya. Note that for the Sun the maximum brightness corresponds to the maximum activity (or spottedness), while the reverse is true for the other stars. Taken from Berdyugina (2005).

rotation rates converge on a single rotation period that is purely dependant upon stellar mass (e.g. Soderblom et al. 1993). The length of time required to achieve this convergence is itself mass dependant (e.g. Scholz & Eislöffel 2004) but is of the order of a few 100 Myr. By the age of the Hyades cluster the observed spread in rotation rates in G and K stars is very small (Radick et al. 1987).

This thesis focuses on young pre-main sequence and ZAMS stars, sometimes referred to as post T-Tauri stars. The two young single stars (AB Dor and Speedy Mic) studied are two of the most rapidly rotating stars in the solar neighbourhood (with rotational periods less than 13 hrs). As such, it is likely that these particular stars had small (or 'weak') discs and so experienced a shorter period of disc braking than their slower rotating contemporaries. Furthermore, due to the fact that these stars are just arriving onto the main sequence, magnetic winds have not yet significantly braked the stellar rotation.

1.1.3 Stellar activity

On the Sun, chromospheric plage regions produce Ca II H & K emission. When solar activity is at a maximum there are more plage regions on the stellar surface and hence more Ca II H & K emission. The search for a similar correlation in other stars was initiated by Olin Wilson at the Mt. Wilson Observatory and led to the discovery of stellar activity cycles. The project resulted in the long-term monitoring of 111 stars between spectral types F2 and M2 with most having been observed for 30 years (Baliunas et al. 1995). The survey showed that the presence of cyclic activity is strongly correlated with age. Younger rapidly rotating stars exhibited high levels of activity and rarely showed a smooth cyclic variability. Older, slowly rotating stars, like the Sun, showed lower activity and evidence of smooth cycles analogous to the 11 year solar-cycle. Subsequent follow-up photometric data on a subset of the Wilson survey stars showed that young stars become fainter at their activity maximum, in contrast to the Sun and other slower rotating stars (Radick et al. 1998 and Lockwood et al. 2007). This implies that the activity cycles on young stars are better seen as brightness variations caused by dark spots than the emission from bright faculae (e.g. Fig. 1.3).

The apparent positive correlation between rotation and activity suggested above can be examined in more detail. The driving mechanism for stellar activity is thought to be the magnetic field that is generated by the dynamo deep in the stellar convection zone. The strength, or efficiency, of this dynamo will be related to the internal structure of the star and its rotation rate. These two variables are parametrised together as the dimensionless "Rossby number" (R_0) which is essentially a dynamo activity index. It is defined as the ratio of the rotational period (P) to the convective turn-over time (t_{conv}):

$$R_0 = \frac{P}{t_{conv}} \tag{1.1}$$

The convective turnover time is obtained directly from theoretical stellar interior models (see Montesinos et al. 2001). For two stars with the same interior structure, the more rapidly rotating star will have a stronger dynamo (smaller Rossby number). Similarly, for two stars rotating at the same rate, the less massive star (with the deeper convection zone) will typically have the stronger dynamo.

The close relationship between dynamo efficiency (Rossby number) and activity was first described by Noyes et al. (1984). It is illustrated in Fig. 1.4 using the ratio of the
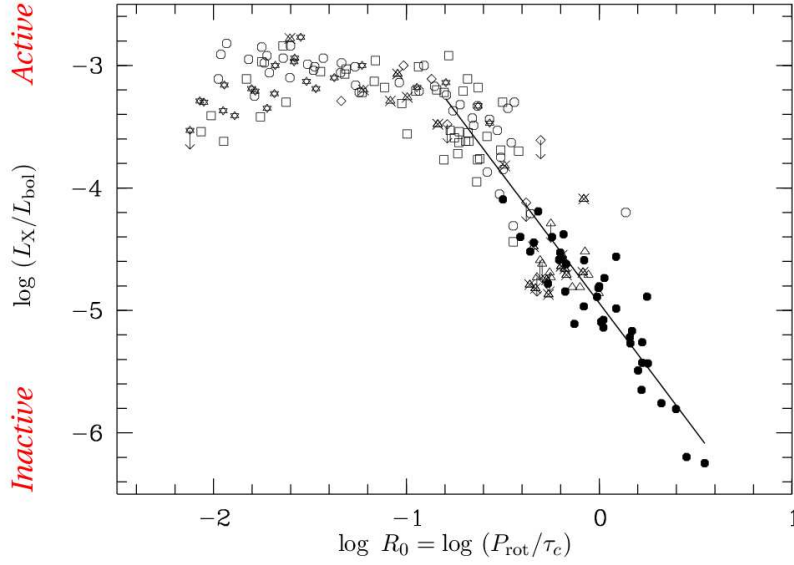
Figure 1.4: Stellar activity (L_X/L_{bol}) is plotted as a function of Rossby number (R_0). The straight line shows $L_X/L_{bol} \propto R_0^{-2}$. Adapted from Randich (2000).

X-ray to bolometric luminosity (L_X/L_{bol}) as the activity indicator. For stars that are approaching the zero age main-sequence, the interior structure becomes fixed (the depth of convection zone changes little) and so the Rossby number effectively becomes a proxy for rotational rate alone. Fig. 1.4 shows that stellar activity increases with decreasing Rossby number (e.g. increasing rotation rate) in a tight relation ($L_X/L_{bol} \propto R_0^{-2}$) until $R_0 \simeq 0.1$. Thereafter, the activity plateaus and further increases in rotation rate do not result in increased activity. Instead the X-ray luminosity becomes a fixed function of L_{bol} ($L_X/L_{bol} \simeq 10^{-3}$). This is known as the saturated regime. At extreme rotation rates (for $R_0 < 0.01$, corresponding to $v_{eq} > 100 \, \text{km s}^{-1}$) the activity actually starts to decline again and therefore is described as being supersaturated. All the stars studied in this thesis are in the saturated or super-saturated regime.

The causes of saturation and supersaturation are still not fully understood; see Güdel (2004) for a recent discussion. One intriguing explanation was put forward by Jardine & Unruh (1999) and involves the stripping of the corona at high rotation rates. As the rotation rate of a star increases, its co-rotation radius (the location at which centrifugal and gravitational forces balance) moves closer to the stellar surface. At the same time centrifugal forces lead to a rise in the pressure in the outer parts of the largest closed

loops. If the co-rotation radius comes inside of the extent of the closed corona then the gas pressure in such loops may be sufficient to blow open the magnetic loops. The resulting open field lines would be X-ray dark and so could explain the observed drop in X-ray luminosity at very high rotation rates. This coronal stripping model also predicts that the remaining corona will be more 'patchy' and so prone to rotational modulation. Extreme rotational modulation was observed in the supersaturated G dwarf VXR45 (Marino et al. 2003).

Once a single star has reached the main-sequence, its rotation rate slows with the passage of time (as described in the previous section). As a consequence the stellar activity also declines. For example, the stellar X-ray luminosity in F-G stars decays as:

$$L_X \simeq (3 \pm 1) \mathrm{x} 10^{28} t^{-1.5 \pm 0.3} \quad [\mathrm{erg\ s^{-1}}], \tag{1.2}$$

where t is the age of the star in Gyr (Guedel et al. 1997).

1.2 Starspots

Starspots are the most easily observed result of magnetic activity. This is true both for the Sun and other stars. The first suggestion for the existence of starspots was by Kron (1947) to explain observed irregularities in eclipsing binary lightcurves. In the intervening 60 years huge progress has been made in the techniques we can use to observe starspots and hence our understanding of their physical properties.

1.2.1 Techniques for observing starspots

The easiest, and most widely applicable, way to detect starspots is simply to monitor the brightness of stars and search for amplitude modulation of the resulting lightcurves. Provided starspots do not uniformly cover the stellar surface then a sinusoidal pattern will emerge with a period equal to that of the stellar rotational period. The number of wide-field survey instruments that routinely observe large areas of the sky each night has increased rapidly over the last decade. This is mainly a consequence of the push to find transiting extra-solar planets. One such project is named SuperWASP (Pollacco & et al. 2006) and consists of two robotic telescopes (one in each hemisphere) each equipped with an array of eight cameras and CCD detectors. SuperWASP monitors literally millions

of stars each night and has become one of the most successful transiting planet surveys with a current published total of six planets at the time of writing (e.g. Cameron & et al. 2007). The photometric precision required to detect the $\approx 1\%$ dip caused by a hot Jupiter transiting its parent star is also ideal for detecting brightness modulation by starspots. The archives of such projects promise to provide a wealth of information on the spot-induced variability of stars in the solar neighbourhood.

Photometric observations provide only limited information about starspots. Crucially they are very insensitive to the latitudinal distribution of stellar spots. Doppler imaging is a technique used on rapidly rotating stars to map their surfaces. It was first introduced for cool stars by Vogt & Penrod (1983) who used it to map the evolved primary star in the RS CVn binary, HR 1099. The technique of Doppler imaging is discussed in detail in Chapter 5. Briefly, Doppler imaging tracks the movement of deformations caused by starspots in the stellar rotational profile. By taking many high-resolution spectra at different stellar rotational phases the stellar surface brightness distribution can be recovered. The main limitation of Doppler imaging is that it can only be applied to relatively rapidly rotating stars, typically those with projected rotation velocities ($v \sin i$) greater than 15 km s^{-1} (c.f. the Sun has a rotational velocity of ≈ 2km s^{-1}). This bias means that our understanding of starspots on slowly rotating stars is far more limited. A number of new techniques for the study of starspots on slowly rotating stars are becoming available, two of which are discussed below.

Optical interferometric observations are beginning to spatially resolve some of the nearest and largest stars. For example, Monnier et al. (2007) used the CHARA array to image the surface of the rapidly rotating A7 dwarf, Altair. The authors found stronger than expected gravity darkening which challenges current models for very rapidly rotating stars. A very exciting project in the near future will involve contemporaneous Doppler imaging and interferometric observations of very nearby cool stars (Pedretti, private communication). Ideal targets for such campaigns are RS CVn binary systems, e.g. HR 1099. Firstly, the binary motion should be easily detectable using interferometry which will lead to a direct measure of the binary orbital inclination. Secondly, due to the large radius of the evolved giant primary component, several resolution elements will be possible across the stellar surface. Such projects should be able to verify the features observed in Doppler imaging studies, such as polar spots (discussed in the next section).
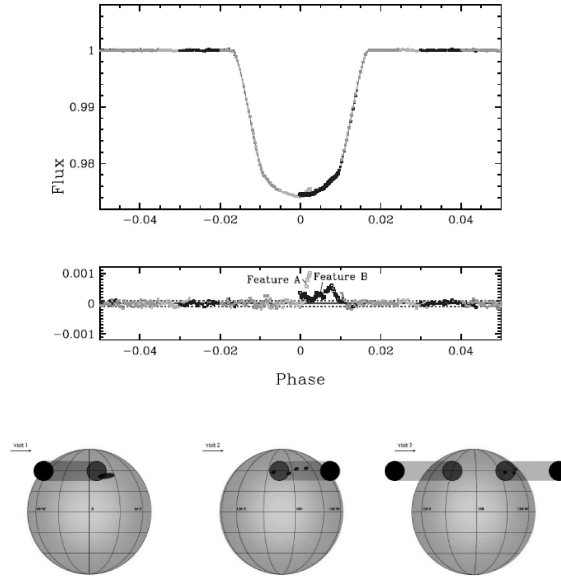
Figure 1.5: *Top* - The HST lightcurve of HD 189733. Note the anomalies in the transit fit plot residuals due to the occultation of starspots. *Bottom* - The models of the starspot occultations, note the sensitivity this technique provides to very small structures on the stellar surface of slowly rotating stars. Taken from Pont et al. (2007).

Another promising technique exploits the discovery of transiting planets. As the planet transits the stellar disc it can occult star spot groups as shown in Fig. 1.5. The exceptional signal-to-noise (15000:1 on each data point) available from space-based photometry allows for such features to be detected in the transit lightcurve. This is analogous to eclipse mapping techniques used to map starspots in close binary systems (e.g. Lister et al. 2001). However, given the small size of the planet relative to the surface of the star we can probe the sizes of starspots to less than 10,000 km across. This level of surface resolution is better than that produced by Doppler imaging on even the most rapidly rotating stars (e.g. Speedy Mic, Barnes 2005). By looking for occultations of starspots at different wavelengths during planetary transits we can also place limits on the temperatures of the starspots.

1.2.2 Physical properties and distributions

From the amplitude modulation observed in stellar lightcurves we can estimate the fraction of the stellar photosphere covered in dark spots. Essentially this provides a minimum spot

filling factor as the observed amplitude could be the contrast between one side of the star being unspotted and the other having a single large spot. The largest amplitudes ever observed have been approximately $\Delta V = 0.6$ mag and therefore require spots to cover at least 20 % of the stellar surface (e.g. HD 12545, Strassmeier 1999). A more accurate, albeit far more challenging, way of accounting for the true spot coverage is to model the amount of absorption in molecular lines which are only formed at the cool temperatures found inside of dark spots (e.g. O'Neal et al. 1996 and O'Neal et al. 2004). These studies also find evidence for high spot filling factors of up to 60 %.

Doppler imaging studies are much more sensitive to starspot distributions. The entire range of cool star spectral types (G, K and M dwarfs) have now been Doppler imaged in addition to T Tauri stars. All these stars are young rapid rotators, but Doppler imaging has also been applied to close binary systems. Due to tidal synchronisation in a close binary, the components can be rapidly rotating without necessarily being young. For example, RS CVn binaries have been popular targets for Doppler imaging. Spots on rapidly rotating stars can be found at all latitudes. This is unlike our Sun where spots are normally seen in an equatorial band extending to $\pm 35°$. In general, the more rapidly rotating the star the more sensitive Doppler imaging is to small scale surface structure. A good example of this is the very rapidly rotating K3 dwarf Speedy Mic which was revealed by Barnes (2005) to have a very densely spotted stellar photosphere.

Many stars show evidence of a large, dark polar spot (sometimes referred to as a 'polar cap'), first seen by Vogt & Penrod (1983) on the RS Cvn star HR 1099. Polar spots have been a controversial topic in Doppler imaging circles. The flat-bottomed appearence of rotationally broadened stellar line profiles appear to require the existence of polar spots (as we shall see in Chapter 6). There is no analogous phenomenon on the Sun and consequently the problem of how to form polar spots has proven to be a considerable theoretical challenge. Recent models of flux emergence and transport in rapidly rotating stars suggest that the Coriolis force can deflect rising flux tubes in the convection zone to emerge at higher latitudes on the stellar surface (Schüssler & Solanki 1992). This results in a distinctly different breed of 'stellar butterfly' to the solar one presented in Fig. 1.1. This must then be combined with strong meridional flows of the order of ≈ 100 km s^{-1} that sweep magnetic flux from decaying active regions towards the pole (e.g. Schrijver & Title 2001, Mackay et al. 2004, Holzwarth et al. 2006 and Holzwarth 2007).

A recent study of the eclipsing RS CVn system SV Cam by Jeffers (2005) and Jeffers et al. (2006) examined the flux deficit observed between eclipse mapping observations and model atmospheres. They found that both small stellar spots (with sizes that are unresolvable by Doppler imaging) were needed at low latitudes *and* a large polar cap was required in order to account for the flux difference. As mentioned above, Doppler imaging on even the most rapid rotators cannot resolve very small stellar spots and so can underestimate the true spot coverage.

1.3   Stellar magnetic fields

Zeeman broadening and polarisation measurements are highly complementary techniques to measure the magnetic fields of stars. Polarisation measurements are difficult on most cool stars due to the mutual cancellation of opposite polarities on the unresolved stellar surface (discussed further in Chapter 5). A notable exception however, is the strong polarisation discovered in emission lines formed at the base of accretion funnels on T-Tauri stars (Johns-Krull et al. 1999). This detection is partly possible because of a simple field structure (Symington et al. 2005) which avoids the cancellation of polarisation signatures from opposite polarities. On rapidly rotating stars the velocity information can be used to disentangle the surface magnetic structure with opposite polarities. This is exploited by the technique referred to as Zeeman Doppler imaging (ZDI) and is extensively used in the second half of this thesis (recent results are also discussed below in §1.3.1). For now we examine the technique of Zeeman broadening.

Zeeman broadening is insensitive to the field geometry and so does not suffer the same problems as polarisation measurements. It is therefore responsible for most of our current knowledge on the magnetic field strengths of stars other than our Sun. The degree of Zeeman splitting is directly proportional to the magnetic field strength B:

$$\Delta\lambda \propto \lambda^2 g_{eff} B \tag{1.3}$$

where g is the magnetic Landé factor and λ is the wavelength. Due to the fact that the splitting is proportional to the square of the wavelength, measurements are best made using red or IR lines. For the field strength to be estimated reliably, the splitting must be at least as great as the intrinsic width of the line in the absence of a magnetic field (Valenti & Johns-Krull 2001). For this reason, the technique is best applied to slowly
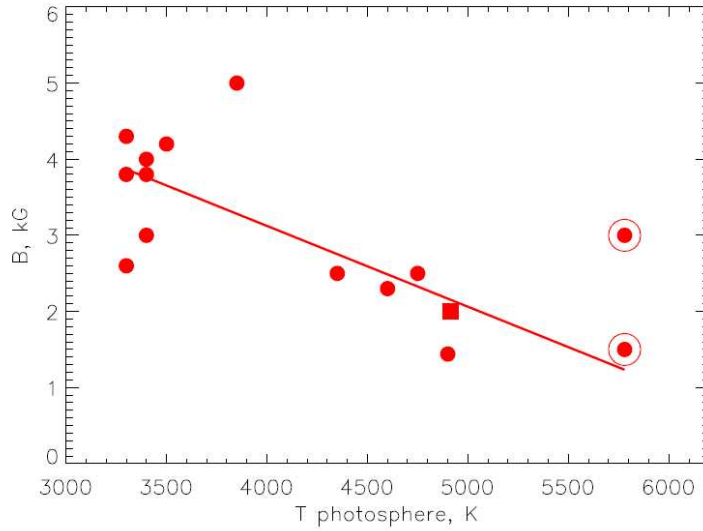
Figure 1.6: Magnetic field strength is plotted as a function of effective surface temperature. The circled dots show the umbral and penumbral magnetic field strengths for the Sun. The line is an unweighted fit to the data. Taken from Berdyugina (2005).

rotating stars, in contrast to the ZDI technique discussed below.

Zeeman broadening has been used to measure the magnetic field strengths of active dwarfs and giants (e.g. Saar 1994 and Valenti & Johns-Krull 2001). The results from these studies were collated by Berdyugina (2005) and are shown in Fig. 1.6, which shows that field strengths appear to increase as effective surface temperature decreases.

1.3.1 Successes of Zeeman Doppler imaging

In the past decade, our understanding of the surface magnetic topologies of stars beyond our Sun has greatly increased thanks to the ZDI technique (Semel 1989). ZDI combines Doppler imaging principles with the observation of circularly polarised light (Stokes V). The ZDI method is discussed in detail in Chapter 5; for now we discuss some of the results of ZDI.

ZDI has now been applied to many rapidly rotating active stars with some surprising results (see Donati et al. 2007 for a recent review). The magnetic maps of active G and K dwarfs show regions of strong surface azimuthal field. For many of these targets the recovered azimuthal field strengths are in excess of the radial field (e.g. for AB Dor and

LQ Hya, Donati et al. 2003), thus suggesting that the magnetic energy is concentrated in the toroidal field rather than the poloidal field. This is quite different from what we find on the Sun where most of the resolved magnetic structures are radially orientated field lines. Current solar dynamo theory tells us that strong azimuthal field should only be found at the shear layer between the radiative core and convective envelope (the tachocline). Donati et al. (1999) therefore suggest that the observation of strong surface azimuthal field on these rapidly rotating stars leads to the conclusion that the ω dynamo component is not confined to the tachocline but instead may be distributed throughout the convective envelope.

The field of ZDI has greatly benefited from the newly commissioned high-throughput spectropolarimeters 'ESPaDOnS' on the 3.6-m Canada-France-Hawaii Telescope (CFHT) and its clone 'NARVAL' on the 2-m Telescope Bernard Lyot (TBL). These instruments enable ZDI to be applied to fainter targets, or those with weaker fields, and to achieve the same S/N in a shorter amount of time compared to previous targets. Due to the increase in the range of targets available for ZDI there have been a number of exciting discoveries in the last couple of years during the period of my thesis work. Below I briefly discuss three discoveries on three very different types of stars: a fully convective M dwarf, a T Tauri star and finally a F dwarf hosting an extra-solar planet.

Donati et al. (2006) investigated the field structure of the M4 dwarf V374 Peg. The surprising result was that this very low-mass, fully-convective star has a mainly axisymmetric large-scale poloidal magnetic field (i.e. similar to an aligned dipole). This is illustrated in Fig. 1.7 which shows the coronal field extrapolation resulting from the recovered radial magnetic maps. The discovery was confirmed by Morin et al. (2008) using data collected a year later than Donati et al. (2006). Remarkably the authors were able to merge these two datasets and still obtain a good fit (χ^2=1.15) to the observed magnetic Stokes V profiles by including differential rotation. The level of differential rotation found was about a tenth that of the solar rate, in good agreement with the prediction of Barnes et al. (2005); (Fig. 1.8) of weak differential rotation. The lack of inherent evolution of the field structure seems to be a direct result of the low rate of differential rotation. Therefore this fully convective star has very weak (but non-zero) differential rotation and yet exhibits a stable axisymmetric poloidal large-scale field. These observations represent a major challenge for current dynamo theories of fully convective stars. For example, Chabrier & Küker (2006) predict that such stars should produce purely non-axisymmetric
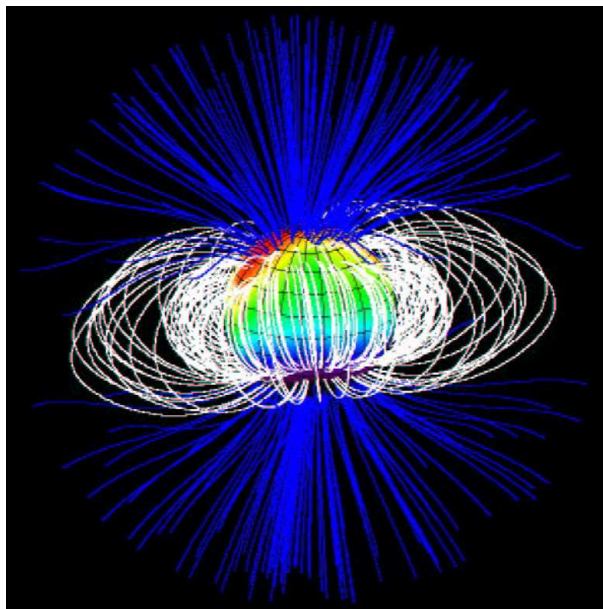
Figure 1.7: Coronal field extrapolation of the M4 dwarf V374 Peg from radial field maps by Donati et al. (2006). Taken with permission from Jardine (2007)

magnetic fields in the absence of significant differential rotation.

Two classical T Tauri stars (cTTS), V2129 Oph and BP Tauri (Donati et al. 2007 and Donati et al. 2008, respectively), have also been recent ZDI targets. Here the authors have been able to detect Stokes V signatures in photospheric lines and also in emission lines resulting from magnetospheric accretion. Using these, the large-scale magnetic topologies and the locations of the accretion spots on the stellar surfaces were recovered. The latter were found to coincide with the two main high-latitude octupole poles and to overlap with dark photospheric spots. Subsequent modelling of both stars suggested that their magnetospheres extend out to 4 R_* and 7 R_* (BP Tau and V2129 Oph, respectively). This implies that the magnetic field extends far enough from the stellar surface to couple to the accretion disc. Such observations lend direct weight to the theory that the rotation rates of T Tauri stars are braked by the interaction of the stellar magnetic field with the disc.

Another ZDI study examined the F7 V extra-solar planet host star τ Bootis. Catala et al. (2007) found a relatively complex large-scale magnetic field and detected a strong rate of surface differential rotation using the Fourier transform technique described in §1.4. Furthermore, the stellar surface was found to be synchronously rotating with the

17
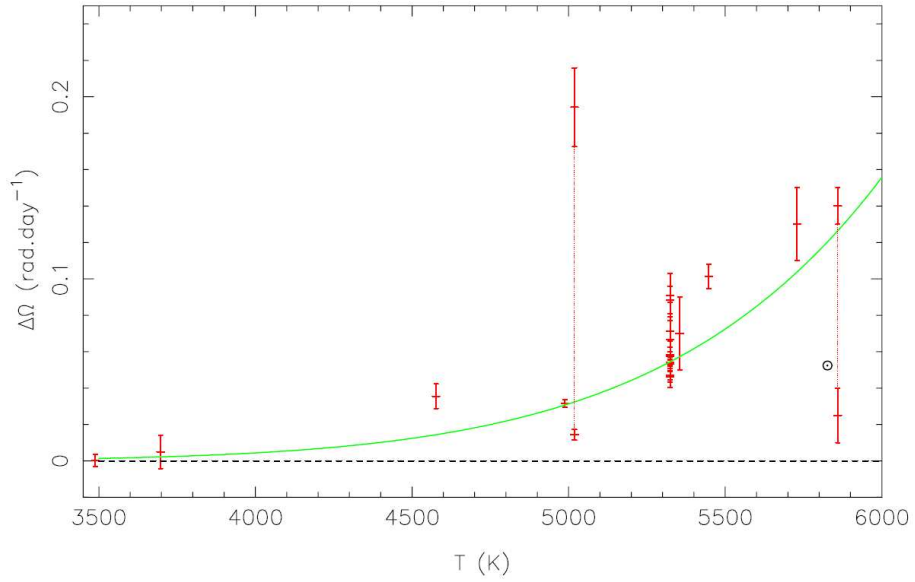
Figure 1.8: Differential rotation as measured from Doppler imaging studies is plotted as a function of surface temperature. The circled dot is the Sun, measurements joined by lines are for the same star. Superimposed is a power-law fit (see text). Taken from Barnes et al. (2005) with permission.

planet's orbital period of 3.31 d (e.g. Leigh et al. 2003). These findings were confirmed by Donati (2008) who was also able to measure differential rotation directly from the Stokes V spectra using the image shear technique (again, see §1.4). The differential rotation of τ Boo was found to be 6 to 10 times that of our Sun. Remarkably Donati (2008) discovered that the overall polarity of the magnetic field had reversed since the Catala et al. (2007) observations. This represents the first observation of a global magnetic polarity switch for a star other than our Sun. The authors speculate that the short magnetic cycle duration (as inferred from the likelihood of capturing the polarity switch) is a consequence of the observed strong differential rotation.

1.4   Differential rotation

Differential rotation is a key factor in the generation of stellar magnetic fields. In the Sun it is differential rotation that transforms a large-scale poloidal field into a stronger toroidal component. In the solar case this is thought to occur in the thin interface layer

between the radiative core and the convective envelope called the tachocline. In the last section we discussed how the observation of strong surface azimuthal magnetic fields on other stars suggests that the dynamo may be distributed throughout the convection zone. It is therefore important to measure stellar differential rotation to see if this provides any clues to explain these observations.

Doppler imaging and ZDI can also be used to determine the rate and sense of stellar differential rotation. At first, independently derived image maps were cross-correlated to determine the phase shift at each latitude (e.g. Donati & Collier Cameron 1997). This was largely superseded by the sheared-image technique (Donati et al. 2000) which incorporates a shear into the imaging process. In Chapter 5 (§5.6) we implement this technique for binary systems. The relative merits of the different techniques for measuring differential rotation are discussed further in Chapter 7. For now, we discuss some of the results from studies of differential rotation using the image shear technique.

Barnes et al. (2005) collated all published differential rotation results from Doppler imaging and investigated trends with stellar effective temperature (or spectral type) and rotation rate (Ω_{eq}). The authors found that the rate of differential rotation was only weakly dependant on Ω_{eq} but strongly correlated with the surface temperature (T). In Fig. 1.8 we show the plot from Barnes et al. (2005) which includes a power-law fit of the form:

$$\Delta\Omega \propto T^{8.92\pm0.31}. \tag{1.4}$$

Cool M dwarfs with deep convection zones have weak differential rotation while early G dwarfs with shallow convection zones have strong differential rotation. Earlier type F stars are generally unsuitable targets for measuring differential rotation with Doppler imaging related techniques due to the fact that they are relatively unspotted. Instead, Reiners & Schmitt (2003) used the pattern of zeroes in the Fourier transform of an optimally-weighted composite line profile to establish both the stellar $v \sin i$ and the rate of differential rotation. Reiners (2006) combined their measurements of differential rotation of F-stars with those of Barnes et al. (2005). The authors found that the extension of the Barnes et al. (2005) power law fit (Eqn. 1.4) also provided a good description of the differential rotation of these earlier spectral type stars.

Since the publication of Barnes et al. (2005), the number of measurements of differential rotation using magnetic regions (Stokes V as opposed to Stokes I spectra) has
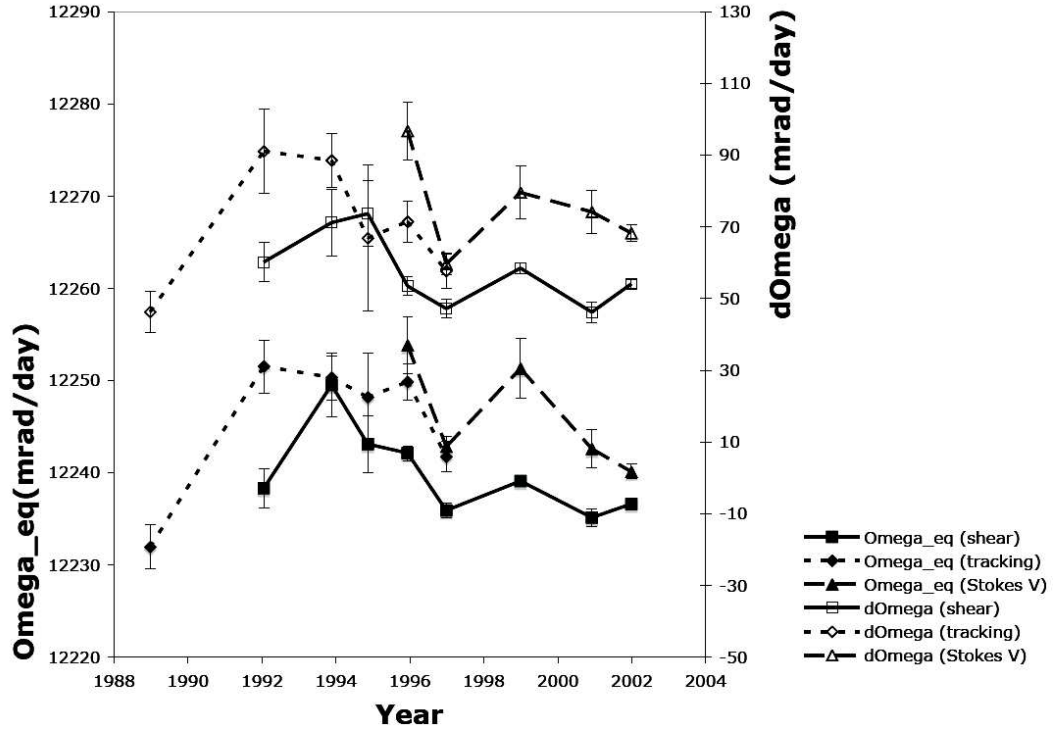
Figure 1.9: Temporal changes in the strength of the differential rotation and absolute rotation rate are plotted for AB Dor using three different techniques. Taken from Cameron (2008) with permission.

increased. These show the same qualitative trend with spectral type as shown in Fig. 1.8, but they show a systematically higher rate of differential rotation (illustrated in Fig. 1.9). This was first observed by Donati et al. (2003) for AB Dor and HR 1099. The authors suggested that the offset between the differential rotation measured from spots and that measured from magnetic regions originates from the differing depths at which each of these features is anchored in the convection zone. They speculated that the spots are anchored deep in the convection zone whereas the magnetic regions are essentially on the stellar surface.

Another way to measure the surface differential rotation from stellar spots is to track spots directly by means of a matched-filter technique applied to the Least Squares Deconvolved (LSD) profiles. This was introduced by Collier Cameron et al. (2002) and was subsequently applied by Collier Cameron & Donati (2002) to multi-year observations of AB Dor in order to search for secular changes in the strength of differential rotation. In a similar analysis, using the image shear technique for both spots and magnetic re-

20

gions, Donati et al. (2003) also produced differential rotation measurements for a similar timespan of observations. Measurements from all three techniques were recently collated by Cameron (2008) and are displayed in Fig. 1.9. The direct tracking technique, like that of magnetic regions, appears to find systematically higher differential rotation rates than those from Doppler imaging. Donati et al. (2003) and Jeffers et al. (2007) attribute this to the fact that the matched-filter technique is more sensitive to smaller spots than the Stokes I technique. This is due to the fact that the direct tracking technique incorporates a high-pass spatial filter which favours small structures. The implication is therefore that the small spots have a higher rate of differential rotation than the larger spot groups. A possible explanation for this is that the larger spots are anchored deeper in the convection zone. Donati et al. (2003) explained that by observing temporal changes in the strength of differential rotation, or equivalently the different probes of depth in the convection zone, we can learn about the stellar internal structure. We discuss this in more detail in Chapter 7.

To date, differential rotation has been measured on three binary systems; the evolved primary star of the RS CVn systems HR1099 (Petit et al. 2004) and IM Peg (Marsden et al. 2007) and the main-sequence secondary star of the pre-cataclysmic variable star V471 Tau (Hussain et al. 2006). In all cases a very weak rate of differential rotation was detected. This led the authors to suggest that binary tidal forces inhibit stellar differential rotation. I examine this hypothesis in detail in Chapter 7.

1.5   Stellar prominences

In Fig. 1.10 I show, what is by solar standards, a 'giant' prominence - although strictly speaking this was observed during eruption. The majority of stable solar prominences are found relatively close to the solar surface. Here we describe the evidence for the existence of prominences on other stars.

The first report of the detection of a stellar prominence was made by Schröder (1983). This used *IUE* UV observations of the eclipsing binary system 32 Cygni which contains a K supergiant primary and a hot B-star V secondary. Schröder (1983) used the B star as a pencil-beam probe of the K star's atmosphere. When the B star came out of eclipse there was a secondary dip observed in the UV flux. The authors attributed this
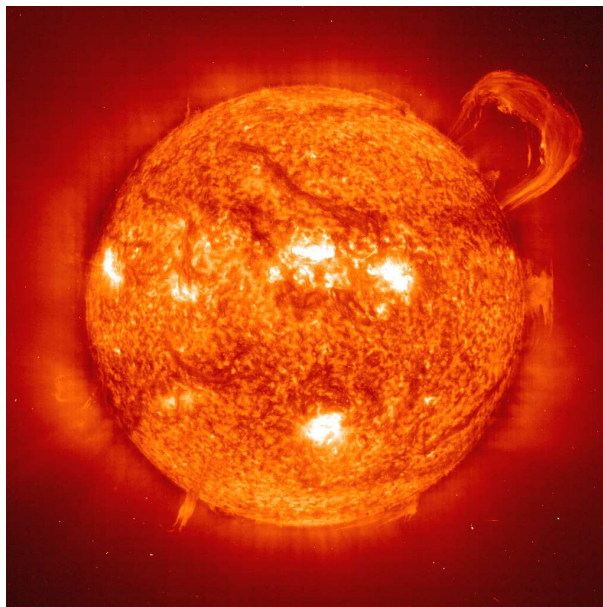
Figure 1.10: This image shows a giant prominence erupting from the solar surface in 1999 September. The image is recorded in the extreme-ultraviolet and also shows bright surface active regions on the stellar disc in addition to dark 'filaments'. Picture credit: SOHO-EIT Consortium, ESA, NASA.

post-eclipse dip to Rayleigh scattering in the HI ground state and calculated a hydrogen column density of $N_H = 10^{24}$ cm^{-2}. A number of similar pencil-beam studies followed. Jensen et al. (1986) found soft X-ray dips on the K0V + white dwarf pre-cataclysmic binary system V471 Tau corresponding to $N_H = 10^{20}$ cm^{-2}. Also on V471 Tau, Guinan et al. (1987) found absorption lines such as C II, C III, C IV, and Si IV superimposed on the white dwarf UV continuum shortly after the white dwarf comes out of eclipse. This was found to be particularly apparent when a large spot group was near the stellar limb that the white dwarf was to emerge from. The authors therefore attributed this to large loops of material overlying the spot features, some of which were observed to extend as far as 1 R_* above the stellar surface. A study of ten eclipsing RS CVn systems by Hall & Ramsey (1992) found that eight showed evidence of intra-system material providing excess absorption in the H$_\alpha$ line.

Stellar prominences have also been observed on a number of cataclysmic variable (CV) systems as low velocity emission features within the binary reference frame. Steeghs et al. (1996) found such emission in the H$_\alpha$ lines of the dwarf novae SS Cyg and IP Peg.

For SS Cyg, emission was also observed in HeII which allowed the authors to estimate the temperature of the prominence material to be ≈20 000 K. Similarly Gänsicke et al. (1998) found evidence for highly-ionized material located at low velocities in the AM Her system and attributed it to a stellar prominence. More recently Watson et al. (2007) reported a prominence on the CV system BV Cen, again at a low velocity (≈0 km s^{-1}) in the binary system. Interestingly, this feature was seen not in emission lines but instead in the combined profiles (LSD profiles) of weak metal lines. The low velocity nature of these observations suggest that the material in these CV systems is located between the cool secondary and hot primary components, often near to the inner Lagrangian (L_1) point. At this location the material could be subject to considerable irradiation from accretion light and so may explain the observed strong emission and high temperatures.

Some of the earliest observational evidence for the existence of stellar prominences on single stars came from observations of stellar flares. Stellar flares are often observed at UV, X-ray and occasionally optical wavelengths. Haisch et al. (1983) observed an increase in hydrogen column density (by a factor of 10 to 100 times) during a stellar flare on the flare star Proxima Cen. The authors attributed this to a prominence passing over the flaring region and absorbing soft X-ray emission, much like that seen on the Sun. The indirect evidence for stellar prominences provided by X-ray observations is interesting and a subject we return to briefly in Chapter 4. For now though we consider stellar prominences observed on rapidly rotating stars.

1.5.1 Slingshot prominences on AB Dor and other single rapid rotators

Robinson & Collier Cameron (1986) reported rapid changes in the H$_\alpha$ line of the K0 dwarf AB Doradus. These changes were observed on timescales of approximately one hour, much shorter than the stellar rotational period ($P = 0.51$ d). Two such features are illustrated in Fig. 1.11. Many explanations were suggested to explain this behaviour by Robinson & Collier Cameron (1986) and later in more detail by Collier Cameron & Robinson (1989a). The authors favoured a model whereby the observed rapidly moving H$_\alpha$ absorption was created by clouds of material co-rotating high above the stellar surface. Strong support was given to this model when Collier Cameron & Robinson (1989b) were able to recover very similar H$_\alpha$ transients at the same rotational phases on subsequent nights.

From well sampled H$_\alpha$ timeseries (e.g. Fig. 1.11), Collier Cameron & Robinson
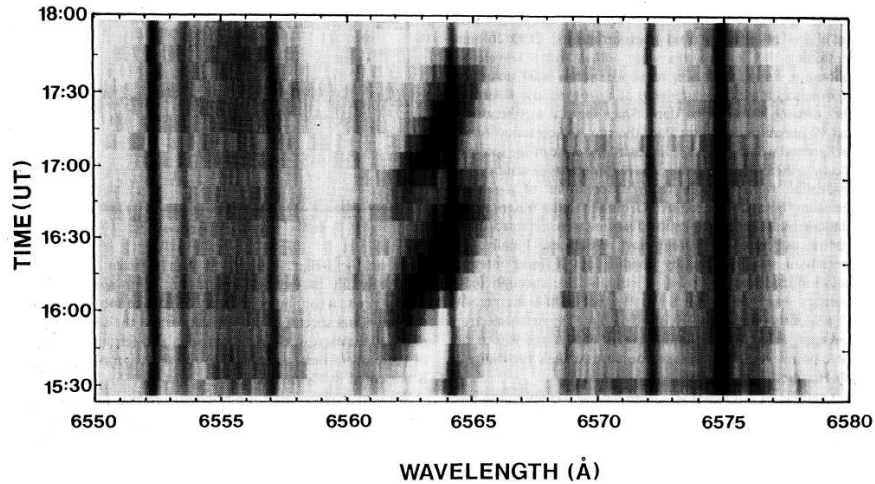
Figure 1.11: Two of the first stellar prominences observed on AB Dor in 1984. The prominences are seen as large dark features moving from blue wavelengths to red (left-to-right) through the rotationally broadened H_α line. The dark vertical lines are Earth atmospheric telluric lines. The greyscale is such that black is at 0.8 and white is at 1.03 times the local continuum intensity. Taken from Robinson & Collier Cameron (1986).

(1989b) inferred the spatial distribution (longitude and height) of the prominence structures from the rate at which absorption features were seen to drift through the profile. This is illustrated in Fig. 1.12 and discussed in more detail in Chapter 2. It was found that these co-rotating clouds of material were located far above the stellar surface at heights up to 8 R_*. The clouds are therefore far above the AB Dor stellar co-rotation radius of 2.7 R_* and must also be considerably above the equatorial plane in order to still be seen transiting the stellar disc at the AB Dor inclination of $60°$. These two results require that large magnetic loops must be present in order to supply a magnetic tension term to balance the outward centrifugal force. If this were not the case then the material would be centrifugally ejected from the star. Due to their apparent similarity with solar prominences the AB Dor clouds were dubbed 'slingshot prominences'.

1.5.2   Prominence lifetimes and support

Stellar prominences have now been observed on many other stars (see Cameron et al. 2003 for a recent review) but, AB Dor remains the most-studied object to date. Typically, stellar prominences are observed to be stable on timescales of 3 - 4 days (Cameron et al. 2003).

Three prominences have been observed to increase their height on nights immediately prior to their disappearence (Collier Cameron & Robinson 1989b, Collier Cameron et al. 1999 and Donati et al. 1999). This suggests that stellar prominences may have then been ejected from the star. It should be noted however that to date no stellar prominence has been caught in the act of eruption.

AB Dor prominences have consistently been reported (e.g. Donati & Collier Cameron 1997; Collier Cameron et al. 1999; Donati et al. 1999; Hussain et al. 2007) to lie at a range of distances from the stellar rotation axis from 2 to 8 R_*, with a concentration at the co-rotation radius ($2.7R_*$ on AB Dor). In contrast to AB Dor, prominences on the M dwarfs HK Aqr and RE J1816+541 (Byrne et al. 1996 and Eibe 1998 respectively) were found to be well inside the stellar co-rotation radii. Mechanisms for supporting prominences both inside and outside the co-rotation radius are therefore required.

The magnetic support of prominences which are located both in the equatorial plane and outside of the co-rotation radius is relatively simple and an aligned dipole field is adequate. The magnetic tension (Lorentz) force provided by the curvature of the magnetic loop can confine a prominence provided it is equal to, or greater than, the net effective gravity which points radially outward due to centrifugal acceleration. This can be written:

$$\frac{B^2}{4\pi R_c} \geq \rho g_{\text{eff}} \tag{1.5}$$

where B is the magnetic field strength at the top of the loop, R_c is the loop radius of curvature, ρ is the mass density of the prominence material and g_{eff} is the effective gravity. Unfortunately this simple model cannot explain the observation of prominences transiting the stellar disc on AB Dor. Due to the stellar inclination of $60°$ prominences on AB Dor must be located significantly above the equatorial plane in order to transit the stellar disc. This combined with the above mentioned observation of prominences significantly inside the co-rotation radius requires a more complex model.

Ferreira (2000) showed that there are two general conditions that must be satisfied in order to produce stable prominence locations. Firstly, the component of the magnetic field along the field must be zero ($\mathbf{B} \cdot \mathbf{g}_{\text{eff}} = \mathbf{0}$) for equilibrium. In order for the equilibrium point to be stable it must be able to recover from perturbations. Effectively this means that it must be in a potential minimum along the direction of the field and hence satisfy the criterion $(\mathbf{B} \cdot \nabla)(\mathbf{B} \cdot \mathbf{g}_{\text{eff}}) = \mathbf{0}$. Ferreira (2000) found that stable equilibria locations for
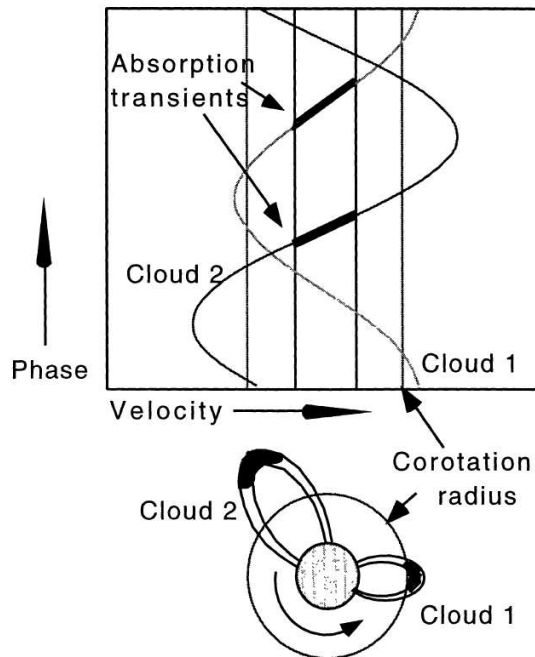
Figure 1.12: A sketch to illustrate how the drift rate of a prominence through the H_α line is related to its distance from the stellar rotation axis. Taken from Collier Cameron (1996) with permission.

prominence formation exist inside the co-rotation radius, even for a simple dipole field. He also found that prominences could be supported considerably above the stellar equator if the field had a strong quadrapole component. Jardine et al. (2001) considered the stable locations for prominences by considering potential field magnetic configurations derived from Zeeman-Doppler imaging maps. The authors concluded that in order for prominences to be supported at sufficiently high latitudes to be seen transiting the stellar disc, then the field structure near the co-rotation radius needs to be more complex than a dipole. This was found to be the case using the available Zeeman-Doppler images of AB Dor (discussed in §1.3.1) and Jardine et al. (2001) found many possible locations that satisfy the above equilibrium and stability criteria (however prominences are not observed at all these locations).

Observations of stellar prominences provide a unique probe of stellar magnetic fields out to distances of many stellar radii into the corona and can therefore be compared to other tracers of coronal extent (e.g. X-ray observations). The exact nature of prominence support is still largely an open question and one to which I return in Chapter 2.

1.5.3 Physical properties of stellar prominences

When we observe stellar prominences as dark absorption features (as in Fig. 1.11) they are analogous to the solar phenomena referred to as 'filaments'. Stellar prominences have also been observed as emission features seen outside of the stellar rotational profile by Donati et al. (2000) on the G-type post T Tauri star RX J1508.6-4423. A very similar observation was made for the G-dwarf AP 149 (a member of the young α Persei cluster) by Barnes et al. (2001). These prominence systems are only seen in emission and not, as in AB Dor, in absorption. We discuss how the geometry and physical environments of stellar prominence systems dictate the way in which we observe them in Chapter 3.

The physical properties of AB Dor prominences were studied in the third of the original series of papers by Collier Cameron et al. (1990). This work used observations of prominences in the CaII and MgII resonance lines, in addition to H_α, in order to estimate their column densities, temperatures, projected areas and masses. They found that prominences had column densities of $N_H \approx 10^{24}$ m^{-2}, a projected cross-sectional area of $A \approx 3$ x 10^{25} m^2, temperatures of $T \approx 8000 - 9000$K and masses of $M \approx 2 - 6$ x 10^{14}kg. This mass is two to three orders of magnitude greater than that for quiescent solar prominences.

1.6 Thesis outline

The thesis essentially splits into two distinct but related parts. In the next three chapters (Chapters 2 - 4) I will detail my work on stellar prominences. Then the subsequent three chapters (Chapers 5 - 7) focus on Zeeman Doppler imaging and measuring differential rotation in binary star systems. I briefly outline below a short description of the content of each chapter.

Chapter 2 presents the first detailed observations of the prominence system of the K3 dwarf Speedy Mic. The distribution of prominence heights are investigated and compared with the predictions from theoretical models of prominence support.

Chapter 3 examines the physical properties of Speedy Mic prominences using a very high S/N dataset. The masses of stellar prominences are estimated and evidence for off-disc emission from prominences is sought.

Chapter 4 describes the prominence system of the K0 dwarf AB Dor during 2002 and attempts to correlate prominence positions with X-ray data. Also presented is the apparent observation of a stellar prominence ejection.

In Chapter 5, I outline the development and testing of a binary Zeeman Doppler imaging code. The modifications to model differential rotation in a binary system are also described.

Chapter 6 presents the first magnetic maps of a pre-main sequence binary system (HD 155555). Temporal changes in the relative field strength and field orientation of the two binary components are also examined.

In Chapter 7, I model the differential rotation on both components of HD 155555. The results are compared with those of young single stars and the evolved primary stars of RS CVn binary systems.

Finally, Chapter 8 presents a summary of my conclusions and briefly describes avenues for future research.

CHAPTER 2

Prominence mapping

"the sun getting out of his eclipse was preceded by a blood-red streak of light from its left limb, which continued not longer than six or seven seconds of time."

- Captain Stannyan, after observing the total solar eclipse of 1706.

This chapter is based on a paper published in the Monthly Notices of the Royal Astronomical Society by:

Dunstone, N.J., Barnes, J.R., Collier Cameron, A., Jardine, M. (2006, MNRAS, 365, 530)

All the work described here was carried out by myself.

2.1   Introduction

Here we present new observations of the prominence system on one of the fastest and brightest young, rapidly rotating stars in the solar neighbourhood. Speedy Mic (BO Mic, HD 197890) is a K3V dwarf with an equatorial rotation velocity $v \sin i \simeq 132$ km s^{-1} (Barnes, 2005). Recent studies of X-ray variability have shown Speedy Mic to be one of the most active stars in the solar neighbourhood. Singh et al. (1999) found $\log(\mathrm{L_X/L_{bol}}) \simeq -3$ placing it in the saturated regime (see 1.4). More recently Makarov (2003) reported $\log(\mathrm{L_X/L_{bol}}) \simeq -2$, although this may be due to flaring as otherwise it would put Speedy Mic's X-ray luminosity an order of magnitude greater than any other star in its class. Stellar prominences (see Chapter 1) were first observed on Speedy Mic by Jeffries (1993). Two prominences were reported at radial distances of $1.36 \pm 0.09 R_*$ and $2.96 \pm 0.14 R_*$. Barnes et al. (2001) also reported four prominences at radial distances in the range $1.3 < R < 3.8 R_*$.
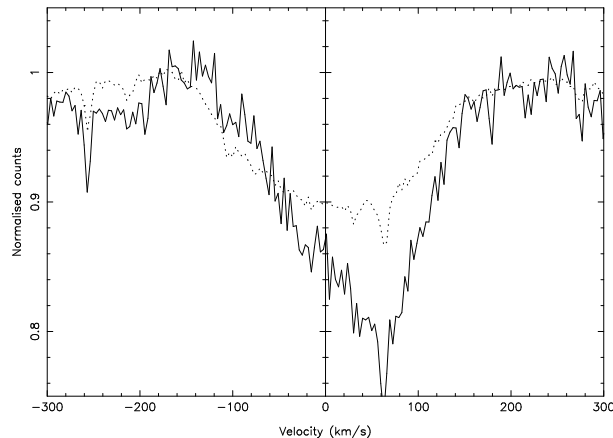
Figure 2.1: An example observed H_α profile (solid line) shows an absorption transient. Also plotted is the average profile (dotted line) for comparison. The sharp telluric line features (e.g. located at 60 km s^{-1}) are removed during the unsharp masking process.

In §2.2 we present observations with uninterrupted and complete phase coverage of the Speedy Mic H_α line on consecutive nights. This strategy is combined with an improved technique for tracking prominences described in §2.3. The relatively large number of resulting prominences allow us to examine the distribution of prominence heights and evolution timescales in §2.4. We discuss the implications these results have on the nature of supporting magnetic structures in §2.5. Finally we present our conclusions in §2.6.

2.2 Observations

Observations were made by John Barnes using the University College London Échelle Spectrograph (UCLES) at the 3.9-m Anglo Australian Telescope (AAT) on 2002 July 18, 19 & 23. A slit width of 1.2 ″ was used, providing a mean resolution of ~ 45000 at H_α with coverage from 4376Å to 6892Å in 47 orders on the 2kx4k EEV CCD. Full phase coverage was obtained on both July 18 and 19 corresponding to 100 and 97, spectra respectively. The typical signal-to-noise (S/N) achieved was 80 in a 300 s exposure. On July 23 time was lost due to bad weather and thus only resulted in 67 usable spectra ($\sim 70\%$ phase coverage) some of which have poorer S/N.

Spectral extraction was performed using ECHOMOP, the échelle reduction package

Table 2.1: System parameters for Speedy Mic from Barnes (2005)

P [d]	0.38007 ± 0.00005
v_r [kms^{-1}]	-8.0 ± 1.0
$v \sin i$ [kms^{-1}]	132 ± 2
Axial inclination [deg]	70.0 ± 5

developed by Mills (1994), and its implementation of the optimal extraction algorithm developed by Horne (1986). Further details of the extraction process and a journal of observations can be found in Barnes (2005). Throughout this chapter we shall be using the system parameters found using the same dataset by Barnes (2005). These are summarised in Table 2.1. We note that Wolter et al. (2005) find very similar parameters from data taken a few weeks later using the 8.2-m Very Large Telescope (VLT).

We take the H$_\alpha$ order and normalise the continuum of each individual spectrum. Any residual tilt in the spectrum is corrected by using a rigid spline fit after masking out the H$_\alpha$ line region. In Fig. 2.1 an example observed H$_\alpha$ profile can be seen with a prominence absorption feature finishing its path across the stellar disc. The spectra are stacked together and phased according to their times of observation using midnight (UT) of the first night as the epoch of phase zero.

The phased raw H$_\alpha$ time series are shown in Fig. 2.2. A visual examination of the time series reveals Speedy Mic to have a remarkably active prominence system. Many rapid transient absorption features are seen to drift through the stellar H$_\alpha$ profile. The most noticeable feature however is a very dark region between phases $0.8 < \phi < 1.0$. Further examination suggests that the timeseries splits into two halves, with a lighter region between phases $0.2 < \phi < 0.7$ and the rest of the timeseries being dominated by darker absorption features. We will briefly discuss these contrasting regions in §2.6. The rest of this chapter concerns the rapid transients seen in the H$_\alpha$ profile.

2.3   Prominence tracking

The spatial distribution of prominences can be inferred from the timeseries. The phase at which any individual prominence transits the center of the stellar rotation profile can be
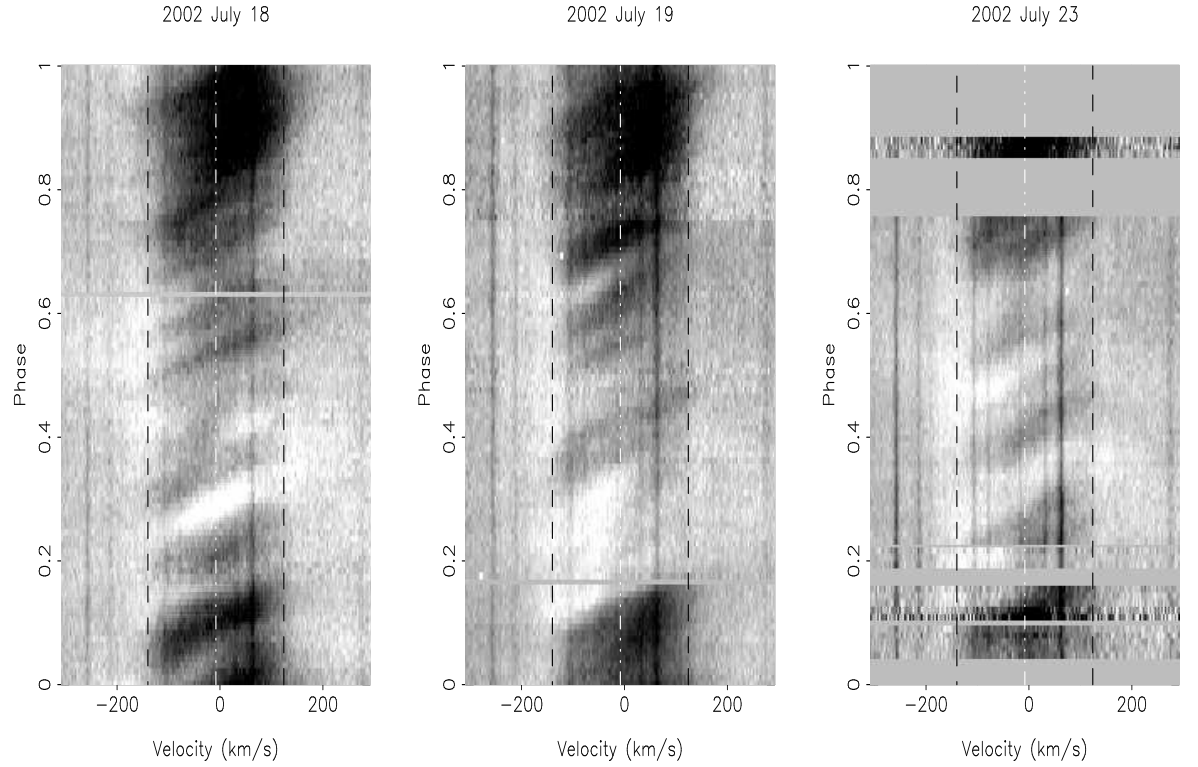
Figure 2.2: Raw H$_\alpha$ time series spectra for 2002 July 18, 19 & 23, with phase plotted against velocity. Dashed black lines show the $v \sin i$ limits and the central dashed white line shows the radial velocity of Speedy Mic. The grey-scale runs from black at 0.80 times the local continuum level, to white at 1.02 times continuum.

easily identified. In addition to this, by assuming that the prominences are in co-rotation with the surface of Speedy Mic (this assumption is validated by re-acquisition of the same prominence on subsequent nights) then we can calculate the axial distances (heights). This is due to the fact that the drift rates of the absorption transients through the stellar rotation profile are directly proportional to their radial distances from the rotation axis (as was illustrated in Fig. 1.12). Due to the relatively large heights of the prominences their orbital velocity sinusoids are well approximated by straight lines while they are transiting the stellar disc.

The projected height is given by:

$$\frac{\varpi}{R_*} = \frac{\dot{v}}{\Omega v \text{sini}} \tag{2.1}$$

where $\varpi = R\cos\theta$ is the distance of a prominence at latitude θ from the rotation axis. $\dot{v}$ is the observed drift rate through the stellar rotation profile and is obtained directly from the phased timeseries. Ω is the stellar angular velocity, R_* is the stellar radius and $v \sin i$ is the projected equatorial rotation speed.

Previous authors have used a number of different methods to estimate the drift rates of the prominence absorption signatures through the line profile. When the S/N is poor, or there are gaps in the phase coverage of the prominence tracks, estimates can be made directly by drawing a by-eye best fit line through the prominence absorption signatures as was done in Barnes et al. (2001). However the associated uncertainties were quoted as being $\simeq 1R_*$. With more complete datasets the skew-mapping technique as devised in Collier Cameron & Robinson (1989a) and updated by Donati & Collier Cameron (1997) can be used. In order to bring out just the ridge-lines of the absorption features an unsharp-mask is often applied to the raw H_α timeseries. Further details will be given in the next section.

These techniques do not attempt to use a prior model for the prominences as they pass through the profile. The advantage of using a model is that we can obtain a confidence assessment through a χ^2 analysis. This describes how well the model fits the data and so is not as biased by strong areas of absorption but rather favours a consistent track across the profile. We describe the use of such a matched filter analysis technique with a Gaussian model in §2.3.2. The first stage in the analysis however is to remove the atmospheric telluric lines from the timeseries spectra shown in Fig. 2.2, while at the same

time bringing out the ridge-lines of the prominences.

2.3.1   Unsharp masking

Previous studies tracking prominences through the H_α profile have subtracted or divided by a mean profile in order to remove the telluric lines. As Fig. 2.2 shows however the Speedy Mic H_α profile is filled with many strong absorption signatures and it is difficult to establish a base reference level for the H_α line. The mean profile of the H_α line obtained by collapsing the timeseries in the temporal direction is therefore in strong absorption (see Fig. 2.1). When the timeseries is divided by the mean profile we obtain spurious regions of relative emission, in which weak absorption transients can be seen. This is undesirable for further analysis as the absorption features should be below the continuum level. Another problem when using a mean profile is the assumption that the H_α profile is symmetric, i.e. every transient absorption feature is symmetric around the centre of the stellar H_α profile. Again, though just from looking at some of the absorption transients, it can be seen that this not the case, especially around the $0.8 < \phi < 1.0$ region where an excess of absorption in the red is seen.

In order to remove the telluric lines and to bring out the ridge lines of the absorption features we perform an unsharp mask in the temporal direction. We thus smooth the timeseries using a Gaussian-weighted running mean with $\sigma = 1500$ s. This corresponds to approximately half the duration of a typical absorption transient. We then divide the original timeseries by this smoothed version. The resulting timeseries spectra are shown in Fig. 2.4. This process has two main advantages. Firstly it removes the telluric lines very well as it does so on localised regions rather than the whole timeseries. This then allows for changes in the strengths of the telluric features as observations are made through varying amounts of the Earth's atmosphere during the night. Such a procedure also brings out the ridge lines of the transients making them more obvious. It is important to realise however that this is achieved because this technique essentially simplifies the timeseries, removing the underlying slow variations of the H_α profile. Another point also worth remembering is that the absolute strengths of the absorption (or indeed emission) with respect to the continuum level are not maintained. However this technique provides us with a higher contrast version of the timeseries which has brought out the rapid absorption transients that we are interested in.

2.3.2 Matched filter analysis tracking of prominence features

In order to track the absorption features as they move across the rotational ($v \sin i$) profile of the star we use a matched filter analysis technique. This is based upon the spot tracking technique of Collier Cameron et al. (2002) adapted for the prominence situation. We model the absorption features as Gaussians of fixed width moving linearly with time through the H$_\alpha$ profile. We adopt $\sigma =$25km s^{-1}which was found to be approximately the width of the weakest absorption transients. We then sample the timeseries at a frequency of just over (the inverse of) twice the number of spectra, a spacing of 0.004 in phase, to ensure precise determination of prominence phases. At each phase the path through the profile of a potential prominence at that meridian crossing is considered for a range of possible prominence heights. Heights are considered from the stellar surface out to 7.5 R_* with a resolution of 0.015 R_* to ensure adequate radial resolution for any low-lying prominences located well inside the co-rotation radius. Hence over a hundred thousand possible prominence tracks are tried throughout the timeseries.

At each prominence height the model Gaussian is then optimally scaled to fit the data along the whole prominence track. The result is a single scale factor for the potential prominence moving through the $v \sin i$ profile at that particular phase and height, along with an associated χ^2 for the fit. Initially all points that fell between the $v \sin i$ limits of the star were selected for Gaussian fitting, so that equal weight was given independent of position along the $v \sin i$ profile. This resembles a step function along the profile, with a value of one inside the $v \sin i$ range and zero outside. This approach was found to be an over-simplification when tested on actual absorption transients. The strength of a given absorption transient is determined by the physical properties of the cloud and its orientation with respect to our line of sight. If the cloud appears to transit the stellar disc at a high latitude then the extent of the absorption transient in the rotational profile will be reduced. The finite size of the cloud means that it takes time to move fully onto the disc. This combined with the velocity dispersion within the cloud itself and stellar limb darkening all change the strengths of the absorption features as they cross the disc.

For prominences at larger heights the path of the absorption signatures samples less spectra. At the maximum height that we consider, the absorption signature samples only five spectra. This produces discontinuities in the resulting χ^2map, since as we increase the height we jump from considering n spectra to *n-1* spectra.

Weight 0.5

−200 −100 0 100 200
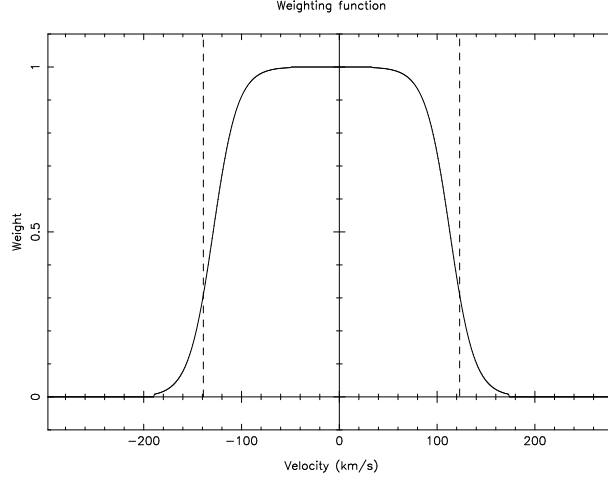
Velocity (km/s)

Figure 2.3: The weight given to the scale factor of the Gaussian model as it crosses the stellar $v \sin i$ profile. Function is centred on Speedy Mic's radial velocity, $v_r = -8$km s^{-1}

In order to make a more realistic model for the absorption strength across the profile we parameterised all these factors into a single weighting function, shown in Fig. 2.3. This took the form of a Fermi-Dirac like function:

$$W = \frac{1.0}{\left(1.0 + \exp\left(\alpha \frac{(v_{cent} \pm v)}{\Delta v_{prom}}\right)\right)}, \tag{2.2}$$

where the parameter α controls the nature of the fall-off away from the line centre and Δv_{prom} is an approximation to the internal prominence velocity dispersion. We approximated Δv_{prom} to be roughly twice the width of the fitted absorption features, $\sigma = 25$ km s^{-1}. The parameter α was changed to crudely optimise the fit to observed prominences passing through the profile, resulting in the profile shown in Fig. 2.3. This gives less weight to the extremes of the $v \sin i$ limits and it also produces smooth χ^2 minima by removing the sharp and discontinuous jumps in the number of spectra sampled. Note that this function is of course only an approximation as the precise strength of any given feature is unique.

The Gaussian scale factors obtained through this procedure are either negative or positive, corresponding to prominence absorption signatures or emission features respectively. It should be noted however that most of the emission features are merely a product of the unsharp-mask process and are therefore not real. Just relying on the scale factor of the Gaussian is insufficient to reveal the prominence heights. This is because the scale factor alone will tend to overestimate the height of the prominences as it can join neigh-
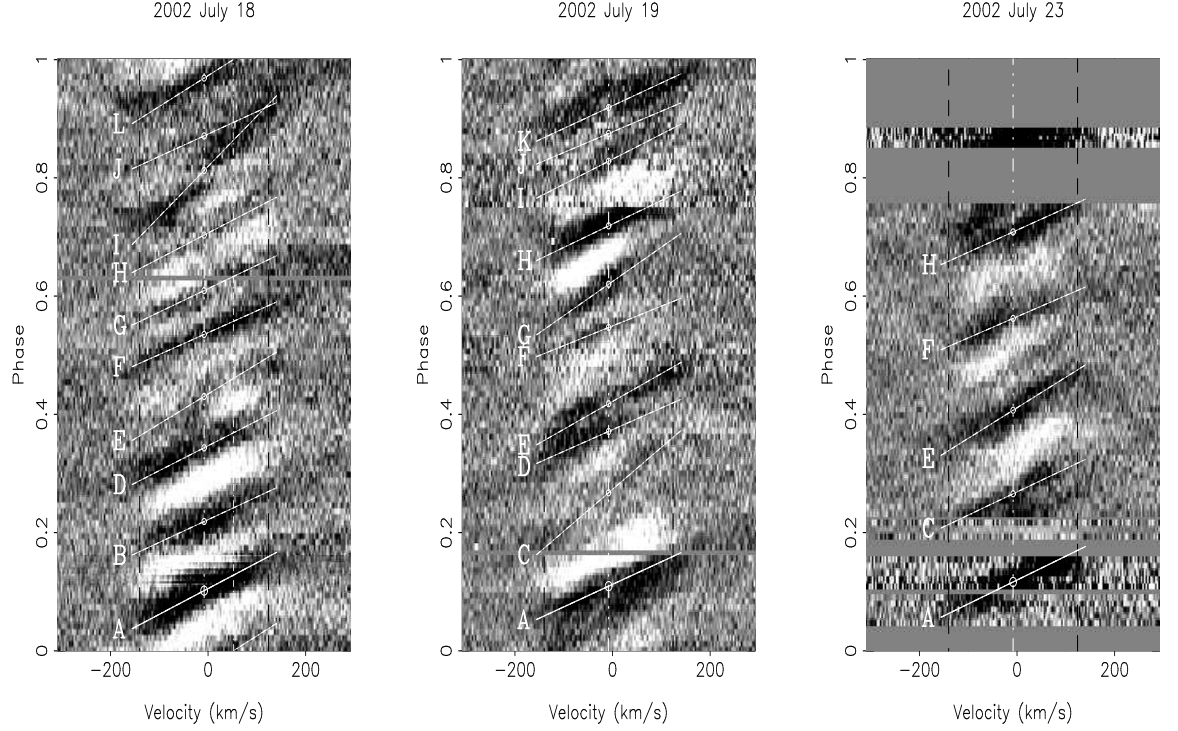
Figure 2.4: As Fig. 2.2 but after the unsharp masking process described in the text. The grey-scale now runs from black at 0.97 times the local continuum level to white at 1.03 times continuum. Superimposed are the fits achieved by the prominence tracking technique.

bouring prominences together. The heights we find are therefore based upon the cuts (at constant phase) through the resulting χ^2 map at each phase considered. The resulting χ^2 minimum in height is then compared to neighbouring phases (constant height) to establish a local χ^2 minimum for a particular prominence. This results in much better determined minima and are used to produce the prominence tracks that are overlaid on the unsharp-masked timeseries in Fig. 2.4. Overlaying the tracks upon the timeseries in this manner allows quick visual confirmation that a suitable fit has been achieved.

The uncertainty in the prominence heights can then be estimated from the curvature of the χ^2 slices. However, due to the asymmetry in the χ^2 minima the reported uncertainties are mean estimates and almost certainly over-estimate the formal error on the prominence heights. The results of this improved tracking technique on the Speedy Mic dataset are displayed in Table 2.2.

Table 2.2: The results of the prominence tracking analysis displayed with phases of meridian crossing and calculated heights for each day of observation. The quoted phases have a measuring uncertainty not greater than $\Delta\phi = 0.002$

| Prominence | *July 18* | | | *July 19* | | | *July 23* | | |
	Cycle	Phase	$\frac{\varpi}{R_*}$	Cycle	Phase	$\frac{\varpi}{R_*}$	Cycle	Phase	$\frac{\varpi}{R_*}$
A	2	0.102	2.79 ± 0.11	4	0.109	3.18 ± 0.16	15	0.116	3.00 ± 0.19
B	1	0.219	3.16 ± 0.15						
C				4	0.267	1.71 ± 0.09	14	0.273	3.09 ± 0.17
D	1	0.343	2.88 ± 0.14	4	0.371	3.31 ± 0.26			
E	1	0.430	2.40 ± 0.24	4	0.434	3.00 ± 0.42	14	0.407	2.35 ± 0.11
F	1	0.535	3.28 ± 0.18	4	0.547	3.64 ± 0.70	14	0.562	3.39 ± 0.38
G	1	0.609	3.06 ± 0.34	4	0.620	2.10 ± 0.12			
H	1	0.703	2.82 ± 0.37	4	0.726	2.49 ± 0.10	14	0.709	3.24 ± 0.17
I	1	0.813	1.43 ± 0.05	3	0.828	2.87 ± 0.40			
J	1	0.871	3.21 ± 0.22	3	0.875	3.48 ± 0.63			
K				3	0.919	3.16 ± 0.21			
L	1	0.969	2.32 ± 0.12						

2.4 Properties of the prominence system

The resulting prominence system is illustrated by the circular back projections displayed in Fig. 2.5. A total of ten prominences are found on the observable hemisphere of Speedy Mic on both nights with full phase coverage with a further five on the July 23 due to only partial phase coverage. For reference the most studied stellar prominence system, on AB Dor, is typically quoted as having 6 to 8 prominences at any one time (e.g. Collier Cameron et al. 1999). It should be noted however that obtaining full and *continuous* phase coverage of a single rotation combined with applying the improved prominence tracking technique may affect this comparison.

In total 25 prominences are found in the range $1.4 < R_c < 3.6$ stellar radii above the surface. This is the largest number of prominences observed at any single epoch on any star thus far. Such a large number allows us to perform a statistical analysis of the prominence locations. The distribution of prominence heights is shown in the form of a histogram in Fig. 2.6.

2.4.1 Prominence heights and the stellar co-rotation radius

System parameters for Speedy Mic have been constantly improved over the last decade. Using the same dataset as this chapter Barnes (2005) were able to further constrain the period, stellar $v \sin i$ and axial inclination (see Table 2.1). Such accurate parameters help us to identify Speedy Mic's co-rotation radius using:

$$R_k = \sqrt[3]{\frac{GM_* P^2}{4\pi^2}}. \tag{2.3}$$

The co-rotation radius is essentially only as uncertain as the mass we adopt and even then is only proportional to the cube root of the stellar mass. This gives the absolute position of the co-rotation radius however we need the co-rotation radius in terms of the Speedy Mic stellar radius for comparison with prominence height locations. To calculate this we can use a simple dynamical argument assuming circular motion, using the observed $v \sin i$, inclination and period. We perform a Monte Carlo error analysis using the values and Gaussian-distributed 1σ uncertainties from Table 2.1. Note that for the uncertainty in the period we adopt the photometric period of 0.380 ± 0.004 days as given by Cutispoto et al. (1997). As this uncertainty is based on a much longer observing run and so is probably
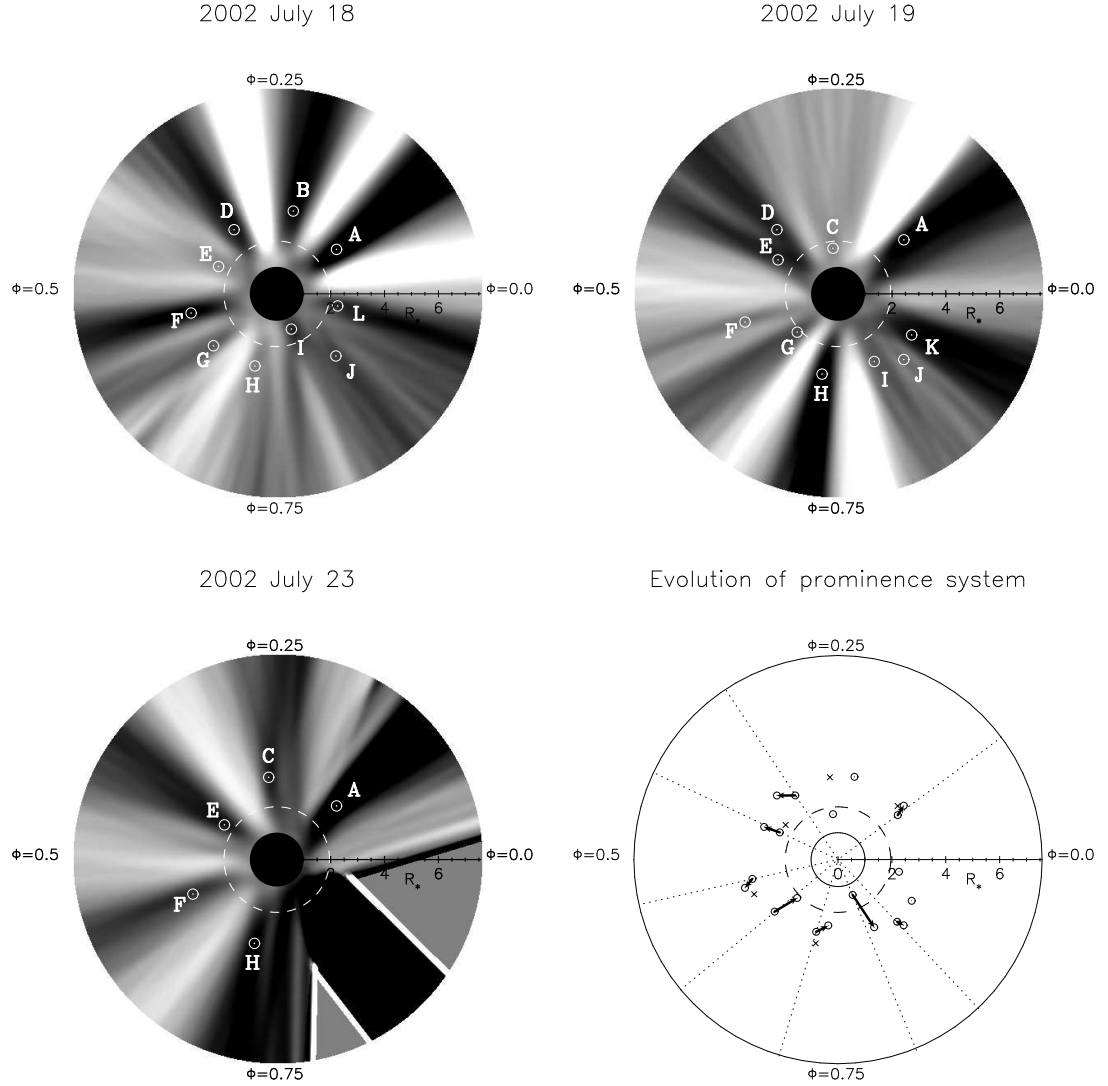
Figure 2.5: Circular back projections of prominence system. Phase increases anti-clockwise, radial distances interior to the star (the black circle at the centre) have been suppressed and the dashed circle shows the location of the co-rotation radius. The grey scale represents the scale factor of the fitted Gaussian with black at -0.5 and white at +0.5. Black (negative) features show prominence absorption transients. Circular markers show the locations of the prominences from the χ^2 analysis. The bottom right circle is a composite diagram of all prominences; those features identified on both July 18 and 19 have been joined by an arrow and crosses are July 23 data points. The dashed lines are radial and pass through the July 18 data point to aid the eye.
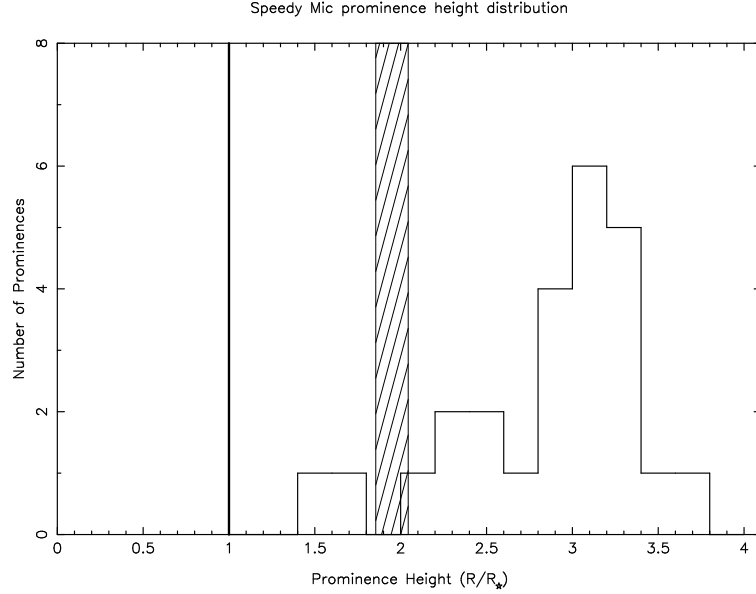
Figure 2.6: Distribution of 25 prominence heights is shown. The solid line is the stellar surface and the hatched area shows the 1σ confidence interval on the location of the co-rotation radius.

more realistic. These parameters give a mean radius for Speedy Mic of $R = 1.06 \pm 0.04\ R_\odot$, which as one might expect is considerably larger than the $0.73\ R_\odot$ (Gray, 1992) Zero Age Main Sequence (ZAMS) radius that the K3V spectral type would suggest. Using Speedy Mic's determined radius and its associated error we can feed these back into another Monte Carlo trial to find the co-rotation radius in stellar radii. For the mass we adopt $M_* = 0.82 \pm 0.08\ M_\odot$. This covers a range of masses including the $0.74\ M_\odot$ (Gray, 1992) K3V ZAMS and the $0.9\ M_\odot$ determined by Wolter et al. (2005) using pre-main sequence evolutionary models of Siess et al. (2000). The location of the equatorial co-rotation radius is found to be $R_k = 1.95 \pm 0.07\ R_*$.

The histogram of prominence heights shown in Fig. 2.6 clearly has a strong peak near $3\ R_*$. This is considerably above the co-rotation radius, as illustrated in Fig. 2.6 by the hatched region. The mean of the prominence distribution is at $2.85 \pm 0.54\ R_*$, with a median of $3.00\ R_*$ which is less affected by the two prominences found below co-rotation. After the $3\ R_*$ peak the number of prominences falls off steeply with only two prominences found above $3.4\ R_*$.

2.4.2 Evolution of prominence system

This dataset provides us with the opportunity to study the evolution of the prominence system on two different timescales, that of consecutive nights and then four nights later. In Table 2.2 we attempt to match prominences found on different nights based on the simple criterion of a phase difference less than $\Delta\phi = 0.03$. This corresponds to approximately the extent in phase (the size) of the largest prominences. It is important, especially when considering consecutive nights, to note what physical rotation cycle each part of the phased timeseries belongs to. The interval varies from 2 to 3 rotations between July 18 and July 19 and this is given in Table 2.2 for each identified feature.

Using the above criterion to match the prominences we find that 8 of the 10 prominences observed on July 18 have matching features on July 19. Furthermore, that all 8 are observed at slightly later phases on the second night than on the first night. We also find that 6 of the 8 are observed to have moved outwards (increased in height) away from the star. These observations are shown in graphical form in the bottom-right panel of Fig. 2.5.

It is worth briefly mentioning individual prominences in slightly more depth. Some prominences are easily identified on multiple nights. The strong absorption transient labelled as prominence A in Figs. 2.4 & 2.5 and Table 2.2 at phase $\phi \simeq 0.11$ is present at all three epochs. Prominence F at $\phi \simeq 0.54$ is also present in all three epochs also. In addition, the faint absorption feature at $\phi \simeq 0.87$ is clearly visible on July 18 and 19.

Prominence B at $\phi \simeq 0.219$ on July 18 seems to have disappeared by the next night. Prominence G at $\phi \simeq 0.61$ is observed at a much lower height on July 19 than on July 18. We think this to be a newly formed prominence and in fact the feature observed on July 18 is still present but is much weaker than the new feature and is too blended in phase for the tracking technique to resolve the feature's unique χ^2 minimum.

Prominence H at $\phi \simeq 0.70$ is faint on July 18 and at the start of observing on July 19 at phase $\phi \simeq 0.73$ a corresponding faint feature can just be seen finishing its track across the H_α profile. At the end of that night however a much stronger absorption feature is seen at a slightly later phase. We think this is most probably a new feature. This is interesting as it suggests a very rapid formation timescale. In less than 9 hours a new prominence has formed with a height of $R = 2.49 \; R_*$.

Prominence I at $\phi \simeq 0.82$ is seen to experience a large increase in height between July 18 and July 19. This particular prominence signature has a slightly ambiguous fit on July 18 and the lower height is only marginally favoured over that of a prominence at a considerably greater height. It is possible therefore that the matching of prominence I with the feature on July 19 is just coincidence.

The observations on July 23 give us a valuable opportunity to study evolution on a longer timescale, with a gap greater than 10 stellar rotations. Somewhat surprisingly, all five features found on July 23 have counterparts on July 19. The heights of the features appear fairly randomly distributed (and often in between) with respect to their July 18 and 19 counterparts. We therefore suggest that all five prominences have re-formed in the intervening time.

2.5   Discussion

It is clear that the Speedy Mic prominence system is densely packed and relatively evenly spaced in longitude around the surface of the star. This high level of prominence activity is what might be expected on this luminous X-ray ultra-rapid rotator. Interestingly we find that the prominences are concentrated at $\simeq 3\ R_*$, well above the surface of the star and at twice the height of the co-rotation radius above the stellar surface. The traditional model of stellar prominence systems by Collier Cameron & Robinson (1989a) describes prominences at a range of heights but with a concentration at the co-rotation radius. This dataset certainly challenges this, as 23 of the 25 prominences are found above the co-rotation radius. This immediately requires large extended magnetic loops that go well beyond the co-rotation radius to support such structures.

At first glance this would appear to be at odds with the high coronal densities measured with FUSE, Chandra and XMM-Newton of a range of rapid rotators (Dupree et al. 1993; Schrijver et al. 1995; Brickhouse & Dupree 1998; Audard et al. 2001; Mewe et al. 2001; Young et al. 2001; Güdel et al. 2001; Sanz-Forcada, Brickhouse & Dupree 2003; Sanz-Forcada, Maggio & Micela 2003). These measurements suggest that the coronae of rapid rotators must be compact, since such high densities could not be confined at large distances above the stellar surface. The lack of significant rotation modulation in the X-ray emission can be explained if most of the emission comes from high-latitude regions that

never pass behind the star as it rotates. This suggestion was given very striking support by the BeppoSax observations of two flares on AB Dor that showed no rotational modulation of the emission, despite the fact that the flares lasted for more than one rotation period of the star (Maggio et al., 2000). Modelling of the decay phase of the flare suggested that the flaring regions were compact, and therefore must have been located close to the rotation pole. Emission from high latitudes on rapid rotators is not perhaps surprising given the very common appearance of high-latitude (even polar) spots on these stars (Strassmeier, 1996). The relationship between the high-latitude flux and the coronal distribution of X-ray emission has been determined by extrapolating the surface magnetic field on AB Dor obtained from Zeeman-Doppler imaging and calculating the structure of the X-ray emission, assuming a simple heating law (Jardine, Collier Cameron & Donati 2002; Jardine et al. 2002a). The resulting X-ray emission is confined fairly close to the stellar surface and has a large component at high latitudes. By comparing the results of this technique with Chandra observations obtained simultaneously with the optical spectra used for Zeeman-Doppler imaging, Hussain et al. (2005) showed that not only the magnitude and rotational modulation of the X-ray emission, but also the line shifts were consistent with the results of modelling based on field extrapolation.

If the coronae of fairly rapid rotators such as AB Dor are compact, then it might be expected that at even higher rotation rates such as that for Speedy Mic the coronal extent might be even less. For the supersaturated star VXR45, Marino et al. (2003) found a large X-ray rotational modulation, showing that there is significant structure in the corona with clearly-defined bright and dark regions. This is what would be expected if the corona had been centrifugally stripped as a result of the rapid rotation (Jardine & Unruh, 1999; Jardine, 2004), leaving a corona that is very compact with only a patchy coverage of X-ray bright regions. In the case of Speedy Mic which appears to lie in the saturated part of the L_x - period relation it also appears unlikely that gas at coronal temperatures could be confined by the star's magnetic field at the heights at which the prominences are observed. The large number of prominences shows that the confining magnetic field must still possess a significant degree of complexity even out to these large heights.

One recent theoretical model by Jardine & van Ballegooijen (2005) puts forward a new model for prominence formation that does *not* require a complex global magnetic field with large extended loops in the X-ray corona supporting these prominences. Instead they propose that the prominences are supported by the re-connection of oppositely directed

wind-bearing field lines over coronal helmet streamers. This would result in long thin highly curved loops extending out to large radii. These could then fill up with gas that was originally part of the wind and be dragged outward in radius. Jardine & van Ballegooijen (2005) find a maximum height for the summits of the coolest magnetic loops (y_m) in terms of the stellar co-rotation radius (R_k) given by:

$$\frac{y_m}{R_*} = \frac{1}{2}\left(-1 + \sqrt{\left(1 + 8\left(\frac{R_k}{R_*}\right)^3\right)}\right).$$ (2.4)

Using the Speedy Mic co-rotation radius $R_k = 1.95\ R_*$ we find that $y_m = 3.35$ R_*. This would seem to be consistent with the observed prominence heights. However it should be noted that while Jardine & van Ballegooijen (2005) illustrate that such magnetic loops can achieve equilibrium they do not attempt to model the prominence structures themselves.

The fall-off in the number of prominences detected beyond $R \simeq 3\ R_*$ may suggest quite a different scenario to the one outlined above. The traditional model of prominence support requires large magnetic loops in the X-ray corona. The strongest component at large distances away from the star is the simple dipole, however, this could only provide effective support for prominences near the equatorial plane (as discussed in Chapter 1). Now if we assume that the observed prominences are actually in the equatorial plane then the highest prominence that would still transit the stellar disc assuming the inclination of $i = 70 \pm 5^o$ is at $R \simeq 3.73\ R_*$. The highest detected prominence was feature F at $R = 3.64$ R_* on July 19, so for Speedy Mic we cannot exclude the possibility that prominences are being supported in this manner. If this were the case, the highest prominences would only start to graze the stellar disc at high latitudes resulting in a smaller absorption signature.

2.5.1   Evolution of the prominence system

As described in §2.4 we have been able to identify prominences at similar longitudes on multiple epochs. On the timescale of consecutive nights (2 to 3 rotations) we have witnessed the evolution, apparent formation and disappearance of several prominences. The fact that prominences are observed at similar phases more than 10 rotations later is also interesting as it suggests considerable stability of the prominence-supporting magnetic structures.

Examination of the reported prominences heights and phases in Table 2.2 reveals a prominence system that appears to increase in height and lag behind in phase on the timescale of consecutive days. It should be noted though that the apparent changes in height of many of the prominences is still consistent, within the uncertainties, with a static prominence system. The observed phase lags are probably more accurate measurements. This is especially true of the narrow absorption features where the ridgeline of the absorption transients are distinct. The problem with the larger and often stronger absorption features is that they can be comprised of multiple components. This makes the confident re-identification of features on subsequent nights more difficult.

The observed phase lag between the epochs could be the result of a number of factors. Donati & Collier Cameron (1997) and Donati et al. (1999) attribute similar observations on AB Dor to the differential rotation of the prominence footprints. This then allows the latitude of the footprints to be located. In doing so though they assume that the supporting magnetic field lines are rigid and thus maintain prominence co-rotation. For Speedy Mic however we find that the phase lags between the consecutive days are generally of the order of $\Delta\phi \simeq 0.01$. This results in prominence periods that are longer than the surface rotation rate at any latitude on the stellar surface and so cannot be explained by differential rotation. Instead, it may suggest that the stellar magnetic field is unable to enforce co-rotation. If we consider this in the context of prominences moving away from the star then the observed phase lag between consecutive days could be the result of the prominences being dragged back in phase due to conservation of angular momentum. As such the phase lags observed between consecutive days have the potential to inform us about the rigidity of the confining magnetic field.

If the above model is correct then we need to explain why there are more noticeable phase lags between epochs on Speedy Mic than on AB Dor. This may simply be due to the location of the prominences relative to the co-rotation radius. We find that prominences group around a height which is twice that of the co-rotation radius above the stellar surface yet, as already discussed, prominences on AB Dor are found at or just above the co-rotation radius. Therefore it may be more difficult for the magnetic field to enforce co-rotation of the prominence structures on Speedy Mic. Larger phase lags have, however, been observed before on very high prominences on AB Dor. During observations in 1994 Collier Cameron et al. (1999) found that a prominence they observed moving radially outward from 3 or 4 stellar radii to 8 stellar radii lagged behind in phase. The authors

attributed this to the prominence conserving angular momentum.

Examining now the two prominences confidently identified in all three epochs, prominences A and F, we find that they both have relatively large phase lags between July 18 and 19 (two and three stellar rotations, respectively). Then approximately ten rotations later we observe only a similar additional lag in phase on July 23. This would suggest that the prominences have reformed at least once in the intervening ten rotations. This slower lag in phase may indeed be due to differential rotation of the prominence footprints. Barnes (2005) fitted a solar like differential rotation law to starspots observed on Speedy Mic of the form $\Omega(\theta) = \Omega_0 - \Delta\Omega\sin^2(\theta)$, (where θ is the stellar latitude and Ω_0 the equatorial rotation velocity). The values obtained were $\Omega_0 = 16.5361 \pm 0.0006$ rad.day^{-1} and $\Delta\Omega = 0.033 \pm 0.003$ rad.day^{-1}. We can use this to attempt to locate the latitudes of the prominence footprints, as was done for AB Dor by Donati & Collier Cameron (1997). The observed phase lag over the ten rotations corresponds to a period for prominence A that would place it at a latitude of $\simeq 50 \pm 10°$ on the stellar surface. Similarly prominence F would correspond to a latitude of $\simeq 80 \pm 20°$. The associated uncertainties on these latitudes come from the uncertainty in the recurrence time and the uncertainty in the strength of the differential rotation. These are similar latitudes to those found by Donati & Collier Cameron (1997), suggesting that the prominence footprints are located well above the stellar equator.

Given the picture of prominence evolution that we have just described, it seems that much care must be exercised in performing such an analysis of the prominence footprint locations. If the phase at which a prominence is observed is a function of its height then this must be taken into account. In order for a valid assessment of the phase lag due to differential rotation we need to observe the prominence at the same height on multiple epochs. It seems that this would require observing a prominence that has reformed at a similar phase and is at a similar stage in its height evolution. Due to our lack of understanding of the prominence formation mechanism we cannot be sure that we are really observing the same loop structures. This is brought home by the data in Table 2.2 where we find that the two prominences (G and H) thought to have reformed between July 18 and 19 were actually observed at slightly later phases than the original structures. This may point to a re-organisation of field at the prominence footprints such that the newly formed loops are not at exactly the same locations as the previous ones. If so then this would invalidate our analysis of the prominence footprint latitudes.

While most of this chapter has focussed on the rapid absorption transients interpreted as stellar prominences there are clearly other interesting things happening in the H_α line. The raw timeseries in Fig. 2.2 shows slower variations in the underlying H_α absorption. These seem to split the star into two longitude bands, for one half of the observed stellar rotation we see dark regions of absorption while for the other half we see much less absorption. This is quite different from the H_α profile of AB Dor, where no such obvious contrast has been observed and as such requires further study.

2.6   Conclusions

The improved prominence tracking technique allows for the fast, relatively automated detection and tracking of multiple prominences as they cross the stellar $v \sin i$ profile. This involved a matched filter analysis technique and fitting a Gaussian model with a simple stellar limb-weighting function using a χ^2 analysis. The Speedy Mic H_α timeseries has revealed one of the most (if not the most) densely packed and active prominence systems seen to date.

We have shown that the distribution of prominence heights peaks considerably above the co-rotation radius. This provides further evidence against the traditional model of prominence support via large magnetic loops in the X-ray corona. Having discussed an alternative theoretical model of prominence support it would be very interesting to carry out Zeeman Doppler Imaging of Speedy Mic to map the surface magnetic field.   In principle this could be done using SEMPOL at the AAT, but Speedy Mic is too faint to avoid excessive phase smearing. Unfortunately Speedy Mic has too southerly a declination for observation with the new echelle spectropolarimeter 'ESPaDOnS' (see Donati 2003) on the 4-m Canada-France-Hawaii Telescope. Ideally, an analagous high-throughput spectropolarimeter at a 4-m or 8-m southern-hemisphere telescope is required.

This study provides tentative evidence for a coherent picture of prominence evolution on Speedy Mic. Whether prominences are actually moving away from the star and lagging behind in phase as they attempt to conserve their angular momentum is still subject to interpretation. Further observations will be necessary in order to more confidently distinguish between this effect and that of the differential rotation of the prominence footprints. These should focus on tracking the evolution of individual prominence structures

with the shortest time intervals possible. If we can obtain repeat phase coverage on three or more consecutive nights then we could hope to track multiple prominences through their entire evolution. Thus we could hope to define the relationship between prominence height and observed phase lag. This should give us an insight into the strength and nature of the magnetic support and further constrain angular momentum loss through prominence ejection.

CHAPTER 3

Determining the physical properties of stellar prominences

This chapter is based on a paper published in the Monthly Notices of the Royal Astronomical Society by:

Dunstone, N.J., Collier Cameron, A., Barnes, J.R., Jardine, M. (2006, MNRAS, 373, 1308)

All the work described here was carried out by myself.

3.1 Introduction

As described in Chapter 1, stellar prominences were first reported by Collier Cameron & Robinson (1989a) as rapid transient absorption features passing through the Doppler broadened H_α line of the rapidly rotating K0 dwarf AB Doradus (AB Dor). From subsequent observations these clouds of material were shown to be in presumably magnetically enforced co-rotation with the stellar surface and so dubbed "prominences". Since their discovery prominences have now been reported on around a dozen rapidly rotating late-type stars (see Cameron et al. 2003 for a recent review). These observations have been primarily restricted to the strong Balmer lines, often only (H_α) and occasionally hydrogen beta (H_β).

As was discussed in the previous chapter, a model for prominence support which does not require closed magnetic field lines to extend to several stellar radii above the surface was put forward by Jardine & van Ballegooijen (2005). Instead, they propose that prominences are supported by the re-connection of oppositely directed wind-bearing field lines over coronal helmet streamers. This would result in long thin, highly curved, loops extending out to large radii. These could then fill up with gas that was originally part of the wind, forming the observed prominences. However while Jardine & van Ballegooijen

(2005) show that such magnetic loops can achieve equilibrium they do not attempt to model the prominence structures themselves. In order to test such models we need more information on the physical properties, evolutionary scenarios and lifetimes of prominence systems.

Solar prominences are observed in the H_α line as emission features seen off the solar limb. Photons at this wavelength originating from the surface of the Sun can be absorbed by a hydrogen atom in the prominence, thus exciting its electron from the first (n=2) to the second (n=3) excited state. Providing such an atom does not undergo a collision, the electron will de-excite either to the ground state (n=1) via the emission of a Lyman beta (Ly_β) photon or, almost equally likely, back to the first excited state via the release of another H_α photon. Ly_β photons are re-absorbed almost immediately, creating new H_α photons. As this emission is isotropic most photons originating from the part of the solar surface occulted by a prominence are 'scattered' out of our line-of-sight, creating an absorption feature. Similarly, photons can be scattered into our line-of-sight by a prominence seen off the solar limb, creating an emission feature. Observing a stellar prominence as both an absorption and an emission feature could potentially provide important insights regarding its physical and geometrical properties.

The initial motivation for this study arose from a fortuitous coincidence. Two weeks after we obtained the AAT Speedy Mic observations presented in Chapter 2, a separate team performed very similar high-resolution spectroscopic observations of Speedy Mic with the VLT. Two papers using this dataset have been published by the original observers, Wolter et al. (2005) and Wolter & Schmitt (2005). Wolter et al. (2005) provides a full account of the observations and then goes on to perform Doppler imaging. Wolter & Schmitt (2005) focus on the potential of the CaII H & K lines for future Doppler imaging of the stellar chromosphere.

Here we compare the two epochs of observations in §3.2, then in §3.3 we use the VLT observations to obtain prominence physical properties. In §3.4 we report the observation of loops of emission and show that these are caused by prominences seen off the stellar disc. We discuss our results in the context of the coronal structure of Speedy Mic in §3.5. Finally we present our conclusions in §3.6.

51

3.2 Observations

The Speedy Mic observations were obtained from the ESO Science Archive Facility. They consist of two nights (2002 August 02 and 07) of data using the 8.2-m Very Large Telescope (VLT) UT 2. The spectra cover a large wavelength range by using the UVES spectrograph in dichroic mode, 3260Å to 4450Å (the "blue-arm") and 4760Å to 6840Å (the "red-arm"). A 1″ slit width gave a spectral resolution of $\lambda/\Delta\lambda \approx 40\ 000$. Speedy Mic was observed continuously on both nights yielding complete and uninterrupted phase coverage of one revolution on each night.

We re-extracted the data using ECHOMOP, the échelle reduction package developed by Mills (1994) and its implementation of the optimal extraction algorithm developed by Horne (1986). During the data reduction we encountered the same problem reported by Wolter et al. (2005) of variations in the MIT-CCD red-arm continuum, presumably due to the CCD manufacturing process. In order to correct for the small scale structure we created a "balance frame" that included these variations.

In total there are 125 spectra on August 02, each with an exposure time of 200 s. The readout time of 70 s makes the cadence of exposures 270 s, therefore 122 exposures were required to cover the 0.38 day period of Speedy Mic. The situation on August 07 is slightly more complicated with the exposure times being adjusted between 120 s and 200 s to compensate for variable sky conditions. Four spectra had to be abandoned during reduction due to over-exposure, yielding a total of 141 usable spectra.

After each spectrum was extracted, we normalised the spectral orders by fitting the continuum using splines. Due to the difficulty in locating the continuum level in the blue orders we used a two-dimensional fit that constrained the local shape of the continuum. We discuss the limitations of this technique in §3.3. The resulting signal-to-noise (S/N) of individual spectra were very high. For example near the centre of the order containing the H_α line the unbinned S/N ranges between 350 and 600 per 0.05Å wavelength element throughout the night.
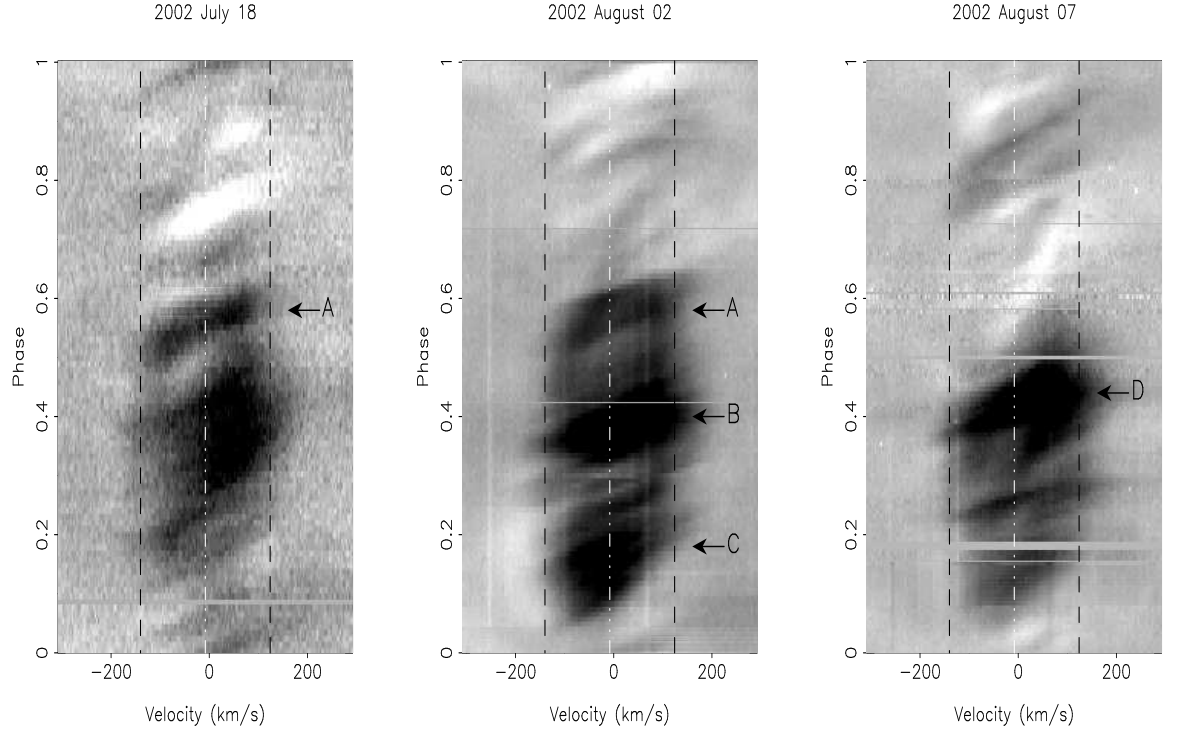
Figure 3.1: Raw H$_\alpha$ timeseries spectra for 2002 July 18, August 02 & 07, with phase plotted against velocity. Dashed black lines show the $v \sin i$ limits and the central dashed white line shows the radial velocity of Speedy Mic. The grey-scale runs from black at 0.85 times the local continuum level, to white at 1.05 times continuum. The large prominences discussed in the text are labelled.

3.2.1 A fortnight of evolution

Thanks to the fortuitous coincidence of two different Doppler imaging groups (using different telescopes) both observing Speedy Mic within two weeks of each other we now have an exciting and unique opportunity. The two to three week time gap is not normally an easy one to achieve with high-resolution spectroscopy. Practical considerations like instrument availability on any given telescope normally limit the time span of observations at any given epoch to mere days.

In Fig. 3.1 we have plotted the H$_\alpha$ trailed spectrum (timeseries) of July 18 from Chapter 2 and compare it to August 02 and 07. Note that for comparison with this work the July 18 timeseries has been re-phased taking the epoch of phase zero to be the first observation on August 02. There are fifteen days between July 18 and August 02, which

equates to approximately 40 stellar rotations and there are twenty days or 53 rotations between July 18 and August 07. Despite the differences in the quality of the data between the two epochs it is clear that qualitatively the timeseries appear similar.

A visual examination of Fig. 3.1 shows that August 02 does indeed share features of both July 18 and August 07. We can see that one half (the 'dark' side) of the Speedy Mic rotation still has increased absorption due to large prominences. In the other half (the 'light' side) of the stellar rotation cycle the surface is more easily seen and we observe weaker prominences embedded in and around bright surface 'plage' features. Identifying and comparing individual prominences is difficult as there has been considerable evolution between the July and August epochs. Very few of the weaker prominences observed on the light side can be re-identified. The large dark region at $\phi \approx 0.35$ appears stronger and more compact in phase in the August observations. The strong group of prominences at $\phi \approx 0.15$ seen on both August epochs has no counterpart in the July observations.

The only prominence that can be compared with any confidence is prominence A at $\phi \approx 0.55$. This prominence was reported in Chapter 2 (again labelled 'A') as being present on all three nights (July 18, 19 and 23). On August 02 we find a prominence at a very similar phase. Yet on August 07 there is no evidence of the prominence - only a bright surface region. So can this prominence seen on August 02 really be the same structure that was observed fifteen days earlier? The main properties of a prominence that we can measure at *both* epochs are its location in the rotational phase, the projected distance from the Speedy Mic rotation axis (height) of the prominence and the maximum fractional depth below the continuum. The first two of these are found from the Gaussian matched-filter tracking technique described in detail in Chapter 2. The difference in the two phases of observation between July 18 and August 02 is $\Delta\phi = 0.007$, which is the same as the phase separation between consecutive exposures. The height of the prominence A was quoted as 2.79 ± 0.11 for July 18 and is found to be 2.99 ± 0.07 on August 02. The maximum fractional depth relative to the continuum when the prominence is transiting the disc center is ≈ 0.87 on July 18 and ≈ 0.88 on August 02.

The similarity of the properties of this prominence at both epochs lead us to conclude that this is almost certainly the same structure. As we shall discuss in §3.5, however, we are not suggesting that this prominence necessarily contains the same material at both epochs.

3.2.2   Spectral lines showing prominence signatures

After each spectral order was extracted we stacked the exposures to create a timeseries for each order. We then collapsed this timeseries to create a mean spectrum and subtracted it from each individual spectrum. This left us with only time varying features, i.e. star-spots, surface plage regions and prominences.

We performed a visual inspection of all orders for evidence of prominence absorption features moving rapidly through the line profile, just as we observe in the H_α line. This dataset is ideal for an unbiased search, as it is of exceptional S/N and the large wavelength range gives us plenty of lines to examine. As was expected, the lines of the Hydrogen Balmer series all show evidence of prominence material. Starting with the strong H_α line the same characteristic prominence pattern is repeated, with different strengths, in each line. It is possible to visually identify this pattern all the way down to H_{14} at $\lambda = 3721$Å. Prominences in the later hydrogen lines are so optically thin that only the very strongest prominence is identifiable. Furthermore the star-spot residuals from the many photospheric metal lines present at these blue wavelengths have strengths of the same order of magnitude as the prominence signatures. Therefore for the rest of this chapter we restrict our analysis to lines down to H_{10} at $\lambda = 3835$Å, all of which are shown in Fig. 3.2.

The singly ionised calcium (CaII) H & K lines at $\lambda = 3968$Å and $\lambda = 3933$Å have strong emission cores and show strong prominence absorption signatures. These lines are discussed at length in §3.3.2. Finally, we find very weak prominence signatures in the sodium doublet at $\lambda = 5890$Å. Unfortunately these are poorly placed at the very start of an order; this combined with their strengths make them unsuitable for further analysis. No other lines showed evidence of prominence material.

3.3   Prominence masses

3.3.1   Column density of hydrogen in the n=2 level

Due to the large wavelength range and the high S/N of these observations it is possible to compare the strengths of individual prominences in different hydrogen Balmer lines.

In order for such a comparison to be possible each line has been re-binned to the same velocity scale, 3.1 km s^{-1} per pixel.

The trailed spectra of all eight Balmer lines being considered are shown in Fig. 3.2 for August 02. Some of the lines have small problems with their reduction. H$_\beta$ clearly has four bad spectra, which arise due to a bad column in the earlier part of this spectral order. When ECHOMOP traces this order it rejects and interpolates over these bad pixels; however this procedure was unsuccessful for these four spectra and a good trace was not obtained. Consequently they are not used in further analysis. H$_{10}$ shows a vertical line which is due to another chip defect. Finally it should be noted that the H$_\epsilon$ line is superimposed with the CaII H line and due to the strong prominences seen in CaII we do not use H$_\epsilon$ further in this analysis.

Calculating the curve of growth

The ratio of the equivalent widths (EWs), or strengths, of individual prominences in different hydrogen lines can be used to calculate the column density of hydrogen atoms in the $n = 2$ level. In order to do this we need to first calculate the absorption cross-section of a hydrogen atom at the centre of each Balmer line. This is given by:

$$\sigma_\nu = \frac{g_u}{g_l} \frac{c^2}{8\pi\nu^2} \Phi\left(\nu\right) A_{ul} \tag{3.1}$$

where g_u and g_l are the statistical weights of the upper and lower levels of the transition, c is the speed of light and ν is frequency. A_{ul} is the Einstein A-coefficient and gives the probability of spontaneous decay from the upper to the lower level. Φ is the line profile for which we use a Voigt profile approximation. The Lorentz parameter was taken to be natural (radiative) dampening. This is justified because of the scattering mechanism that causes us to observe the prominences in absorption whilst transiting the stellar disc. This tells us that the time between collisions within the prominence is longer than the spontaneous de-excitation time and so collisional broadening is unimportant. We assume the dominant broadening comes from two sources. Firstly the thermal Doppler velocity of hydrogen at a prominence temperature of 10,000 K which is 12.9 km s^{-1} and secondly a random turbulent velocity.

Solar prominences exhibit random turbulent motions at least as great as a few km s^{-1} (Engvold, 1998). The amount of turbulence we include in the line profile will have
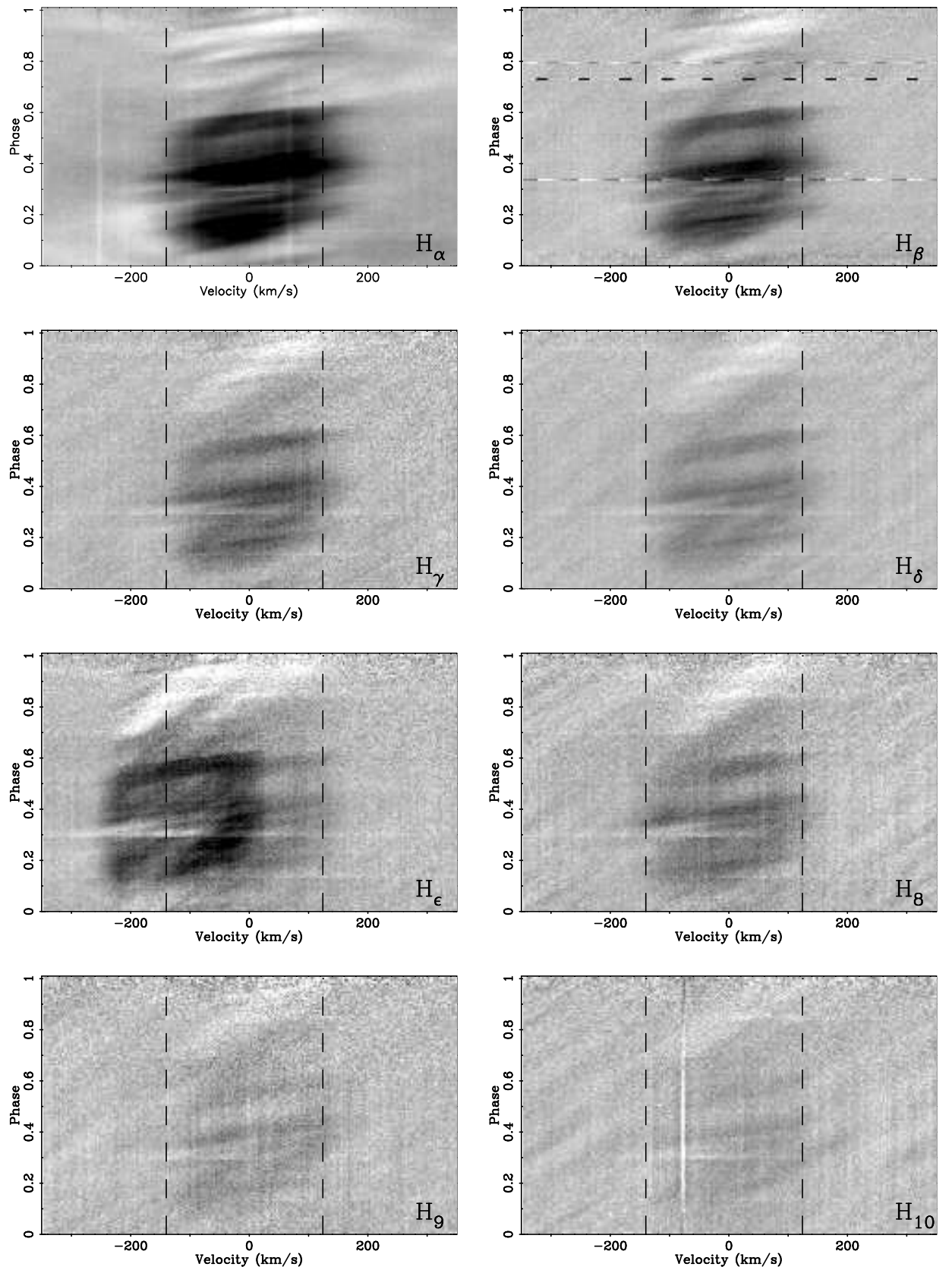
Figure 3.2: The first eight lines of the hydrogen Balmer series for August 02 are shown. An average profile has been subtracted from each timeseries (see text). The contrast is such that black is 0.85 and white is 1.05 times the local continuum level. Dashed vertical lines show the $v \sin i$ limits. Note H_ϵ is blended with the $CaII\ H$ line and H_β has four bad spectra (see text).

57

a greater effect on the CaII H&K observations (discussed in §3.3.2) than on those of the hydrogen Balmer lines. This is because the calcium atom is heavier than the hydrogen atom and so has a much smaller thermal Doppler velocity of 2.0 km s^{-1}. We can place an upper limit on the possible turbulent velocity in Speedy Mic prominences by measuring the widths of the smallest prominences in the CaII H&K lines. A width of approximately 18 km s^{-1} is found for the smallest absorption features as they cross the centre of the stellar disc. If we assume that these small prominences are unresolved then the measured width should be due to turbulence, but we also need to consider the rotational smearing that occurs during a 200 s exposure. The average prominence height found in Chapter 2 of 3 R$_*$ corresponds to an orbital velocity of 400 km s^{-1}. The Speedy Mic radius was calculated in Chapter 2 (Eqn. 2.3) from a simple dynamical argument to be 1.06 ± 0.04 R$_\odot$, considerably more bloated than its K3V main-sequence radius. Therefore during a single exposure such a prominence travels approximately 11% of the Speedy Mic radius which in velocity space is 14 km s^{-1}, the majority of the observed width. If we assume that these velocities add in quadrature then we arrive at an upper limit of 11 km s^{-1} for the turbulent velocity. The validity of these assumptions are discussed further in §3.5.2. Now we assume a turbulent velocity of 5 km s^{-1} for the following results.

The optical depth is found by multiplying the absorption cross-section per atom by the column density (N_2 - the total number density of hydrogen atoms in the $n = 2$ level per square meter):

$$\tau_\nu = \sigma_\nu N_2 \tag{3.2}$$

Therefore the EW is found for each line by integrating over the line profile:

$$EW = \int \left(1 - \exp^{-\tau_\nu}\right) d\nu \tag{3.3}$$

By considering a range of different values for the column density of atoms in the $n = 2$ level we obtain a *curve of growth* for each line. This describes how the EW of the line changes as we increase the density of absorbers. At low densities (optically thin) the curve of growth is a linear increase in the EW proportional to the probability of the transition. As we increase the column density, each line eventually starts to saturate in its core leading to a slowing in the growth of the EW. When the Doppler core is totally saturated (optically thick) then further growth of the EW occurs at a rate determined by the opacity in the Lorentzian line wings.

Once we have the EW of each line as a function of column density it is then possible to express each line's EW as a fraction of $EW(H_\alpha)$. These ratios are shown as the solid lines in the left panel of Fig. 3.3. This shows that H_α starts to saturate first. Its growth of EW slows and the relative strength of the later lines increases. One by one the other lines start to saturate also. Therefore by measuring the ratio of the observed EWs from the timeseries it should be possible to find a unique value for the column density of each prominence.

Measuring the EW ratios

As mentioned earlier it is unfortunately impossible to use H_ϵ in this analysis due to it being blended with the CaII H line. Even those parts of the line not directly superimposed on the calcium line could be subject to off-disc emission from it (as discussed in §3.4). We also had to abandon measuring the H_8 line due to anomalous results caused by a very strong neighbouring metal line. The star-spot residuals in this line appeared strong enough to affect our prominence EWs. Thus the analysis is now restricted to: H_α, H_β, H_γ, H_δ, H_9 and H_{10}.

To measure the EW of the prominence absorption signatures it is first necessary to remove the 'time-invariant' background stellar spectrum. For Speedy Mic this is a rather more difficult task that one might first anticipate, the problem being that much of the timeseries is in strong absorption due to the prominence material. Other parts of the timeseries, however, show strong surface emission features (plage regions). The nature of the background surface spectrum for the regions covered by large prominences is unknown from H_α alone. It could well be that these phases are in even stronger emission. By examining the later Balmer lines in Fig. 3.2, where even the strongest prominences become optically thin, we can see that this is probably not the case. It is also important to remember that the bright surface plage regions contribute to the flux that the prominences receive and so should not simply be ignored. We finally chose to represent the background spectrum by taking the mean of the 'light' half of the timeseries which is devoid of strong prominences. Specifically the phases 0.65 to 1.0 were used to create the mean profile that was then subtracted from the entire timeseries. Initially we tried a much smaller range of phases which apparently had no prominences. However this produced an asymmetric mean profile and upon further examination a bright surface feature was present. Using
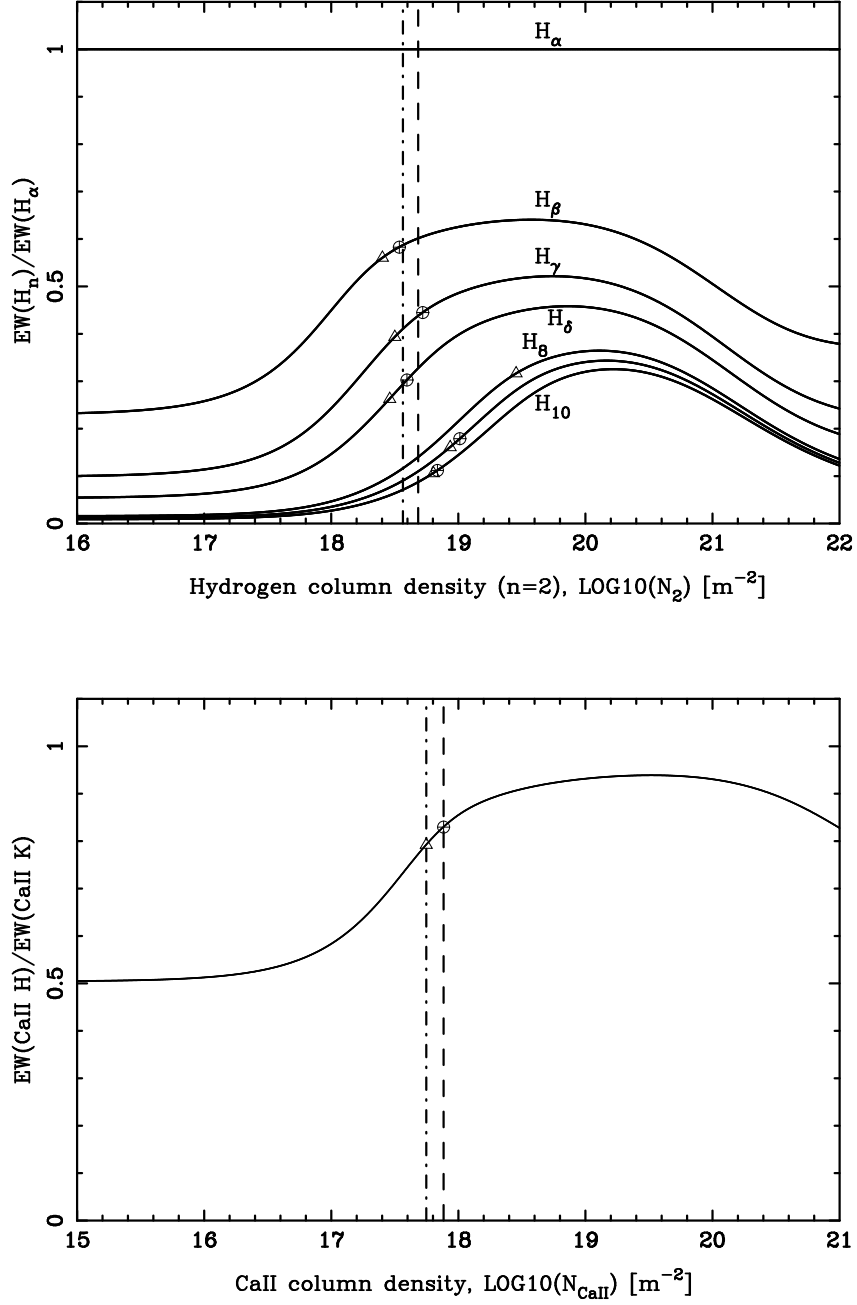
Figure 3.3: Obtaining column densities in n=2 of hydrogen (top panel) and CaII (bottom panel). Solid lines show theoretical curve of growth EW ratios, as described in §3.3.1 for an example turbulent velocity of 5 km s^{-1}. Circles show intersection with observed ratios for prominence A and triangles for prominence B. The dashed vertical line is the optimal average column density for prominence A and the dot-dashed line for prominence B. Note H$_\epsilon$ is absent due to blending with the CaII H line and that H$_8$ is anomalous (see text).

this mean profile we obtained column densities that differed by a factor of 1.25 to 2.5 from those reported below. This is similar to the level of uncertainty we find on the prominence column densities.

We use the high S/N H_α timeseries to identify which pixels in the timeseries are to be used for the analysis. In practice this was done by selecting a box around a single prominence feature and selecting all the negative pixels within that box. The EWs are then simply the ratio of the sum of the corresponding pixels in each line to that of H_α. Associated uncertainties on these ratios are also derived.

The points where the observed EW ratios intersect the theoretical ratio of the curves of growth are shown for each line in Fig. 3.3. The uncertainties in measured EW ratios are then translated into uncertainties in column density using the model curves of growth ratios. Thus we can take an inverse variance weighted average of these points to obtain a single estimate for the column density in the n=2 level of hydrogen. The final uncertainty on the column density of each prominence is estimated from the standard deviation of the different line ratios.

Obviously the high S/N of the stronger Balmer lines like H_β allow us to measure the ratio of their EWs to H_α to a much greater precision than some of the weaker, later, Balmer lines. However because it turns out that the cloud is quite optically thick in H_β it means that there is a larger uncertainty on the column density once the measurement uncertainty has been converted to an uncertainty in the column density. Therefore H_γ and H_δ have most weight when calculating the optimal column density.

This technique only works for the very strong prominence features. As already discussed there are many weaker prominences that cross the star's brighter hemisphere (phases 0.6 - 1.0), most of which can only be detected in H_α and H_β. We therefore limit our analysis to the three strongest prominence signatures on August 02 (labelled A,B and C in Fig. 3.1) and the strongest prominence on August 07 (labelled D in Fig. 3.1).

Table 3.1: The measured values and derived quantities are display along with their uncertainties. These results assume a turbulent velocity of 5 km s^{-1} (see text). Note that there is a systematic uncertainty on the CaII column density of log N_{CaII}=±0.25 (see text). We also report the average and standard deviation of the four prominences for various physical properties.

Prominence	Fractional Depth	Optical depths		Column densities [m^{-2}]			Areas	Masses
		$\tau(H_\alpha)$	τ(CaII K)	log N_2	log N_{CaII}	log N_1	log A [m^2]	log M [kg]
A	0.12±0.015	25.7	21.3	18.68±0.19	17.88±0.25	23.53±0.25	17.31±0.06	14.06±0.26
B	0.25±0.005	19.5	15.8	18.56±0.21	17.75±0.25	23.40±0.25	17.63±0.03	14.25±0.25
C	0.19±0.01	22.4	13.5	18.62±0.19	17.68±0.25	23.33±0.25	17.51±0.04	14.06±0.25
D	0.24±0.01	21.9	11.7	18.61±0.18	17.62±0.25	23.27±0.25	17.61±0.04	14.10±0.25
Averages		22.4 ± 2.6	15.6 ± 4.2	18.61 ± 0.05	17.73 ± 0.11	23.38 ± 0.11	17.52 ± 0.15	14.12 ± 0.09

The results of this analysis are shown in Table 3.1. We find that the prominences have a relatively small spread of column densities in the $n = 2$ level of hydrogen, with the mean being $\log N_2 = 18.61 \pm 0.05$ m^{-2}. Prominence A has the highest column density at $\log N_2 = 18.68 \pm 0.19$ m^{-2}. As the uncertainty on each individual prominence is greater than the scatter in observed prominence column densities, we quote a final representative column density of $\log N_2 = 18.61 \pm 0.2$ m^{-2}. Multiplying the column densities by the central absorption cross-section in each Balmer line we find the optical depths of prominences in each line. In Table 3.1 we give optical depths in H$_\alpha$ for each prominence. These range between $19 < \tau < 26$ confirming that the prominences are indeed optically thick at the H$_\alpha$ line centre. The optical depth drops to unity at around H$_\delta$ or H$_8$ depending upon the individual prominence.

For the results shown in Table 3.1 we assumed a turbulent velocity of 5 km s^{-1}. As this is considerably smaller than the thermal Doppler velocity of 12.9 km s^{-1}, turbulence had little effect on the resulting column densities. If we increase the turbulent velocity to the upper limit of 11 km s^{-1} the column density increases by $\log N_2 = 0.1$ m^{-2} (or a factor of 1.25). This is smaller than the uncertainty quoted on each prominence column density in Table 3.1.

3.3.2   Column density of CaII

In order to find the masses of the prominences it is necessary to look at resonance lines, that is transitions down to the ground state. While we were able to use many Balmer lines to estimate the column density in the n=2 level, the number of atoms in the ground state (n=1) is so far unknown. The ratio between the populations of the n=1 to n=2 depends on the excitation of the cloud. Two strong lines of singly ionised calcium, CaII H&K, are transitions down to the ground state.

We plot the CaII H&K timeseries spectra in Fig. 3.5. Just as for each of the Balmer lines in Fig. 3.2, we have subtracted a mean stellar spectrum obtained from the same range of phases. The overall general appearance of the prominence pattern looks quite similar to that in the Balmer series. One half of the timeseries shows dark prominence absorption signatures crossing the stellar disc. The other half shows bright plage active regions on the stellar surface. Also visible in the timeseries is a stellar flare at $\phi \approx 0.3$.

This CaII H&K dataset has already been published by Wolter & Schmitt (2005) in the context of using Doppler imaging to map the Speedy Mic chromosphere. They refer to unexplained 'changes on rapid timescales'. As can be seen from Fig. 3.5 these are almost certainly due to the prominence material transiting the stellar disc. As an aside, it is interesting to note that by plotting the spectra as a two dimensional image in Fig. 3.5, it is very much easier to identify and follow common features from one spectrum to the next. Wolter & Schmitt (2005) plotted the same data but as a stacked one dimensional line plot and so unfortunately missed the significance of the rapid absorption transients. It is likely the fact that our brains are developed to be highly proficient at processing and identifying patterns in images that make two dimensional visualisations of data so powerful.

Calculating the curve of growth

We again use the ratio of the measured prominence EWs in order to ascertain the column density in CaII. The curves of growth are calculated in the same manner as for hydrogen. As in §3.3.1 the turbulent velocity is fixed at 5 km s^{-1} for the following work.

The oscillator strength of the CaII K line is exactly twice that of the CaII H line. Therefore, when examining optically thin material the EW of CaII H will be half that of CaII K. As we increase the column density and the CaII K line starts to saturate, the rate of EW growth slows, so the ratio of the strengths of the two lines decreases. This is shown in the bottom panel of Fig. 3.3.

Measuring the EW ratios

In order to measure the EWs both CaII lines were binned onto the same wavelength scale as the Balmer lines. The same points in the timeseries identified from the H$_\alpha$ timeseries were used to find the EWs. The only difference, however, is that we only used the left-hand side, the side with negative velocity with respect to the centre of both lines. This is because of the H$_\epsilon$ contamination of the CaII H line. This extends to just under half of the CaII H line profile. To investigate what effect this may have on our results we performed the same analysis on the hydrogen Balmer lines and compared it to our results in §3.3.1 which used the whole of the timeseries. We found that this produced a scatter in the derived column densities of up to log N$_2$ = 0.2 m^{-2} (or a factor of 1.6). However
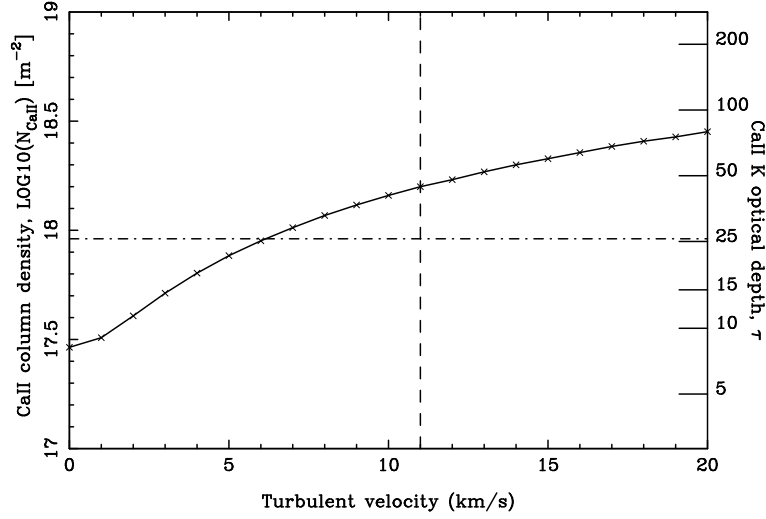
Figure 3.4: The CaII column density is plotted as a function of the turbulent velocity for prominence A. The axis on the right of the plot shows the corresponding optical depth of the CaII K line. The vertical dashed line at 11 km s^{-1} gives an observational upper limit on the turbulence. The dot-dash horizontal line shows the optical depth of the H$_\alpha$ line for reference.

the order of column densities remained unchanged, e.g. prominence A was still the most optically thick prominence.

From Fig. 3.3 there appears to be an ambiguity on the CaII column density due to there being two potential solutions. The results using the first (lower column density solution) are shown in Table 3.1. A similar spread is observed in the column densities of CaII as in the Balmer lines with a mean of (log $N_{CaII} = 17.73 \pm 0.11$ m^{-2}). Prominence A is also found to have the highest column density at log $N_{CaII} = 17.88$ m^{-2}. We also quote in Table 3.1 the optical depth of each prominence in CaII K, finding $12 < \tau < 21$, less than the optical depths in H$_\alpha$ ($19 < \tau < 26$). This is actually similar to the optical depths in H$_\beta$. Visual comparison of the H$_\beta$ line in Fig. 3.2 with the CaII K line in Fig. 3.5 shows the prominence pattern to be similar in strength. This is why we can safely exclude the second solution shown on Fig. 3.3. The second solution gives a column density approximately a thousand times higher than that of the first solution. Therefore the prominence optical depths in CaII K would also be a thousand times higher. Such optical depths are simply not supported by the visual appearance of the CaII K line in Fig. 3.5 when compared to the hydrogen lines in Fig. 3.2.

As there are only two calcium lines, the uncertainty in the derived CaII column densities are more difficult to estimate. The formal errors on each individual CaII column density are almost certainly underestimates of the true uncertainties. The normalisation of the continuum in these blue orders is likely to be the primary source of error due to the difficulty of locating the continuum. The CaII H&K lines are in subsequent echelle orders. We ran a Monte Carlo simulation assuming that the continuum of each of these orders may be inaccurate by up to $\pm 5\%$. The standard deviation of the resulting probability distribution provides a systematic uncertainty on all calculated CaII column densities, giving log $N_{CaII} = 17.73 \pm 0.25$ m^{-2}. A further check was made using a template reference star taken during the observing run, GL 472. This is a K0V dwarf observed as a slow rotating reference template for use in Doppler imaging. The narrow lines of this star make the continuum easier to fit. We therefore performed the same analysis, using instead the CaII H&K continuum fits of GL 472. The resulting average is log $N_{CaII} = 17.63$ m^{-2}, very similar to the result quoted above and within the systematic uncertainty determined above.

We investigate the result of increasing the turbulent velocity from 0 - 20 km s^{-1} in Fig. 3.4. A vertical dashed line on the plot shows the maximum allowed turbulent velocity of 11 km s^{-1}. The resulting CaII column density increases by a factor of five over the range 0 - 11 km/s from log $N_{CaII} = 17.46$ m^{-2} to log $N_{CaII} = 18.2$ m^{-2}. This is discussed further in §3.5.2.

3.3.3 Weighing prominences

From the previous sections we now have the column densities and optical depths for the four prominences in the n=2 level of hydrogen and in the ground state of singly ionised calcium. In order to calculate the mass of each prominence we need to know the column density in the ground state of hydrogen.

At the expected prominence temperatures of approximately 10,000 K we assume that the calcium atoms are singly ionised. Then we can use solar abundance ratios to find the amount of neutral hydrogen. The ratio of calcium to hydrogen in solar prominences is approximately log $\frac{H_{n=1}}{Ca} = 5.65$ (Gouttebroze & Heinzel, 2002). We adopt this ratio to obtain column densities in the ground state of hydrogen, displayed in Table 3.1.
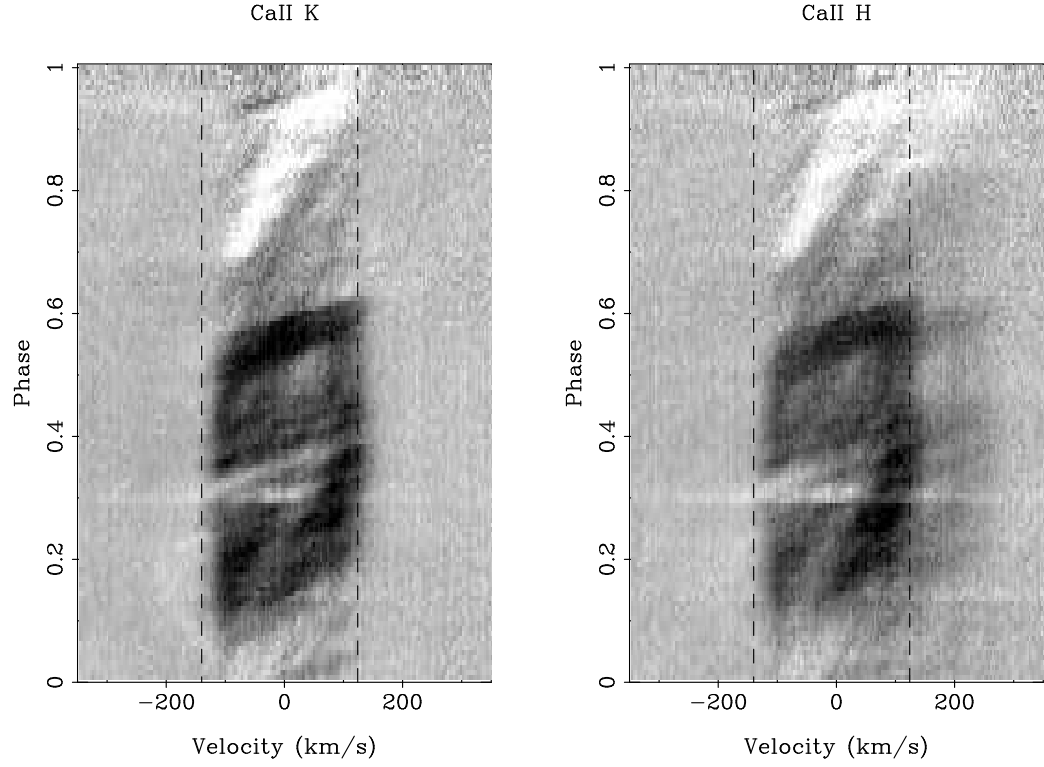
Figure 3.5: The August 02 CaII K (left) & H (right) timeseries are shown with contrast set so that black is at 0.85 and white is at 1.05 times the local continuum. An average profile has been subtracted (see text). Dashed vertical lines show the $v \sin i$ limits. Again, note that the CaII H line is blended with the H_ϵ line. Bright surface plage regions are visible as well as weak off-disc emission. A stellar flare is present at phase ≈ 0.3.

We now require an estimate of the area of the prominences. Here we use the same approximation as Collier Cameron et al. (1990). From §3.3.1 we know that the prominences are optically thick at H_α ($\tau \approx 22$) line centre. Therefore when they transit the centre of the stellar disc, the fractional depth of the absorption profile gives us the fraction of the star obscured by the prominence. This is analogous to how the fractional depth of a planetary transit gives the ratio of the areas of the planet and star. We use this to calculate the absolute areas of the prominences, using the Speedy Mic radius of 1.06 ± 0.04 $R_\odot$ found in Chapter 2. These are shown in Table 3.1. The average area is found to be 20% of the stellar disc. The masses of the prominences can now be calculated as simply the product of the hydrogen column density, the prominence area and the mass of a hydrogen atom:

$$M = m_H N_1 A$$

The results are again shown in Table 3.1. Prominences A, C and D are found to have very similar masses while prominence B has considerably higher mass. For a turbulent velocity of 5 km s^{-1} the average mass of the four prominences is 1.3×10^{14} kg. We note that the individual uncertainty on each prominence arising from systematic error (as discussed in §3.3.2) exceeds the scatter in the prominence masses, resulting in the range $0.7 - 2.3$ x10^{14} kg.

The CaII column densities found in the last section, from considering the full range of permitted turbulent velocities, provide an estimate of the minimum and maximum prominence masses. These are found to be $0.5 - 3.4$ x10^{14} kg. We discuss these limits further in §3.5.2.

3.4 Prominences seen in emission

Solar prominences are visible as bright emission features when they are seen off the limb of the Sun. In theory it should be possible to detect stellar prominences as bright emission features when they are off the limb of the star. The source function of a prominence will be stellar H_α photons that have been scattered (see §3.1) into our line-of-sight by the prominence, plus any additional source function from the thermal properties of the cloud itself. The relative intensity we observe will be proportional to the size and optical thickness of the prominence in H_α and inversely proportional to the square of the prominence height

above the stellar surface. As Speedy Mic prominences are found at least two stellar radii above the stellar surface these features are likely to be very faint. It is also worth noting that, depending upon the geometry of the system, a prominence seen off the stellar disc need not transit the star as seen from our line of sight.

3.4.1 Detecting loops of emission

The exceptional signal-to-noise of the VLT H$_\alpha$ timeseries allows us to examine the regions beyond the stellar $v$sin$i$ limits for evidence of off-disc emission. To do this we created a mean profile, this time using the whole of the timeseries as there are no dominant strong features present outside of the stellar H$_\alpha$ profile. This was then subtracted from the entire timeseries to search for time-varying features.

We first need to ascertain a conservative estimate for our sensitivity to weak off-disc features. The formal errors on each pixel, derived from Poisson statistics during the reduction, are underestimates as they take no account of systematic variations throughout the night. Thus a featureless section of the timeseries adjacent to, but unaffected by, the H$_\alpha$ line and also avoiding any strong iron lines was chosen. The standard deviation from the mean in this section which included all phases was $\sigma = 0.004$, or 0.4% of the local continuum level. This gives us a guide to the significance of any of the features we identify.

In the right-hand panels of Fig. 3.6 we show the resulting H$_\alpha$ timeseries for both August 02 and 07, with contrast limits set to reveal small fluctuations above or below the continuum level. Fig. 3.6 shows a number of bright emission loops. In particular there is a very distinct loop of emission on August 02 to the red (positive velocity) side of the H$_\alpha$ line, centred on $\phi \approx 0.8$. The emission peaks at 2.5% of the continuum level but weakens beyond the maximum elongation. The loop starts just after prominence A finishes transiting the stellar disc (at $\phi \approx 0.56$). One immediate observation is that there is no corresponding emission loop on the blue side of the H$_\alpha$ line.

There are two other loops of emission both centred on $\phi \approx 0.15$. The smaller loop shows very strong emission, peaking at 3% of the continuum, but it cannot be separated from the H$_\alpha$ line. This is probably a prominence very close to the stellar surface. The larger loop peaks at around 2% of the continuum level. Again it is apparent that there is no corresponding loop on the red side of the H$_\alpha$ line. The observations on August 07 are
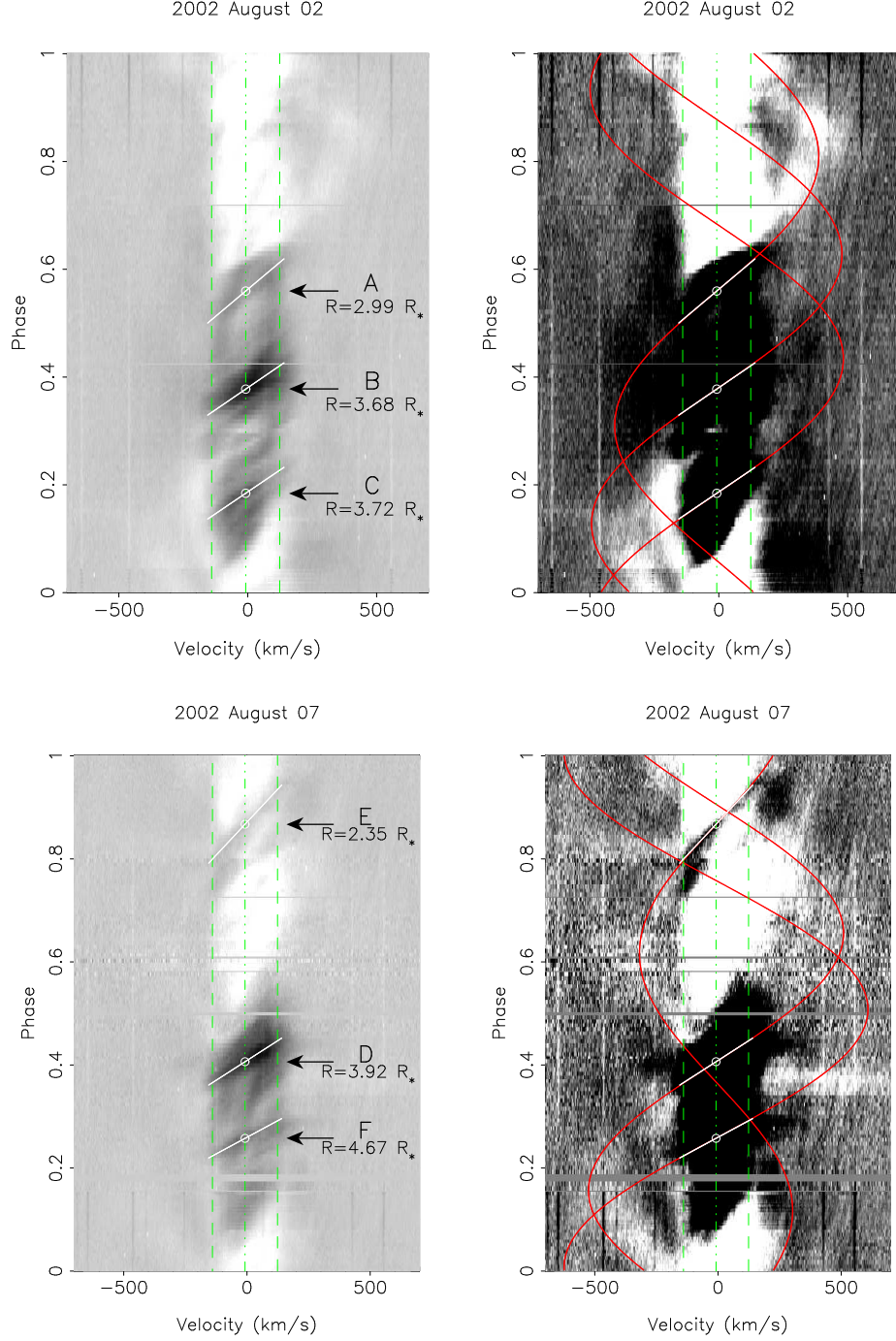
Figure 3.6: H$_\alpha$ timeseries to show loops of off-disc emission. The left panels show the fits to the transiting absorption features and have a grey-scale that runs from black at 0.85 to white at 1.05 times the local continuum level. Similarly the top-right panel is set 0.98 to 1.02, while the bottom-right panel has 0.99 to 1.01, in order to highlight the weak emission. The fits from the left panels are extended as velocity sinusoids (red) on the right panels. Dashed vertical lines (green) show the $v \sin i$ limits and the dot-dashed line shows the radial velocity of Speedy Mic.

Table 3.2: The results of the prominence tracking analysis are displayed with phases of meridian crossing and calculated heights.

Prominence	Phase	Height ($\frac{\varpi}{R_*}$)
A	0.560	2.99±0.07
B	0.378	3.68±0.26
C	0.184	3.72±0.20
D	0.406	3.92±0.21
E	0.867	2.35±0.07
F	0.258	4.67±0.16

generally of a lower quality yet similar emission loops can be seen in Fig. 3.6.

3.4.2 Understanding the emission

In order to attempt to understand the nature of the relationship between the on-disc absorption and off-disc emission features we can use what we have learnt from tracking the prominences in absorption. For a detailed explanation of this matched filter technique we refer the reader to Chapter 2. We use the calculated phases and heights displayed in Table 3.2 to complete velocity sinusoids which we trace out in Fig. 3.6. We do this for the three strongest prominences on the stellar disc for both nights. These are prominences A, B and C on August 02 and prominence D on August 07. We also include the next two strongest prominences on August 07, labelled E and F.

In general there is good agreement between the extended sinusoids and the observed loops of emission. For example prominences A and B on August 02 clearly account for the two strong loops of emission. Prominence C, however, does not seem to correlate with any emission feature. A similar off-disc emission pattern is seen on August 07. Prominence D appears to account for most of the emission on both the blue and the red side of the timeseries. While the low lying prominence E appears to correlate with a loop of emission seen to the blue side of the line at $\phi \approx 0.65$. The high prominence F (like C) does not appear to be associated with any emission loop.

Furthermore, the paths of prominences as estimated from tracking the absorption
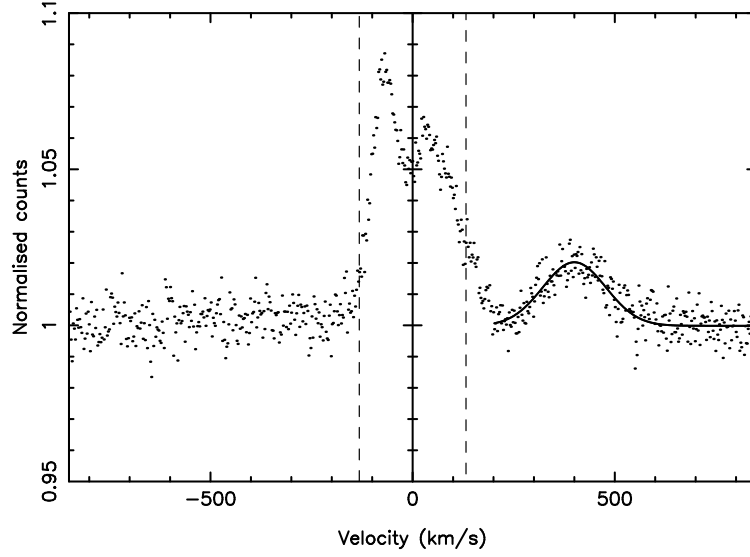
Figure 3.7: An example of a single H_α spectrum at maximum elongation of the strongest observed loop of emission seen at $\phi \approx 0.8$ on August 02. The dashed lines show the stellar $v\sin i$ limits. The solid line shows the Gaussian model we have fitted to the emission, which is found to peak at 2% above the continuum level. The FWHM is 260 km s^{-1} giving an estimate of the prominence thickness of 2.0 R$_*$.

features appear to have systematically greater velocity amplitudes than the majority of the corresponding off-disc emission features. This can be explained in the context of the prominence optical depths as obtained in §3.3. The average optical depth of these prominences was found to be $\tau = 22.4$. Thus as stellar photons travel through the prominence interior they are scattered into random directions, some into our line of sight. However because of this scattering the beam loses intensity and so the number of photons reaching the highest parts of the prominence is reduced.

When finding prominence heights from tracking the absorption features we are naturally following the 'lack of photons'. Yet when we examine the off-disc emission we observe where these photons have gone. As such, the observed emission provides us with information on the radial extent (or thickness) of the prominences. Clearly from a visual examination of Fig. 3.6 the prominences we observe do not extend to the stellar surface. We scale a Gaussian model to the most prominent loop of emission on August 02, fitting for the width of the feature. An example fit for a spectrum taken at maximum elongation of this emission loop is shown in Fig. 3.7. Both the amplitude and width of these emission features vary considerably along the emission loop. We find a range of full width at half

72

maximum (FWHM) that corresponds to a prominence thickness of between 1.7 and 2.5 R_*.

3.5 Discussion

3.5.1 Prominence stability

In Chapter 2 we investigated prominence stability on the timescale of days; we found that many prominences could be re-observed on consecutive days, while a few were still recoverable some five nights later. In §3.2.1 we extended the timebase by comparing the Chapter 2 observations with the VLT data taken more than two weeks later.

The main result of this comparison is that the overall circumstellar distribution of prominence material remains the same. While there is clearly evolution of the detailed structure of the individual prominences, the locations at which prominences are likely to be found are largely unchanged. In particular, prominence A was the structure we could most easily identify between the two epochs of observations. We found that its phase of observation, height and strength were all remarkably similar. This does not necessarily mean that this feature has remained unchanged for two weeks (without observations of the intervening period it would be impossible to tell). What it does suggest, however, is that the magnetic structure within which this prominence was trapped is stable on these timescales. Within this structure, individual prominences may have formed and either been ejected or drained back to the surface within the two week gap when we do not have observations, but if this is the case, then another prominence must have reformed in the same place and under very much the same conditions.

It is interesting that this prominence, which appears to be the most stable, is also one of the largest. This is also true of solar prominences (Schrijver & Zwaan, 2000). Small solar prominences which form close to active regions tend to be most unstable while the longest-lived are also typically the largest. In the solar case, the largest prominences are sheared out over their lifetimes by the action of differential rotation and they are carried poleward over a lifetime of months to form the polar crown. Their poleward migration is halted when they encounter the open field of the polar cap. Whether something similar is happening on Speedy Mic is not clear. Certainly, the apparent lack of high-latitude

prominences (discussed in §3.5.3) suggests that the prominences are constrained to a range of latitudes, rather like their solar counterparts. This is in stark contrast to the distribution of spots on Speedy Mic which can be seen at all latitudes, including the pole (Barnes 2005, Wolter et al. 2005).

3.5.2   Prominence masses

In §3.3 we used the ratio of the strengths of multiple Balmer lines to determine the column densities of prominences in the first excited state of hydrogen to be ($\log N_2 = 18.61 \pm 0.2$ m^{-2}). This is in good agreement with Collier Cameron et al. (1990) who found ($\log N_2 = 18.4 \pm 0.2$ m^{-2}). Consequently, similar optical depths are also derived. From direct measurements of the EWs of prominences in the CaII H&K lines, and then use of solar prominence abundance ratios, we were able to estimate the column density in the ground state of hydrogen. This was found to be ($\log N_1 = 23.38 \pm 0.25$ m^{-2}). Then using the projected areas of the prominences we estimated their masses to be $0.7 - 2.3$ x10^{14} kg.

The results outlined above were for a turbulent velocity of 5 km s^{-1}. The turbulent velocity could be in the range 0 - 11 km s^{-1}, producing a larger prominence mass range of $0.5 - 3.4$ x10^{14} kg. However there are reasons why we believe that the turbulent velocity probably lies towards the lower end of this range. Firstly we can examine the assumption that the smallest prominences are unresolved. The smallest features for which we could determine the widths have fractional depths in H$_\alpha$ that correspond to areas that cover at least 2% of the stellar disc. Assuming a circular cloud cross-section, this gives a radius of 14 % that of the Speedy Mic radius. Hence in velocity space a width of 18 km/s would be observed. This in itself accounts for the observed widths.

Another argument for small turbulent velocities comes from comparing the optical depths of prominences in the H$_\alpha$ and CaII K lines. On Fig. 3.4 we include a second axis that shows the corresponding optical depth in the CaII K line. For the range of turbulent velocities 0 - 11 km s^{-1}, optical depths of $8 < \tau < 40$ are found. We also plot on Fig. 3.4 a horizontal dot-dash line to show the optical depth at the centre of the H$_\alpha$ line at $\tau = 25.7$. If we now compare the CaII K line in Fig. 3.5 with that of the hydrogen lines in Fig. 3.2, the prominence absorption features in the CaII K line appear to be less optically thick than the H$_\alpha$ line. This includes the lack of an emission loop associated with prominence A. The CaII K timeseries is of sufficient S/N that we would expect to detect scattered

photons from this loop if it had a similar optical depth to that of H_α. We suggest then that the optical depth of the CaII K line is less than the H_α line and thus the turbulent velocity should be less than 6 km s^{-1}. This is therefore similar to the level of turbulence seen in solar prominences. Hence our adopted turbulent velocity of 5 km s^{-1} seems valid in the previous sections. Therefore we arrive at a narrower range for prominence masses of $0.5 - 2.3$ x10^{14} kg.

We can now compare some of the physical properties of the Speedy Mic prominence system found in §3.3 with those of the only other similar analysis on a stellar prominence system. Using different techniques to this work, Collier Cameron et al. (1990) derived parameters for another rapidly rotating star, AB Dor. They found prominence masses of $4 - 5$x10^{14} kg, slightly greater than we find for Speedy Mic. Given the good agreement between this work and Collier Cameron et al. (1990) on the column density of the n=2 level of hydrogen, it seems unlikely that the above discrepancy on prominence masses represents a physical difference between AB Dor and Speedy Mic prominences. Rather it is probably just a difference between the two techniques employed due to the quality of data available at the time. With the advent of new highly-efficient spectrographs and increased detector size and efficiency (particularly in the blue part of the spectrum) it is now possible to obtain simultaneous high-resolution spectra in the majority of the optical wavelength range. In particular, we are now able to obtain *simultaneous* observations of the H_α line and both CaII H&K lines. This was not possible at the time of the Collier Cameron et al. (1990) observations and they therefore had to rely on a geometrical argument to obtain estimates of the column densities.

We can also compare Speedy Mic prominences with their solar namesakes. For example, a giant eruptive solar prominence was observed by Gopalswamy & Hanaoka (1998) to have an initial mass before eruption of 6x10^{13} kg. This is comparable to the lower end of our mass estimate. However to have three such prominences on the Sun at any one time would be unusual indeed.

As we have the column densities in the first two levels of hydrogen we can estimate the excitation temperature of the prominences by assuming that they are in local thermodynamic equilibrium (LTE). We note that this can not strictly be the case, or else the 10,000 K prominences would appear as emission rather than absorption features whilst transiting the stellar disc. However given that we have shown H_α to be just optically

thick, we consequently know that Lyman alpha must also be very optically thick. As it is this transition that is largely responsible for detailed balance between the first two levels of hydrogen, the LTE approximation should be reasonably accurate.

Comparing the column densities of hydrogen in the ground state with that in the first excited state, the average shows that there are $10^{4.77} = 59,000$ times more atoms in the ground state than in the first excited state (assuming a turbulent velocity of 5 km s^{-1}). Therefore the ratio of the LTE level populations is given by the Boltzmann equation:

$$\frac{N_2}{N_1} = \frac{g_2}{g_1}\exp\left(-\frac{\Delta E}{kT}\right) \tag{3.4}$$

where g_1 and g_2 are the statistical weights of the two levels, ΔE is the energy difference between them, k is the Boltzmann constant and T is the temperature sought. This results in an excitation temperature of 9569 K. This is very similar to the kinetic temperature of 10,000 K we used in section §3.3. While we realise that this is a circular argument, the results of this analysis are not found to depend strongly on the thermal Doppler temperature used in creating the theoretical line profiles. For example if we start with a lower thermal temperature of 8000 K we obtain an excitation temperature of 9463 K.

3.5.3 Distribution of prominence material

In §3.4 we showed that some of the strongest absorption features (the largest prominences) could be observed as loops of emission. However we found no emission counterparts for prominences C and F. This probably reflects the relationship between the size of the prominence and the height above the stellar surface. Here C and F cover slightly larger areas of the stellar disc than say prominence E. Yet because prominence E is very much closer to the stellar surface ($R = 2.35\,\mathrm{R_*}$) than either C or F ($R = 3.72\,\mathrm{R_*}$ and $R = 4.67\,\mathrm{R_*}$, respectively), and the intensity drops as the square of the distance, it is seen in emission whilst prominences C and F are not.

If prominences were evenly distributed in latitude around Speedy Mic then one would expect to observe loops of emission which can not be associated with prominences crossing the stellar disc. However this seems not to be the case; from Fig. 3.6 we *can* associate all the observed emission loops with transiting prominences. If large prominences, at similar heights to those observed, existed at latitudes of around 60° then they should be visible as emission loops. So this either suggests that Speedy Mic does not have such large

high-latitude prominences, or that they must be extremely centrifugally flattened towards the equatorial plane. It should be noted though that if higher latitude prominences were smaller or indeed higher then they may exist without detectable emission.

Similar conclusions have been reached before from the lack of prominences observed on low-inclination rapid rotators. Jeffries et al. (1994) found no prominences transiting the stellar disc around the rapidly rotating K dwarf BD+22°4409 which is observed at an inclination of $50 \pm 10°$. Unfortunately, as discussed in the §3.1, the Speedy Mic inclination is relatively poorly constrained and restricts what we can determine. If the inclination is actually the 70° that both Doppler imaging teams found then even a prominence above $R = 3$ R_*, located in the equatorial plane would not be seen crossing the stellar disc. Indeed, these observations may favour a higher stellar inclination.

Speedy Mic is not the first rapidly rotating young star to show rotationally modulated emission outside of the H_α line. Two G dwarfs RXJ1508.6-4423 (Donati et al., 2000) and AP149 (Barnes et al., 2001) also show emission beyond their stellar $v \sin i$ limits which were attributed to a ring (or torus) of prominence material. These two stars are very different cases to Speedy Mic though. On neither star are prominences seen transiting the stellar disc, nor is there any evidence that some prominences eclipse the off-disc emission of others (see next paragraph). This is probably because both stars are seen at low inclination angles ($i = 35°$ and $i = 30°$, respectively). Furthermore the strength of the emission is very different. The amplitude of the emission in these systems is around 20% of the local continuum as opposed to the 2-3% we observe on Speedy Mic. This is probably due in part to the increased ionising UV flux from these early-type G dwarfs. This, coupled to the fact that the co-rotation radius of these stars is closer to the surface than in Speedy Mic means that the prominences receive greater irradiation. This drives the H_α source function closer to the thermal equilibrium value than to the pure-scattering value.

Our analysis of the Speedy Mic prominence system has considered only individual prominences that we can track across the stellar disc. This is a simplification of the real distribution of prominence material. For example if we look back at the H_α timeseries shown in Fig. 3.2 we can see that prominences A and B are not totally separate entities. The H_α line is still in weak absorption at the phases between these two prominences. Yet if we compare this with the later Balmer lines (like H_γ in the panel below H_α in

Fig. 3.2) the absorption weakens considerably. This indicates that this material has a lower column density than the material in what we refer to as prominences A and B. The large prominences that we have been studying therefore appear to be more like dense condensations in a 'semi-torus' of gas. This would also help to explain why some prominences do not show off-disc emission loops on *both* sides of the H_α line, as observed in §3.4. It is the intervening material between some of the prominences that obscure us from observing this emission, i.e. the prominence system is 'self-eclipsing'. Therefore there appears to be similarities between the Speedy Mic prominence system and that of the low inclination systems RXJ1508.6-4423 and AP149. The observed differences between these systems and Speedy Mic in many respects appear to be due to the different stellar inclinations.

3.6 Conclusions

The first analysis of the evolution of a stellar prominence system on a two to three week timescale has been performed. Whilst we see considerable evolution of most individual prominences, the overall prominence pattern remains broadly similar. One half of the stellar rotation is still covered in stronger prominence signatures than the other. We have shown that at least one individual prominence supporting structure appears to be stable over two weeks. Any theoretical models for prominence support will have to be able to reproduce such stability.

We show that the prominence pattern is visible in the first eight lines of the hydrogen Balmer series and the CaII H&K lines. The column density of hydrogen in the first excited state and the derived H_α optical depth are very similar to that of the prominences on AB Dor reported by Collier Cameron et al. (1990). This analysis, however, finds a lower total hydrogen column density from direct observations of CaII. This leads us to find prominence masses of $0.5 - 2.3$ x10^{14} kg, intermediate between the masses of the largest solar prominences and those reported on AB Dor. We suspect that the difference in the derived masses of the prominence systems on these two rapidly rotating stars is not physical but is probably a result of the different techniques used and the data quality available.

We have identified loops of emission outside of the rotationally broadened H_α profile.

These are shown to be caused by the same prominences we see transiting the stellar disc in absorption. The emission loops confirm the heights found from tracking the absorption signatures as the visible emission is shown to appear at smaller radii in all cases. This observation can be explained by the optical thickness of the clouds in H_α. By combining these two methods of observing prominences we have been able to develop a more complete picture of the geometry and physical parameters of the prominence system. All the strong loops of emission we observe can be associated with particular prominences seen transiting the stellar disc. This limits the number of large high-latitude prominences. Furthermore, combined with the high degree of self-eclipse observed in the Speedy Mic prominence system, we suggest that it is indeed highly flattened, most probably near to the stellar equatorial plane. This apparent flattening of the prominence system could result from the presence of a unidirectional field in the polar cap. If there is a strong dipolar component in the stellar field then prominences will form in the equatorial plane (McIvor et al., 2003). From Doppler imaging of the Speedy Mic surface, Barnes (2005) found that there was no single uniform polar spot. So it may be the case that the stellar field has a high degree of complexity and prominences that form at high latitudes are centrifugally driven into the equatorial plane.

It is clear that the Speedy Mic prominence system is complex, with the distribution of co-rotating prominence material not restricted to the dense clumps that we have identified as prominences. We note that there seems to be interesting parallels between these observations and those of the low inclination G dwarfs RXJ1508.6-4423 and AP149. In the future it may be informative to develop a model where we could change the physical parameters and the viewing angle of such prominence systems. The results could then be compared directly with these observations.

CHAPTER 4

Prominences on AB Doradus

The first part of this chapter (§4.2) has been published in a Monthly Notices of the Royal Astronomical Society paper by:

Hussain, G.A.J., Jardine, M., Donati, J.-F., Brickhouse, N.S., **Dunstone, N.J.**, Wood, K., Dupree, A.K., Collier Cameron, A., Favata, F. (2007, MNRAS, 377, 1488)

Specifically, §6 of this paper was written by myself.

4.1 Introduction

In the two last chapters we performed the first detailed analysis of the prominence system of Speedy Mic. As discussed in Chapter 1, these clouds of co-rotating material were first identified on the K0 dwarf AB Doradus (AB Dor) by Collier Cameron & Robinson (1989a). It therefore seems fitting that we should return to AB Dor in order to further investigate the properties of stellar prominences. This chapter is split into two distinct parts. In §4.2 we present observations of the AB Dor prominence system in 2002 and investigate whether there is any evidence for a correlation with coincident X-ray observations. In §4.3 we present a preliminary analysis of what appears to be the first observation of an erupting stellar prominence in 2004.

4.2 Prominences, plage and X-ray lightcurve

The AB Dor H_α line is subject to variability caused primarily by bright surface plage regions and rapidly moving dark absorption features, just like those discussed for Speedy Mic in the last two chapters. They are typically found to be between 2 and 8 R_* from the

stellar rotation axis (Collier Cameron & Robinson 1989a; Collier Cameron & Robinson 1989b, Donati & Collier Cameron 1997; Collier Cameron et al. 1999; Donati et al. 1999) and therefore often above the Keplerian co-rotation radius of 2.7 R_*. In 2002 the first attempt to obtain surface brightness and magnetic maps simulataneous with X-ray data was made. A detailed analysis of correlations between these different tracers of stellar activity is presented in Hussain et al. (2007). In this section, I present the associated H_α observations and examine whether any of the observed prominences correlate with features in the X-ray lightcurve.

4.2.1 An unusually low number of prominences in 2002

Observations were made using the University College London Échelle Spectrograph (UCLES) at the Anglo Australian Telescope (AAT) with the SemelPol polarimeter over the period 2002 December 11 to 15. Here we only use the first four nights as there were very few observations obtained on December 15. A full account of the observations and data reduction is given in Hussain et al. (2007). In Fig. 4.1 we display the stacked H_α (timeseries) spectra for each of the four nights of observations. We approximate the stellar background H_α line by creating a mean spectrum which is then subtracted from the entire timeseries. This leaves only time varying features such as bright active regions (plage) and rapid absorption transients (prominences). When examining Fig. 4.1 the most striking observation is the *lack* of prominences seen at this epoch. Despite the fact that over the four nights almost 90% of the stellar rotation was observed, only four prominences are found. This is substantially less than the average number of 6 to 8 prominences that are observed at most other epochs (Cameron et al. 2003). The distribution of prominences around the star also appears to be peculiar. Between phases 0.3 to 0.8 there do not appear to be any large prominences transiting the stellar disc, and instead we observe bright chromospheric emission from surface plage regions. This is unusual for AB Dor as previous observations of the star have not revealed such an asymmetric distribution of prominence material.

By tracking the prominence absorption signatures as they drift through the H_α line profile we can establish their spatial and radial extent. We use the simple technique of Gaussian fitting (Collier Cameron & Robinson 1989a) rather than the matched-filter technique outlined in Chapter 2. This is because the many gaps in phase coverage of this dataset make the unsharp masking technique impractical. As for Speedy Mic, we use
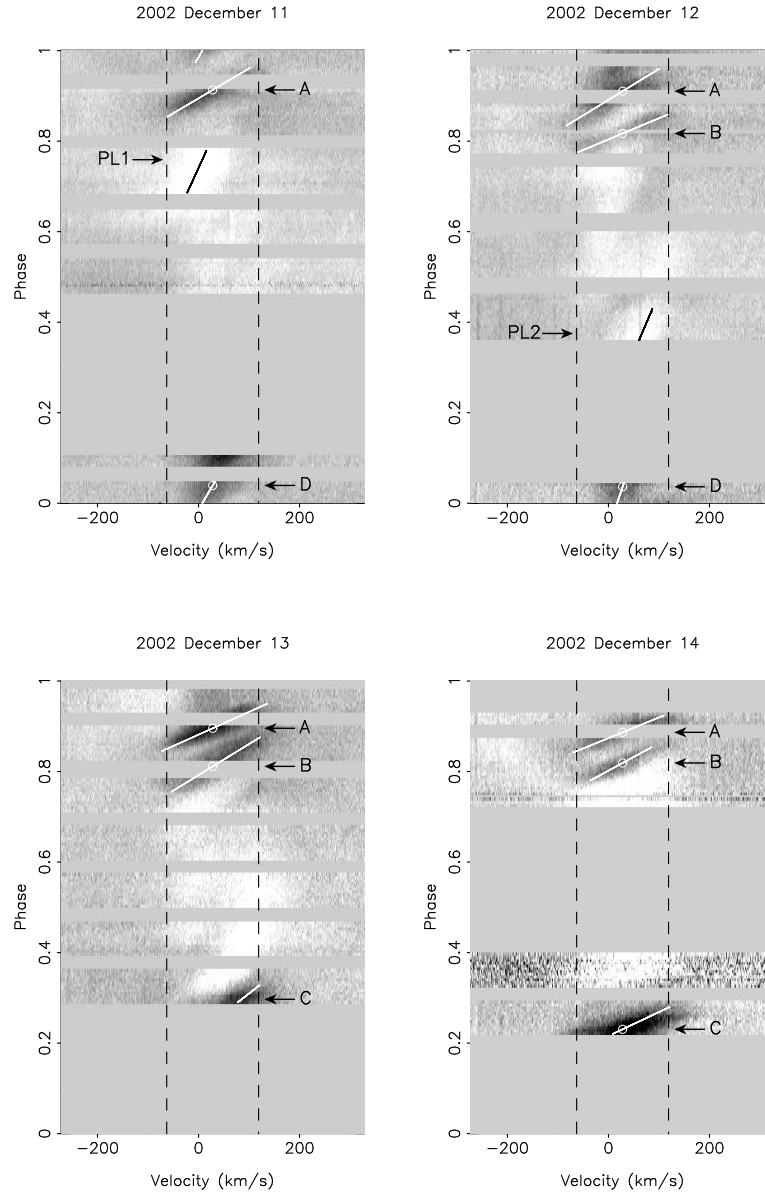
Figure 4.1: Raw H$_\alpha$ time series spectra for 2002 December 11, 12, 13 & 14, with phase plotted against velocity. Dashed black lines show the stellar $v \sin i$ limits. White lines are the superimposed fits to obtain prominence heights. The grey-scale runs from black at 0.80 times the local continuum level, to white at 1.05 times continuum. A mean spectrum has been subtracted from the entire timeseries. For reference with Table 1, prominences are labelled A,B,C and D and two of the bright surface regions are labelled PL1 and PL2.

Table 4.1: The results of the prominence tracking analysis displayed with phases of meridian crossing and calculated distances from the rotation axis ($\frac{\varpi}{R_*}$ - see Eqn. 2.1).

Feature	December 11		December 12		December 13		December 14	
	Phase	$\frac{\varpi}{R_*}$	Phase	$\frac{\varpi}{R_*}$	Phase	$\frac{\varpi}{R_*}$	Phase	$\frac{\varpi}{R_*}$
A	0.913	2.64 ± 0.05	0.910	2.55 ± 0.03	0.896	3.48 ± 0.05	0.887	3.84 ± 0.12
B			0.817	3.74 ± 0.04	0.811	2.55 ± 0.03	0.819	2.88 ± 0.03
C					0.247	2.00 ± 0.04	0.231	3.31 ± 0.05
D	0.039	0.91 ± 0.03	0.035	0.52 ± 0.19				
Plage 1	0.809	0.72 ± 0.02						
Plage 2			0.274	0.66 ± 0.02				

the rates at which the prominences drift through the stellar rotation profile to establish their distances from the AB Dor rotation axis. The results of this analysis are shown in Table 4.1. Prominences A, B and C are found at distances of between 2 and 4 R_*, which is consistent with previous observations. A quite different behaviour is observed for prominence D. The distance from the rotation axis indicated by its drift rate is 0.91 R_* on December 11 and 0.52 R_* on December 12, and it therefore must be at high latitude in order to be appreciably above the stellar surface. Prominence D first appears as an absorption feature in the H_α line at a velocity of -10 km s^{-1} as opposed to the $\approx$ -60 km s^{-1} of prominence A, B and C. This confirms that the prominence is crossing the stellar disc at a latitude of approximately 60°. Unfortunately the end of the transit of prominence D was not observed and so limits the accuracy with which we can determine its height. It is nevertheless unusual to find such a low lying, high latitude, prominence on AB Dor.

In addition to the prominence absorption features, we also track two bright plage regions. They are labelled PL1 and PL2 in Fig. 4.1. Both of these, like prominence D, are found to have distances from the rotation axis of less than 1 R_*. If we assume that PL1 and PL2 are indeed active plage regions on the AB Dor surface then their latitudes are 44° and 49° respectively. It is interesting how near their phases of observation are to those of prominences B and C, respectively. This is similar to the observation by Jeffries (1993) that prominences on Speedy Mic were followed or preceded by strong emission transients.
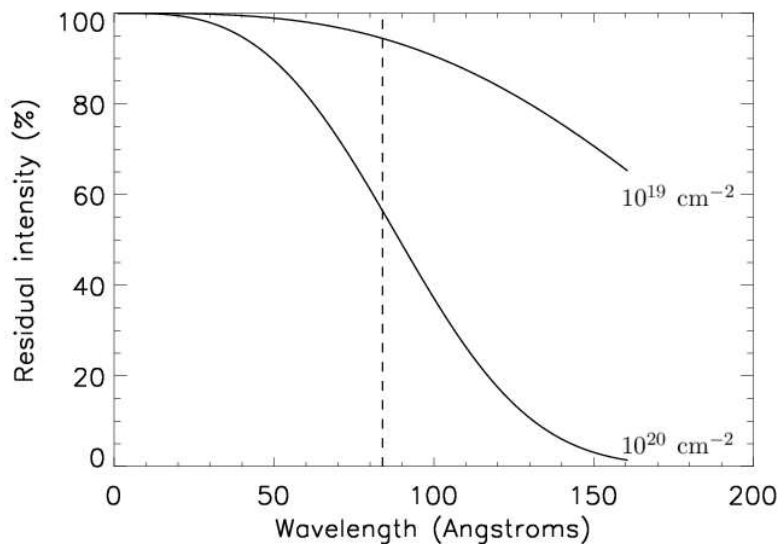
Figure 4.2: Computing the amount of X-ray absorption that can be expected through different column densities of neutral hydrogen. The two curves show column densities of 10^{19} cm^{-2} and 10^{20} cm^{-2} which is the range expected for stellar prominences. The dashed vertical line shows the flux weighted average wavelength of the 50 - 130 Å X-ray lightcurve. This plot also shows that little absorption would be expected for the 1 - 50 Å lightcurve. Computed using an IDL program written by W. Landsman, based on previous code used to compute interstellar medium optical depths (e.g. Rumph et al. 1994).

4.2.2 X-ray absorption by prominence?

Now that we know the phases at which prominence material is transiting the stellar disc we can compare these to the X-ray light curve. The possibility of soft X-ray emission being shadowed by cool prominence material, as observed on the Sun, was briefly discussed in Hussain et al. (2005). Stellar prominences on rapidly rotating stars have higher hydrogen column densities than their solar namesakes. Collier Cameron et al. (1990) found a column density for AB Dor prominences of $N_H \approx 10^{20}$ cm^{-2}, while in the last chapter we found column densities in the range $N_H = 1 - 4 \times 10^{19}$ cm^{-2} on Speedy Mic. This is an order of magnitude more than the $N_H \approx 10^{18}$ cm^{-2} found for solar prominences (e.g. Kucera et al. 1998). We would thus expect to see more absorption of soft X-rays from stellar prominences.
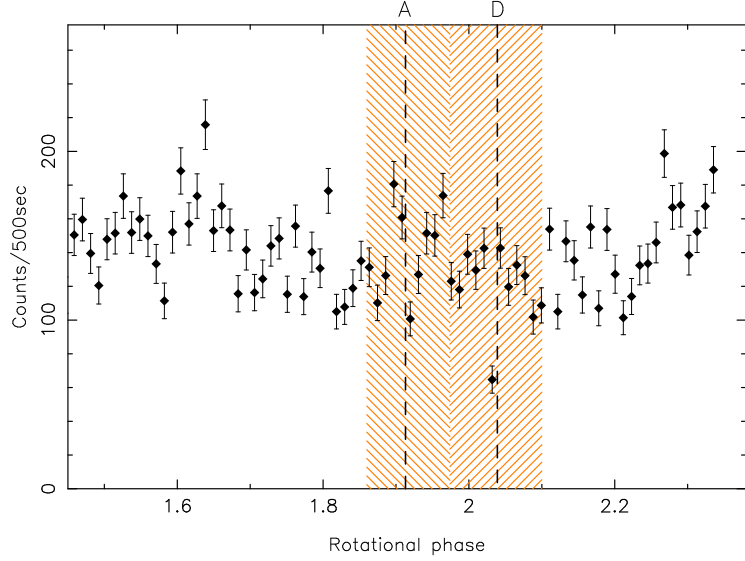
Figure 4.3: EUV light curve obtained by summing up counts over the 50 - 130 Å range. The hatched region shows the phases at which prominences A & D are transiting the stellar disc, while the vertical black dashed lines show the phase of central meridian crossing. Note the apparent correlation between a rapid dip in the lightcurve at phase 2.03 and prominence D.

Co-temporal X-ray observations of AB Dor were obtain using the *Chandra* satellite. These are described in full by Hussain et al. (2005). Gaitee Hussain reduced the X-ray data and provided me with two X-ray lightcurves, one covering the X-ray 1 - 50 Å regime and another in the soft X-ray 50 - 130 Å range. The hydrogen continuum has an upper bound of 911 Å, below which the absorption cross-section decreases as λ^{-3}. We are therefore better off examining the light curve from the longer wavelength range of 50 - 130 Å as opposed to the 1 - 50 Å (as illustrated in Fig. 4.2). The flux weighted average wavelength of the 50 - 130 Å range is 83.9 Å, placing it in the extreme ultraviolet (EUV). At this wavelength for hydrogen column densities in the range 10^{19} cm^{-2} to 10^{20} cm^{-2} we would expect a prominence to absorb between 5 and 45% of EUV photons, as illustrated in Fig. 4.2. If we also consider a case where the prominences contain HeI at an abundance of 5% that of hydrogen, then the absorption would increase to between 15 and 75%. Furthermore if the prominences have a fragmented structure similar to solar prominences, then this would increase the local density and thus also the absorption. So there is reason to expect that we may be able to observe a significant reduction in EUV flux if a prominence is seen to eclipse a region of stellar EUV emission.

In Fig. 4.3 we plot the 50 - 130 Å light curve and overlay the locations of the prominences. It should be noted that the only co-incident data between the X-ray and the optical observations is for phases labelled 1.5 to 2.1, which is the December 11 timeseries. Initial investigation using 1 ksec bins revealed a possible weak correlation between the location of prominence D and a very sharp dip in the X-ray light curve. To establish the duration of this event more accurately we re-binned the light curve into 500 s bins. This is plotted in Fig. 4.3. We find that the dip becomes stronger but is still only a single point. Increasing the sampling to 250 s shows that point split into two equal fluxes. So it appears that for 500 s the EUV flux decreases considerably and it does so at a phase that is very similar to that of the central meridian crossing of prominence D. The phase difference is $\Delta\phi = 0.007$ (or ≈ 300 s), which is the same as the exposure time for an H_α spectrum.

In order to establish the strength of this 500 s dip and its significance we need to compare it to a reference flux level. Firstly, if we consider a local comparison to the four points immediately either side of this one, then we find that the dip is 52% and has a significance of 8 σ. This may be the most accurate comparison as it takes account of what the background EUV flux is at this time. If we simply find the optimal average flux of the whole light curve, we find a very similar result: the dip is 54 % with a 9 σ significance. However this will be influenced by the active (flaring) phases, for example those at the end of the light curve. Finally we attempt to find a minimum background level by an iterative 10 σ clip of all points above the optimal average level. This produced a dip of 43% and a significance of 6 σ.

Of the other three prominences, C may not even be present at the epoch of the X-ray light curve as we only observe it on December 13 and 14. Prominence B was also not present in the December 11 H_α timeseries. Prominence A does not correlate with any statistically significant dip in the light curve. We are left asking ourselves, what is so special about prominence D? In fact, we found earlier that this prominence is unusual in that it is probably a high latitude feature, although again we should emphasise the uncertainty on this prominence's parameters. The fact that the absorption is seen so close to the meridian crossing of prominence D supports the idea that the prominence eclipsed a region near the stellar pole. The relatively short duration of the eclipse suggests that both the prominence and the EUV emitting region are spatially narrow in extent. Given that the observed dip is approximately 50 % of the entire EUV flux coming from AB

Dor this would suggest that the majority of the emission is highly localised. While this statement follows from our observation, I would stress that this single X-ray datapoint does not allow us to provide any sort of conclusive statement. Instead it should just be viewed as encouraging further coincident X-ray and prominence observations.

4.3 An erupting stellar prominence

During the last twenty years of prominence observations on AB Dor many prominences have been reported (Collier Cameron & Robinson 1989a; Collier Cameron & Robinson 1989b, Donati & Collier Cameron 1997; Collier Cameron et al. 1999; Donati et al. 1999). From the rate of appearance and disappearance of individual prominences the lifetimes of AB Dor prominences have been estimated to be 3 - 4 days (Collier Cameron et al., 1999). Very few stellar prominences however have actually been observed on consecutive nights over this time interval. This is normally due to poor weather, the demands of other programs during the observing run and the need to obtain full phase coverage of the AB Dor surface for Doppler Imaging (DI) studies.

The ultimate fate of individual stellar prominences is uncertain. Some studies (e.g. Collier Cameron & Robinson 1989b, Chapter 2) have provided tentative evidence that prominences are seen to increase in height over consecutive nights before disappearing. The explanation is that they underwent some sort of ejection event, much like many large solar prominences are seen to erupt from the surface of the Sun. This is largely conjecture however, as no prominence has been caught in the act of being ejected. Here we describe an attempt in 2004 December to follow a single AB Dor prominence through its evolution. The aim is to gain a better understanding of the lifecycle of a stellar prominence.

4.3.1 Observations

Observations were made by the author using the University College London Échelle Spectrographs (UCLES) at the Anglo Australian Telescope (AAT) using the SemelPol polarimeter over the period 2004 December 25 to 31. Using the 31 gr mm^{-1} grating full wavelength coverage between 4377 and 6819 Å is achieved, thus recording the Balmer H$_\alpha$ and H$_\beta$ lines. A resolution of 70,000 (i.e. 4.3 km s^{-1}) is obtained using this set-up. We

use only the individual, unpolarised, spectra which were optimally extracted using the ESpRIT reduction package (Donati et al. 1997). An exposure time of 200 s was used which, after CCD read-out time, gave a cadence of 276 s between consecutive exposures.

During the observing run itself the order containing H_α was reduced at the telescope, with a lag time of approximately thirty minutes. This was achieved using the calibration frames taken at the start of the night and an approximate normalisation of the H_α continuum. As each batch of spectra were taken and reduced they were added to new rows in that nights stack, creating a two dimensional image (trailed spectrum). A mean spectrum was then produced and subtracted from each row. This strategy allowed us to locate the phases at which prominence absorption features were present and so predict their times of observation on subsequent nights.

On-site data reduction also allowed us to spot a problem with the instrumental set-up during the night of December 29. We noticed that the atmospheric telluric lines showed a slow drift in wavelength. This was subsequently tracked down to the spectrograph subsiding on its air bags because of a fault with the nitrogen supply. As a consequence this was quickly corrected during the night. For the spectra that were affected during this period we have used the telluric lines as a reference to correct the wavelength scale.

After the observing run the data were re-reduced using a more complete set of calibration frames. We took the two orders containing H_α and H_β and normalised the continuum of each spectrum. Many of the resulting H_α spectra had a residual tilt which we corrected by using a rigid spline fit after masking out the H_α line itself. We combined the H_α spectra from all nights using inverse-variance weights to create an approximation to the time-invariant H_α background spectrum. This was then subtracted from each individual spectrum. Atmospheric telluric lines were subtracted in a similar manner but on a night-by-night basis.

4.3.2   Studying the temporal evolution of a large stellar prominence

In order to study the evolution of a single stellar prominence we were able to combine the time allocation of two observing programs to achieve a longer timebase. The priority therefore on the first night was to identify a suitable prominence. Due to the rotational period of AB Dor (0.51479 d) we needed to find a prominence that was observed quite
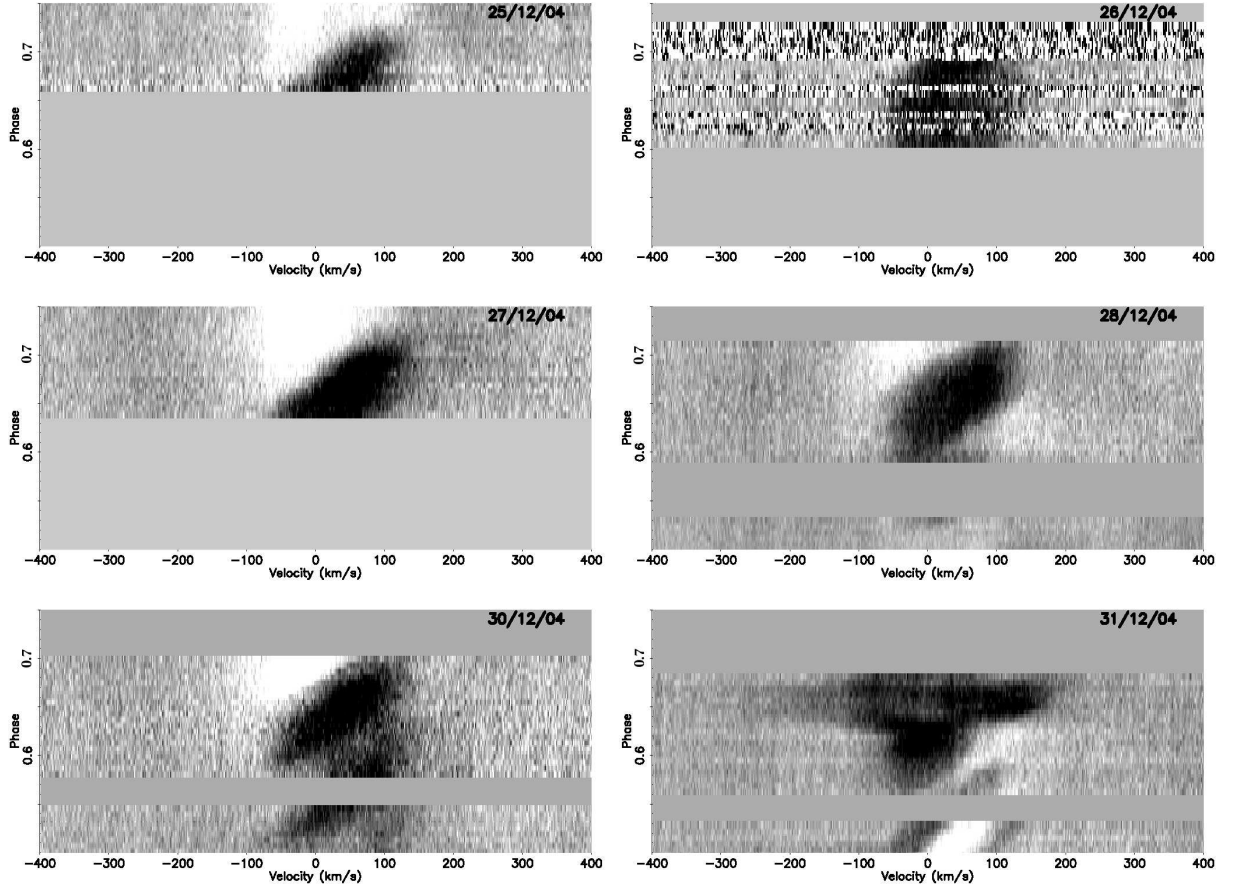
Figure 4.4: Six nights of H$_\alpha$ timeseries spectra from 2004 December are shown. Phase (time) increases on the y-axis. Dark absorption signatures are seen to move from left-to-right which is characteristic of the transit of stellar prominences. Note that at least part of the prominence at phase $\phi \approx 0.65$ is observed every night. On December 31 (bottom right) part of the absorption signature has an unexpected shift from red-to-blue. The greyscale goes from black at 0.8 to white at 1.05 times the local continuum.

early in the night at the start of the observing run. This was so that we had a chance of re-observing it for many subsequent nights. The other criterion for the prominence was that it should be large enough (produce a significant amount of H_α absorption) so that it could be easily observed against any changes in the emission from the Balmer lines of this active star. As it happened the choice of prominence was obvious.

During the first clear night of the run (December 25) a dark absorption feature was observed just leaving the stellar disc at a rotational phase of $\phi \approx 0.65$ (see Fig. 4.4). On each subsequent night we attempted to observe this rotational phase. This was not always easy given the demands of our other observing programs, the need to obtain complete phase coverage of AB Dor for Doppler imaging studies and, of course, the whims of the clouds. Fig. 4.4 shows that we were successful at being able to re-observe at least some of the phases of our chosen prominence on all of the nights December 25 to 31 (except December 29). Unfortunately we had poor weather on December 26, although the prominence is clearly present. On December 27 we observed approximately three-quarters of the prominence. On December 28 we observed virtually the whole track of the prominence and found that the morphology of the prominence had changed from the previous night. The data taken on the night of December 29 are of very poor quality and so are not shown in Fig. 4.4. We observed the prominence again on December 30. Finally, on December 31 we observed the unusual behaviour which is discussed below. The observations taken on previous nights indicate that this prominence is located at a height of approximately 2.7 $R_\odot$, which means that it is at the equatorial co-rotation radius of AB Dor.

4.3.3   Prominence undergoes eruptive event

It is clear, even from the initial data reduction at the telescope, that something unusual was observed on December 31. The bottom-right panel of Fig. 4.4 shows that during the prominence's passage across the stellar disc there is a sudden disruption. Immediately after this there is an unusual red-to-blue movement of the absorption feature. Then absorption appears at extreme negative velocities (blueshift), well beyond that of the stellar rotation profile. This is accompanied by absorption seen at large positive velocities (redshift).

The first question we must ask ourselves is whether what we have just described is real. As a result of the UCLES set-up, we obtain an additional copy of the H_α line at the
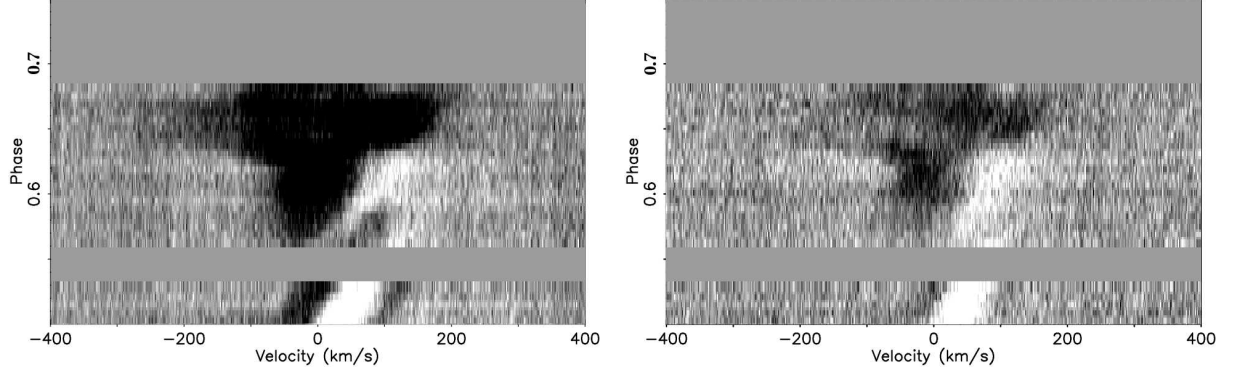
Figure 4.5: The prominence eruption seen in both H_α (left) and H_β (right). Both panels are on the same greyscale contrast range of black at 0.95 and white at 1.02 times the local continuum level. Both of these Balmer lines show the prominence eruption event. Broad emission can be seen in the H_β line just before the eruption event (see text).

extreme end of a subsequent echelle order. This too shows the same behaviour, albeit with a lower signal-to-noise. Furthermore the H_β line also shows a weaker version of the same event. This has been reproduced in Fig. 4.5 alongside the H_α line, which is on a slightly different greyscale to that of Fig. 4.4 in order to highlight the weak blue and red-shifted absorption. Prominences are considerably less optically thick in H_β than in H_α; in the last chapter we found that large prominences on Speedy Mic are more than a factor of two less optically thick in H_β than H_α. This means that we are able to better discern what is happening beneath the prominence in H_β than in H_α. In Fig. 4.5, the H_β line shows an emission component with broad wings just before (at phases $0.61 < \phi < 0.63$) the observed disruption to the prominence. This is one of many flares that are observed in the Balmer lines of AB Dor which are likely the result of a magnetic reconnection event.

In Fig. 4.6 we show each individual H_α spectrum as a line plot, with their phases of observation written on the right-hand side. We now examine the event in detail. The reader should refer to Fig. 4.6 as well as Figs. 4.4 & 4.5. Furthermore we reiterate that successive spectra are separated by 276 s, or 0.0062 in phase. The first few spectra (phases $0.566 < \phi < 0.585$) show the prominence we are considering coming onto the stellar disc and another (smaller) prominence just leaving the disc. During phases $0.591 < \phi < 0.610$ more of the prominence comes on to the stellar disc and the fractional line-of-sight absorption increases to more than 0.1. At phase $\phi = 0.610$ the above mentioned emission
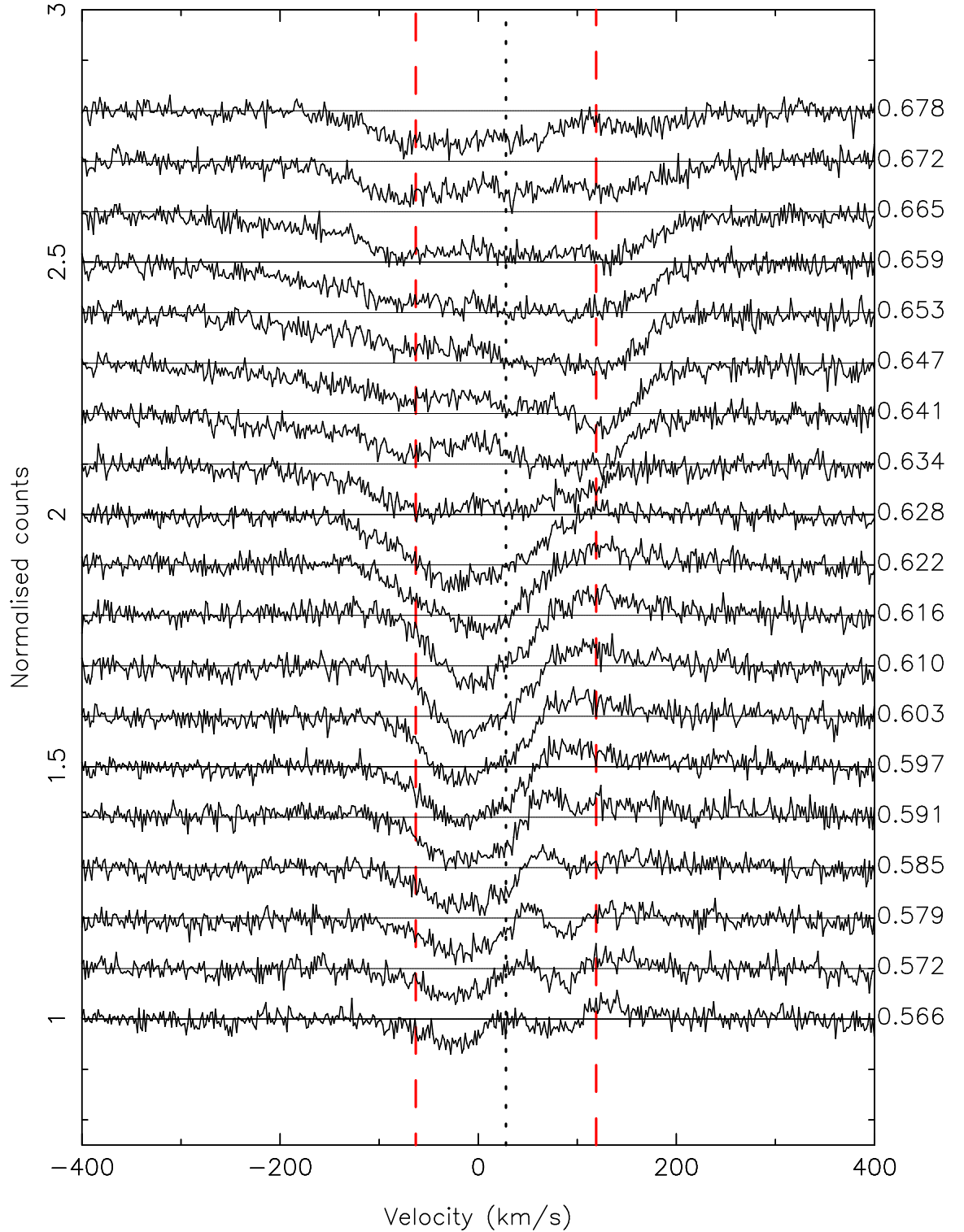
Figure 4.6: Individual H$_\alpha$ spectra are plotted for the entire prominence eruption. The phases of observation are written to the right of the plot. The vertical red dashed lines show the stellar $v \sin i$ limits, while the black dotted line is at line centre. Thin black horizontal lines show the continuum level at each vertically shifted spectrum for reference.
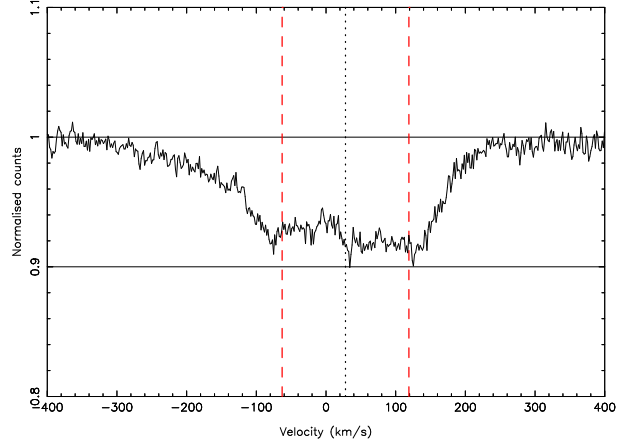
Figure 4.7: This plot combines H$_\alpha$ spectra between phases $\phi = 0.641 - 0.665$ in order to produce a single high S/N spectrum. Absorption is clearly seen at blue-shifted radial velocities in excess of 300 km s^{-1} and red-shifted velocities of more than 200 km s^{-1}. Red vertical lines show the stellar $v \sin i$ limits, while the black dotted line is at line centre.

can be seen in H$_\beta$. We get the first evidence of the start of the event in H$_\alpha$ at phase $\phi = 0.622$ when the negative velocity (blue) edge of the prominence starts to grow. The very next spectrum ($\phi = 0.628$) shows the pronounced move of the core of the absorption to the blue by some 50 km s^{-1}. Next we see a further blue-shifted absorption (both in the core and the far blue wing) and the start of a red-shifted absorption at phase $\phi = 0.634$. Through phases $\phi = 0.641 - 0.665$ we see the growth of both the blue and red-shifted absorption. In the last two spectra however, the extreme blue-shifted absorption starts to disappear.

In order to better see the extent of the absorption observed beyond both the red and blue stellar $v \sin i$ limits we have combined the spectra from the phase range $\phi = 0.641 - 0.665$. The resulting higher signal-to-noise spectrum is shown in Fig. 4.7. Here it is easy to see that the blueshifted absorption extends to velocities of at least -350 km s^{-1}. The redshifted absorption goes out to 250 km s^{-1}.

4.3.4   Discussion

It is clear from the last section that the prominence underwent some sort of disruptive event as it was crossing the stellar disc on December 31. The most obvious explanation for the observations is that there was a magnetic reconnection event in the supporting

magnetic field that triggered the eruption of the prominence. We now attempt to see if the derived properties of this event can be explained in the context of a simple 'toy' model.

From the observations of this prominence made on the nights prior to December 31, we have estimates for its phase of meridional crossing and height. The prominence is found to have a height near the stellar co-rotation radius (2.7 R_*), so we therefore set this to be the starting height of the prominence in our model. We also assume that the prominence crosses the meridian at the same phase as it did the night before ($\phi = 0.641$). The eruption phase is taken to be at $\phi = 0.610$, which is when the broad-winged emission is seen in the H$_\beta$ line. We then calculate the position of the prominence at the epoch of each individual spectrum shown in Fig. 4.6. This is achieved by measuring the maximum extent of the blue shifted absorption for each observed phase (see Table 4.2) and then assuming that this is the outward velocity of the prominence during that exposure. This then allows us to calculate how far the prominence has moved during that time. We further assume that the prominence moves *radially* outward from the star. This would be the case if the material is guided by the now open magnetic field lines that once contained the prominence. We display our estimates for the outward velocities and the prominence heights in Table 4.2. Note that for phases $0.610 < \phi < 0.647$ the prominence appears to be accelerating. After this, phases $0.647 < \phi < 0.665$ show a constant outward velocity of approximately 360 km s^{-1}. This is similar to the typical expansion velocities of erupting solar prominences (e.g. Haisch et al. 1983). The velocities in Table 4.2 are used to generate the red curve shown in Fig. 4.8 which shows the path of the erupting prominence. The black squares trace the path of the prominence had it not erupted, i.e. if it had stayed at the co-rotation radius (dashed line).

We can now compare our model (Fig. 4.8) to the observed behaviour (Fig. 4.6). According to the model, we should not see the prominence transiting the stellar disc in the first two spectra, yet we see weak (but significant) absorption at those phases in Fig. 4.6. This immediately suggests that part of the prominence is at a considerably lower height (nearer to the AB Dor surface) than our assumed starting height for the prominence of 2.7 R_*. This fits with how slowly the prominence is observed to move on to the stellar disc. According to the model, at the epoch of the last observed spectrum, the fastest moving parts of the erupting prominence should have achieved a height (measured from the stellar rotation axis) of 3.9 R_*. At this time the fastest moving parts of the erupting prominence are predicted to be just moving off the projected stellar disc, as shown in Fig.

Table 4.2: Detailed here are the outward velocities as estimated from Fig. 4.6. Note that these are measured with respect to the AB Dor radial velocity of 28 km s^{-1} and also include the offset in velocity caused by the projected velocity of the 'unerupted' prominence position. The quoted velocities are used to calculate the height of the prominence during the event and are plotted in Fig. 4.8. The last two spectra show a reduced outward velocity and we therefore simply assume that the prominence maintains the same velocity as observed at phase $\phi = 0.665$ (see text).

Phase	v_{out}	Height
ϕ	km s^{-1}	R_*
0.565	0.	2.70
0.572	0.	2.70
0.578	0.	2.70
0.584	0.	2.70
0.591	0.	2.70
0.597	0.	2.70
0.602	0.	2.70
0.610	0.	2.70
0.615	70.	2.72
0.621	123.	2.77
0.628	158.	2.83
0.634	226.	2.92
0.640	312.	3.04
0.647	353.	3.17
0.652	355.	3.31
0.658	358.	3.44
0.665	362.	3.58
0.671	362.	3.72
0.677	362.	3.86
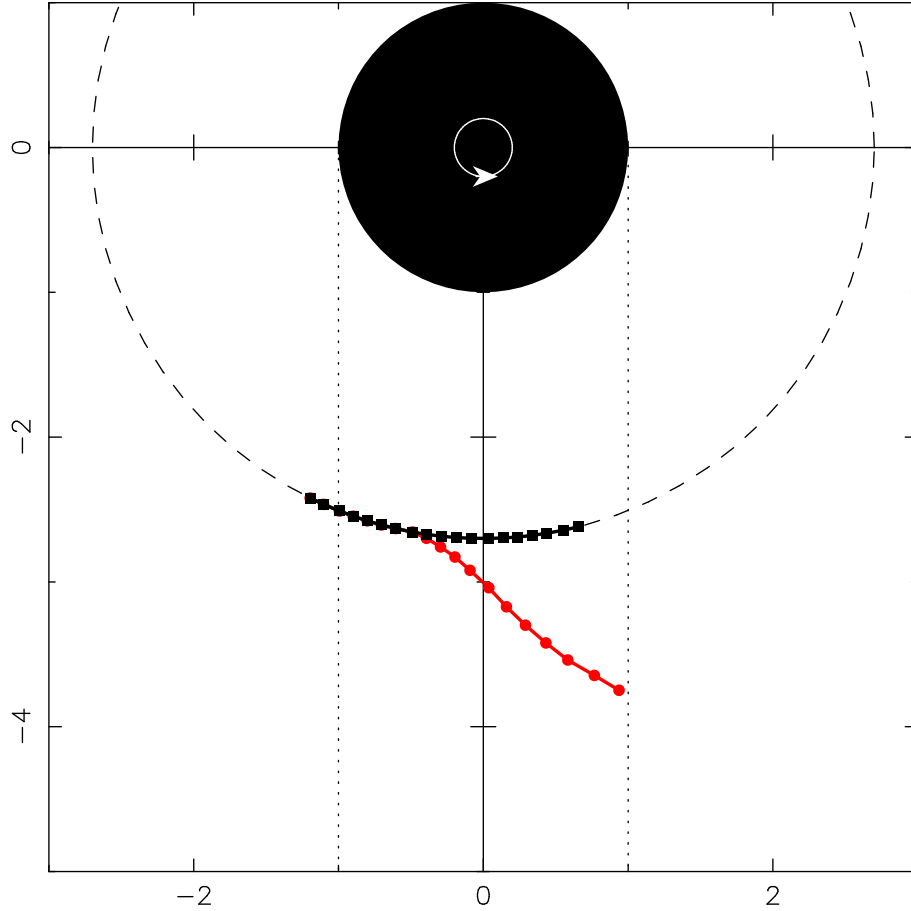
Figure 4.8: An illustration of a simple model for the dynamics of the prominence eruption. The system is seen from above, with axes centred on AB Dor and units in stellar radii. The observer is at the bottom of the plot with the dotted lines showing the lines-of-sight to the star (analogous to the stellar $v \sin i$). The large dashed circle shows the location of the co-rotation radius at 2.7 R_* and is also assumed to be the starting height of the prominence. The filled black points show the predicted path of the prominence had no eruption occurred. Similarly, the red points show the calculated positions of the prominence from the measured maximum radial velocities during the eruption and assuming outward radial motion (see text for further details). The model shows that the red line reaches the edge of the observed disc before the non-erupting points. Hence by the last observed spectra the fastest moving parts of the prominence are predicted to be finishing their transit of the stellar disc.

4.8. Looking at the last two spectra (at phases $\phi = 0.672$ and $\phi = 0.678$) in Fig. 4.6 we can see that the extent of the blue-shifted absorption is significantly reduced. The previous spectrum at phase $\phi = 0.665$ shows a maximum blue-shifted velocity of approximately 360 km s^{-1} while these two subsequent spectra have a velocity less than 200 km s^{-1}. Therefore, at least in a qualitative way, our simple model of the prominence eruption explains why the blue-shifted velocity of the absorption decreases in the last spectra. The fastest erupting prominence material simply leaves the stellar disc as seen from our line-of-sight and becomes invisible to us. The fact our model reproduces some of the observed behaviour supports the conclusion that we have indeed witnessed a stellar prominence eruption. Unfortunately, from this data alone, it is not possible to establish how much of the prominence was ejected. If we had data of the event in the CaII H & K lines, as we did for Speedy Mic in the last chapter, then we would have been able to better assess the energetics of the eruption.

Prominences have been observed on AB Dor for the last 20 years. Observations at many epochs have shown prominences that appear and disappear on a 3 to 4 day timescale (Collier Cameron et al. 1999). If the fate of large stellar prominences is to be ejected from the star, then why have we only now seen such an event? Or put another way, is the observation of just one prominence eruption consistent with their observed lifetimes? To answer this we need to consider the probability that a prominence erupts as it is transiting the stellar disc. Examining the AB Dor H$_\alpha$ data for the ten year period between December 1995 and December 2004 (the epoch of these observations) approximately 70 prominences have been observed. Note that we only count a prominence if more than half of its transit across the stellar disc is observed and we make no attempt to re-identify prominences on subsequent nights (so if a prominence is observed twice it is counted twice). If we assume that all of these prominences were located at the co-rotation radius then we know that they take approximately an hour to transit the stellar disc. Therefore if we assume that the average prominence lifetime is 3.5 days, then we observe a single prominence for approximately 1.2 % of its total lifetime. Consequently, from observing 70 prominences we would expect to have seen 0.83 eruptions. Although this is an extremely rough 'back of the envelope' calculation, the fact that we have observed only a single prominence eruption appears to be reasonable. Many other questions are left unanswered however; for example, how does the presence of lower lying prominence material seen before the eruption relate to it?

4.4 Conclusions

Some of the observations presented in this chapter are the first efforts of their kind and as such are very interesting but should be interpreted with caution. One observation that is quite obvious though is that there were relatively few prominences seen on AB Dor in 2002 and that they were restricted to one half of the stellar rotation. This then raises the question, was this just a statistical fluke or is it telling us something about AB Dor at this epoch? If the latter then it is possible that the numbers and positions of prominences are tracers of the extent of closed magnetic loops in the stellar corona. As such, a future methodical study that compares the numbers and distribution of all prominences observed on AB Dor over the past twenty years with surface brightness and magnetic maps from Doppler imaging techniques may be very interesting.

In §4.2 we also presented tentative evidence that a high latitude stellar prominence was observed eclipsing a lower height EUV region. At face value, this observation suggests that the EUV flux comes predominantly from a small number of compact emitting region at high stellar latitude (quite possibly near to the stellar pole). In the future more temporal overlap between X-ray (particularly EUV) and optical (H_α) observations would allow us to verify this result. If stellar prominences are found to eclipse EUV regions then this may lead to a better understanding of both the physical properties (e.g. filamentary structure) of the prominences and also the sizes and distribution of EUV/X-ray emitting regions.

The chance observation in §4.3 of an unusual event that occurred during the transit of a large prominence on AB Dor is fascinating. The most likely explanation for the blueshifted and redshifted velocities appears to be that we have caught this stellar prominence in eruption. As such we are seeing material being flung outward from the star and also material flowing back down on to the stellar surface, much like we see in giant solar prominence eruptions. Although this particular event requires more analysis, it furthers the analogy between stellar prominences and their solar namesakes. Future observations of the prominences on other stars are strongly encouraged and then hopefully we will not have to wait another decade to observe the next erupting stellar prominence!

CHAPTER 5

Zeeman Doppler imaging of binary star systems

The dome of the Anglo-Australian Telescope against the backdrop of the Southern sky

5.1   Chapter synopsis

This chapter describes the development of a binary star Zeeman Doppler imaging code. It is based upon the binary brightness imaging code DoTS and the single star ZDI code of Hussain et al. (2000). We have therefore named our new binary code 'ZDoTS'. Before I go into details of the code (in §5.4) I will first briefly outline the methods to observe stellar magnetic fields in §5.2 and the LSD technique to boost signal-to-noise in §5.3. Then in §5.4 I will describe the basics of Doppler imaging before progressing onto Zeeman Doppler

imaging and then to describing the development of ZDoTS. In §5.5, I present tests of ZDoTS using synthetic data. Finally, in §5.6 I describe the necessary modifications to incorporate stellar differential rotation into the binary Doppler imaging process.

5.2 Stellar magnetic fields

Measuring the magnetic fields of cool stars is an intrinsically complex problem due to the fact that stars (like our Sun) are covered in magnetic regions of alternating polarity. Early experiments attempted to measure the relative line shifts of right and left circularly polarised light in order to obtain the average magnetic field component along the line-of-sight. However because of the aforementioned complex magnetic surface topologies the opposite polarities mutually cancel and leave only a very weak magnetic signature. For example, the net circular polarisation measurement of the Sun, if viewed as a star, would correspond to a maximum mean magnetic field of only 2 G (Plachinda & Tarasova 2000, from collapsing solar magnetograms). This is barely measurable using current instrumentation.

Direct measurements of magnetic field strength from the splitting or broadening in unpolarised spectra have had more success (Robinson et al. 1980, Saar 1988, Valenti & Johns-Krull 2001). This is due to the fact that broadening signatures do not suffer mutual cancellation like that experienced by polarisation signals. Essentially it provides an estimate of the relative surface area covered by magnetic field, together with an average magnetic intensity. As discussed in Chapter 1, this technique is responsible for the majority of current estimates of stellar magnetic field strengths. However, this technique is almost completely insensitive to magnetic field topology. Instead we now consider Zeeman Doppler imaging (ZDI), as introduced by Semel (1989).

5.2.1 The Zeeman effect

Atomic spectral lines are split in the presence of an external magnetic field (B) as the result of the Zeeman effect (Zeeman 1897). The extent of the splitting is dependent upon the Landé factor (g) which represents the ratio of the magnetic to the mechanical moment of a given state:

$$g = 1 + \frac{j(j+1) + s(s+1) - l(l+1)}{2j(j+1)} \tag{5.1}$$

where j is the total angular momentum, s is the spin angular momentum and l is the orbital angular momentum.

The Zeeman effect therefore splits a line, that would otherwise be single when no magnetic field was present, into three separate components (in the case of the normal Zeeman effect where transitions occur between states with the same g). One of the three components (called the π component) corresponds to the unshifted component found at the rest frequency, ν_0. The other two components (named $\sigma^{\pm}$) are found shifted from the rest frequency by $\nu_0 \pm \mu_0 gB$ where $\mu_0 = eh/2mc$ is the Bohr magnetron. Note that the degree of splitting is directly proportional to the strength of the applied field B.

In addition to splitting a spectral line, the Zeeman effect also introduces a polarisation. In the presence of a magnetic field parallel to the observers line-of-sight (referred to as a *longitudinal* field) the π component vanishes and the $\sigma^{\pm}$ components have opposite circular polarisations. If the magnetic field is perpendicular to the line-of-sight (a *transverse* field) then the π component is linearly polarised parallel to the direction of the field and the $\sigma^{\pm}$ components are linearly polarised perpendicular to the field direction. The presence of a magnetic field thus leads to the splitting of lines which are polarised in different ways depending upon the orientation of the field. The Zeeman effect therefore encodes information about both the intensity and geometry of the local magnetic field.

5.2.2   The Stokes parameters and measuring polarised light

Elliptically polarised light is the result of the combination of linear and circular polarised light. In Fig. 5.1a we illustrate the polarisation ellipse of the electric vector of a beam of radiation as seen if looking along the direction of propagation. The state of polarisation can then be described by giving the semi-major (A) and semi-minor (B) axes of the polarisation ellipse and its rotation (ϕ). However, this is not a very useful way to observationally measure the degree of polarisation.

The four Stokes parameters (I, Q, U and V) were introduced to fully describe the state of polarisation of light. Stokes I represents the total intensity information, Q and U describe linearly polarised light and V corresponds to circularly polarised light. Their particular formalism is useful because any polarisation state can be generated from the sum or differences of measurable intensities. Observationally it is useful to think in terms
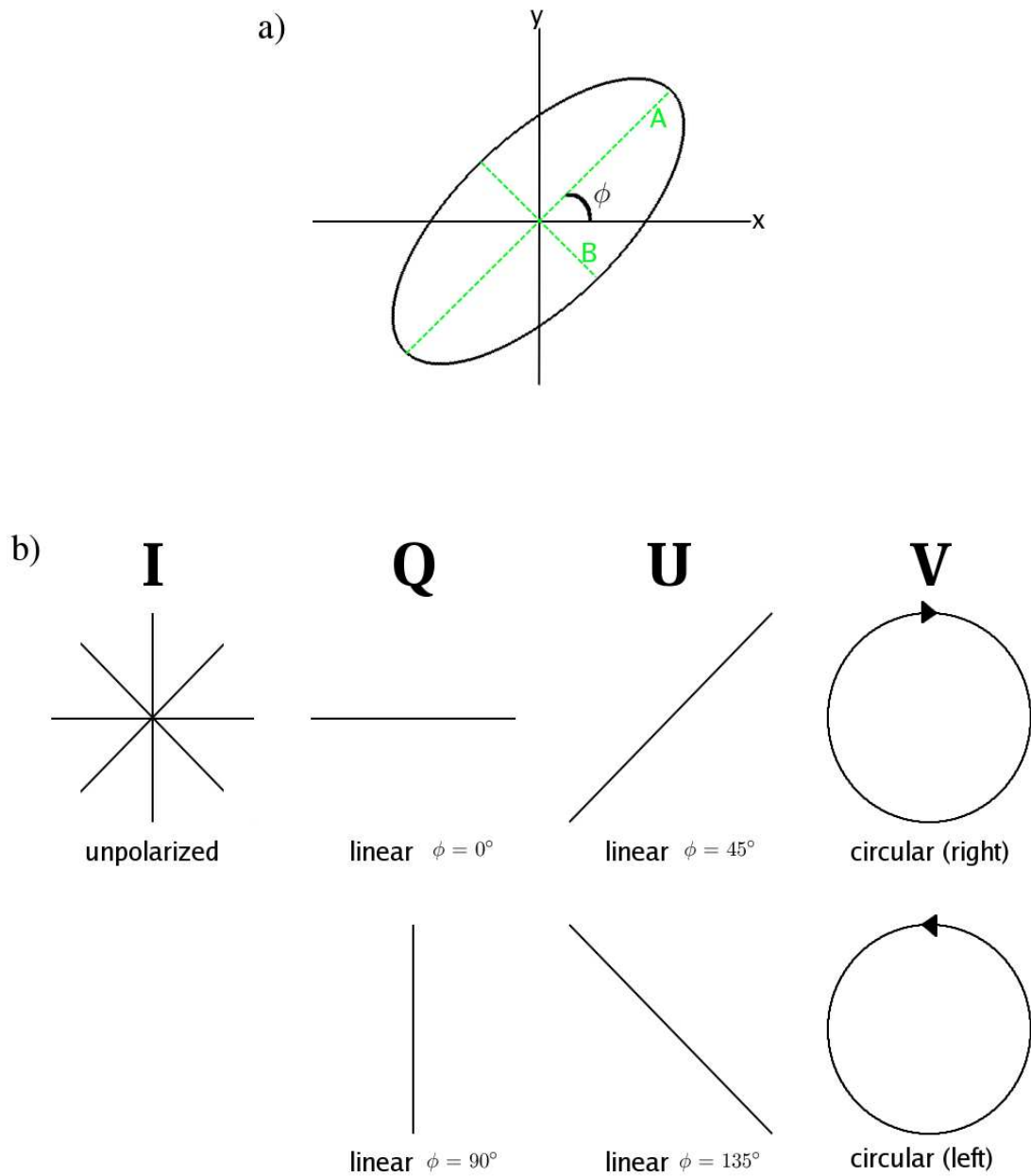
Figure 5.1: In the top panel (a) the electric vector of elliptically polarised light is shown. In the bottom panel (b) the filters that can be used to generate the Stokes parameters are illustrated.

of different filters which, when used in combination, can measure the degree of each type of polarisation. The Stokes parameters are found by combining the filters shown in Fig. 5.1b:

$$I^2 = Q^2 + U^2 + V^2$$

$$Q = I_{\phi=0} - I_{\phi=\pi/2}$$

$$U = I_{\phi=\pi/4} - I_{\phi=3\pi/4}$$

$$V = I_{right\ circ} - I_{left\ circ}$$

The linear polarisation profiles, Stokes Q and U, observed for cool stars are at least an order of magnitude smaller in amplitude than the Stokes V signatures (e.g. Brown et al. 1991). Therefore currently ZDI of cool stars has only made use of the longitudinal Zeeman effect to observe stars in circularly polarised light (Stokes V).

Modern spectropolarimeters are carefully designed so that they minimise the effects of spurious polarisation signals that can be introduced by instrumental effects. For example, the SemelPol instrument used in this thesis is mounted directly at the Cassegrain focus of the Anglo-Australian Telescope. Here the quarter-waveplate and calcite beamsplitter measures and converts right and left circularly polarised light into two perpendicular beams of linearly polarised light. This light is then fed down to the UCLES spectrograph using optical fibres. This set-up minimises the effects of instrumental polarisation which would be experienced if the Coudé optical train were used. Further efforts to minimise spurious polarisation signals are made by introducing a particular observing procedure. Between subsequent exposures the quarter-waveplate in SemelPol is rotated by $\pm45°$, which causes a switch of the left and right polarisation carried in each fibre. As a consequence all polarisation signals are exchanged throughout the entire instrumental set-up, suppressing all spurious polarisation signals down to first order. The same basic principles have recently been applied in the construction of the dedicated high-throughput spectropolarimeters ES-PaDOnS on the 3.6-m Canada-France-Hawaii Telescope (CFHT) and its twin NARVAL on the 2-m Telescope Bernard Lyot (TBL). For more information on spectropolarimetric observations the reader is referred to Semel et al. (1993), Donati et al. (1997) and Donati et al. (2006).

5.3 Least squares Deconvolution

Once the raw spectra have been reduced and the Stokes V spectra generated then the technique of least squares deconvolution (LSD) is applied to significantly boost the signal-to-noise. This is an especially important step for Stokes V spectra where the signatures typically have amplitudes of the order 10^{-3} that of the Stokes I continuum. To have any realistic chance of inverting these signatures into a magnetic field distribution on the stellar surface they need to be measured to an accuracy of 10^{-4}.

The LSD technique was developed by Donati et al. (1997). It effectively combines the absorption line profiles of thousands of photospheric lines to construct a single high S/N line profile. An input linelist (mask) appropriate to the stars spectral type is used which can be obtained from online databases such as the Vienna Atomic Line Database (VALD, Piskunov et al. 1995, Kupka et al. 1999). For each absorption line the linelist contains the wavelength (λ), the central line depth intensity (d) and the magnetic sensitivity or Landé factor (g). The lines are then combined according to the weight (w): $w = g\lambda d$.

Strong chromospheric lines such as the Hydrogen Balmer series and CaII lines are typically removed from the linelist. It should be noted however that recent promising work in reconstructing the magnetic field distribution in the chromosphere by using only these lines has been made (e.g. Petit 2007). The multiplex gain in signal-to-noise resulting from the LSD procedure is proportional to the square root of the number of lines ($\propto \sqrt{N_{\text{lines}}}$). Stokes V spectra are better suited to the LSD procedure than Stokes I spectra (see Donati et al. 1997) and often approach this theoretical limit. For 2000 spectral lines, typical multiplex gains are 20 - 45 for Stokes V and 10 - 20 for Stokes I spectra. This transforms a Stokes V spectrum with an input S/N of 100 - 200 into a single profile with an effective S/N of 2000 - 9000. It is therefore no exaggeration to say that LSD makes Zeeman-Doppler imaging possible.

LSD is, however, not without its limitations and drawbacks. It essentially assumes that the shape of the Stokes V signature is the same in all individual lines. The *mean* LSD profile can therefore only be described in terms of average properties of the input lines, for example an average wavelength and Landé factor. A newer technique being developed for effectively boosting the signal-to-noise of Stokes V spectra whilst at the same time preserving information about individual lines is Principal Component Analysis
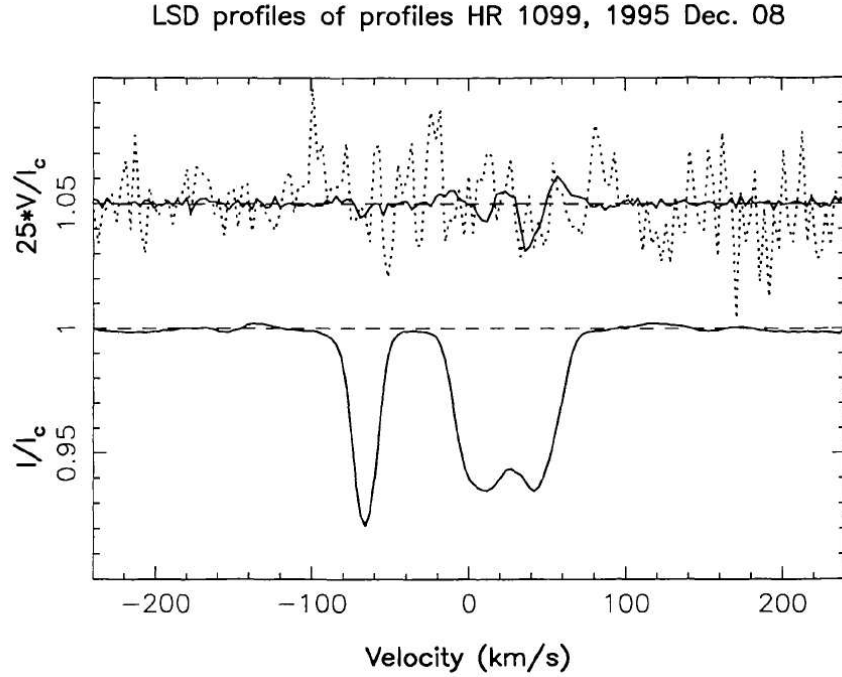
Figure 5.2: Example LSD profiles from HR 1099. The lower plot shows the Stokes I LSD profile where the two binary components can clearly be seen. The top plot shows the resulting Stokes V LSD profile (solid line) from combining thousands of lines and an earlier attempt at combining only three lines (dotted line). These profiles have been shifted up by 0.05 and multiplied by a factor of 25 for display purposes. The significant increase in S/N provided by the LSD technique is clear to see. Also note that the amplitude of the Stokes V signature for the secondary star is very much smaller (or negligible) compared to that of the primary star in this RS CVn binary. Taken from Donati et al. (1997).

(PCA) (Carroll et al. 2007). The technique effectively removes incoherent effects such as noise while allowing the reconstruction of individual line profiles so that the known line parameters can be used in the ZDI process.

Fig. 5.2 shows example Stokes I and V LSD profiles of the RS CVn system HR 1099, obtained by Donati et al. (1997). It clearly illustrates the power of the LSD technique in the detection and measurement of Stokes V signatures. Fig. 5.2 also introduces the idea of studying the Stokes V profiles of stars in binary systems. This brings us to the point where we can now discuss the development of a binary ZDI code.

5.4 ZDoTS - a binary Zeeman Doppler imaging code

5.4.1 Why do we need one?

Magnetic maps of stars in binary systems have been produced before for a limited number of systems, so why do we need a binary ZDI code? All previous magnetic maps have been produced using ZDI codes designed to work on single stars. The few maps of the primary stars of binary systems that have been produced to date were obtained by performing the initial step of correcting the LSD profiles for the orbital motion. The data can then be treated as that of a single star. This is a common procedure for modelling of both Stokes I and V data by codes that are not capable of modelling the contribution from both stars. Due to the continuum present in Stokes I spectra this is particularly difficult. The binary conjunction phases are either not observed, or the part of the primary rotational profile that overlaps with the secondary star is masked out, or the secondary profile is removed by subtraction of a Gaussian.

The situation when using Stokes V data is considerably easier because the continuum is unpolarised. For RS CVn binaries the magnetic field strength of the secondary star is so small (due in part to the ratio of the stellar luminosities) that its contribution to the combined Stokes V signatures can often be assumed negligible. This was illustrated in Fig. 5.2 where it could be seen that the G5V secondary had Stokes V signatures that were within the noise level of the data. It is this assumption of no Stokes V contribution from the secondary star that is used to produce the many magnetic images of the primary star in the RS CVn binary system HR 1099 (e.g. Petit et al. 2004). In a binary system with more similar components, both Stokes V signatures can be detected and measured. A good example of this is the pre-main sequence binary system HD 155555 which forms the subject of the next two chapters. We defer further discussion about the impracticalities of using a single star code to model the Stokes V signatures until then.

We therefore set out to develop a new binary star ZDI code. The code itself is based on that of Hussain et al. (2000). For a full and detailed explanation of the code we refer the reader to Hussain (1999) and Hussain et al. (2000). What follows is a brief summary of the principles of Doppler and Zeeman-Doppler imaging and then the details of the changes that were made to enable the modelling of binary star systems. Following this we show tests of our new code.

5.4.2 Doppler imaging principles and DoTS

The majority of cool stars (like the Sun) are relatively slow rotators and therefore have absorption-line widths less than 10 km s^{-1}. In G and K dwarfs macroturbulence is typically the dominant broadening mechanism. A small subset of cool stars however are rapidly rotating, normally due either to youth or from being a member of a close binary system. For these stars the dominant broadening mechanism is rotation and they can have projected rotational velocities ($v\sin i$) in excess of 100 km s^{-1} (e.g. the aptly named star 'Speedy Mic' in the last chapters has $v\sin i=132$km s^{-1}).

The technique of Doppler imaging was first attempted by Vogt & Penrod (1983). Doppler imaging models the stellar surface from observing features moving through the rotationally broadened line profile. A cool surface inhomogeneity (i.e. star spot) is seen as a 'bump' in the line profile. This is well illustrated in Fig. 5.3. From tracking the feature as it moves through the line profile we can ascertain its longitude on the stellar surface by measuring when it is at the centre of the line profile. We can also obtain some information as to the stellar latitude of the spot. By modelling the minimum and maximum velocities attained by a feature and its radial acceleration as it moves through the rotational profile, Doppler imaging codes yield the stellar latitude.

The Doppler imaging code used in Chapters 6 & 7 to recover stellar brightness maps and upon which the Zeeman-Doppler imaging codes are based is called 'DoTS' (*Do*ppler *T*omography of *S*tars). Details of the workings of the code have been published in Collier Cameron (1992), Collier Cameron et al. (1992), Collier-Cameron & Unruh (1994), Collier Cameron (1995), Collier Cameron (1997), Hussain (1999) and Barnes (1999).

The forward problem

DoTS uses a two-temperature model to describe the stellar surface. Here a single temperature is assumed for all spots in addition to a single photospheric temperature. The stellar surface is then characterised by a 'spot filling-factor' (f). Lookup tables are created that contain pre-calculated specific intensity profiles as functions of foreshortening and temperature on a linear interpolation grid. These are used to generate the geometric kernel that contains the local intensity profile for each surface element (pixel) on the stellar surface. The stellar surface is modelled initially by a uniform rectangular grid in latitude
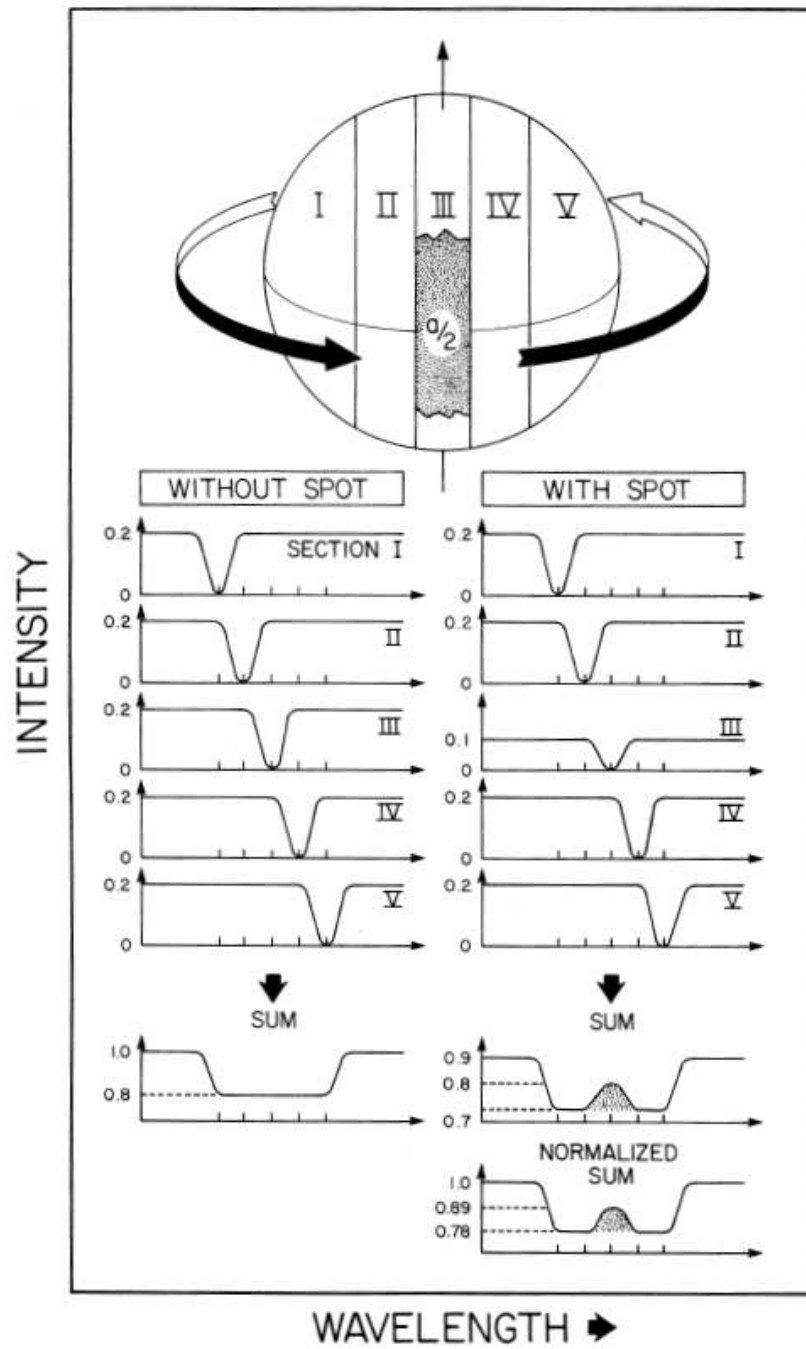
Figure 5.3: An illustration of the principle of Doppler imaging including how star spots create deformations in the rotationally broadened line profile. Taken from Vogt & Penrod (1983)

and longitude. Each pixel on this grid is further subdivided into two triangular pixels. Properties of the surface such as limb darkening and foreshortening angle are calculated on this finer triangular grid. A further grid is constructed with fewer pixels at higher latitudes to maintain approximately constant pixel area at all latitudes. This is referred to as the 'adaptive grid'.

Given a particular surface brightness distribution ($\mathbf{f}$) it is then possible to create a line profile for the star by integrating the specific intensities of all visible pixels. This is achieved by using an intermediate grid called the 'viewplane'. The viewplane is another rectangular grid with coordinates such that its axes, u and v, lie in the velocity frame which is occupied by the stellar disc in the case of a single star. When modelling a binary system the viewplane must cover the entire velocity range of the binary orbit, in addition to the stellar $v\sin i$ (i.e. $u_{\mathrm{range}} \geq K_1 + K_2 + v\sin i_1 + v\sin i_2$). Essentially the viewplane can be thought of as representing the plane of the sky (see Collier Cameron 1997 for further details).

When performing the image-data transformation allowance is made for the shift in velocity of each pixel from the stellar meridian (or binary centre of mass) at that particular phase. This essentially describes the 'forward problem' in Doppler imaging. It is then possible to measure the degree of agreement between the synthetic profile (D) and that of the spectroscopic observations (F) using the goodness of fit statistic:

$$\chi^2(\mathbf{f}) = \sum_{k=1}^{M} \left(\frac{F_k - D_k(\mathbf{f})}{\sigma_k} \right)^2 , \qquad (5.2)$$

where M is the total number of observations.

In theory therefore all we need to do is iteratively modify our initial surface brightness model until we achieve the minimum (best) value for χ^2. Unfortunately Doppler imaging is an ill-posed problem because there are an infinite number of possible brightness maps that can fit the observed data. There is insufficient data for a unique solution to this inversion problem (often referred to as the 'inverse problem' of Doppler imaging). This fact is easy to visualise as pixels on the surface that have the same velocity shift in image-space are not independent of each other.

The inverse problem

We therefore need to introduce an additional constraint into the imaging process, a regularising function. DoTS uses maximum entropy to select the image where there is least correlation between different parts of the image. The exact form of the entropy employed by DoTS is that of Skilling & Bryan (1984) (using the MEMSYS routines):

$$S(\mathbf{f}) = -\sum_{i=1}^{n} w_i \left[f_i \log \frac{f_i}{m} + (1 - f_i) \log \frac{(1 - f_i)}{(1 - m)} \right],$$

(5.3)

where m is the default image and is set to a very small positive number.

$S(\mathbf{f})$ can also be described as the 'penalty function', so called because it favours images with low spot filling factors (where $f = 0$ represents the unspotted photosphere). The entropy decreases smoothly with increasing spot filling factor, pulling the image towards the unspotted photospheric level in the absence of further observational data constraints. This effectively attempts to produce the simplest image (with least structure) that still fits the data. In order to find the maximum entropy, S, DoTS attempts to find the extremum of the function:

$$Q(\mathbf{f}) = S(\mathbf{f}) - \alpha \chi^2(\mathbf{f}),$$

(5.4)

where α is the Lagrange multiplier. The value of α is fixed by demanding that $\chi^2 \simeq M$. Thus f_i is found by solving $\delta Q(\mathbf{f})/\delta \mathbf{f_i} = 0$, i.e.

$$w_i \left[\log \frac{m}{1 - m} - \log \frac{f_i}{1 - f_i} \right] = \alpha \frac{\delta \chi^2(\mathbf{f})}{\delta \mathbf{f_i}}.$$

(5.5)

With the exception of the modification to enable differential rotation on binary systems (described in §5.6), I make no changes to DoTS and so refer the reader to the above publications for further details of the code. We now focus on the closely related technique of Zeeman-Doppler imaging.

5.4.3 Zeeman-Doppler imaging

The idea of combining the Zeeman effect and Doppler imaging for mapping the surface magnetic fields of stars was first suggested by Semel (1989). Hussain (1999) took the then latest version of DoTS and converted it into a ZDI code capable of recovering the magnetic field distributions of single stars. This code was extensively tested in Hussain (1999) and

was compared to the code of J.-F. Donati (Donati & Brown 1997) using data of AB Dor in Hussain et al. (2000).

The Hussain ZDI code models the Stokes V contribution from each surface element as a magnetic flux filling factor. Like the spot filling factor in Doppler imaging, the magnetic filling factor ranges from 0 to 1. This is essentially a constraint imposed by the use of the MEMSYS maximum entropy regularising function described above in Eqn. 5.3. Magnetic fluxes in the range -5000 to +5000 G are mapped on to this range of filling factors. A zero filling factor represents -5000 G, 0.5 corresponds to zero magnetic field and 1.0 is +5000 G. The default image (m) is set to 0.5 in the case of ZDI. This means that the entropy function (Eqn. 5.3) is symmetric around this point, corresponding to zero magnetic field.

The code models the local line profile of each pixel as a Gaussian. For field strengths in the range -5000 to +5000 G the *weak field approximation* is assumed to hold. Therefore the contribution of each surface pixel (i), to the combined circular polarisation (V_i) can be written as a function of the unpolarised, Stokes I, profile (I_i):

$$V_i(v) \propto g\lambda \frac{\delta I_i}{\delta v}. \tag{5.6}$$

In Fig. 5.4 we show an illustration of how well the weak field approximation holds for magnetic field strengths of a few kG. While in reality the profiles should have Lorentzian wings the Gaussian model is found to be quite satisfactory given the large rotational broadening of the profiles. Therefore three dimensional lookup tables are constructed which store the Stokes V profiles for field strengths of 5000 G as a function of wavelength (velocity) and limb darkening.

For further details on the ZDI code we refer the reader to Hussain (1999) and Hussain et al. (2000).

5.4.4 Implementation of binary ZDI code

The ZDI code of Hussain et al. (2000) described in the last section is capable of modelling single stars only. This is despite the fact that it was originally spawned from the DoTS code which can produce surface brightness maps of stars in binary systems. There are a number of reasons that the functionality of a binary star code was not incorporated into
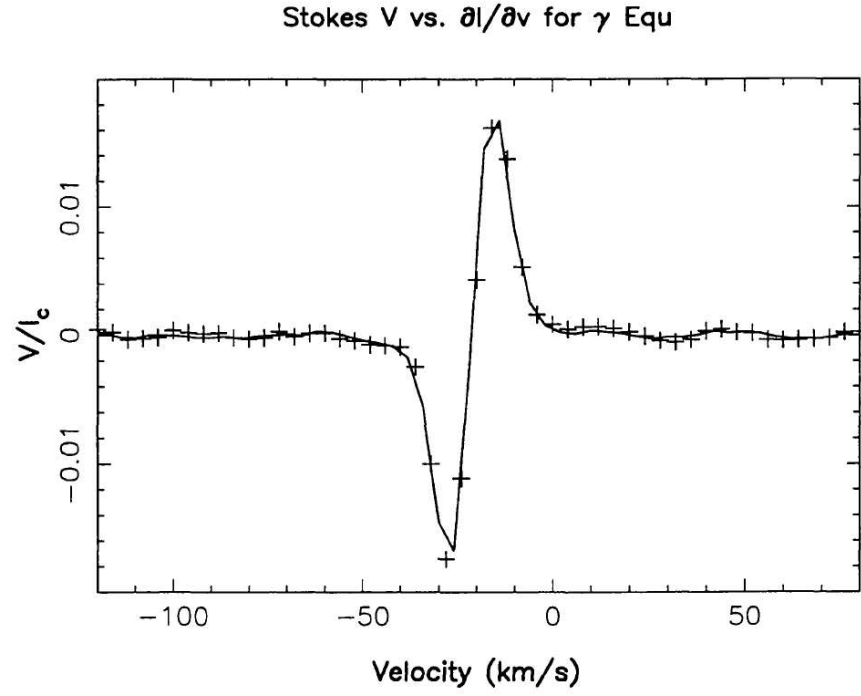
Figure 5.4: The Stokes V LSD profile (pluses) of the Ap star γ Equ is plotted with the first derivative of its LSD Stokes I profile superimposed (solid line). The level of agreement shows that the weak field approximation (Eqn. 5.6) does indeed hold, at least for the field strengths of a few kG observed on γ Equ. Taken from Donati & Collier Cameron (1997).

the Hussain et al. (2000) code, e.g. the computational demands required to model both stars simultaneously. At the start of this project there were essentially two directions along which we could have proceeded. We could either change the ZDI code of Hussain et al. (2000) to model a binary system, or we could modify the latest version of the DoTS code to perform ZDI. After some consideration it was decided that the latter option would be the most efficient way to progress. The majority of the work was carefully propagating the additional magnetic vectors through many of the (over one hundred) subroutines that make up the DoTS code. The remainder of the work involved testing of the code which we describe in §5.4.5 and 5.5. What follows is a brief outline of some of the notable changes made to DoTS to make ZDoTS.

DoTS was adapted to read-in and store maps of the three magnetic field orientations (radial, azimuthal and meridional) for both the primary and secondary star. An option was also included to generate synthetic magnetic spots, again for each type of field and each star. The code was also modified to read in separate Stokes V lookup tables, discussed in the last section, for each star. This is in addition to the Stokes I lookup tables which were already being loaded by DoTS. For ZDI we still need the intensity information in order to renormalise the Stokes V data.

At each observational phase (k) the Stokes V specific intensities are summed over the viewplane (described in the last section) for each pixel (i) on both stars in order to compute the total Stokes V contribution (V) to each velocity element (j) in the binary velocity range. This is performed for each field orientation (Hussain 1999):

$$D_{jk} = \sum [V(\Delta\lambda_{ijk}, \mu_{ik}) \cos\theta_{ik}(2f_i - 1)], \tag{5.7}$$

where $V(\Delta\lambda_{ijk}, \mu_{ik})$ represents the Stokes V specific intensity. This has been calculated using linear interpolation from the lookup tables for the limb angle, μ_{ik}, and shifted by the instantaneous line-of-sight velocity of the individual pixel, u_{ik}, (such that $\Delta\lambda_{ijk} = \Delta\lambda_j - \lambda_0 u_{ik}/c$). The line-of-sight component for the field orientation is $\cos\theta_{ik}$ for image pixel i at phase k. $(2f_i - 1)$ converts the filling factor stored between 0 and 1 to a number between -1 and 1 where 0 then represents no magnetic flux. This allows cancellation of opposite polarity magnetic regions. Normalisation is achieved using the Stokes I specific intensities for the immaculate stellar discs. Therefore when the two stars are in conjunction the resulting Stokes V spectra is modelled as the sum of all surface elements at that velocity on the viewplane grid.

Storing the specific intensities for both Stokes I and V for each pixel on each star is very expensive on computer memory. This is because the specific intensity profiles must span the entire velocity range of the binary orbit (i.e. they have the same dimension as the viewplane u axis). Given that the instantaneous contribution from each surface pixel covers a very small range of velocities, this is very wasteful. Furthermore, a ZDI code needs to store all the intensities of all three magnetic vectors (the radial, azimuthal and meridional fields) for each surface element, therefore immediately tripling the memory demand.

The latest version of DoTS includes memory saving compression of arrays implemented by John Barnes. In the case of the local Stokes I intensity profiles, DoTS calculates the most 'common' value in the profile (the continuum) and stores this number. Then it finds the point where the profile first significantly deviates from this value and stores that index. Similarly, the code then works backwards from the end of the profile to find the index where the last value significantly differs. Therefore only a single value for the continuum needs to be stored, along with the indices of the start and end of the non-continuum parts of the profile. In the case of a binary system this represents a huge saving in computer memory. Initially it was thought that this would be more difficult to implement for Stokes V profiles due to the fact that they can be positive or negative. However, the fact that the Stokes V continuum generated in the lookup tables has a value of zero (to machine rounding tolerance) allows the same technique as outlined above to be used to compress the local Stokes V profiles. Without compression, to model the stellar surfaces of the HD 155555 binary system (in the next chapters) at a resolution of 2° per latitude bin with 50 phases of observation requires in excess of 4 Gb of Random Access Memory (RAM). Given that when we consider differential rotation for HD 155555 (in Chapter 7) we need to model 106 phases, this is clearly not practical. Using the compression described above, however this can be achieved in less than 2 Gb of RAM.

5.4.5   Properties of ZDI and testing the forward module of ZDoTS

ZDI attempts to recover the three different magnetic field components (radial, azimuthal and meridional) in order to map the flux density for each surface magnetic field vector. At any given phase we are only able to record the line-of-sight component of the magnetic field ($\mathbf{B}$). The key to ZDI is that by sampling many rotational phases we are able to

observe how Stokes V signatures, produced by distinct locations on the surface of the star, change with time. We illustrate this in Fig. 5.5.

Unfortunately ZDI is only weakly sensitive to meridional field on stars with mid to high inclination angles. Given that the rotational broadening used in Doppler imaging strongly favours observation of stars at high inclination angles ($v_{obs} = v_{rot}\sin i$), maps of meridional field have rarely been recovered. The field that we do recover is mostly cross-talk with the radial and occasionally the azimuthal field components. For a more detailed discussion of the effects of field orientation on Stokes V signatures see Donati & Brown (1997) and Hussain (1999). We also discuss meridional field on HD 155555 in Chapter 6. For now, and during the tests of ZDoTS in the following sections, we consider only radial and azimuthal field.

In Fig. 5.5 we show a small simulation which uses our new ZDoTS code to simulate magnetic regions on the stellar surface and then generate synthetic spectra. The purpose of this is to compare the behaviour of the Stokes V signatures as magnetic regions of radial or azimuthal field rotate into and out of our line-of-sight. Three identical magnetic spots, with peak fluxes of 1000 G and radii of $10°$, are placed on to the surface of a star of radius 1 $R_\odot$ and rotating with $v\sin i$=91km s^{-1} and $i = 90°$(therefore simulating the K0 dwarf AB Dor except for the increased inclination angle). All three spots are located at the stellar equator, one is on the stellar meridian (position B) while the other two are at longitudes of $\pm 60°$ either side of this (positions A and C). The magnetic spots can either be thought of as three unique regions seen on the stellar surface at a particular rotational phase or equivalently as a single magnetic region observed at three different phases.

First we consider that the magnetic regions shown in Fig. 5.5 are composed of radial field. In this case the amplitude of the Stokes V signature increases as the spot rotates further onto the stellar disc. The amplitude of modulation of Stokes V signatures is simply $V_{rad} \propto \cos(\Delta\phi)$, where $\Delta\phi$ is the angular distance away from the meridian. At position B in Fig. 5.5 the magnetic spot is on the meridian ($\Delta\phi$=0°) so the radial field lines are directly pointing into our line-of-sight and we observe the maximum amplitude of the Stokes V signature. At positions A and C ($\Delta\phi$=60°) and so the amplitude of the Stokes V signature should be half that observed at B. A close examination of Fig. 5.5 reveals that the amplitude of the signatures at A and C are in fact less than half that at B. This is because the effect of limb darkening must also be taken into account.
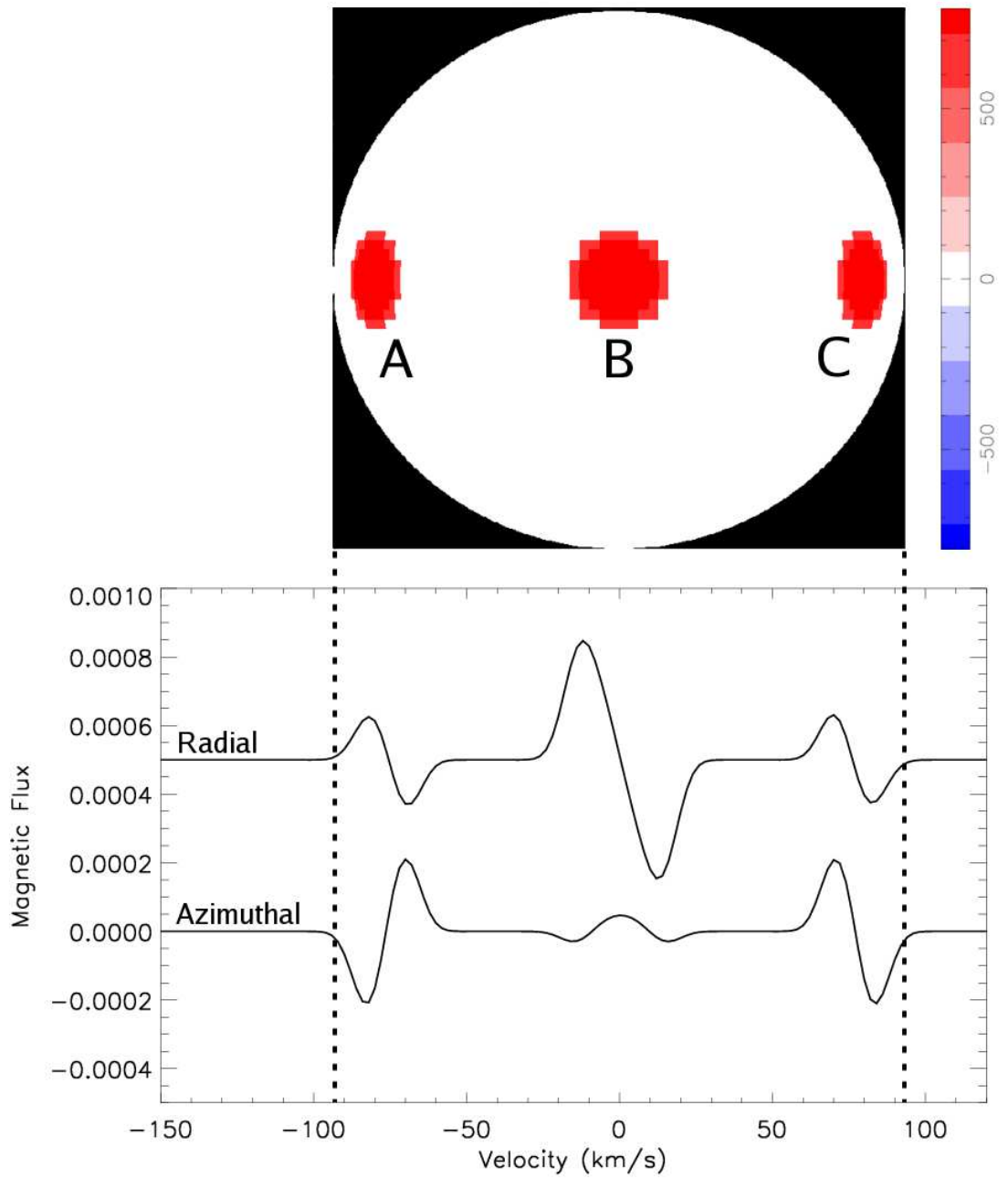
Figure 5.5: An illustration of the basic principles of ZDI. A single magnetic region is shown at three rotational phases: A, B and C on a star of $v \sin i$=91km s^{-1} and $i = 90°$. The observed amplitude of the Stokes V feature is dependent upon the nature of the field, the line-of-sight component of the magnetic field **B** and the local limb darkening (see text). At position B the azimuthal field should go to zero as the region crosses the stellar meridian. This is because the horizontally orientated field has no component in our line-of-sight. In the diagram however there is a small residual signature which arises purely from the finite size of the magnetic region.

We now consider magnetic regions that are instead composed entirely of azimuthal field. Fig. 5.5 shows that quite different behaviour is seen to that of the radial field. The Stokes V signatures appear to have the largest amplitude away from the meridian and virtually no signature on the meridian. Furthermore, the Stokes V signature 'reverses' when it crosses the meridian (the shape is different at A and C). This is because the sign of the field changes when it crosses the meridian: field that was at A pointing towards the observer is then pointing away at C. The amplitude modulation of the azimuthal field is $V_{azi} \propto \sin(\Delta\phi)$; therefore when on the meridian at position B, V_{azi} will tend to zero. Fig. 5.5 shows some residual flux which is due to the fact that the magnetic region has a finite size. In theory the maximum amplitude would be observed when at a longitude $90°$ away from the stellar meridian when the azimuthal field is directly into our line-of-sight. When the effects of limb darkening and foreshortening are taken into account, ZDI is most sensitive to azimuthal field approximately $70°$ (or 0.2 in phase) away from the stellar meridian. This is of course dependent upon the nature of the limb darkening and so the temperature of the star.

In summary, it is the characteristic behaviour described above and illustrated in Fig. 5.5 that allows ZDI to distinguish between radial and azimuthal field. This simulation just illustrates part of the properties of ZDI outlined in detail by previous authors (e.g. Donati & Brown 1997). However it has also been useful to show that ZDoTS is capable of performing the forward operation of generating Stokes V spectra from a surface magnetic field distribution. We now focus on tests of the maximum entropy reconstruction (inverse operation) of ZDoTS to recover magnetic maps from synthetic spectra.

5.5   Testing ZDoTS - synthetic data

The first test of any new code should focus on its ability to reproduce the same results as its predecessor. I follow the example of Hussain (1999) and generate a synthetic input map consisting of a number of magnetic spots. The stellar parameters used are those based on the components of HD 155555, details of which are outlined in the sections below. ZDoTS is then used to generate synthetic spectra with the same signal-to-noise as that obtained for HD 155555 using the Anglo-Australian Telescope and SemelPol (approximately 200 per 1.9 km s^{-1} pixel - see Chapter 6). In total 53 spectra are generated with an equal
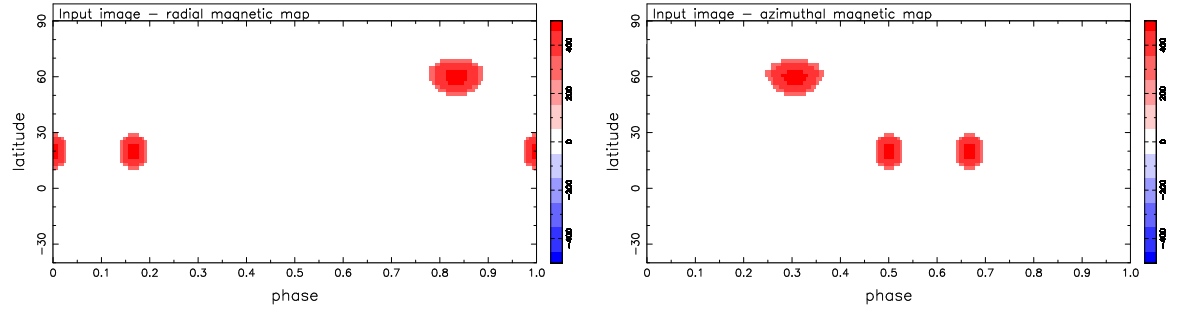
Figure 5.6: Left: Three radial magnetic spots, two of which are located at a latitude of 20° while the other is at 60°. Right: Similarly, three azimuthal spots with an identical latitudinal distribution. Each spot has a peak field strength of 500 G. See text for further information regarding the choice of spot longitudes.

spacing in phase when modelling a single star and a more complex spacing, described in §5.5.2, when modelling a binary system.

All magnetic spots are modelled by Gaussians, have a central peak magnetic field strength of 500 G and a radius of 10°. The input map is shown in Fig. 5.6. The exact positions of the spots were carefully selected to simultaneously test the ability of ZDoTS to reconstruct maps when modelling a single star and also a binary system. Radial and azimuthal magnetic spots are positioned at phases (stellar longitudes) that minimise the chance of cross-talk. In both radial and azimuthal maps we place one spot at a latitude of 60° and two at 20°. This will enable us to assess the ability of ZDoTS to determine latitudinal position and allow us to directly compare with the similar tests performed by Hussain (1999). Two spots are placed at a latitude of 20° so that we can test the binary mode of ZDoTS. In each of the radial and azimuthal maps one of these spots is placed at what is defined as a conjunction phase (either $\phi = 0$ or $\phi = 0.5$).

5.5.1 Single star mode

Simulating observations of a single star

In the top panel of Fig. 5.7 we show the recovered magnetic maps from ZDoTS when modelling a single star, fitted to χ^2=1.0. The fit of our model to the synthetic data is shown in the top panel of Fig. 5.8. The parameters of the star used in this test matched

that of the primary star of HD 155555 ($v \sin i \simeq 34.9$ km s^{-1}, $R_* = 1.47$ R$_\odot$, $i = 52°$). Essentially the maps show the same behaviour as found by Hussain (1999) and described in Donati & Brown (1997). In order to fully evaluate the reconstruction we collapse both maps in the latitude direction - spot positions were carefully chosen to ensure that this could be achieved with a minimum of overlap between neighbouring spots. The resulting plots are shown in the bottom panel of Fig. 5.7 as the blue line.

The collapsed radial field fluxes in Fig. 5.7 matches the input map (black line) very well with only a slight reduction in flux. The peak value in the recovered map is 354 G which is 70 % of the maximum input flux. Slight cross-talk with the azimuthal field can be seen in the radial field maps. The recovered azimuthal fluxes are considerably lower than the input fluxes at both high and low latitudes and are consistently lower than the radial fluxes. The peak flux in the azimuthal map is only 243 G which is just under half the peak flux in the input map. Particularly evident is a greater degree of longitudinal smearing for the high latitude azimuthal spot. Again, cross-talk is evident on the azimuthal field map with the radial field. All these findings are entirely consistent with the almost identical simulations of Hussain (1999). In summary, we therefore conclude that our integration of the single star code developed by Hussain (1999) into the latest binary star version of the DoTS code has been successfully achieved.

Simulating observations of a binary system

Now that the ZDoTS code has been shown to reproduce the same results for single stars as the previous code, we can start to examine the binary system problem. If both stars in a binary system show strong Stokes V signatures, and the code is not capable of performing ZDI on a binary system, then the only option is to observe the non-conjunction phases of the binary. For my next test I assume that 53 spectra can still be obtained (in reality this may be optimistic) but that the conjunction phases of HD 155555 corresponding to $\phi = 0.42 - 0.58$ and $\phi = 0.92 - 0.08$ are not observed.

The recovered maps are shown in the middle panels of Fig. 5.7 and are represented by the red line in the collapsed plot (bottom panels). Again the fit to the input spectra was χ^2=1.0 and is shown in the middle panel of Fig. 5.8. Examining the radial field first, it is clear that the map is of a lower quality with a peak flux 60 G lower than that recovered in the single star version. Note that the spot at phase $\phi = 0.0$ is reconstructed
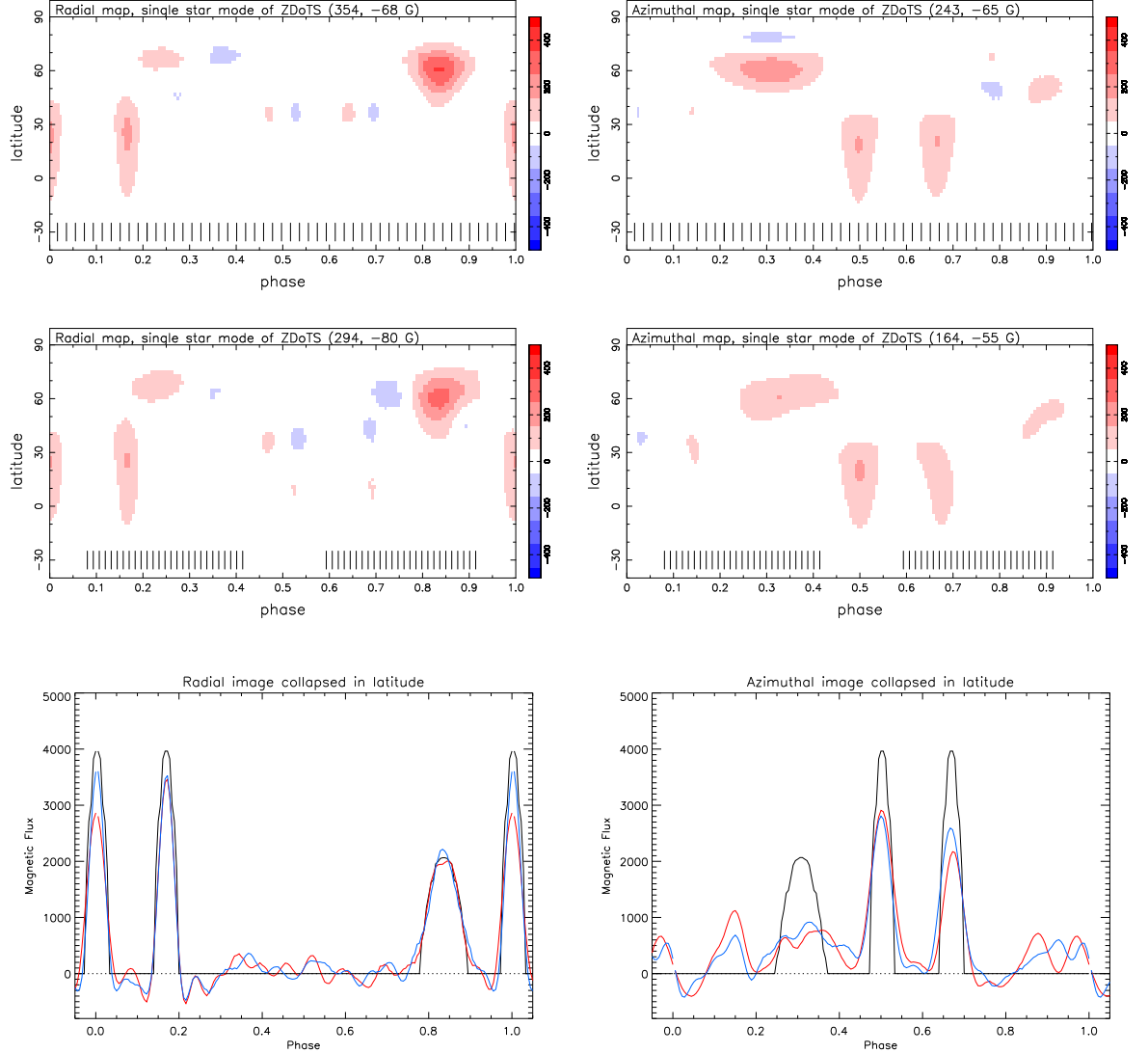
Figure 5.7: Recovered maps using ZDoTS in single-star mode. Top panels: the recovered radial and azimuthal field maps from modelling a star with observations equally spaced around the stellar surface. Middle: as top but with an uneven distribution of spectra to simulate the observation of a binary system where the conjunction phases cannot be used. Vertical tick marks show the phases of the synthetic spectra. The peak magnetic flux values are quoted in brackets in the title of each recovered map. Bottom: The above maps are collapsed in latitude and compared to the original input map (black line). The blue line corresponds to the collapse of the top panel while the red line shows that of the middle panel.

significantly weaker than the spot located at phase $\phi = 0.17$. This is because (as we saw in §5.4.5) radial field is most sensitive to observations taken at a phase when the object is crossing the stellar meridian. It should also be noted that the spot at phase $\phi = 0.17$ is now slightly slanted off vertical and that the shape of the high latitude spot at phase $\phi = 0.83$ is no longer circular.

The corresponding azimuthal field maps show an even higher level of distortion to the effects of the missing phase coverage, with a peak flux 80 G lower than previously. The spot at the conjunction phase $\phi = 0.5$ is well recovered and follows the blue and black lines nicely on the bottom panels of Fig. 5.7. However, this time the spot at phase $\phi = 0.67$ is poorly recovered, resembling an arc rather than a vertical line with the red line is significantly below the blue line and shifted to a slightly higher phase. This is because azimuthal field is most sensitive to observations which are 0.2 away in phase, as discussed in §5.4.5.

5.5.2 Binary star mode

In the last section we learnt that the use of a single star code to perform ZDI of a binary system results in a lower level of recovered flux and distortions in the shapes and locations of magnetic regions. In many ways this simulation was optimistic as it is doubtful, due to the constraints of observational astronomy, that the same number of phases (53) could have been observed if the conjunction phases were ignored. Furthermore, we have only examined the case of well phase-sampled data, which is only possible for bright targets. Many recent ZDI targets are relatively faint and maps are often reconstructed using less than ten phases of observation. In such cases it becomes critically important to achieve evenly sampled phase coverage. We therefore now test the binary ZDI mode of our new code.

The same input map is used to produce synthetic spectra. This time, however, we simulate a binary system with parameters identical to those of the close binary system HD 155555. The full binary system parameters are displayed in Chapter 5, Table 6.1; in summary: $P = 1.68$ d, $K_1 = 86.4$ km s^{-1}, $M_1 = 1.054$ $M_\odot$, $M_2 = 0.986$ $M_\odot$, $R_1 = 1.47$ $R_\odot$, $R_2 = 1.32$ $R_\odot$. We use the same input map as before and paint it onto the surface of both stars in the binary. Due to the fact that each star is 180° out of phase, the combination of signatures seen at conjunction phases should be a good test of the code.
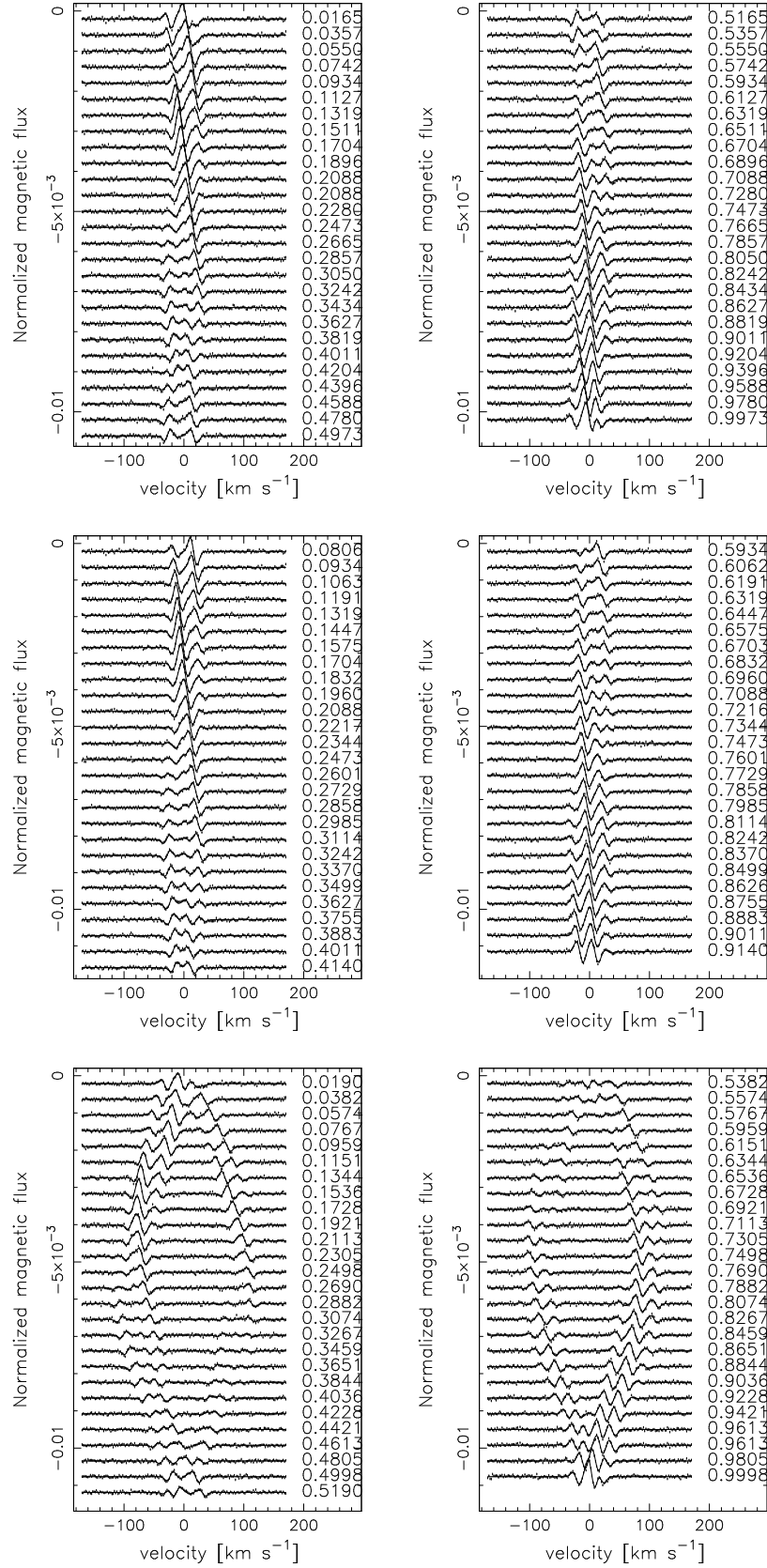
Figure 5.8: Fits are shown to the synthetic Stokes V spectra. Top: the case of a single star observed at all phases. Middle: only phases not in conjunction are observed. Bottom: using the binary mode of ZDoTS to model the combined binary Stokes V signatures.
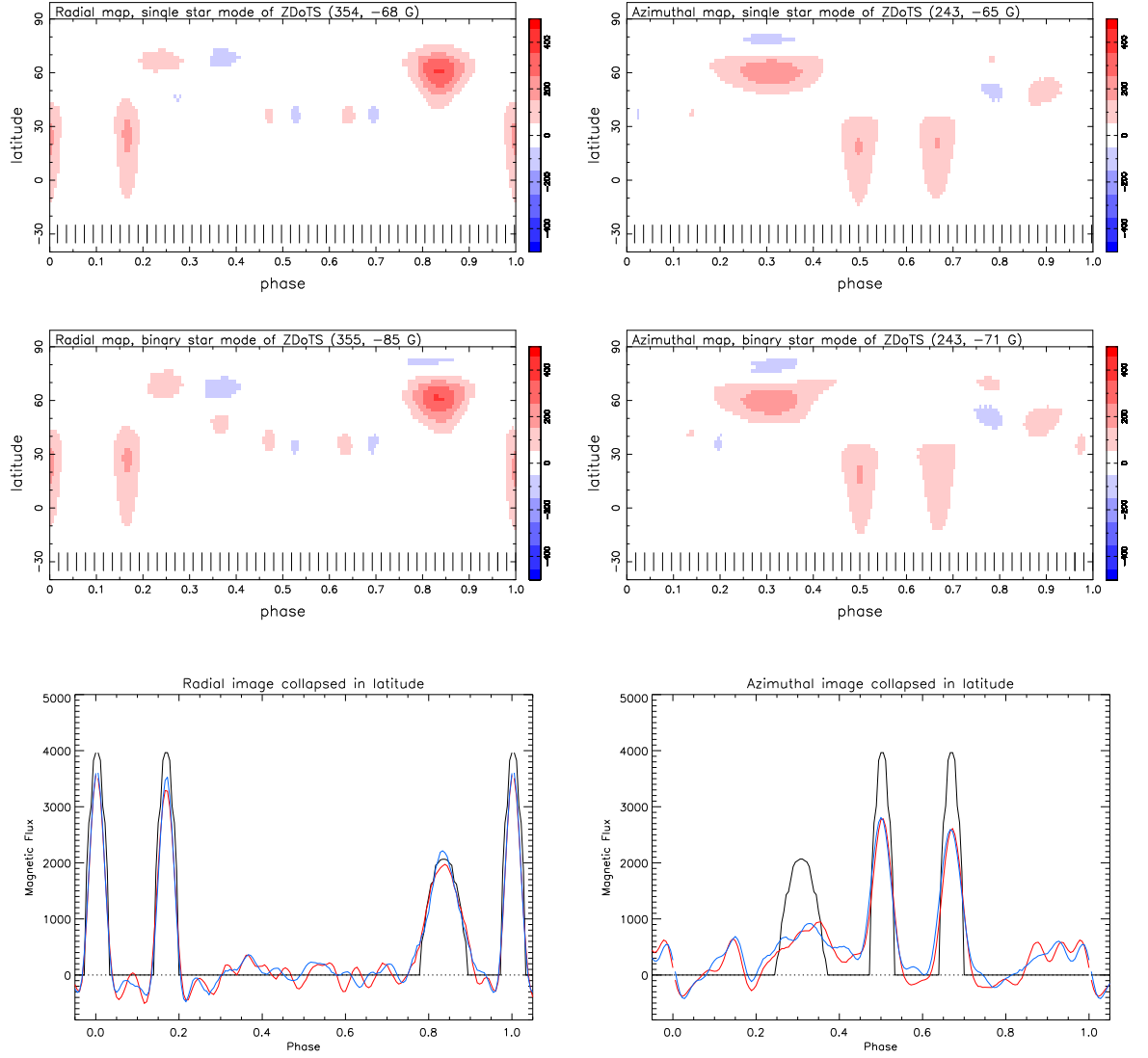
Figure 5.9: Recovered maps using ZDoTS in binary-star mode. Top panels: exactly the same as those in Fig. 5.7, i.e. the maps recovered from spectra of a single star. Middle panels: now using the ZDoTS in binary mode to reconstruct the maps of the primary star from spectra which include the conjunction phases with the secondary star. Vertical tick marks show the phases of the synthetic spectra. The peak magnetic flux values are quoted in brackets in the title of each recovered map. Bottom: The above maps are collapsed in latitude and compared to the original input map (black line). The blue line corresponds to the collapse of the top panels while the red line shows that of the middle panels.

We only consider the map we recover from the primary star as it was this star's parameters that were used in the single star tests.

We show the maps we recover of the primary star in Fig. 5.9 (middle panels), along with those of the last section for the single star case with full phase coverage (top panels). The data were again fit to χ^2=1.0 with the fits shown in the bottom panel of Fig. 5.8. The two sets of maps in Fig. 5.9 are very similar. The peak values of the recovered fluxes are identical to the level of ± 1 G. Furthermore there appear to be no obvious distortions of the shapes or locations of the recovered spots in the binary case. The plot collapsed in latitude shown in the bottom panel of Fig. 5.9 shows again that the binary reconstruction is virtually identical to the single-star case.

In summary, our synthetic simulations show us that our new binary ZDI code is as capable of recovering magnetic flux distributions on binary systems as it is for single stars, at least for well sampled data. This represents a considerable improvement over using a single star code to model a binary system using data collected outside of conjunction phases. ZDoTS is used in Chapters 6 & 7 on real observations of HD 155555.

5.6 Differential rotation in a binary system

The most recent measurements of differential rotation rate using Doppler imaging come from the application of the sheared image technique (see Chapters 1 & 7 for a discussion of the relative merits of different methods of obtaining differential rotation parameters). The sheared image technique was first implemented by Donati et al. (2000). A model of differential rotation is included in the imaging code, such that each latitude strip has its own angular rotation rate given by:

$$\Omega(l) = \Omega_{eq} - \Delta\Omega\sin^2 l \tag{5.8}$$

where Ω_{eq} is the equatorial rotation rate and l is the stellar latitude. This was implemented into the DoTS code by Barnes et al. (2001) to work for single stars. The HD 155555 dataset, fully described in Chapters 6 and 7, presents the opportunity to measure differential rotation on both binary components simultaneously.

The version of DoTS (the brightness Doppler imaging code) that I inherited was first tested to see if, in its current manifestation, it could correctly model differential

rotation in the binary case. Somewhat amusingly this turned out not to be so, as the stars 'unpeeled' themselves much like you might an orange[1]. The subroutine responsible for implementing the surface shear in DoTS is the same as the one that rotates a single star to the required phase in the single star mode of DoTS. However, in binary mode this routine is used to rotate the stars in the orbital plane. Due to the fact that DoTS assumes synchronous rotation, this is equivalent to rotating a single star. Unfortunately though, when a latitude dependant rotation rate is applied this results in each latitude strip of the star rotating at a different rate in the orbital plane. Needless to say this is undesirable.

A simple change was made to the binary version of the DoTS code whereby the surface shear was applied by rotating each latitude in the frame of reference of the stellar rotational axis. Only after this was each star rotated in the orbital plane (with no latitudinal dependence). The code is therefore now able to model differential rotation of both stars. The user now inputs the four rotational parameters, two for each star.

5.6.1 Surface grid

When the newly modified code was run, black pixels started to appear on the surfaces of both stars. Their number increases with increasing shear strength and they are not present when no differential rotation is applied. This was also found to happen in the original single star version of the code. This is illustrated in the top panel of Fig. 5.10. The explanation for the null pixels lies in the way the surface grid was sheared.

The vertices of each surface triangular pixel (see §5.4.2) lie on lines of constant latitude. Therefore, a triangular pixel either has two vertices on the upper latitude and one on the lower latitude or vice-versa. The latitude of each pixel is stored and this is transferred to the subroutine responsible for performing the rotations described above. The problem with this is that when differential rotation is applied, all three vertices of the triangle are sheared by the same amount, irrespective of the small latitude difference that one of the vertices must have to the other two. The result of this is that, as differential rotation is applied, adjacent latitude bands no longer tessellate perfectly. Due to problems of numerical accuracy gaps can then start to appear when this triangular grid is 'painted' on to the viewplane (again see §5.4.2).

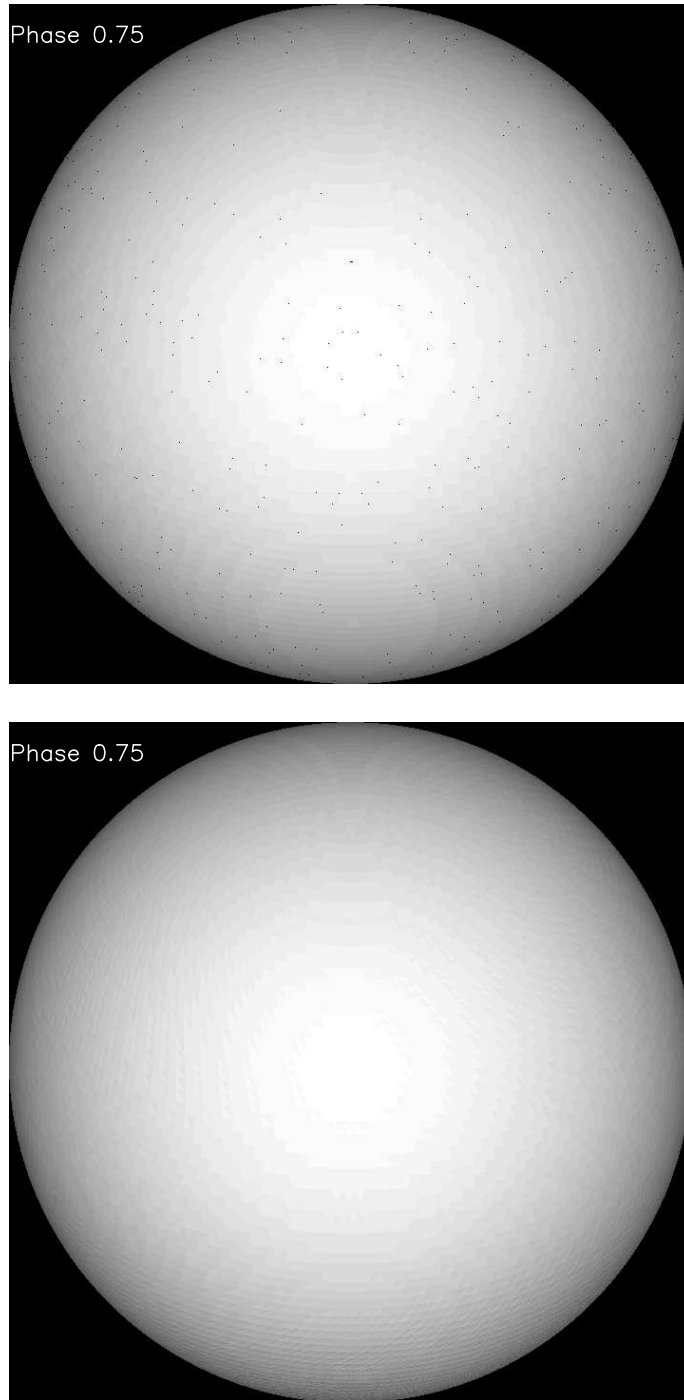[1]http://www.wikihow.com/Peel-an-Orange-in-One-Peel

Figure 5.10: The viewplane surface showing the model of a star after a shear of 90deg has been applied. Top: the original implementation showing black pixels. Bottom: after shearing each vertex individually (see text), note no black pixels.

While the black pixels make up a very small fraction of the total number of pixels, it was feared that they might be introducing noise into the final maximum entropy reconstruction. Therefore, when we run a grid of different differential rotation parameters (described in chapter 7) in order to locate the best fitting combination of parameters, the black pixels would be biasing our results. This is particularly worrying as the number of blank pixels is correlated with the rate of differential rotation.

In order to solve this problem the latitude of each *vertex* of each triangle was stored and this was transferred to the subroutine responsible for applying the latitudinal dependant shear. So now each vertex is sheared individually, rather than the whole pixel. Consequently, neighbouring latitude bands remain in perfect alignment with each other. This is illustrated in the lower panel of Fig. 5.10, where no black pixels are visible. Naively one may think that this changes the area of the pixel. However, given that the area of a triangle is $\frac{1}{2}(base \ \times \ height)$ and neither the base nor the height are changing, the area will be preserved. So effectively the triangle becomes progressively more stretched out as the star is subjected to increasing amount of shear.

Unfortunately this solution brings about its own problems. If the rate of differential rotation is extreme, or equivalently the duration of observations is long, then each pixel will become grossly stretched out. Consequently parts of the pixel are no longer representative of the positional dependent parameters that were calculated for the original pixel centre (e.g. the pixel outward normal). Ultimately this can cause the stellar surface to resemble a 'disco ball' which is also undesirable. There likely exists a limit on the total shear beyond which the original version with black pixels will again become preferable. In theory, therefore, when this limit is approached the code could pause and resample the pixel grid. In practice, however, this would be computationally expensive and may itself introduce a discontinuity in the reconstruction process.

On a practical level, increasing the number of latitudes of the surface grid will allow a larger shear to be used before the above effects will start to come into effect. In Fig. 5.10, ninety latitudes are used and a total shear (between pole and equator) of 1.5 radians (or approximately 90 °) is used. Here only very slight distortion of the surface grid occurs near the bottom of the image (corresponding to mid-to-high latitudes in the largely unseen hemisphere). This level of shear was chosen because it represents the maximum amount of shear that occurs on either star of HD 155555 over 11 nights of observations (see Chapter

7).

The changes described above to the DoTS code were also implemented in our new ZDI code, ZDoTS, allowing us to obtain a separate measurement of the stellar differential rotation from Stokes V spectra.

CHAPTER 6

The first magnetic maps of a pre-main sequence binary system - HD 155555

All the work described here was carried out by myself with the exception of the spectral synthesis in §6.3.2 and the coronal field extrapolations in §6.6. This is clearly highlighted in the text.

6.1 Introduction

The only tidally-locked binary star to date for which published magnetic maps are available is the evolved primary star of the RS CVn system HR 1099. A strong latitudinal dependence on the polarity of the radial field maps is found and HR 1099 often exhibits a unipolar cap (Donati et al. 2003). Also present are strong, and often complete, axisymmetric rings of azimuthal field on the stellar surface. Petit et al. (2004) confirmed the existence of an anti-correlation between the polarity of the radial and azimuthal fields. This is not observed on young rapidly rotating stars but is present on the Sun. Due to the evolved nature of RS CVn primary components, it is difficult to interpret their magnetic maps with respect to those of young rapidly rotating single stars. Therefore in an attempt to establish the relative importance of tidal locking and youth on surface magnetic field distributions, we present observations of the young pre-main sequence binary system HD 155555.

The HD 155555 (V824 Ara) system is composed of a G5 IV primary and a K0 IV secondary and has an orbital period of 1.68 d. This makes it a good target for observing over a five day observing run, as outlined in §6.2. HD 155555 was first discovered as a close binary system by Bennett et al. (1967). It was later classified as an RS CVn binary (Strassmeier et al. 1993) based upon the activity and binarity of the system. Pasquini et al. (1991) suggested that HD 155555 was more likely a young pre-main sequence binary. This was based upon the high Li (6708 Å) abundance (re-visited here in §6.3.2) and the presence of a very active dMe companion (LDS587B). More recently Strassmeier & Rice (2000) derived an age of 18 Myr using the *Hipparcos* distance of 31 pc and the pre-main-sequence evolutionary tracks of D'Antona & Mazzitelli (1997).

HD 155555 is a particularly active system with an X-ray luminosity of 2.7×10^{30}erg s^{-1} (Dempsey et al. 1993), and both components show CaII H & K core emission and filled in H$_\alpha$. Therefore given its proximity and activity it is unsurprising that HD 155555 has been the subject of a number of recent papers. In 1996 it was the target of a multi-wavelength study by Dempsey et al. (2001). The authors detected considerable flare activity, with several flares being observed simultaneously in the UV and radio wavelengths. As part of this campaign, optical spectroscopy was also obtained and surface brightness images were produced using Doppler imaging by Strassmeier & Rice (2000). An earlier Doppler image of HD 155555 produced from data obtained in 1990 was published by Hatzes & Kürster (1999). In addition, a magnetic field detection has also been reported for both components of HD 155555 by Donati et al. (1997).

In this chapter we present new surface brightness maps (§6.3) and the first magnetic maps of HD 155555 (§6.4.1). To achieve this we have developed a binary ZDI code in order to model the contribution of each star to the combined Stokes V profiles that are observed during conjunction phases (see Chapter 5). The more recent, and numerous, 2007 observations of HD 155555 are described first. Then in §6.5 we present a smaller set of observations taken in 2004. In obtaining magnetic maps for both components of a binary system we open up many interesting possibilities to explore the effects of binarity on the magnetic fields of both stars. Possible interaction between the stellar fields are of interest because it will determine many of the system's X-ray properties and the location of stellar winds. In §6.6 we use the magnetic maps recovered of both the primary and secondary components in order to perform an initial analysis of the likelihood of interaction between the two stars. We discuss our results in §6.7 and present our conclusions in §6.8.

6.2 Observations and data reduction

Spectropolarimetric observations of HD 155555 were made by the author at the Anglo-Australian Telescope (AAT) using the University College London Échelle Spectrograph (UCLES) which is fibre fed by the SemelPol visiting polarimeter (Semel et al. 1993) mounted at the Cassegrain focus. In total, eleven uninterrupted nights of observations were secured on our target star HD 155555 in 2007 from March 30 to April 09. In this chapter we only use data collected on five of these nights, from March 31 to April 04. The remaining six nights of observations are used in Chapter 7 to study the surface rotation properties of both stars. The 1.68 d orbital period means that good phase coverage can be obtained in five nights, corresponding very closely to three stellar orbits.

The instrumental set-up is the same as that used on many previous Zeeman Doppler imaging runs and is described in detail by previous authors (Semel et al. 1993, Donati et al. 2003). Using SemelPol both left- and right-hand circular polarised light are captured simultaneously on the EEV2 CCD detector. Using the 31 gr mm^{-1} grating, full wavelength coverage between 4377 and 6819 Å is achieved. A resolution of 70,000 (i.e. 4.3 km s^{-1}) is obtained using this set-up. In order to supress all spurious polarisation signals (down to first order) due to instrumental drifts or temporal variations in stellar spectra (e.g. resulting from the orbital motions of the components in a binary system), circular polarisation (Stokes V) observations are made from a sequence of four exposures. Between each exposure the quarter-waveplate in SemelPol is rotated by +/- 45°, causing a switch of the circular polarisation carried in each fibre. The four sub-exposures are then combined using optimal extraction techniques as implemented by the Echelle Spectra Reduction: an Interactive Tool (ESpRIT) software developed by Donati et al. (1997). In the process the normal calibrations pertaining to spectral data are performed and the spectra are wavelength calibrated. As HD 155555 is such a bright target (V = 6.9 mag) we were able to use 200 s exposures which meant that, after readout time, the total time taken for each sequence of four exposures (and so each Stokes I and V spectrum) was approximately 15 minutes.

In total, 53 spectra were obtained over the five nights and are fairly evenly spread over the orbital period of the binary. The signal-to-noise (S/N) ratio of both our Stokes I and V spectra in the peak order vary with the weather conditions between 70 and 230 with an average of around 160 per 1.9 km s^{-1} pixel. In order to greatly boost the signal-to-

noise the technique of Least-Squares Deconvolution (LSD) is used as described by Donati et al. (1997) and implemented in ESpRIT. This effectively combines the absorption line profiles of many thousands of photospheric lines, resulting in a single high S/N ratio line profile. For HD 155555 we use a line-list for a K0 star produced by the VALD database (Piskunov et al. 1995, Kupka et al. 1999). All strong chromospheric lines (such as the Balmer series) are excluded. Approximately 2800 lines are used for LSD which result in a S/N ranging from 2500 to 10,500 for Stokes V spectra and between 680 and 1200 for Stokes I spectra. We take advantage of the strong telluric lines present in the spectra and the LSD technique in order to correct for drifts in our wavelength calibration over the course of the night. Donati et al. (2003) show that this calibration results in radial velocities which are stable to better than 0.1 km s^{-1}.

6.3 System parameters and brightness maps

We use the Doppler imaging code 'DoTS' (Collier Cameron 1997) to map the surface brightness distribution of the surfaces of both stars using the Stokes I intensity spectra. This code uses maximum entropy, as implemented by Skilling & Bryan (1984), to return the simplest possible surface map at a given level of χ^2. A two-temperature model is used to describe the surface of each star (Collier-Cameron & Unruh 1994). Spectroscopic look-up tables are created to model the contribution from each element on the stellar surface. Slowly rotating reference stars are fitted with Gaussian profiles which we use to model both the local intensity profiles of the photosphere and the spot, for each star. It has been shown by Unruh & Collier Cameron (1995) that using synthetic Gaussian profiles instead of those from slowly rotating stars has little effect on the resulting brightness maps. The obvious advantage of using synthetic Gaussians is that they are noiseless. For the primary star we use temperatures of 5300 K and 4050 K for the photosphere and spot respectively. Similarly the cooler secondary star is modelled using a photospheric temperature of 5050 K and a spot temperature of 3787 K. These temperatures come from the spectroscopic analysis described in §6.3.2.

Table 6.1: Orbital and physical parameters for the HD 155555 system.

Element	Unit	Value	Source
Orbital:			
P	(days)	1.6816463	adopted[1]
T_0	(HJD)	2446997.9102	adopted[1]
Φ_0		0.752474	DoTS
e		0.0	adopted
γ	(km s^{-1})	3.72±0.02	DoTS
q	M_2/M_1	0.935±0.001	DoTS
K_1	(km s^{-1})	86.4±0.1	DoTS
K_2	(km s^{-1})	94.7±0.2	(K_1 and q)
i	(degs)	50 (52 adopted)	DoTS
$(v\sin i)_1$	(km s^{-1})	34.9	DoTS
$(v\sin i)_2$	(km s^{-1})	31.3	DoTS
Physical (assuming $i = 52°$):			
M_1	($M_\odot$)	1.054	DoTS
M_2	($M_\odot$)	0.986	DoTS
R_1	($R_\odot$)	1.47	DoTS
R_2	($R_\odot$)	1.32	DoTS
$T_{\mathrm{eff},1}$	(K)	5300±100	SME
$T_{\mathrm{eff},2}$	(K)	5050±100	SME
$\log g_1$		4.05±0.1	SME
$\log g_2$		4.10±0.1	SME

[1] from Strassmeier & Rice (2000).

6.3.1 Determining system orbital parameters

In addition to producing surface brightness maps we can use DoTS to determine the fundamental parameters of the HD 155555 system. This is achieved by finding the values of each system parameter that give the best fit to the stellar profiles (i.e. that minimise χ^2) after a fixed number of maximum entropy iterations (see Barnes et al. 2000). In a binary system the additional orbital parameters greatly increase the computer time required to achieve a global solution. We approached this problem by carefully selecting combinations of two parameters to be minimised for simultaneously. In practice we used a pool of 30 computers to simultaneously run different combinations of the variables. Several iterations were made through the pairs of parameters until a global convergence on a solution with $\chi^2 = 0.6$ was achieved. At this point further changes in the parameters were of the order of their uncertainties as estimated from the curvature of the χ^2 surfaces. Values for system parameters are collated in Table 6.1.

We use the ephemeris of Strassmeier & Rice (2000) which is based on over twenty years of radial-velocity data. We attempted to derive our own value for the period of the system using our 2007 dataset alone and found that it was consistent with that of Strassmeier & Rice (2000), however with larger uncertainty. The value of 0.752474 we obtain for the phase offset (Φ_0) reflects the traditional eclipsing binary definition that we use in DoTS. Here phase zero occurs at stellar conjunction with the primary star furthest away from the observer (i.e. primary eclipse in an eclipsing binary system). We make the simplifying assumption that both components of HD 155555 have rotational axes perpendicular to the orbital plane. Unfortunately, determining the inclination of the binary orbit for non-eclipsing systems is as problematic as the rotation axis of single stars because the Doppler imaging process is only weakly sensitive to this parameter. We derive a value of 50° (using the χ^2 minimisation technique described above) which is consistent with the value of 52° obtained by both Strassmeier & Rice (2000) and Pasquini et al. (1991). For consistency with these works we therefore also adopt a value of 52°.

6.3.2 Atmospheric and evolutionary parameters

A subset of our highest signal-to-noise spectra are selected to determine the atmospheric parameters using spectral synthesis. This analysis was carried out by Eric Stempels,

what follows is a summary of his findings which are of relevance for the rest of this chapter. He used the technique of tomographic separation (see Bagnuolo & Gies 1991) to disentangle the two components using the orbital parameters derived in the last section. Synthetic spectra of each component were then calculated and fitted with the help of the Spectroscopy Made Easy (SME) code (Valenti & Piskunov 1996). This code uses least-squares minimization to determine the atmospheric parameters that best describe the observed spectra. For these calculations, the stellar model atmospheres from the Kurucz (1993) grid were used, along with atomic line data obtained from the VALD database (Piskunov et al., 1995; Kupka et al., 1999). In the calculations, solar abundances were assumed, microtubulence of 1.75 $\mathrm{km\,s^{-1}}$ and a macrotubulence of 2.0 $\mathrm{km\,s^{-1}}$, all typical values for a G5–K0 class pre-main-sequence object.

For the analysis, two wavelength regions were selected, one around the temperature and gravity sensitive Na I D lines, and one between 6000 and 6200 Å, a region that contains a large number of metal lines. The line ratios in the latter regions provide independent leverage on the effective temperatures. Effective temperatures and gravities of the two stars were found to be very similar (primary: $T_{\mathrm{eff},1} = 5300 \pm 100$ K and $\log g_1 = 4.05 \pm 0.1$, secondary $T_{\mathrm{eff},2} = 5050 \pm 100$ K and $\log g_2 = 4.10 \pm 0.1$). The full set of parameters is listed in Table 6.1.

Within their uncertainties, the values found are consistent with the values quoted in Pasquini et al. (1991). The main difference is that the surface gravity of the secondary star is significantly lower than the value of 4.5 quoted by Strassmeier & Rice (2000) and consequently much closer to the value obtained for the primary star. This is also expected from the orbital parameters of the system, since $g \sim \mathrm{G}M/R^2$ and thus:

$$\Delta(\log g) = \log g_1 - \log g_2 = \log[M_1/M_2 * (R_2/R_1)^2] \qquad (6.1)$$

Substituting $M_1/M_2 = K_2/K_1$ and assuming synchronous rotation, $R_2/R_1 = (v\sin i)_2/(v\sin i)_1$ this gives:

$$\Delta(\log g) = \log(K_2/K_1 * [(v\sin i)_2/(v\sin i)_1]^2) \qquad (6.2)$$

Using the values from Table 6.1, one finds $\Delta(\log g) = -0.05$.

The lithium abundance was also re-examined to provide an indication of youth. Using the atmospheric parameters above, $\log n(\mathrm{Li}) = 3.16$ (primary) and 3.15 (secondary) was found. This analysis takes account of the non-LTE corrections published by Carlsson

et al. (1994) that were not available to Pasquini et al. (1991). These lithium abundances are slightly below the primordial values of 3.2-3.3, and suggest a lithium age of 0–30 Myr (Sestito & Randich 2005). This is in good agreement with the age of 18 Myr derived by Strassmeier & Rice (2000) from the pre-main sequence tracks of D'Antona & Mazzitelli (1997). We therefore agree with the conclusions of Pasquini et al. (1991) and Strassmeier & Rice (2000) that HD 155555 is a young pre-main sequence binary system and not an evolved RS CVn object.

6.3.3   Brightness images

Now that the best parameter set for HD 155555 has been found, we can attempt to model the deviations (bumps) in the line profile due to the presence of stellar spots. Unlike earlier in this section where we were interested in the parameter set that minimises χ^2, when generating final spot maps a target χ^2 value is set such that the Maximum Entropy iterations converge before we start over-fitting the data and producing artificially noisy maps. In Fig. 6.1 we show the 53 observed Stokes I LSD profiles and the corresponding fits we obtain using DoTS for a reduced $\chi^2 = 0.7$. A value for χ^2 below unity is often achieved when performing Doppler imaging using intensity spectra (Stokes I); it simply indicates that the S/N values from the LSD process are slightly underestimated. The profiles have been ordered by phase so the binary motion can clearly be seen and individual spots are easily traced. From the LSD profiles alone we can see that the flat-bottomed shape of the rotation profiles of both stars indicates the presence of polar spots.

In Fig. 6.2 the brightness maps produced by the Doppler imaging process are shown. We choose to leave these maps labelled with phase, as opposed to the more conventional stellar longitude, so that the locations of spots can be more easily compared to the binary orbital phase. Note that for the primary star phase $\phi = 0.0$ faces the secondary star, while for the secondary star phase $\phi = 0.5$ faces the primary. The first obvious characteristic of both images are the large polar spots. On the primary star, individual darker spots can be made out at latitudes between 60° and the pole. A band of low-latitude spots between (10 - 40°) is also present and covers three quarters of the stellar circumference. While we have been able to resolve some structure in this band it is likely that in reality it is composed of smaller, unresolved spots. Latitudes between 40 - 60° are remarkably devoid of spot coverage, producing the bi-modal plot of mean spot filling factor versus stellar latitude
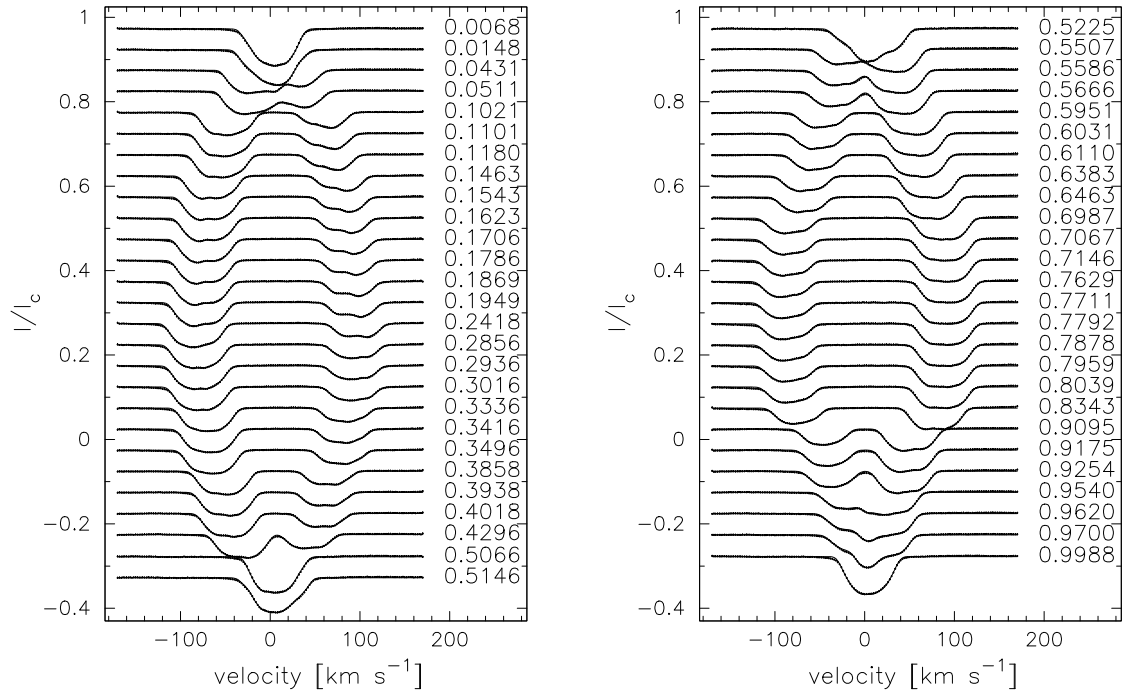
Figure 6.1: The 2007 LSD profiles are plotted along with their uncertainties. The solid line is the maximum-entropy regularised fit we obtain to the data from Doppler imaging. Careful examination of the line profiles reveals the presence of spots, seen as raised bumps in the line profiles. Profiles are ordered by orbital phase (listed to the right of each profile) and clearly show the motion of both binary components. For reference, the primary star is the profile seen generally at negative velocities for phases $\phi = 0.0 - 0.5$.
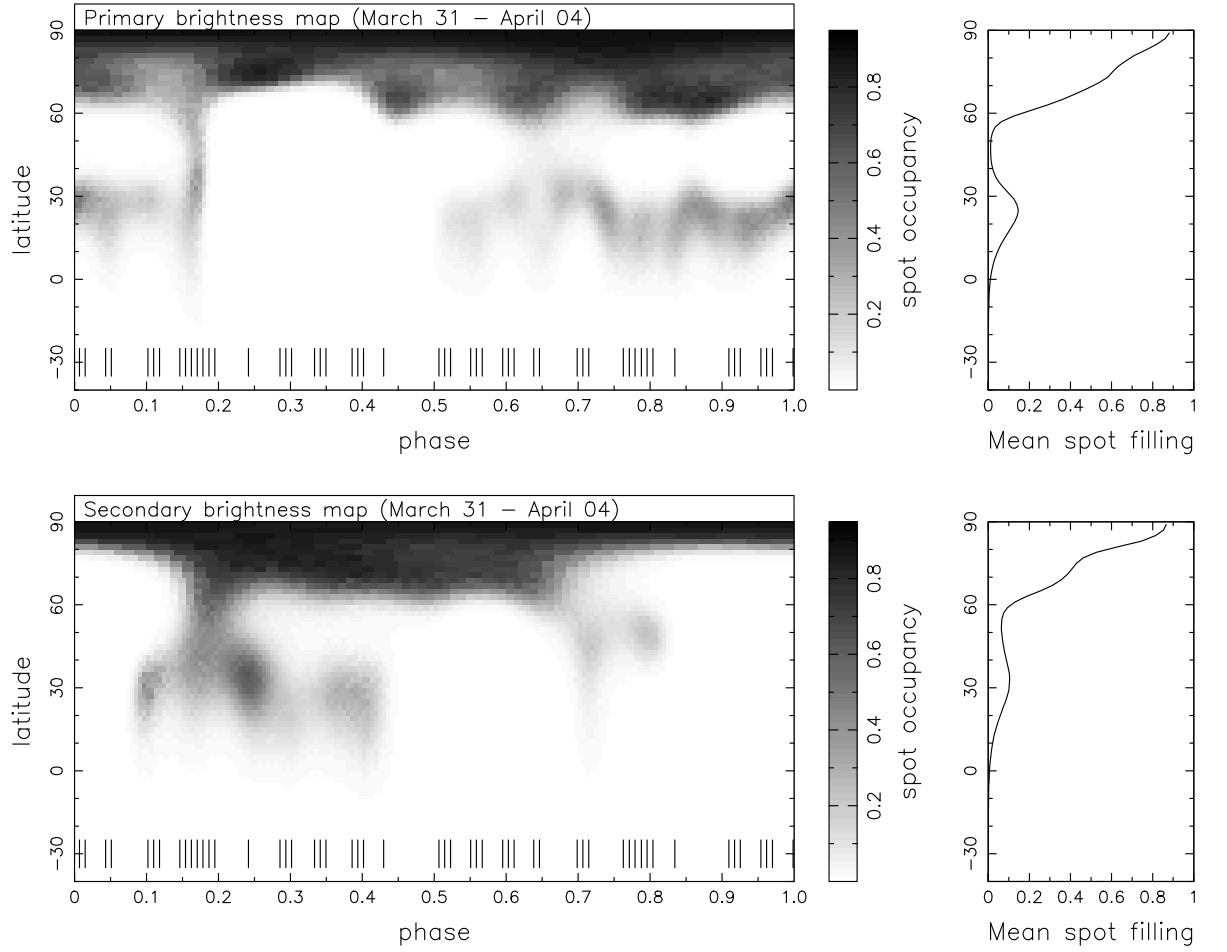
Figure 6.2: Doppler images of the surface brightness distribution of both components in 2007, showing the location of the prominent star spots. The tick marks at the bottom of each main panel mark the phases of observation. To the right of each map is a graph showing the mean spot filling factor as a function of stellar latitude. Note that for the primary star this is significantly bimodal.
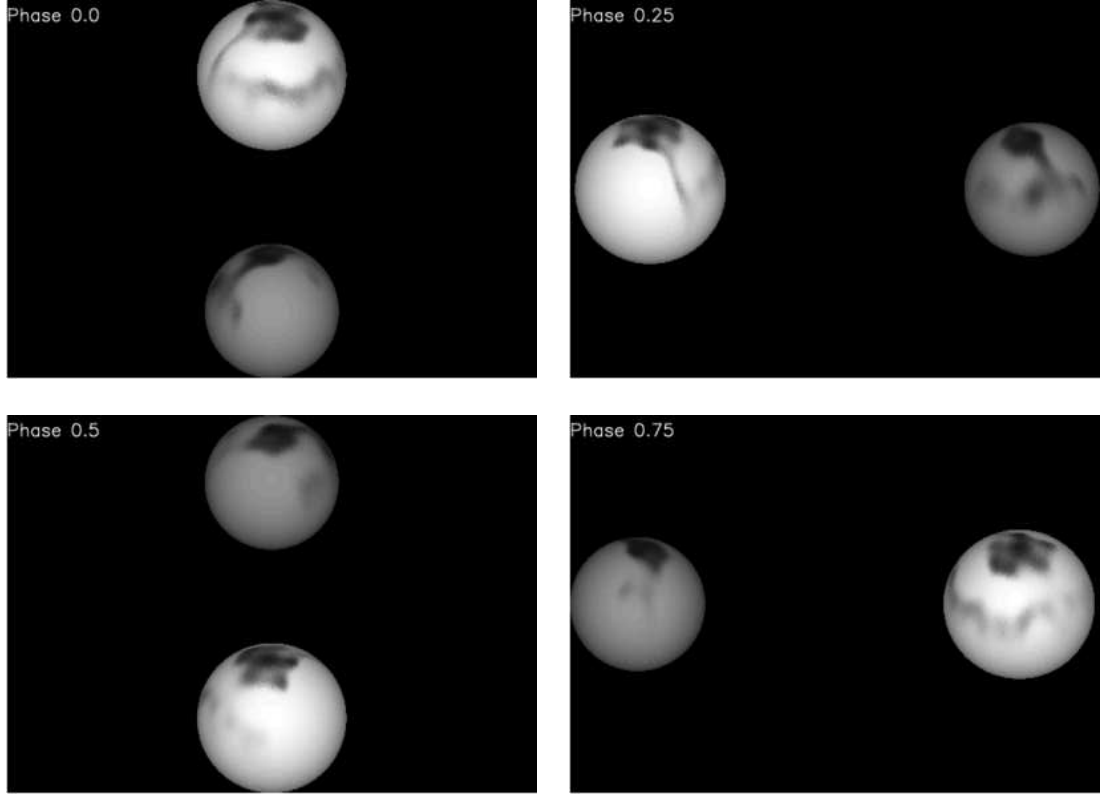
Figure 6.3: The 2007 Doppler brightness images, in Fig. 6.2, are shown projected onto the surfaces of each star at the four quadrature phases. The unspotted photosphere of the secondary star appears darker than the primary star due to the difference in stellar temperatures.

shown in the right panel of Fig. 6.2.

The secondary star has a large, offset polar spot that is centred at phase $\phi = 0.4$ and reaches down to a latitude of $60°$. A large spot group at $\phi = 0.2$ is the lowest latitude feature, reaching down to $20°$, and is clearly seen in the LSD profiles of Fig. 6.1. A weak pair of mid-latitude spots is also recovered at phases $\phi = 0.7$ and $\phi = 0.8$. In Fig. 6.3 we show the brightness maps projected on to the stellar surfaces so that the locations of spots can be compared to the binary orbital phase. We discuss the starspot distributions further in §6.7, where we also compare them to previously published maps.

6.4 Zeeman-Doppler imaging of binary systems

In the previous chapter (§5.4.1) we discussed the need for a binary ZDI code in the case where both components of a binary system exhibit Stokes V signatures. In the case of the near equal mass ratio binary HD 155555, the stars are so similar that no other option is viable. For approximately one third of the orbital period the rotation profiles of the stars overlap to some extent, as illustrated in Fig. 6.1. If one chose to simply not observe the conjunction phases then there would be two phase gaps each of duration $\Delta\phi \simeq 0.16$. These would at the very least reduce the level of detail recovered in the images and may even produce imaging artifacts (as demonstrated in Chapter 5). Gaps in the phase coverage are worse for magnetic than brightness imaging due to the fact that we ascertain the nature of the field (e.g. radial or azimuthal) by the behaviour of the Stokes V signature as it moves through the line profile. As we shall see, the magnetic field strengths on the two stars are comparable. Therefore the only efficient way to proceed is to develop a new code capable of performing full ZDI of a binary star system. Such a code, ZDoTS, was described in the previous chapter.

When the two binary components are in conjunction we model the result as a linear superposition of the two Stokes V signatures from both stars. Just as in Doppler imaging observations, such phases alone do not provide information about the relative contribution to the observed Stokes V spectrum from each star. However, when combined with observations where the two components are separated in velocity space then knowing how the two Stokes V signatures combine helps greatly to constrain the geometry of the magnetic field maps.

As in the single star ZDI code of Hussain et al. (2000), we model the local Stokes V line profiles using a Gaussian profile (which is assumed constant over the stellar surface) and we assume that the weak field approximation holds. Three consecutive Stokes V spectra of HD 155555, shown in Fig. 6.4, illustrate particularly well what can happen when the stars are in conjunction. The Stokes V signatures from the two stars can be seen moving closer together between the top and middle spectra of Fig. 6.4. Then during the conjunction phase in the bottom spectrum we observe, by chance, the exact superposition of the troughs of the two profiles, which produces a large amplitude combined signature. As Fig. 6.4 shows, the ZDoTS code has successfully modelled this. We note that the three spectra shown in Fig. 6.4 were not obtained in the five nights considered in this
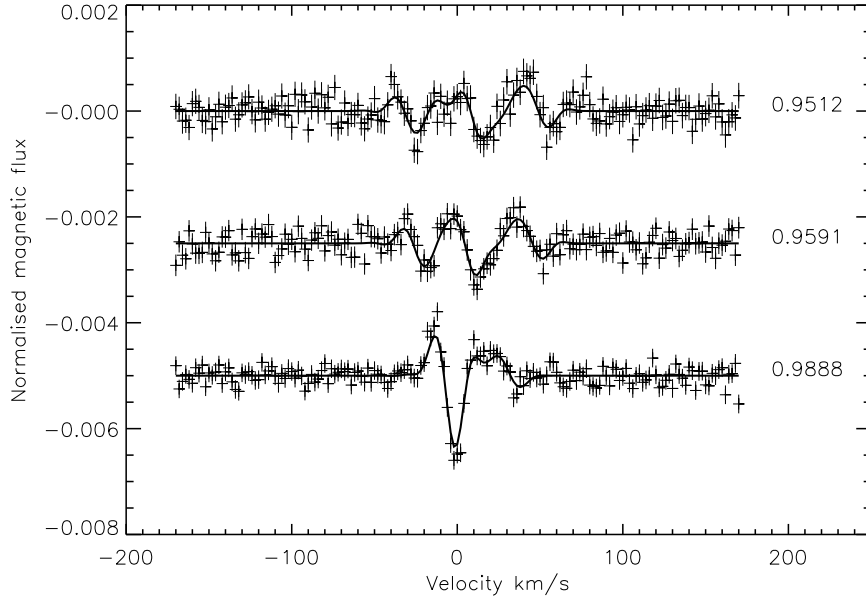
Figure 6.4: Three example Stokes V LSD profiles are shown to illustrate the ability of our code to reproduce the complex superposition of Stokes V signatures that arise when the stars are in conjunction. Note the two Stokes V minima (one from each star) that move closer together due to orbital motion between the top and middle spectra. They then combine in the third spectrum to produce the largest amplitude signal we observe during our campaign. We note that the signal-to-noise of the top two spectra shown here are below average.

publication but from the subsequent five nights of data (specifically, April 05).

In addition to the synthetic starspot distributions used to test ZDoTS in Chapter 5, we also used the surface magnetic maps of the single, K0 dwarf, AB Dor ($v \sin i = 91$ km s^{-1}) from 1996 and 1999 (Donati & Collier Cameron 1997 and Donati et al. 2003). We 'painted' one of these maps on to the primary star and the other onto the secondary and assumed all the same orbital and physical parameters of the HD 155555 system (from Table 6.1). Synthetic spectra were then generated, using the forward module of ZDoTS, of comparable signal-to-noise and at each of the same 53 observational phases as our real data. This resulted in Stokes V spectra of the binary system, including the tangled conjunction phases. The spectra were then used as input into ZDoTS and we attempted to reconstruct the magnetic maps. The results were compared with the performance of the original (single star) ZDI code of Hussain et al. (2000) at recovering the magnetic maps of each star in turn. The results showed that both codes recovered essentially the same maps. When the images were collapsed in latitude the maximum difference between the two magnetic fluxes was always less than 5%. Importantly, there was no visible phase (longitude) dependence on the accuracy of the reconstructed maps. This illustrates that ZDoTS is as capable of reproducing surface maps for binary systems as for single stars, at least for well phase-sampled data.

6.4.1   Magnetic maps of HD 155555

In Fig. 6.5 we show the 53 Stokes V LSD profiles along with the maximum-entropy regularised fits corresponding to $\chi^2 = 1.0$. As in Fig. 6.1, we order the Stokes V profiles by phase and again the binary orbital motion can be clearly seen. Unlike in Fig. 6.1, however, it is easy in Fig. 6.5 to spot the few spectra which have substantially poorer signal-to-noise. These occur around phases $\phi = 0.52$ and $\phi = 0.77$ but still provide some constraints on the surface magnetic field.

The strengths and complexity of both the primary and secondary Stokes V signatures varies with orbital phase. From a visual inspection of Fig. 6.5, it appears from the Stokes V profiles that the primary star often possesses a more complex field with either more changes of polarity and/or different field orientations than the secondary star. This is illustrated by the greater number of sign reversals seen throughout the line profile of the primary star (as many as six seen around phase $\phi = 0.15$). The Stokes V signature
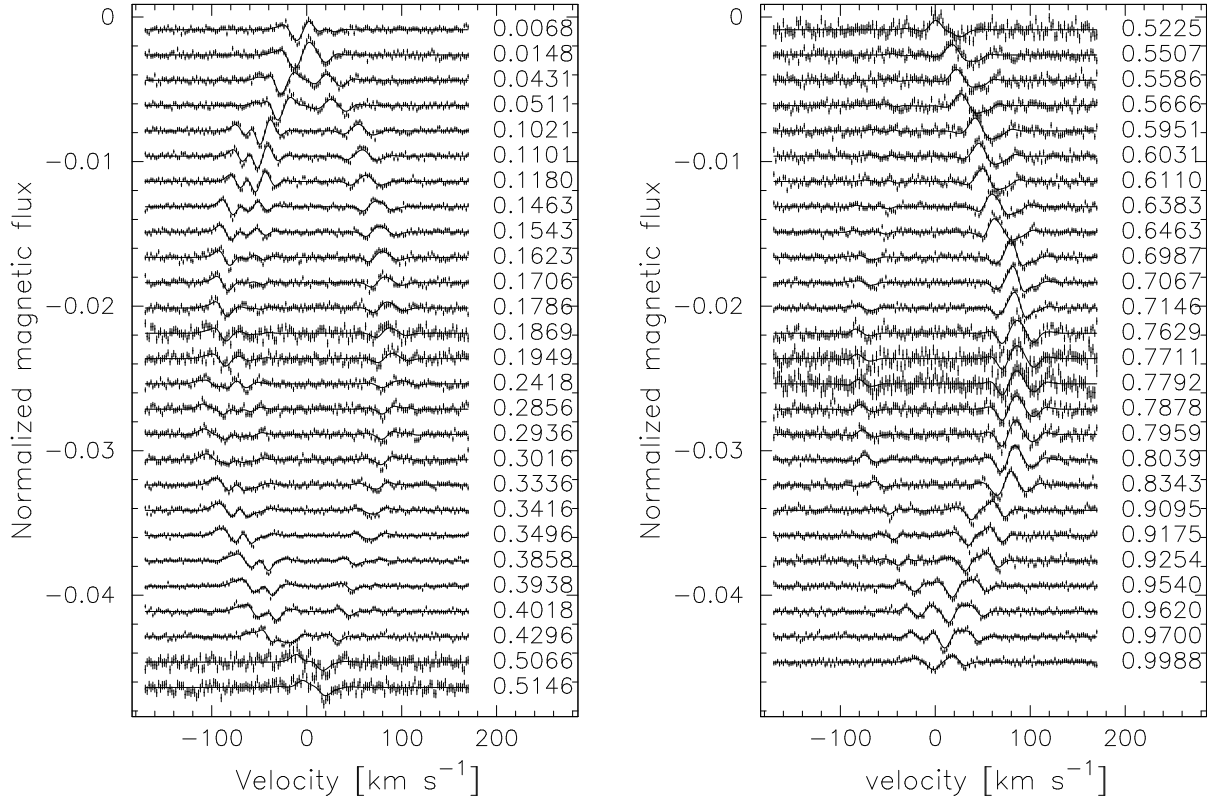
Figure 6.5: The 2007 resulting observed Stokes V LSD profiles are plotted along with their uncertainties. The solid line is the maximum entropy regularised fit we obtain to the data from Zeeman Doppler imaging. Profiles are ordered by orbital phase (listed to the right of each profile) and clearly show the motion of both binary components.

from the secondary star all but disappears around phase $\phi = 0.6$.

The reconstructed magnetic images are shown in Fig. 6.6. We show the radial, azimuthal and meridional field components. The density and coverage of the observations ensures that there are no imaging artifacts that can result from poor phase sampling. Note that ZDI is only sensitive to high latitude meridional flux on stars with moderate to high inclination angles. At low latitudes the meridional map suffers considerable cross-talk with the radial map (Donati & Brown 1997). A comparison of the recovered low latitude meridional field (bottom panels Fig. 6.6) with the radial field (top panels Fig. 6.6) shows this to be the case. The maximum amplitude of both the radial and azimuthal field is approximately twice as large on the primary as on the secondary star.

The radial field map of the primary star shows many small regions of flux of alter-

nating polarities. The level of surface detail recovered is in fact near the limit that our observations of a star with a relatively small $v \sin i$ ($\simeq 35$km s^{-1}) could produce. As an interesting comparison, we note that the radial field maps of the primary star are similar in the level of detail they recover to those produced of AB Dor (actual $v \sin i = 91$km s^{-1}) once spun-down to $v \sin i = 35$km s^{-1}, as was performed during the testing of ZDoTS described earlier.

In Fig. 6.7 we show the radial magnetic field painted on to the surface of each star. This illustrates the field structure near the polar regions better than the mercator projection (Fig. 6.6). It also allows us to consider the distribution of flux on the star with respect to the binary orbital motion. We discuss the magnetic maps further in §6.7.2, where we will also compare them to those obtained in 2004.

6.5 2004 observations

A small number of observations were also acquired at the AAT of HD 155555 during 2004 September 23 - 28. The instrumental set-up and data reduction procedures were identical to those described in §6.2. The exposure time of each individual exposure was 300 s (compared to the 200 s of the 2007 observations). All orbital parameters of HD 155555 were re-calculated for the 2004 observations using the DoTS code and the χ^2 minimisation technique (see §6.3.1). The mass ratio (q) and semi-major velocity amplitude (K_1) were found to be consistent with the 2007 values (within the 2004 values uncertainties), therefore we adopted the higher precision 2007 values shown in Table 6.1. The phase offset (ϕ_0) and the radial velocity (γ) were also re-calculated for the 2004 dataset. A phase offset of $\phi_0 = 0.752606$ (cf. $\phi_0 = 0.752474$, Table 6.1) and a radial velocity of $\gamma = 3.77$ km s^{-1} (cf. $\gamma = 3.72 \pm 0.02$ km s^{-1}, Table 6.1) were found. We note that the value found by Strassmeier & Rice (2000) for 1996 was considerably larger, $\gamma = 5.9 \pm 0.2$ km s^{-1}. One possible source for changes in the apparent radial velocity of HD 155555 is the dMe companion, LDS587B. However, a $\simeq 2$ km s^{-1} change is probably too large to be attributed to the well separated LDS587B. Future observations will be required to determine if long-term trends exist in both ϕ_0 and γ.

Over the six nights a total of seven Stokes V spectra were taken. Two of these were taken close to each other on the same night and on the sixth night a very similar
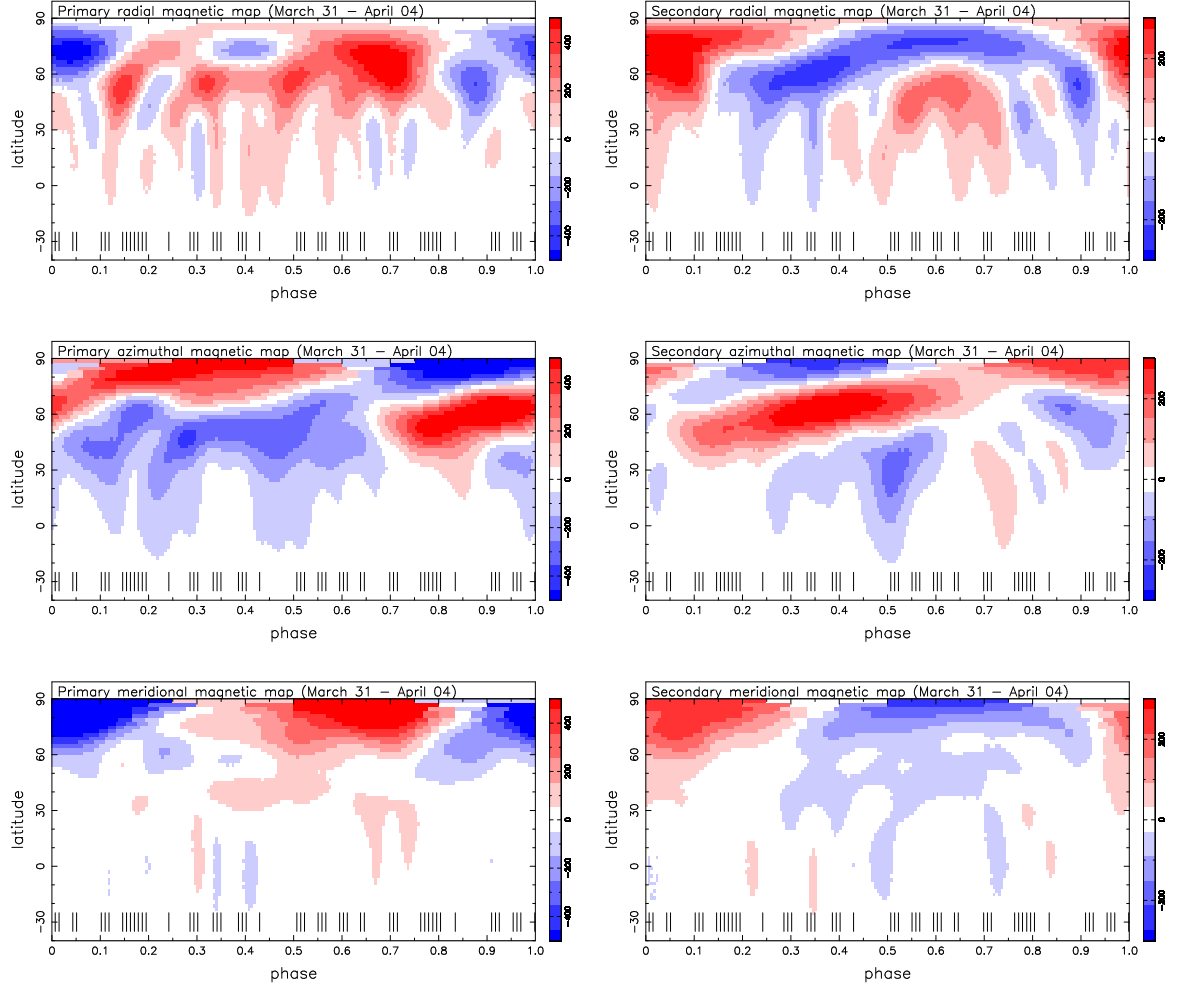
Figure 6.6: The 2007 magnetic surface maps produced from the Zeeman Doppler imaging process. Maps of the primary star are shown on the left, while those of the secondary are on the right. The top panels show the radial magnetic field, the middle shows the azimuthal maps and the bottom panels show the meridional field. In all maps red represents positive polarity and black negative polarity. Note that the contrast range is different between the primary and secondary maps, as illustrated in the key to the immediate right of each map.
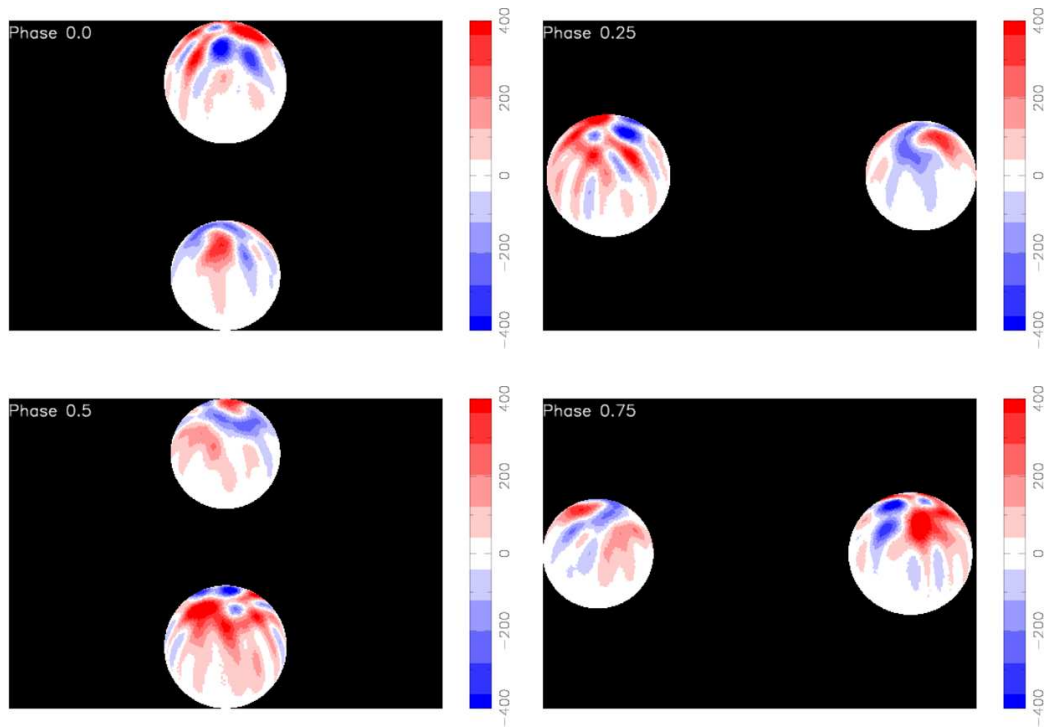
Figure 6.7: The 2007 radial magnetic maps, in Fig. 6.6, are shown projected onto the surfaces of each star at the four quadrature phases, using a single contrast range for both stars, as depicted to the right of each panel.
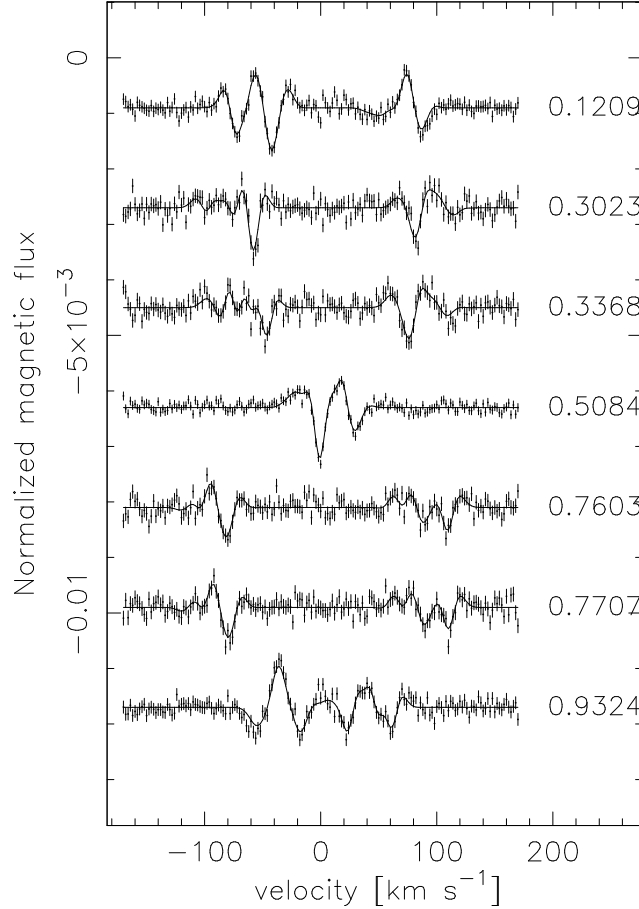
Figure 6.8: The observed 2004 Stokes V profiles from the LSD procedure are plotted along with their uncertainties. The solid line is the maximum entropy regularised fit we obtain to the data from Zeeman Doppler imaging. Profiles are ordered by orbital phase (listed to the right of each profile).

phase as was observed on the first night was obtained. Therefore together the Stokes V spectra effectively only sample five unique phases. The largest gap in the phase coverage is $\Delta\phi \simeq 0.25$ between phases $\phi = 0.51$ - 0.76. The signal-to-noise in the peak order ranged from 180 - 220 on six of the nights and was 290 on September 25. In Fig. 6.8 we show the 2004 Stokes V spectra and the fits. From these alone it is possible to ascertain that the field structure has changed on both stars. The secondary star generally shows a greater peak-to-peak amplitude than it did in 2007 and is now comparable to the primary star.

The relatively small number of observations in 2004 compared with the 2007 dataset result in lower quality maps with less detail and increased phase smearing. This is especially true for the brightness maps shown in Fig. 6.9. Here, the weak low latitude spots

147

are only recovered by pushing the maximum entropy regularised fits to the point where noise starts to appear. Despite this fact, the 2004 data can still be compared with the 2007 data to provide valuable insight into the evolution over the intervening 2.5 year period, as discussed in §6.7.1.

The magnetic maps we recover are also shown in Fig. 6.9. The meridional magnetic maps show considerable cross-talk with the radial map. This is much more severe in 2004 than the 2007 maps (Fig. 6.6). This is to be expected due to the poor phase coverage at this epoch (see Donati & Brown 1997 for further details). We note that on close comparison of the 2004 maps with those in Fig. 6.6 (2007) it is apparent that regions in the 2004 maps are more stretched out in latitude than those in 2007. We suspect that this is a result of the poor phase sampling of the 2004 data. In order to assess the impact this has on the 2004 magnetic maps, we created a subset of seven spectra from the 2007 dataset that were nearest in phase to those of 2004. We then proceeded to use only these spectra in the ZDI process to re-produce the 2007 maps. The results of this procedure were that essentially the same maps were recovered but with increased latitudinal smearing present. This also led to a reduction by nearly 50% in the field strengths of the recovered magnetic regions.

These results are not surprising given that the Doppler imaging process is inherently more sensitive to longitude than latitude position and it is only by repeatedly observing the same features as they move through the stellar rotational profile that we can accurately determine their latitude position. Also, as mentioned earlier, ZDI is only able to ascertain the orientation of the field by observing how the Stokes V signature behaves as it rotates into and out of our line of sight. Therefore the poorer the phase sampling the greater the cross-talk between the radial, azimuthal and meridional fields. Interestingly though, because this affects both stars equally, the ratio of the amplitudes of the field strengths recovered between the primary and secondary stars remained similar for the subset of 2007 data. We postpone further discussion of the 2004 magnetic maps to §6.7.2.

6.6 Coronal field extrapolations

The surface radial magnetic map of each star can be extrapolated to provide us with an initial idea of the coronal field structure using the coronal X-ray modelling technique of Jardine et al. (2002b), based around a code originally developed by van Ballegooijen et al.

Figure 6.9: Brightness (top) and magnetic maps (radial, azimuthal field and meridional field) are shown for September 2004 observations. Note that unlike 2007 maps, the contrast range of the magnetic maps is the same between the primary and secondary maps, as illustrated in the key to the immediate right of each map.

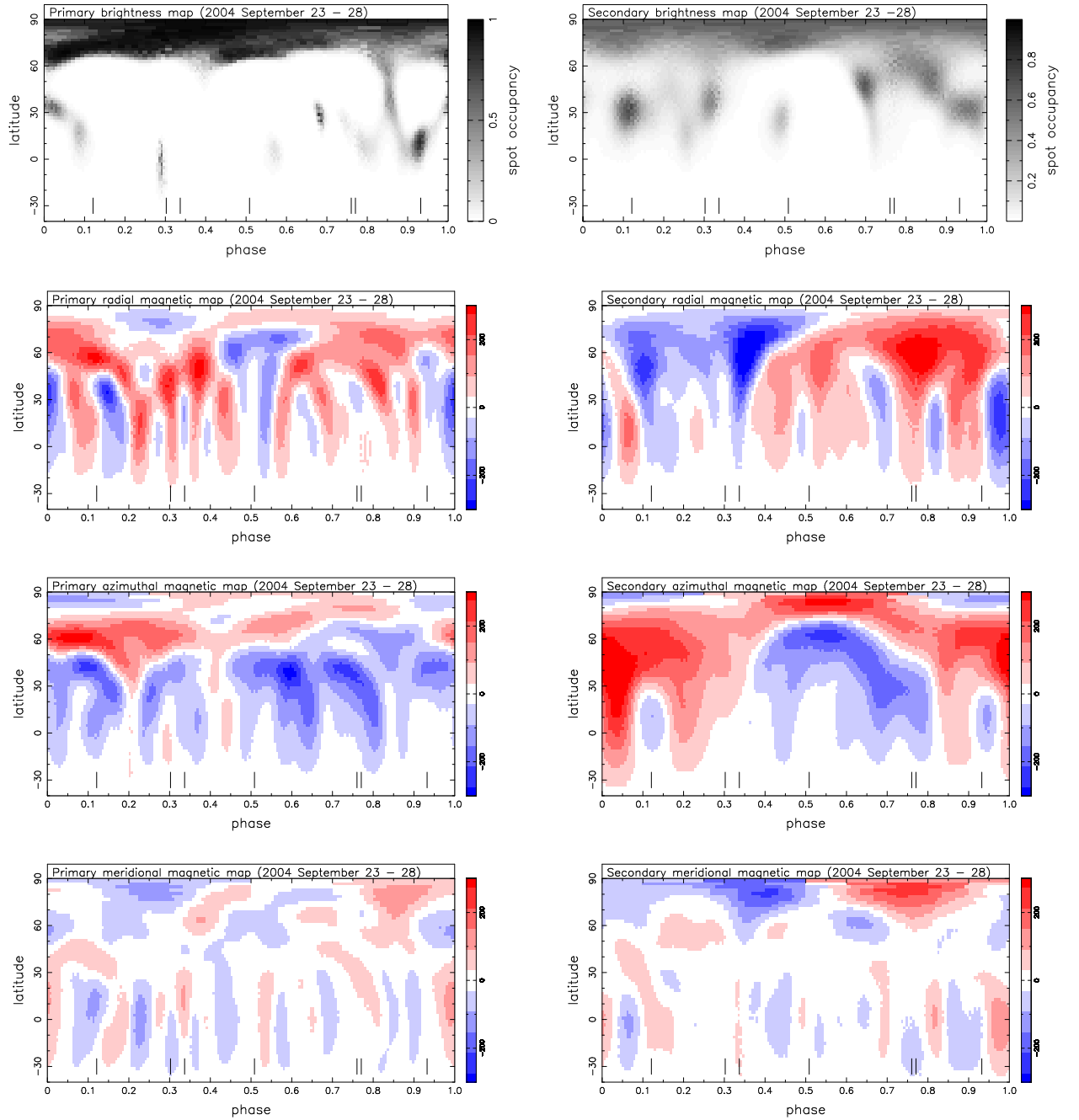(1998). The coronal field extrapolations were carried out by Moira Jardine using the radial field maps found in the last sections. I include below my brief description of what she did and the results that were found, as they are of direct relevance to later discussion in both this chapter and the next.

At present we treat each star separately, making no attempt to model the interaction between the two stars that may occur. While this obviously places limitations on the conclusions we will be able to draw from the field extrapolations, it will have only minimal effect on either the small scale structure near to the stellar surface or the global orientation of the magnetic axis. This technique uses the "Potential Field Source Surface" method which assumes two boundary conditions, the first being that the radial field is equal to that recovered on the radial field map at the stellar surface and secondly that the field becomes purely radial at the source surface. The implication of this is that the magnetic field is forced open by the outward pressure of coronal gas at the source surface radius.

The further we get from the surface of a star the simpler the field geometry becomes. Eventually the outermost groups of closed field lines represent the lowest-order, dipolar, field. From these we can establish whether or not the magnetic axis is aligned with the stellar rotational axis. The largely unseen lower hemisphere contains little magnetic flux. As discussed by Jardine et al. (2002), the nature of the field in the unseen hemisphere can influence the coronal geometry of the low latitude field although the effect is much less apparent for the high-latitude field. The presence of a binary companion may also change the connectivity of the largest-scale coronal field lines, since these may possibly connect the two stars. The orientation of the magnetic axis of the field, however, is not affected by either of these factors since it is determined purely by the surface field of the observed hemisphere. In order to illustrate the coronal topology we choose the source surface to be at a large enough radius for each star that the higher-order components of the field have died away and only the simplest, dipolar, structure remains. This is at a radius of 3.4 R_* for the primary and 6.8 R_* for the secondary component. The true locations of the source surface, and so the radii of the last closed field lines, will of course depend upon the density of X-ray emitting coronal gas. The value obtained for HD 155555 of $\log{(n_e)} = 10.7 \pm 0.23$ [cm^{-3}] determined by Ness et al. (2004) would suggest that the true source surface is probably smaller, perhaps comparable to the values determined for AB Dor by Hussain et al. (2007). We note, however, that on single rapidly rotating stars, stellar prominences have been observed at several stellar radii above the surface. For example, in Chapter 2 we

found that Speedy Mic had a complex prominence system located at twice the height above the stellar surface as the calculated co-rotation radius. This leads to the requirement of large, closed magnetic loops in order to enforce co-rotation. In comparison the co-rotation radius of HD 155555 is in effect the orbital separation of 7.5 $R_\odot$ (by virtue of the fact that this is a tidally locked system).

In Fig. 6.10 we show a representative sample of field lines from both regions close to the surface of the star and the larger scale field. As we described in the last section, the radial surface maps of both stars, but the primary star in particular, show a complex magnetic field with many small magnetic regions. We can thus expect there to be significant structure at relatively small distances from the surface of each star. Such regions will produce small closed loops. This indeed is what we see from the coronal field extrapolations in Fig. 6.10.

6.7 Discussion

6.7.1 Distribution of stellar spots

In addition to the September 2004 and April 2007 brightness maps presented in this work, there are two previously published Doppler images of HD 155555. Hatzes & Kürster (1999) present observations taken in September 1990 and Strassmeier & Rice (2000) those obtained in May 1996. These four well-spaced epochs provide a valuable opportunity to study the evolution and stability of the spot groups in this tidally-locked binary system. The details of the different Doppler imaging codes, phase coverage and signal-to-noise of observations mean that we have to be careful in our interpretation of the strength and sizes of individual features that we see. However, a general comparison of the distribution of spots should be possible.

Considering the primary star first, all four maps show a polar spot. In 1990, Hatzes & Kürster (1999) observed a significantly decentred polar spot that was tilted in the direction of the secondary star. The other three epochs show a more centrally located polar cap that extends down to a latitude of $+60°$. The well sampled 2007 dataset shown in Figs. 6.2 and 6.3 suggest that the polar cap is not homogeneous but is composed of a number of large dark spots. All four epochs show a lack of mid-latitude spots and a band of
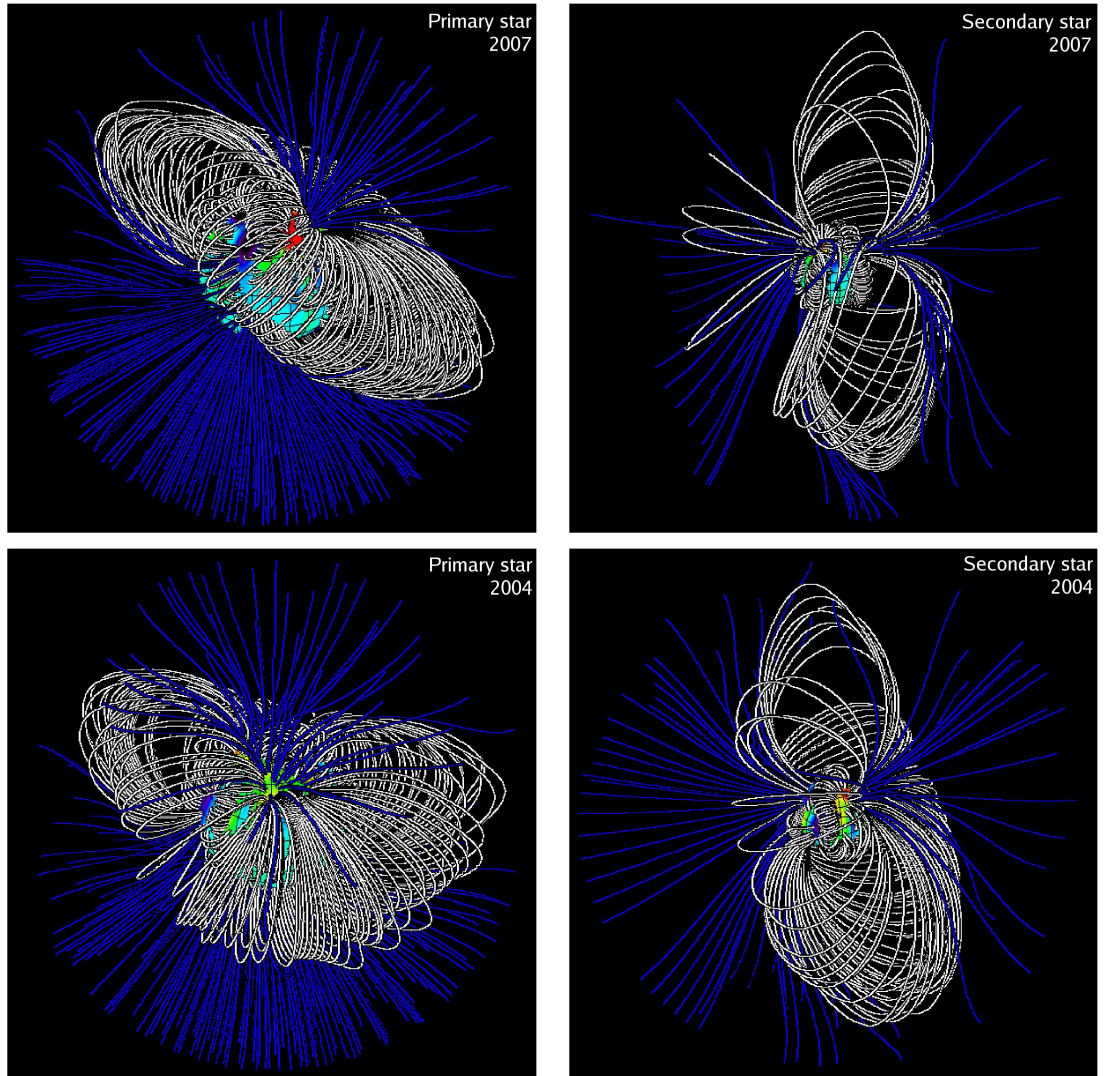
Figure 6.10: Coronal field extrapolations are shown for the primary star (left panels) and secondary star (right panels) for 2007 data (top panels) and 2004 data (bottom panels). These particular phases were chosen as they best illustrate the large scale field orientation. The primary is shown at phase $\phi = 0.8$ (and so near to the trailing hemisphere), while the secondary is at phase $\phi = 0.9$ (nearest to the anti-facing hemisphere). Open and closed field lines are represented by blue and white lines respectively. The radial magnetic maps are shown on the stellar surfaces with blue corresponding to negative, green to zero and red to positive magnetic flux.

low latitude spots at approximately $+30°$. This bi-modality in the latitudinal distribution of spots seems to be a consistent feature of the G5IV primary. This is reminiscent of the brightness maps found for G dwarfs in the young α Persei cluster by Barnes et al. (1998) and more recently of the G dwarf HD 171488 by Marsden et al. (2006). All these stars show spots emerging near the polar or at low latitudes but with a distinct lack of spots at intermediate latitudes. Theoretical flux-tube modelling by Granzer et al. (2000) predict a bimodal spot distribution for very young pre-main sequence stars. Strassmeier & Rice (2000) considered these models for the particular case of HD 155555 and found that the predictions did not match the observed spot patterns. Instead, meridional flows may explain how flux is transported to the poles. Or else two distinct flux emergence mechanisms may be in operation.

Hatzes & Kürster (1999) revealed a string of such low-latitude spots on the anti-facing hemisphere (i.e. the side of the primary facing *away* from the secondary star). This was also reported by Strassmeier & Rice (2000), although their maps recover spots covering a larger range of stellar longitudes and therefore also revealed a number of spots on the trailing hemisphere (the one that always follows behind with respect to the binary orbital motion). Both our maps for 2004 and 2007 reveal a band of low-latitude spots. The more reliable 2007 maps show that this covers three quarters of the stellar circumference and shows a preference for spots to be located on the facing and trailing hemispheres. The gap that breaks what would otherwise be a complete ring of low-latitude spots occurs between phases $\phi = 0.2 - 0.5$. This corresponds to the leading/facing hemisphere of the primary star and is thus in total contrast to the 1990 map. We are therefore left to conclude that there are no apparent stable 'active longitudes' on the primary star of the HD 155555 system.

With the exception of 2004, the secondary star does not have a true polar cap but instead has a high-latitude spot that just touches the pole. Hatzes & Kürster (1999) found such a spot tilted towards the primary star (at phase $\phi \simeq 0.55$) in 1990, whereas Strassmeier & Rice (2000) recovered a similar feature but on the trailing hemisphere (at phase $\phi \simeq 0.30$) of the secondary star in 1996. Our 2004 spot map shows the secondary star to possess a true (centrally located) polar spot. In 2007 we again find a high-latitude spot that this time is centred on phase $\phi \simeq 0.4$ and so is again tilted in the direction of the primary star. Given our relatively poor understanding of how polar spots form, it is possible that the shifting location of the polar spot may be linked to the extreme tilt of

the magnetic axis found in §6.6.

All epochs reveal spots at mid and low-latitudes on the secondary star. In particular, a large low-latitude ($30°$) spot group is seen at *all* epochs between phases $\phi = 0.1 - 0.3$ (trailing hemisphere). As this appears to be a consistent feature of the secondary star maps it may indeed indicate an active spot longitude.

6.7.2 Surface magnetic topology and dynamo processes

The magnetic maps we produced in the last sections (Figs. 6.6 and 6.9) are the first of a pre-main sequence binary system. Both components of HD 155555 possess large regions of strong azimuthal field near to the stellar surface. These are of equivalent strength (in fact, often stronger than) the recovered radial field. Strong azimuthal field is recovered on all active cool stars that have been mapped so far using ZDI. This is in contrast to the relatively small amounts of horizontal field found on the comparatively inactive Sun. Solar azimuthal field is thought to be buried deep in the base of the convective envelope where dynamo activity is generated. Previous authors (e.g. Donati et al. 2003 and Petit et al. 2004) have therefore postulated that the presence of strong azimuthal field, at the stellar surface of these rapidly rotating stars, suggests that their dynamo may be active throughout the convection zone. While this suggestion is contrary to the classical understanding of the generation of large-scale fields in slowly rotating (solar-type) stars, it has recently gained support from the numerical simulations of Brown et al. (2007). These authors find that global-scale toroidal and poloidal magnetic fields can be built and maintained in the bulk of the convection zone of rapidly rotating stars, despite the presence of turbulent convection. In particular Brown et al. (2007) find strong ordered torodial fields which may explain the observation, as in HD 155555, of strong surface azimuthal field. We can now compare the maps of both components of HD 155555 to each other and look for evolution between the 2004 and 2007 epochs.

Primary star

The radial field map of the primary star shows many small regions of flux of alternating polarities. A visual inspection of the 2007 primary radial maps reveals no real latitude dependence, with both positive and negative field at all latitudes and no preference at the
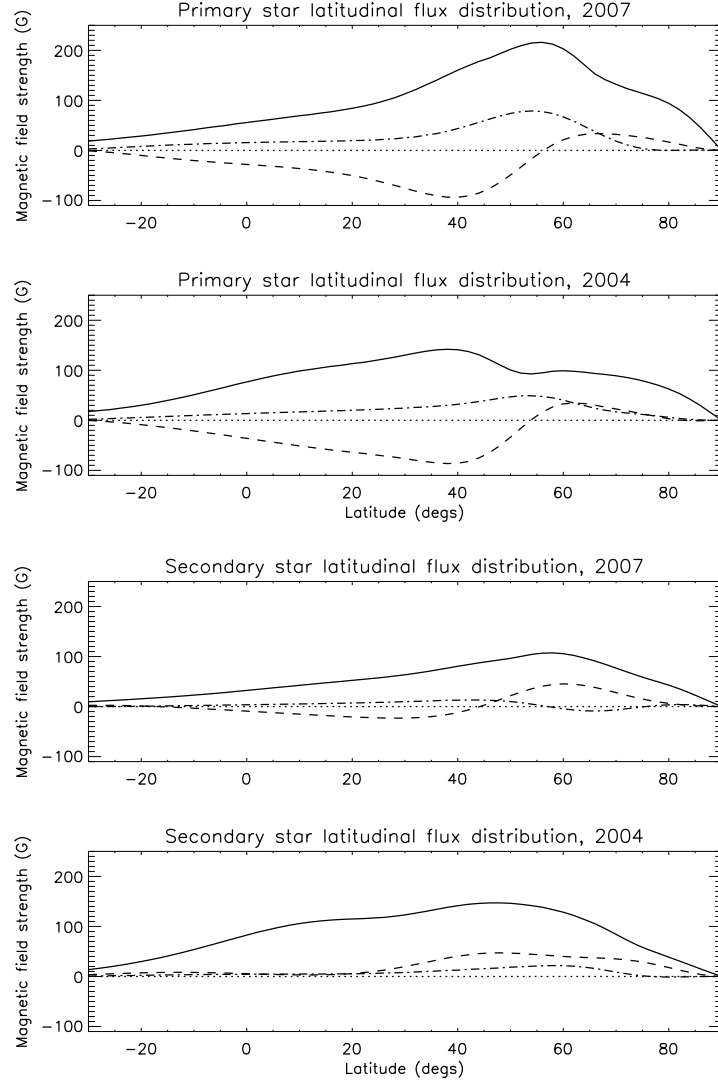
Figure 6.11: The latitudinal flux distribution is shown for each star in both the 2004 and 2007 epochs. In each panel the solid line represents the quadratic magnetic flux, the dashed line shows the azimuthal field and the dash-dot line depicts the radial field. The value of a given quantity is the integration over all longitudes and has been corrected for the relative pixel area at that particular latitude - hence the reduction in all fluxes observed at the pole.

pole. In 2004 the maps do show a slight preference for positive polarities, especially at mid to high latitudes (60 - 80°). The radial field maps are integrated over all longitudes in Fig. 6.11 to test for the presence of a latitudinal polarity dominance. In doing so considerable cancellation of the flux occurs due to the already described complex nature of the maps. However, Fig. 6.11 shows that we are left with a preference for positive radial flux at all latitudes and for both epochs, with a peak flux at 55°.

The azimuthal field maps of the primary star reveal a considerably simpler field structure than the radial maps. This is particularly apparent in 2007 where the surface topology can essentially be described by just two regions. A large region of positive field is seen encircling the star at high latitudes, centred on ($\simeq$75°). This points down to lower latitudes ($\simeq$60°) at phase $\phi = 0.8$. It therefore resembles a ring of positive flux that is tilted by 15° with respect to the rotational axis. Due to the fact that the ring crosses over the rotational pole, part of it then appears as a negative polarity region. The other region is of negative field at lower latitudes. In 2004 the azimuthal maps appear more complex that in 2007, with more mixing of positive and negative polarities. The general latitude distribution is similar to 2007, with positive field at high latitudes and negative field at lower latitudes. However, the field appears more axisymmetric in 2004 with both rings of flux being better centred on the rotation pole. Again, in Fig. 6.11 we integrate the azimuthal maps over all longitudes to find that the primary star indeed shows a dominant negative polarity at all latitudes below 55°, but then switches to positive field at high latitudes. The similarity of the azimuthal flux distribution in both 2004 and 2007 suggests that this is a relatively stable feature of the primary star.

The meridional field maps show two very high latitude regions of opposite polarity in both 2007 and 2004. This is exactly what you would expect to result from a homogeneously oriented ring of horizontal field that crosses the pole. The ZDI process will recover part of the field as azimuthal (as discussed above) and part as meridional. The low latitude features (as already outlined in §6.4.1 and §6.5) are the result of cross-talk from the radial field (particularly severe in 2004). Therefore, the azimuthal and high-latitude meridional flux appears to be attributable to the toroidal field, while the radial and low-latitude meridional flux is part of the poloidal field.

Secondary star

The secondary star has a considerably simpler radial field map than the primary star. Like the corresponding map of the primary star, the radial field map appears to have no latitude dependence on the polarity of the field. Indeed when we collapse the maps in longitude in Fig. 6.11 we achieve almost total cancellation of the positive and negative fluxes. In 2007 the residual trend is for positive polarity at latitudes lower than $55°$ and negative flux at higher latitudes. In 2004 there is a slight indication of preference for positive polarity for both field components.

The maps of azimuthal field of the secondary star are unusually complex. In 2007 we recover low latitude flux of mixed polarity, with a complex region composed of both negative and positive field at phases $\phi \simeq 0.6 - 0.9$. However, we see a positive ring of field at high latitudes, again tilted (like the azimuthal field of the primary star in 2007) away from the rotational axis by $\simeq 15°$ and towards phase $\phi = 0.3$. Fig. 6.11 shows that negative azimuthal field dominates at latitudes below $45°$ then the field becomes positive at higher latitudes. Similarly in 2004, a ring of non-axisymmetric positive azimuthal field can be seen at high-latitudes. Fig. 6.11 shows a preference for positive azimuthal field at all latitudes. Both epochs have a strong, low latitude, region of negative azimuthal field centred on phase $\phi \simeq 0.5$ (the hemisphere facing the primary star). The meridional maps of the secondary star show two high-latitude regions of opposite polarity. They are therefore similar to those of the primary star and thus we refer the reader to the discussion of the primary star's meridional maps in the previous section.

6.7.3 Magnetic regions, polar spots and axis misalignment

To summarise the last section; we find evidence for rings of azimuthal field which are non-axisymmetric but yet show a clear constant polarity structure. The trend for both stars of HD 155555 is to have a high-latitude ring of positive azimuthal field which is tilted with respect to the rotational axis and then for this to be underlined by negative field at low latitudes. Interestingly the rings of positive azimuthal field closely follow the polar spots discussed in §6.7.1. Donati (1999) and Donati et al. (2003) found a similar pattern between the azimuthal field and polar spots on HR 1099.

The similarity of the 2004 and 2007 coronal extrapolations shown in Fig. 6.10 is

striking. On both epochs the secondary star exhibits an extreme tilt of its magnetic axis. From plotting the neutral polarity line at the source surface we calculate that the magnetic axis is approximately 75° misaligned with the rotation axis. The primary stars magnetic field is more closely aligned to that of its rotational axis. We find a ≃30° misalignment to that of the rotational axis in 2004 and a larger ≃45° misalignment in 2007. This may be related to the fact that, as discussed in the last section, the ring of surface azimuthal field shows a tilt of approximately 15° for the primary star in 2007 but more of an axisymmetric ring in 2004. So it appears that both the radial and azimuthal fields were both more axisymmetric in 2004. It therefore seems likely that the surface azimuthal field is linked to the orientation of the large scale field.

6.7.4 Relative field strengths and magnetic energy

In the 2007 maps shown in Figs. 6.6 and 6.9, the magnetic field strength scale needed to be different for each star and yet for 2004 they could be the same. The average quadratic field intensity can be calculated for both stars at each epoch. This can also be examined graphically, as a function of latitude, from the solid line in Fig. 6.11. We find for the well sampled 2007 epoch an average field strength (integrated field modulus over the whole stellar surface) of 68 G for the primary star and 43 G for the secondary star. So in 2007 the primary star appeared to have a field strength 50 % greater than that of the secondary star. For the 2004 maps we find a field strength of 52 G for the primary star and 61 G for the secondary. It therefore appears that the field strength of the secondary star was considerably stronger in 2004, both in absolute terms (42% stronger than in 2007) and relative to that of the primary star.

As mentioned in §6.5 the comparatively poor phase sampling of the 2004 data must be taken into account. We found that using only a subset of the 2007 data (choosing the same number of spectra available in 2004) resulted in an almost 50% reduction in the recovered flux. In addition the observed flux was spread out in stellar latitude. The effect of this can be seen in Fig. 6.11 where the total quadratic flux (solid line) shows a broader distribution in the 2004 panels than those of 2007. The effect of fewer phases of observation is that we effectively miss (do not recover) flux from the stellar surface. Therefore the 16 G weaker field strength of the primary star in 2004 is likely due, at least in part, to this effect. However, reduced phase sampling certainly cannot explain why the

secondary star has a field strength 18 G (42%) *stronger* in 2004 than in 2007. In fact it suggests quite to the contrary, the real difference in the flux between 2004 and 2007 must have been even greater.

Another quantity which we can calculate in an attempt to understand the above observations is that of the magnetic energy. This can be calculated for each of the radial and azimuthal fields. We can then quote the energy stored in each field component as a fraction of the total energy. The meridional field is found to contain between 8 - 12 % of the total magnetic energy (depending upon the star and epoch). It is therefore small compared to the radial and azimuthal contributions and we do not discuss it further. We find that in 2007 the azimuthal field of the primary star stores 58% of the total energy, with 34% in the radial component. This is similar to the case of AB Dor and LQ Hya where the azimuthal field is found to preferentially store more of the field energy than the radial field at most epochs (Donati et al. 2003). In the case of the secondary star, in 2007 the radial field dominates by storing 48% of the magnetic energy while the azimuthal field has 43%.

When we perform the same calculation for the 2004 maps we find that the azimuthal and radial fields store equal energy (44%) on the primary star, corresponding to a decrease in the relative azimuthal field strength. However on the secondary star the opposite appears to have occurred; the azimuthal field is found to contain 54% of the energy and the radial field 38%. We again note that the poor sampling of the 2004 dataset may have an impact on these results. Observations with very poor phase sampling can be prone to cross-talk between the radial and azimuthal field components. This would lead to a reduction in the contrast between the two field components and may partly explain the observation of more equal percentages for the primary star. Also if, by chance, a particularly strong region of field (be it azimuthal or radial) was missed by our observations then this would be reflected in the balance of the magnetic energy. The situation would be considerably worse in the case of poor phase *sampling*. If the observations were very poorly spaced then there would be little constraint on the flux for large parts of the stellar surface. While the 2004 observations are poorly sampled, they are at least reasonably evenly spaced. We therefore conclude that the relative strengths of the field components for 2004 should be treated with caution and as an indication only.

In summary, it appears that the magnetic field of the secondary star has evolved

considerably between 2004 and 2007. The average field strength has become much weaker (both in absolute value and relative to the primary star) and the azimuthal field component appears to have weakened relative to that of the radial. This is accompanied by an apparent change in the azimuthal topology from a comparatively simple field (characterised by a ring of positive flux) in 2004 to a more complex distribution in 2007. If, as suggested by Donati et al. (2003), the strong azimuthal field observed on active stars is closely related to the toroidal component of the large-scale dynamo field then the observed behaviour may represent the decay phase of an activity cycle. There is insufficient evidence to make a similar comment about the primary star at this time.

6.7.5 Comparing HD 155555 with other stars

The HD 155555 system is particularly interesting as it is a young binary system and is therefore a potentially very promising target for disentangling the effects of youth and binarity. As a close binary system, the components of HD 155555 are tidally locked, just like the primary stars in evolved RS CVn binaries such as HR 1099. However, with an age of around 18 Myr (see §6.3.2) HD 155555 is still a pre-main sequence object and therefore younger than the well studied zero-age main-sequence rapidly rotating single stars, AB Dor and LQ Hya (50 - 100 Myr, e.g. Janson et al. 2007). This fact is reflected in the bloated size of both components of HD 155555. Despite the fact that AB Dor and LQ Hya are of approximately equal mass to HD 155555, we find in §6.3.1 radii of 1.5 and 1.3 $R_\odot$ for the primary and secondary stars respectively (c.f. ≈ 1 $R_\odot$ for AB Dor and LQ Hya, Donati et al. 2003). This will lead to increased convection zone depths of both components of HD 155555 relative to AB Dor and LQ Hya. Therefore, somewhat ironically, both the evolved HR 1099 binary (R=3.7 $R_\odot$) and HD 155555 have convection zone depths greater than AB Dor and LQ Hya. Consequently, if convection zone depth uniquely determines the observed magnetic surface topologies, then our attempt to compare the effects of binarity and youth will be ultimately inconclusive.

As already mentioned, the observation of strong surface azimuthal field is common to HD 155555, AB Dor, LQ Hya and HR 1099. Beyond this, HR 1099 is characterised by easily identified rings of azimuthal field that are normally axisymmetric. A similar ring of azimuthal field is often observed on AB Dor but only at high-latitudes. We find that both components of HD 155555 show rings of azimuthal field, but they are often

non-axisymmetric. HR 1099 also possesses a latitudinal dependence on the polarity of the radial field with a unipolar polar cap. In contrast, the young rapid rotators AB Dor and LQ Hya show mixed polarities of radial field at all latitudes, including the pole. At first glance this is essentially what is seen for HD 155555, but when the latitudinal distribution of flux is plotted a clear trend is seen. It can be seen in Fig. 6.11 that the primary star (in both 2004 and 2007) has a bias towards positive radial flux at all latitudes, but increasing so towards high-latitudes. Petit et al. (2004) confirmed the presence of an anti-correlation of the latitudinal distribution of azimuthal and radial field on HR 1099. This is not seen on AB Dor or LQ Hya, but is present on the Sun. Fig. 6.11 shows tentative evidence of a similar anti-correlation for HD 155555 in 2007 for the secondary star, and for the primary star at latitudes below $55°$ in both 2007 and 2004. However, this does not hold for the secondary star in 2004, where both the radial and azimuthal field is positively orientated. Further observations of HD 155555 will be needed to establish long-term trends.

6.7.6 The coronal fields of HD 155555 and binary interaction

In §6.6 we used the radial field maps to extrapolate the coronal structure of both stars in HD 155555. Due to the small binary separation of 7.5 $R_{\odot}$ ($\simeq$ 5.5 R$_*$, see Table 6.1) there is no doubt that the magnetospheres of the two stars will interact. The question is: what will the nature of the interaction be? Due to the relative complexity of the surface radial field maps of both stars, the extrapolated coronal field is also correspondingly complex. As Fig. 6.10 shows, at locations between the stars where the two fields would interact, both fields retain sufficient complexity that their interaction will not be simply modelled by that of two dipolar fields.

It is clear that the next step will be to perform a full binary extrapolation, where the radial field maps of both stars are considered simultaneously. This will model which field lines will preferentially connect with the other star rather than to regions on the same star. The upper limit on the longevity of such 'binary field lines' will largely be defined by the relative differential rotation rates of each star. The surface rotation properties of HD 155555 are the subject of the next chapter.

6.8 Conclusions

We have produced the first simultaneous magnetic maps of both components of a binary system. These show that the technique of Zeeman Doppler imaging can be adapted to the binary case. This opens up the potential to study many short-period pre-main sequence and main sequence binary systems where both components have Stokes V detections. The HD 155555 system provides an interesting first insight into the magnetic fields of a young binary system. In general, we find that the resulting magnetic maps appear to share features in common with both young rapidly rotating stars and the evolved primary stars of RS CVn binaries. The most surprising result is the severe misalignment of the secondary star's magnetic and rotational axes. The impact of this can be seen on the radial and azimuthal maps. Also interesting is the significant weakening of the secondary star's magnetic field strength from 2004 to 2007, especially as this appears to be associated with a decline in the proportion of magnetic energy stored in the azimuthal field.

Once a binary potential field extrapolation code has been completed it will be possible not only to more reliably model the coronal structure of both stars but also their interaction. This will allow us to predict the locations of stellar winds and determine which field lines are capable of containing hot X-ray emitting gas. We can therefore look forward to learning more about the mass loss rates from binary systems and modelling the X-ray properties of binaries, including flare loop lengths and energies.

CHAPTER 7

Differential rotation on both components of HD 155555

This chapter is based on a paper accepted for publication in the Monthly Notices of the Royal Astronomical Society by:

Dunstone, N.J., Hussain, G.A.J., Collier Cameron, A., Marsden, S.C., Jardine, M., Barnes, J.R., Ramirez Vlez, J.C., Donati, J.-F. (2008, In press, MNRAS, astro-ph/0804.2491)

All the work described here was carried out by myself.

7.1 Introduction

Techniques for measuring the strength of differential rotation by tracking the cool spots or magnetic regions have been developed from the results of Doppler imaging and Zeeman Doppler imaging (ZDI) studies. So far, differential rotation has now been measured for more than 20 stars. These include stars of a range of different surface temperatures and so convection zone depths. Barnes (2005) collates many of these results, finding that differential rotation rate is strongly related to surface temperature but only weakly correlated with rotation rate. Near fully convective M-dwarfs (e.g. HK Aqr) exhibit very weak differential rotation, while early G-dwarfs have strong differential rotation.

The stars considered in the Barnes (2005) study were all single, young rapid rotators. Measurements of differential rotation have also been made for binary systems, again using Doppler imaging. The limited published sample currently contains the evolved primary star of the RS CVn systems HR1099 (Petit et al. 2004) and IM Peg (Marsden et al. 2007), and the main-sequence secondary star of the pre-cataclysmic variable star V471 Tau (Hussain et al. 2006). All three stars are found to have weak differential rotation and in the case of V471 Tau it was consistent with solid body rotation. So the question remains

whether it is the evolved nature of the stars or their membership of a binary system that is responsible for the observed decrease in differential rotation strength. In an attempt to disentangle these two effects we observed HD 155555 (V824 Ara), a pre-main sequence binary system consisting of two nearly equal mass components (G5IV + K0IV).

In total, eleven nights of observations were obtained of HD 155555, as detailed in Chapter 6. There we only used a five night subset of data to present the first magnetic maps of HD 155555 and to examine the longer term evolution of magnetic and brightness features. In Chapter 6 we found that both components of HD 155555 have complex radial field magnetic topologies with mixed polarities at all latitudes. Also present were rings of azimuthal field. HD 155555 therefore appears to share properties of both young single stars and the evolved primary stars of RS CVn binaries. In this chapter, we seek further clues as to the nature of dynamo processes occurring on this young binary system. We attempt to measure the differential rotation rates of both stars. In §7.3 we use the subsequent five nights to produce an additional set of surface maps that are independent of those in Chapter 6. These two sets of independent maps are compared using the technique of cross-correlation in §7.4. We subsequently incorporate a latitudinal dependent shear into the binary imaging process in §7.5 and therefore use all available data to measure the differential rotation strength. The results of our analysis are discussed in §7.6 and we present our conclusions in §7.7.

7.2   Observations

This chapter is based upon spectropolarimetric observations made at the Anglo-Australian Telescope (AAT) using the University College London Échelle Spectrograph (UCLES) which was fibre fed by the SemelPol visiting polarimeter (Semel et al. 1993) mounted at the Cassegrain focus. Eleven uninterrupted nights of observations were secured on our target star HD 155555 from 2007 March 30 to April 09. Those observations obtained on the five nights March 31 - April 04 were analysed in Chapter 6. In this chapter we combine all the observations to analyse the surface rotation properties of HD 155555. The spectral extraction and reduction of the complete dataset was the same as that done for the subset of data used in Chapter 6 and we refer the reader to this chapter for a full account of the exact process. In total, we obtain a dataset of 106 Stokes I (intensity) and Stokes V

(circularly polarised) spectra.

7.3   Comparing independent maps

The 1.68 d orbital period of HD 155555 allows us to obtain full phase coverage in five nights. Given that we have a total timebase of eleven nights (March 30 - April 09), we can therefore create two entirely independent maps of both components of HD 155555. One set of brightness and magnetic maps has already been shown in Chapter 6, corresponding to the 53 spectra taken between March 31 and April 04 (hereafter referred to as dataset/epoch one). We use the subsequent five nights, April 05 to April 09 (hereafter referred to as dataset/epoch two), to create a second set of maps. Ten fewer spectra (43) are available for this second epoch, but this still provides excellent phase coverage. We note that the observations taken on March 30 are not used in this part of our analysis. We prefer to have two equal five night datasets and therefore to obtain each complete map in as short a time as possible (to minimise the effect of differential rotation and evolution within each map). The effective time between the mid-points of the two epochs is five nights which is almost exactly three stellar rotations.

7.3.1   Brightness maps

As in Chapter 6, we use the Doppler imaging code 'DoTS' (Collier Cameron 1997) to map the surface brightness distribution of the surfaces of both stars using the Stokes I intensity spectra. The process is described in detail in Chapter 6, including the system parameters in Table 6.1. The signal-to-noise (S/N) of this second five nights of spectra range between 95 - 210 in the peak order and are thus similar to that of the first. For brevity, we do not show the obtained fits to the Stokes I data here but instead refer the reader to Chapter 6 where the fits to the first dataset can be examined.

Observations are phased according to the ephemeris of Strassmeier & Rice (2000), see Table 6.1. Also listed in Table 6.1 are the system parameters for HD 155555 which were obtained in Chapter 6. These orbital and physical parameters for the two stars are used in the Doppler imaging process. In Fig. 7.1 we present the brightness (spot) maps recovered from both epochs, for both stars.
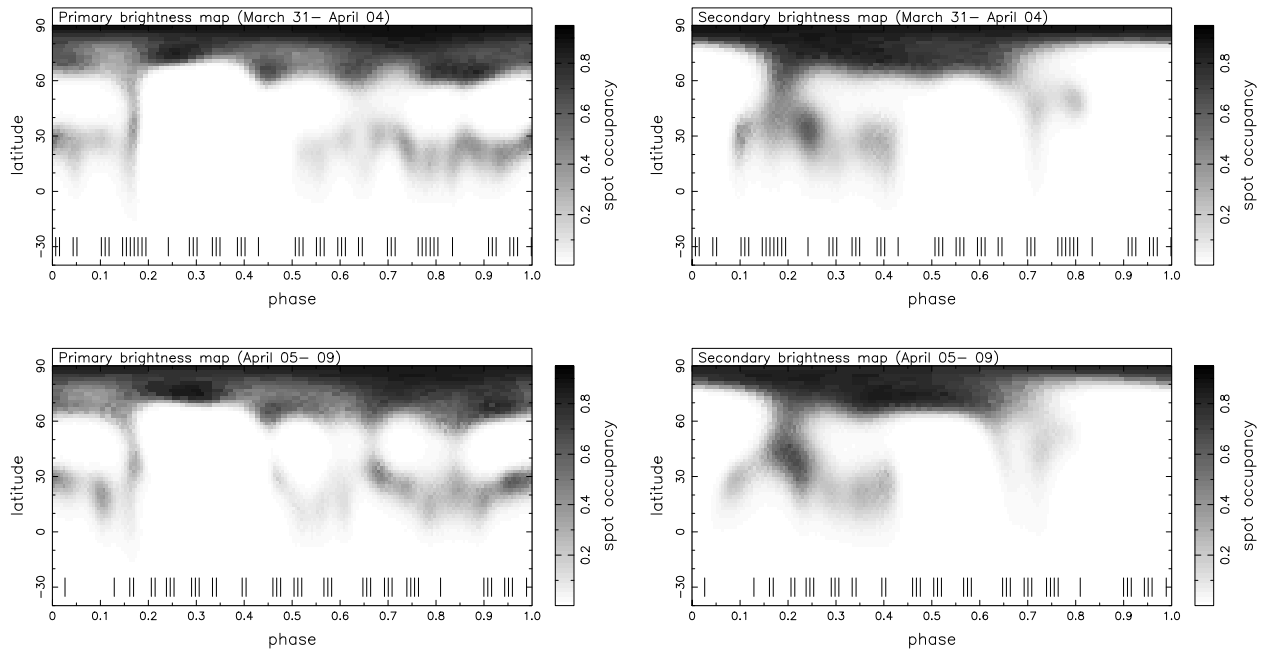
Figure 7.1: Spots maps for both stars (primary - left, secondary - right) are plotted from the original Chapter 6 epoch (top) and the new epoch (bottom). Vertical tick marks show the phases of observation.

It is clear from Fig. 7.1 that both epochs produce very similar maps for the surface brightness distribution. The features described in Chapter 6 are also present in the second dataset. On close examination of the primary star map, a weak low latitude spot is recovered at phase $\phi = 0.45$ in the second dataset which has no counterpart in the first. The secondary star also has the major spot groups in the second epoch that were described in the first, although the two mid-latitude spots at phases $\phi = 0.7 - 0.8$ are not as well defined in the second dataset as in the first. In summary, the maps show little evidence of major evolution between the two datasets. The small differences that we do observe may be caused by one or more of the following factors: a) the presence of differential rotation; b) flux emergence and diffusion; c) small changes caused by differences in the phase sampling of the two datasets.

7.3.2 Magnetic maps

We use our new ZDI code, 'ZDoTS', that was developed in Chapter 5 (based upon the single-star ZDI code of Hussain et al. 2000), to recover the magnetic maps of HD 155555 from the Stokes V spectra. ZDoTS is capable of modelling the contribution from each star to the combined Stokes V spectra and so makes use of the entire dataset, including conjunction phases (see Chapter 5 for full details). In Fig. 7.2 we show the recovered radial and azimuthal field maps of HD 155555 for the two datasets.

As with the brightness maps, the magnetic maps of both components from the two epochs look very similar at first glance. On closer inspection, a number of features have changed their exact locations on the stellar surfaces, particularly on the primary star. As we shall determine in the following sections, this is mainly due to the strong differential rotation for the magnetic features on the primary star.

7.4 Cross-correlating maps

The first technique that was employed to measure stellar differential rotation using Doppler imaging involved cross-correlating image maps. This was done for the early differential rotation measurements on the K0 dwarf AB Dor by Donati & Collier Cameron (1997) and Donati et al. (1999). The technique requires two independent maps that have been
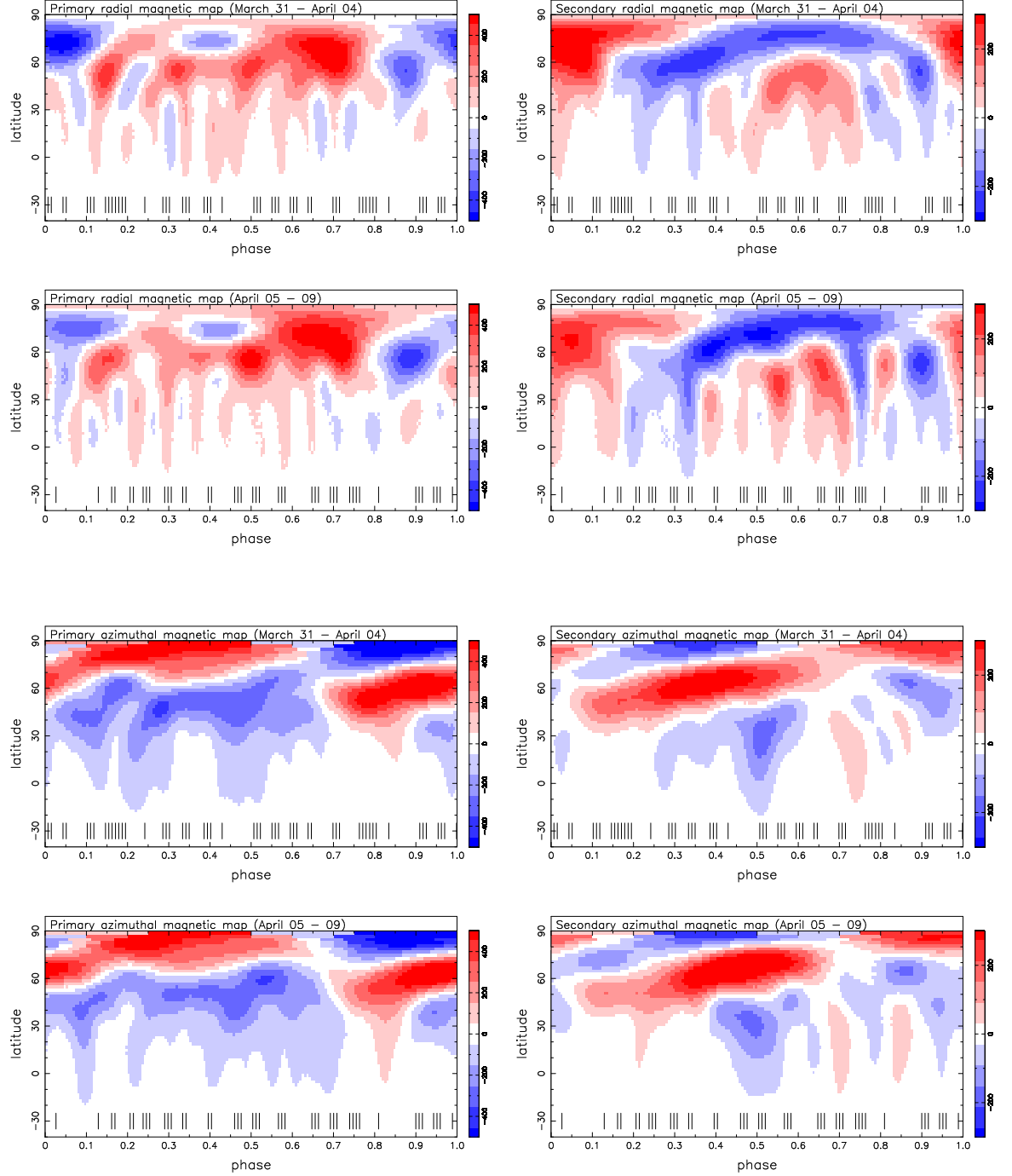
Figure 7.2: Radial and azimuthal field maps are shown from both epochs. Top four plots: radial magnetic field maps for both stars (primary - left, secondary - right) are plotted from the original Chapter 6 epoch (top) and the new epoch (bottom). Vertical tick marks show the phases of observation. Bottom four plots: as top but now for azimuthal field.

derived from observations spanning at least two rotations of the star. This is not difficult to achieve on AB Dor as its 0.51 d rotation period allows almost complete phase coverage in a single night. Therefore, even a two night observing run could, in theory, be used for cross-correlation. However, in practice a couple of night's gap is normally left between epochs to allow enough time for measurable shear to occur. In comparison, the 1.68 d rotational period of the components of HD 155555 means that in 5 nights of observing we achieve complete phase coverage. From the last section we have two independent maps that are effectively separated by 5 nights (3 stellar rotations).

The cross-correlation (Simkin 1974, Tonry & Davis 1979) is performed on each latitude slice of the images. This is carried out in a way that accounts for the continuous nature of the stellar surface, i.e. that the surface maps in Figs. 7.1 & 7.2 wrap around. The resulting cross-correlation functions are shown in Fig. 7.3 and are examined for the characteristic signature of differential rotation. We find the peak of each latitude strip's cross-correlation function by fitting a parabola. This then allows us to obtain sub-pixel accuracy in the resulting fits. Latitudes above $70°$ suffer from significant longitudinal smearing due to the poorer spatial resolution at high latitudes and so are not used. Similarly our maps contain no significant information below a latitude of $-30°$. The peaks of the cross-correlation functions are then themselves fitted with a solar-like $\sin^2 l$ differential rotation law (see below in §7.5) which is overplotted on Fig. 7.3.

The imaging code assumes that the rotational period of each star is equal to the binary orbital period. If this assumption of synchronous rotation is incorrect then the cross-correlation images should show an offset in phase. This would manifest itself as a vertical line offset from zero phase shift in Fig. 7.3, as an incorrect period would not be latitude dependent. From an examination of Fig. 7.3, it is obvious that all four maps show no evidence of uniform asynchronous rotation, as expected given the small binary separation. The binary orbital period is the correct period at a particular stellar latitude. It is also clear that in all cases the equator is rotating faster than the poles.

Out of the four cross-correlation images in Fig. 7.3, the only one that we are unable to fit with a differential rotation law was that derived from the primary star's brightness images. An examination of the primary spot images in Fig. 7.1 shows why. Spots are present near the pole (above $60°$) and at a low latitude band between 5 and $35°$ but there are very few spot features at intermediate latitudes. The corresponding primary magnetic
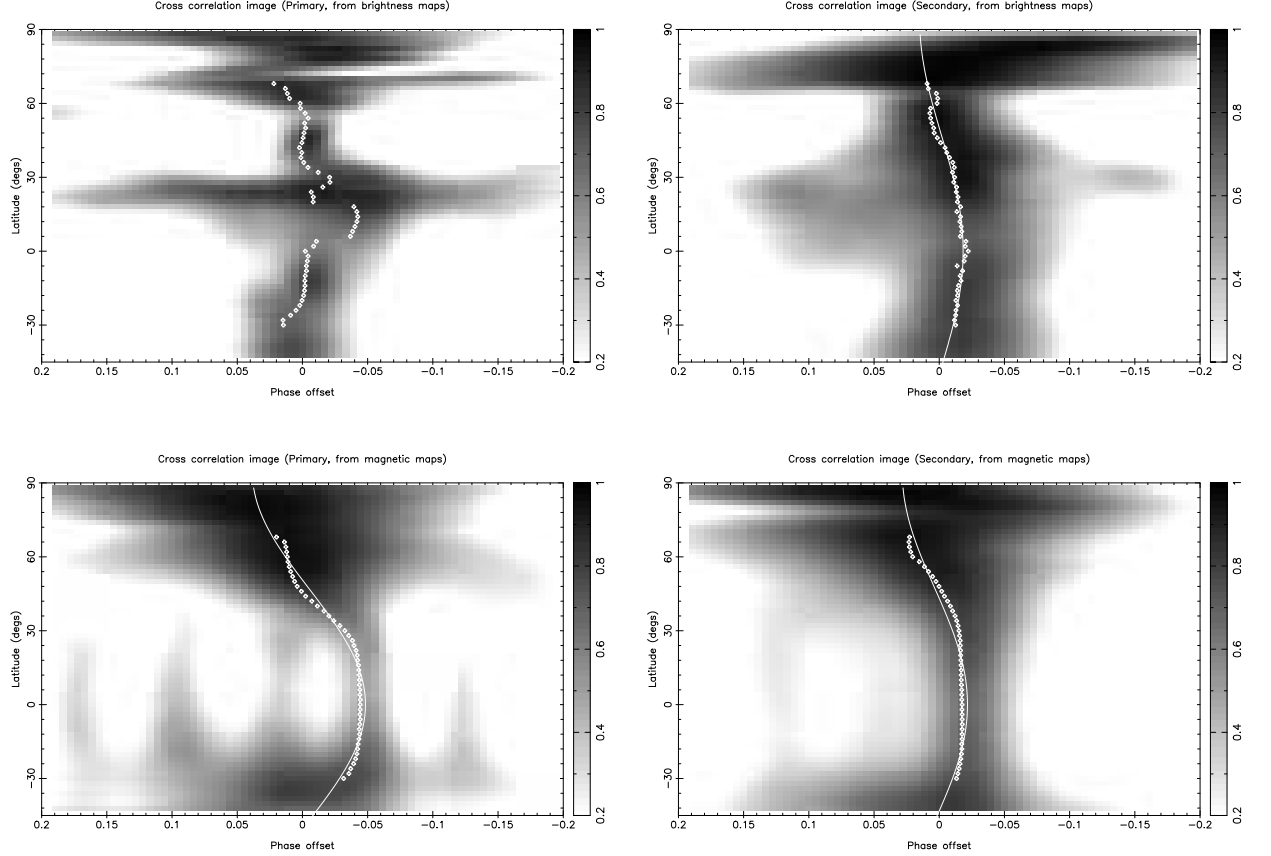
Figure 7.3: The independent maps from the two epochs are cross-correlated to search for latitudinal dependant surface rotation. The two panels on the left are for the primary star, while the two on the right show the secondary star. The top plots come from cross-correlating the spot maps and the bottom plots from the geometric average of the cross-correlation images of the radial and azimuthal field maps. Plus symbols mark the maximum of the cross-correlation function for each latitude strip and the solid lines are the best fits of a simple solar-like differential rotation law for all but the primary spot cross-correlation image (see text). Note that the x-axis plotting phase has been reversed so as to present the reader with the more conventional diagram of differential rotation that would have been obtained if we had adopted to use stellar longitude rather than phase.

images (Fig. 7.2) however, have structure at all latitudes and so produce a far cleaner signal as shown in the bottom-left panel of Fig. 7.3. Here, we find a differential rotation strength of $\Delta\Omega = 0.10$ rad d^{-1}, or an equator-pole lap time of 60 days. If we now compare this fit with the primary brightness map we can see that at the latitudes of 5-20°, within the low latitude band of spots, we find evidence of a similar phase shift.

The cross-correlation of the secondary brightness map produces a much better defined differential rotation signature than the primary star. Again this is because the secondary star has spots at a larger range of latitudes. It is well fitted by a $\sin^2 l$ law and results in a differential rotation measurement of $\Delta\Omega = 0.04$ rad d^{-1}, or an equator-pole lap time of 157 days. The corresponding cross-correlation image using the secondary magnetic maps also produces a definite signature of differential rotation with $\Delta\Omega = 0.06$ rad d^{-1}, or a near solar-like equator-pole lap time of 105 days.

7.5 Image shear

Recent measurements of stellar differential rotation have been made using the sheared image technique, as developed by Donati et al. (2000). Instead of cross-correlating two entirely independent maps, as in the last section, a latitudinal dependant shear is applied within the imaging code to model the effect of differential rotation. As such each latitude strip has its own angular rotation rate given by:

$$\Omega(l) = \Omega_{eq} - \Delta\Omega\sin^2 l$$

, where Ω_{eq} is the equatorial rotation rate and l is the stellar latitude. This was implemented into the DoTS code by Barnes et al. (2001) to work for single stars. Here we implement this into the binary version of DoTS. This is achieved by first applying the latitudinal dependant shear to each vertex of our surface pixel grid for each star and then rotating the star in the co-ordinate frame of the binary orbit (see Chapter 5 for further details). This change was also made to our new ZDI code, ZDoTS, allowing us to obtain a separate measurement of the stellar differential rotation from the Stokes V spectra.

The image shear method has many advantages over that of the original cross-correlation technique that we outlined in the last section. It works in data space directly and can therefore produce formal uncertainties on the differential rotation parameters.

Figure 7.4: The results of the image shear technique for measuring differential rotation using the spot (Stokes I) signatures. Differential rotation rate between the equator and pole is plotted as a function of absolute equatorial rotation rate. The primary star is the upper plot and is found to have stronger differential rotation than the secondary star, which is the lower plot. Contours showing the one parameter 1-σ, 2.6-σ (99%) and 4-σ (99.99%) confidence intervals are superimposed over the $2\alpha S$ surface.

Many of the problems in fitting the differential rotation law to the peaks in the cross-correlation images also disappear. Furthermore, we do not require two complete and independent surface maps. Instead, all that is required is for at least one phase to be re-observed during a subsequent stellar rotation (preferably with both low and high latitude surface features). It is therefore possible to use quite incomplete datasets (poor phase coverage) and will even work for stars with pathological periods near to a multiple of a day. Also, the technique is less sensitive to non-uniform latitudinal spot coverage (a problem we encountered with the brightness images of the primary star in §7.4) as the shear is applied to the model rather than derived from the result.

The values of Ω_{eq} and $\Delta\Omega$ are found by running a grid of models which sample combinations of the two variables. We solve for each set of rotation parameters for each of the two stars separately, as there is no reason to suspect that they should be significantly correlated. When obtaining the stellar parameters (displayed in Table 6.1 from Chapter 6) we set the code to aim for a very small value of χ^2 (in reality this is unobtainable) and then record the actual χ^2 achieved after a fixed number of maximum entropy iterations. The best value is then found by interpolating the two dimensional grid of parameters and searching for the global χ^2 minimum. We use a slightly different approach when obtaining the differential rotation parameters.

The above technique does not take advantage of the image entropy information. The full relative posterior probability is $\exp(\alpha S - \frac{1}{2}\chi^2)$, where S is the entropy of the final image and α is the Lagrange multiplier. Therefore $2\alpha S$ has the same units as χ^2 and when χ^2 is fixed can be used for purposes of determining error regions for the fitted parameters (Ω_{eq},$\Delta\Omega$). So we choose an obtainable value of reduced χ^2 (e.g. χ^2=0.7 for the Stokes I data) and then record the value of $2\alpha S$ once the code has converged. This is subtly different to the former technique and the probability contours are found to be smoother than that produced when using the minimum χ^2. This is probably due to the fact that the recovered image becomes dominated by spurious noise when pushing the image to small χ^2 and so is more susceptible to local minima.

We apply the sheared image technique, as described above, to the entire 11 nights of observations (including the so far unused observations on March 30). In Fig. 7.4 we show the log posterior probability ($2\alpha S$) surface defined by the sets of differential rotation parameters for each star from the intensity (Stokes I spectra) along with probability con-
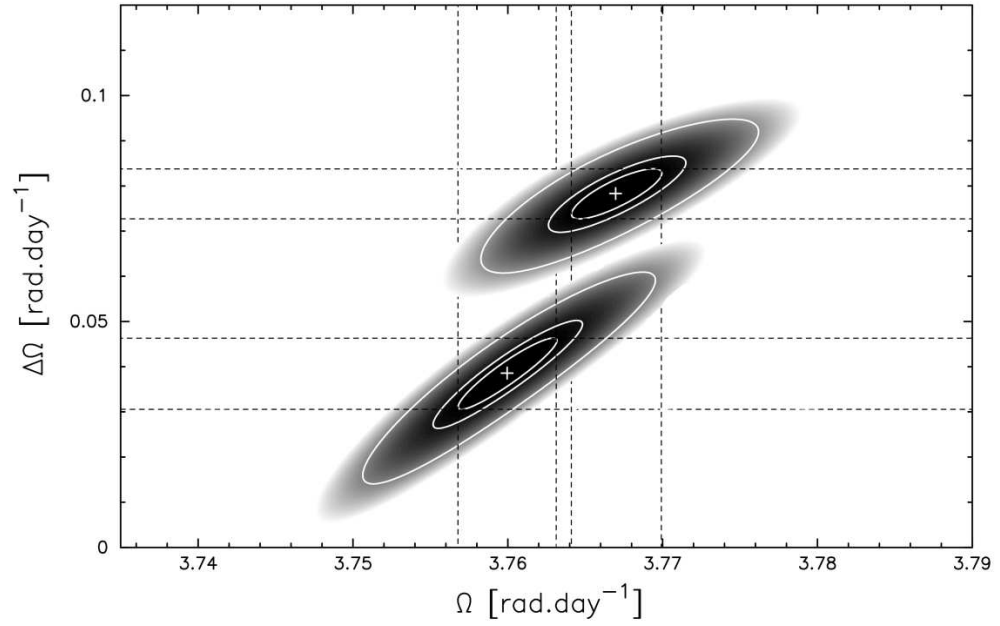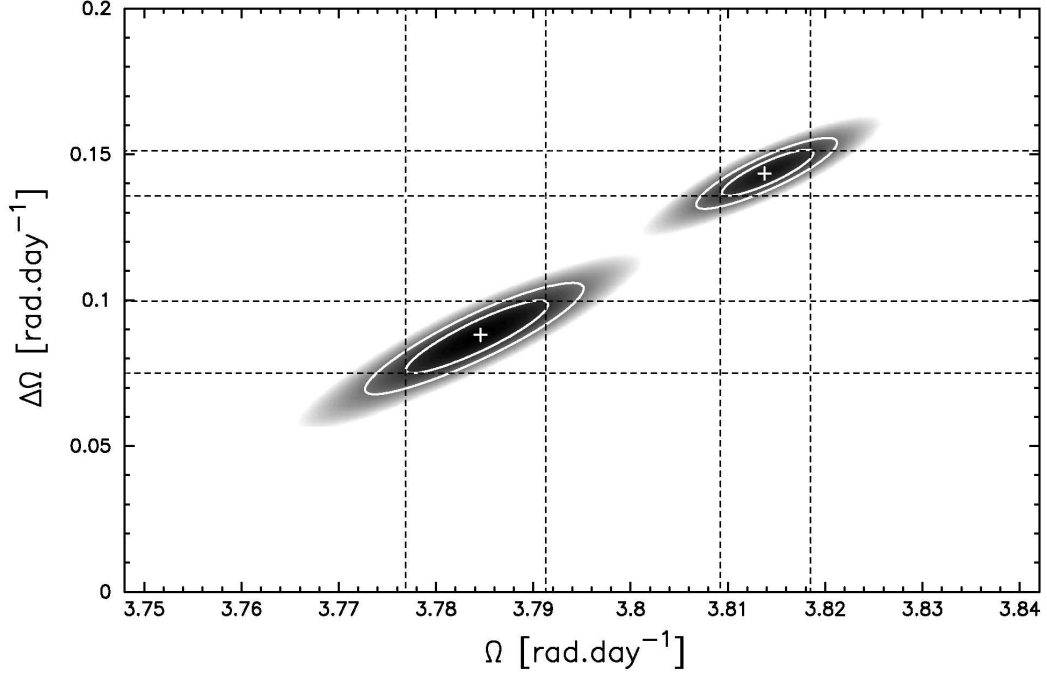
Figure 7.5: The results of the image shear technique for measuring differential rotation using the magnetic (Stokes V) signatures. Axes are as Fig. 7.4. Contours showing the one parameter 1-σ, 2.6-σ (99%) confidence intervals are superimposed over the $2\alpha S$ surface. The primary star is again found to have stronger differential rotation and is therefore the upper plot.

tours. As the two stars have different strengths of differential rotation it has been possible to display both stars on the same plot. Similarly in Fig. 7.5 we produce the same diagram but using the magnetic (Stokes V) spectra. The numerical results for the strength of the differential rotation ($\Delta\Omega$) and the equatorial rotation rate (Ω_{eq}) are tabulated in Table 7.1 along with the results from fitting the cross-correlation functions in §7.4. The tilted ellipses of Figs. 7.4 & 7.5 show that the parameters $\Delta\Omega$ and Ω_{eq} are correlated. This is to be expected due to the fact that the shear rate is most tightly constrained by mid-latitude features to which the Doppler imaging process is inherently most sensitive.

The differential rotation result from the secondary star's intensity spectra of $\Delta\Omega = 0.0386 \pm 0.0061$ rad d^{-1} is very similar (consistent within the quoted uncertainty) to that produced from the cross-correlation technique of $\Delta\Omega = 0.04$ rad d^{-1}. This could have

Table 7.1: Surface rotation parameters for both components of HD 155555. Column 2, labelled 'CCF', are the measurements from cross-correlating the independent maps produced from the two epochs in §7.4. All other columns refer to measurements and associated uncertainties of the differential rotation strength (dΩ), the corresponding equator-pole lap time ('Lap'), equatorial rotation rate ($\Omega_{\rm eq}$) and latitude of synchronous rotation (θ_s) produced from the sheared image technique in §7.5.

	CCF	Image shear			
	dΩ	dΩ	Lap	$\Omega_{\rm eq}$	θ_s
	(rad d^{-1})	(rad d^{-1})	d	(rad d^{-1})	(°)
Brightness Images:					
Primary	-	0.078 ± 0.006	80.2	3.767 ± 0.003	38.8
Secondary	0.040	0.039 ± 0.006	163	3.760 ± 0.003	51.7
Magnetic Images:					
Primary	0.104	0.143 ± 0.008	43.8	3.814 ± 0.005	47.3
Secondary	0.060	0.088 ± 0.012	71.3	3.785 ± 0.007	47.8

been predicted given that the sin^2 law fit to the cross-correlation function of the secondary star's spot features, in the top-right panel of Fig. 7.3, was by far the most acceptable. The magnetic (Stokes V) spectra produce strengths of differential rotation consistently 30 % stronger than was found from the cross-correlation technique for both the primary and secondary components.

We summarise the results of our analysis in Fig. 7.6, which combines all four of the differential rotation measurements from the sheared image technique. The primary star clearly has a stronger surface differential rotation rate from both the spot and magnetic features. Also the results obtained from the Stokes V spectra from both stars reveal that the differential rotation is approximately twice as strong when using the magnetic regions rather than the spots.

Fig. 7.6 also shows that the equators of both stars rotate considerably faster than the binary orbital rate (shown as the vertical dashed line in Fig. 7.6). This then raises the question of whether any stellar latitude is synchronously rotating with the orbit. In order to show this graphically we plot in Fig. 7.7 the differential rotation curves obtained for
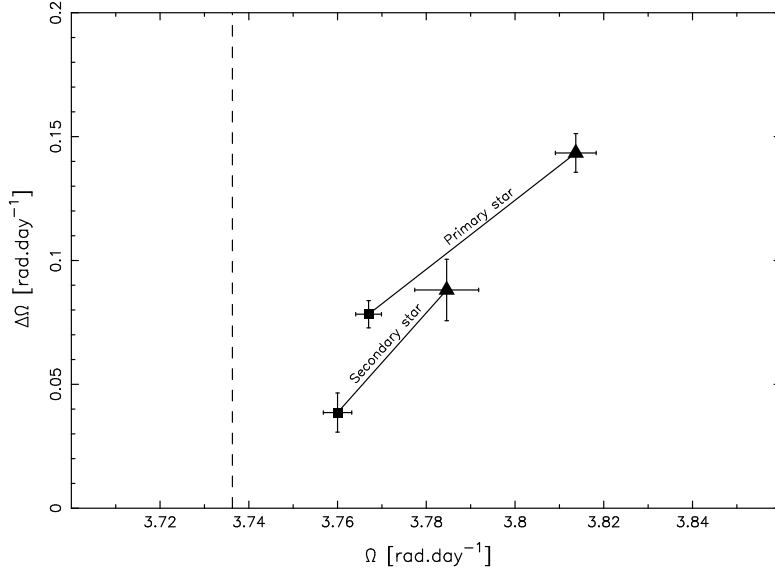
Figure 7.6: All four differential rotation measurements are plotted with 1-σ uncertainties. Axes are as for Figs. 7.4 and 7.5. The two squares are the measurements of differential rotation using spots and the two triangles are from magnetic features. Labelled lines join together measurements on each of the primary and secondary stars. The vertical dashed line shows the rotation rate corresponding to the binary orbital period.

the two stars, for both the spots and magnetic signatures. We clearly find that the poles are rotating sub-synchronously while the equators rotate super-synchronously in all cases. The exact synchronously rotating latitude for each differential rotation measurement is given in Table 7.1.

Curiously the primary and secondary stars share the same synchronously rotating latitude (47°) for the magnetic differential rotation. The resulting synchronously rotating latitude for the primary star's spot distribution is 39° and is thus the lowest of all four measurements. This may be interesting given that this latitude marks the upper boundary of the lower latitude band of spots seen on the primary star.

7.6   Discussion

We have found that both components of HD 155555 have non-negligible surface differential rotation. This result was obtained using both the cross-correlation and the image shear techniques. There are two reasons why the cross-correlation technique (§7.4) should
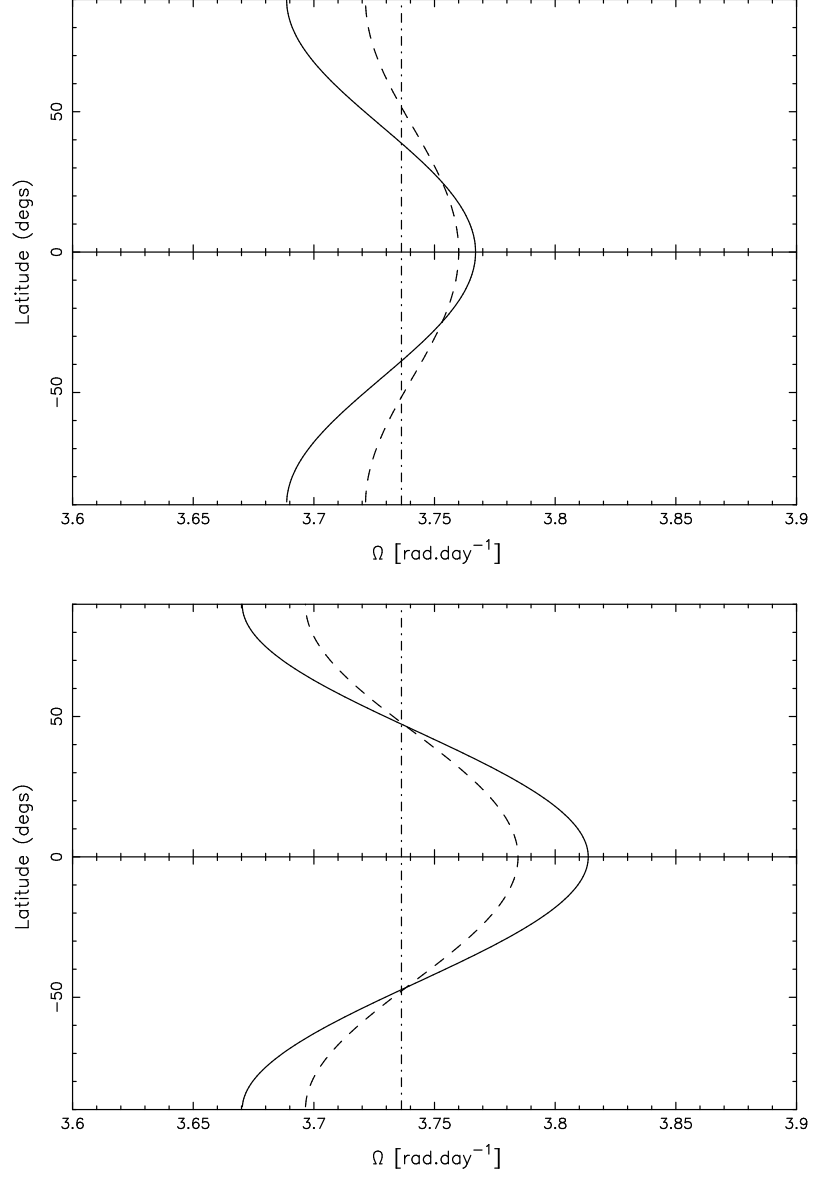
Figure 7.7: The differential rotation curves are plotted from the spots (top) and magnetic regions (bottom). The solid line is the primary star and the dashed line is the secondary star. The dot-dash vertical line corresponds to the orbital rotation period and thus shows that both stars are synchronously rotating with the binary orbit.

probably be carried out whenever sufficient data of a star are available. Firstly, it provides a very literal interpretation of the data and so was useful in validating our implementation of the image shear technique to binary systems. Secondly, the cross-correlation technique does not assume *a priori* knowledge for the form of the differential rotation law which the image shear technique does. Beyond this however, the image shear technique is superior and has many advantages which were outlined in §7.5 and will be touched on again in §7.6.4. We note that the direct spot tracking technique of Collier Cameron et al. (2002) is another alternative which makes few assumptions but requires very good phase coverage and high signal-to-noise data.

7.6.1 Internal velocity fields

To summarise the results of §7.5; the primary star has stronger differential rotation than the secondary star and the magnetic regions produce stronger signatures than do the spots. The latter trend was first revealed by Donati et al. (2003) for AB Dor and HR 1099. The authors suggested that the spots and magnetic regions are anchored at different depths in the convection zones of these stars. The fact that the strength of the shear is so much greater in the magnetic regions suggests that the dynamos of these stars may not be active just at the interface layer between the radiative core and the convective envelope but instead are distributed throughout the convection zone. Recent numerical simulations by Brown et al. (2007) lend support to this idea by showing that global-scale toroidal and poloidal fields can be generated and maintained in the convection zones of rapidly rotating stars.

Donati et al. (2003) attempted to quantify the nature of the internal velocity fields in the rapidly rotating single stars AB Dor and LQ Hya by examining the temporal fluctuations in the differential rotation parameters (Ω_{eq},$\Delta\Omega$). They found that:

$$\Omega_{eq} = \lambda\Delta\Omega + \Omega_{sb}, \tag{7.1}$$

where λ depends on the assumed internal rotation model and on the internal stellar structure and Ω_{sb} is a constant, equal to the rotation rate the stellar convection zone would have if spinning as a solid body.

For HD 155555 we only have a single epoch of differential rotation measurements. However, given the binary nature of the system, we do have a very useful zero-point. We

know that in the absence of differential rotation, the rotation rate of each star would be equal to that of the orbital rotation rate. Therefore we can measure λ directly from Fig. 7.6. On this plot the gradient of the lines joining the zero point (where $\Omega_{eq} = \Omega_{sb}$ and $\Delta\Omega = 0$) with each of our differential rotation measurements will be equal to λ^{-1}. We obtain gradients in the range 1.6 to 2.5. Donati et al. (2003) considered two possible models for the angular velocity fields. Firstly, that angular rotation is constant with radius (like it is for the Sun), then our gradient (λ^{-1}) should be equal to five. Secondly that angular velocity was constant along cylinders symmetric to the rotation axis, resulting in a gradient of approximately two (for stars such as AB Dor and the components of HD 155555). Therefore, like AB Dor, our results show that a model of internal rotation being constant along cylinders is most appropriate for the components of HD 155555. Given their relatively rapid rotation this is what one would have expected.

By adopting this model of internal rotation, we can follow the example of Donati et al. (2003) and calculate the range of possible latitudinal shears. At a given latitude the rotation rate will depend upon how deep the tracers of differential rotation are anchored in the stellar convection zone. The total depth of the convection zone of each star can be expressed as the fractional radius at the base of the convection zone, r_c/R (where a star with $r_c/R=0$ is fully convective and a star with $r_c/R=1$ has no convection zone). Then the maximum expected ratio between the shears we measure from the Stokes V and I data should be $1/(r_c/R)^2$. So if the observed value were to equal this maximum ratio then this would suggest that the magnetic regions are anchored near to the stellar surface, while the spot features were anchored near the base of the convection zone. The value of r_c/R can be obtained using the evolutionary models of Siess et al. (2000). The components of HD 155555 have $r_c/R = 0.68$ for the primary and $r_c/R = 0.63$ for the secondary star. This corresponds to a maximum ratio of 2.16 for the primary star and 2.52 for the secondary star. Using our results for HD 155555, we find that the observed ratio between the shears from Stokes V and I is 1.8 for the primary star and 2.25 for the secondary star. We therefore find that HD 155555 is consistent with the adopted model of internal rotation.

7.6.2 Comparison with other systems

It is now possible to compare our results with those of both single rapidly rotating stars and binary systems. In the left panel of Fig. 7.8 we plot differential rotation rate versus
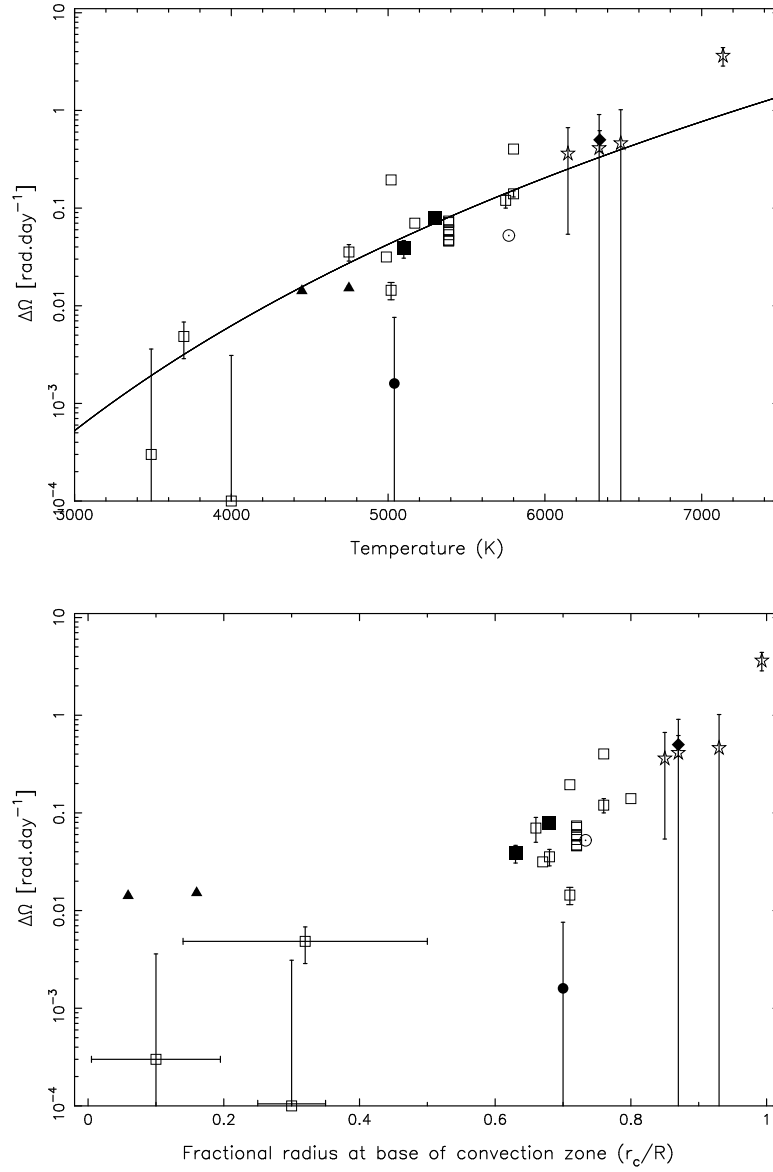
Figure 7.8: Top: Differential rotation is plotted as a function of stellar temperature. The solid line shows the power law fit of Cameron (2008). Bottom: The x-axis now plots the fractional radius at the base of the convection zone (r_c/R) as estimated from stellar evolutionary models (see text). Both plots include the same stars; filled symbols are members of binary systems, open symbols are single stars. The two triangles are the evolved RS CVn systems HR 1099 and IM Peg. The filled circle is the pre-cataclysmic system V471 Tau. Open squares are single G, K and M dwarfs, the 'star' symbols are F stars and the circled dot represents the Sun. The two large filled squares are the components of HD 155555. Error bars are plotted when the uncertainty significantly exceeds the symbol size.

effective temperature. A similar plot was first produced for single G, K and M dwarfs by Barnes (2005) (reproduced in Chapter 1 as Fig. 1.8). The authors discovered that for single stars the strength of differential rotation increases with increasing stellar surface temperature. More recently, Reiners (2006) combined these results with differential rotation measurements on F dwarfs derived from a Fourier analysis of the rotational broadening profile. An extrapolation of the Barnes (2005) power-law fit showed that the two techniques were in good agreement. The latest version of this diagram was made by Cameron (2008) who performed a re-analysis of the power law fit using all latest available differential rotation measurements. This is plotted as the solid line on Fig. 7.8. When we plot the differential rotation parameters for both components of HD 155555 we find that they effectively straddle this line. It therefore appears that the strength of differential rotation on both stars is consistent with single stars of the same temperature.

In addition to the single stars results collated by Barnes et al. (2005) and Cameron (2008), we also consider the results from previous Doppler imaging studies of binary star systems. Fig. 7.8 plots (as solid triangles) the differential rotation measurements of the evolved primary stars of the RS CVn binaries HR 1099 and IM Peg (from Petit et al. 2004 and Marsden et al. 2007 respectively). The main-sequence component of the pre-cataclysmic variable star V471 Tau (Hussain et al. 2006) is also plotted as a filled circle on Fig. 7.8. All three systems show weak differential rotation ($\Delta\Omega < 0.02$ rad d^{-1}). We note, however, that there is only a single epoch measurement for V471 Tau and this is consistent with zero ($\Delta\Omega = 0.0016 \pm 0.006$ rad d^{-1}) differential rotation. The recovered Doppler images suffer from a lack of spot coverage at all latitudes, which may make them unreliable. We therefore encourage future observations to confirm this measurement, but we do not consider V471 Tau further here.

7.6.3 Tidal forces or internal structure?

The RS CVn systems HR1099 and IM Peg have been repeatedly observed, so many measurements of differential rotation are available. When compared to single main-sequence stars of similar mass, HR 1099 and IM Peg have greatly reduced differential rotation. For example, HR 1099 has a mass of 1 $M_\odot$ and yet exhibits a differential rotation rate approximately a third that of the Sun (or approximately an eighth that of the power-law fit shown on Fig. 7.8). Petit et al. (2004) suggested that the reduced differential rotation

was due to binary tidal forces. Over time these have acted to enforce synchronous rotation at all latitudes (i.e. to inhibit differential rotation). The relatively strong differential rotation that we find on both components of the young HD 155555 system adds further complexity to the argument. We have shown that the mere fact that a star is a member of a close binary system does not necessarily result in a reduced differential rotation rate. We are therefore left with two possibilities; that the timescale for tidal forces to suppress the differential rotation is long compared to the age of the HD 155555 system, or that binarity is unimportant and evolutionary state is the dominant factor. We now examine the first of these possibilities.

Our results for the young (18 Myr, Strassmeier & Rice 2000) HD 155555 system show that tidal forces have indeed enforced synchronous rotation of both components, as shown in Fig. 7.7. However, they have been unable to suppress the differential rotation, i.e. tides have not yet been able to synchronise rotation at all latitudes of the convective zone. Both components of HD 155555 are still contracting on to the main sequence. One may naively think that this would result in the stars rapidly spinning up and so might explain why the tidal forces are unable to effectively inhibit differential rotation. Given that HD 155555 is a close binary system we should examine the efficiency of tidal forces. The synchronisation timescale (t_{sync}) can be approximated as $t_{sync} \simeq q^{-2}(a/R)^6$ (Zahn 1977), where q is the mass ratio. Using the parameters for HD 155555, we find a timescale of order $t_{sync} \simeq 10^4$ yrs for both components. Given that this is very much shorter than evolutionary timescales, it appears that tidal forces have ample opportunity to suppress differential rotation. Indeed, as the stars try to spin up, they will rapidly become resynchronised, with angular momentum being transferred from the stars' rotation to the binary orbit. The net result is that the stars will spin down rather than up. The fact that differential rotation is apparently uninhibited on the components of HD 155555 then places doubt on this mechanism also being responsible for the low differential rotation observed on the evolved HR 1099 and IM Peg systems. We futher note that theoretical work (Scharlemann 1982) predicts that tides should not inhibit differential rotation on RS CVn systems.

If binarity is unimportant then the strength of differential rotation is governed primarily by the star's evolutionary stage. HR 1099 and IM Peg are both evolved giants and so have large radii (3.7 and 13.3 $R_{\odot}$, respectively) and correspondingly cool surface temperatures. Therefore when we plot HR 1099 and IM Peg on the left panel of Fig.

7.8 (solid triangles) we find that they show strengths of differential rotation very close to (possibly slightly below but within the scatter) that of a main-sequence single star with a similar surface temperature. This would seem to be a major clue as to the source of the low differential rotation. If tidal forces were solely responsible then there would be no reason to expect such an agreement with single stars. These giant stars have deep convection zones, like those of the cool K and M dwarfs, and therefore their internal structure may determine their differential rotation rates. In an attempt to quantify this we use the evolutionary models of Siess et al. (2000) which quote the fractional radius at the base of the convection (r_c/R). This constant was discussed earlier in §7.6.1.

The evolutionary models are used to estimate the value of r_c/R for all stars that were plotted on the temperature plot of Fig. 7.8. We then plot differential rotation as a function of r_c/R in the bottom panel of Fig. 7.8. Where the models of Siess et al. (2000) did not follow the stellar evolution far enough, the models of Claret (2004) were used. The models are spaced in 0.1 $M_\odot$ intervals and so we use the nearest one appropriate to each stars mass which is obtained from the literature. We only use F-stars from Reiners (2006) that were defined as cluster members so that the cluster age could be used as a constraint to determine the star's position in the evolutionary models. The single M dwarfs are particularly difficult to obtain values for r_c/R. This is because their evolutionary timescales are longer and so the depth of the convection zone continues to change for a longer time. Therefore we show approximate ranges for the value of r_c/R where appropriate.

In Fig. 7.8 we cover the entire range of convection zone depths. A strong trend of increasing differential rotation strength with decreasing convection zone depth is found. This is very similar to the surface temperature plot, which is not surprising as for main-sequence objects temperature essentially defines the depth of the convection zone. The position of the components of HD 155555 therefore match well with the other single main-sequence stars. The RS CVn binaries HR 1099 and IM Peg move over to the left of the plot with values of $r_c/R = 0.16$ and $r_c/R = 0.059$ respectively. This illustrates their huge convection zone depths. At a specific temperature the convective depth is larger for an evolved star than for a main-sequence star. This would certainly seem to explain the observed weak differential rotation. In fact HR 1099 and IM Peg have stronger differential rotation than would be expected for main sequence stars of similar fractional convection zone depth.

We note that, for consistency, we have only considered the differential rotation results from stellar brightness maps (Doppler imaging). As found in §7.5 the shear strength is often higher for magnetic regions than for star spots. Previous studies have shown that it is often easier to measure differential rotation using magnetic maps because there is normally structure present at all stellar latitudes. It would therefore be interesting to extend the scope of this analysis and consider results from ZDI also. For example, Morin et al. (2008) found very weak differential rotation ($\Delta\Omega = 0.0063 \pm 0.0004$) on the fully convective M4 dwarf V374 Peg. In another recent study, Donati (2008) found that the planetary host star τ Boo has very strong differential rotation ($\Delta\Omega = 0.50 \pm 0.12$). This measurement is plotted on Fig. 7.8 (solid diamond) and has a position appropriate for its F7V spectral type. This is despite the fact that the stellar surface has apparently been forced to rotate synchronously with the planetary orbital period (Catala et al. 2007). So τ Boo lends further support to the argument that tidal forces are unable to suppress differential rotation.

7.6.4   Final maps

The differential rotational parameters for both stars can now be incorporated into the imaging process. We use the entire 11 night (106 spectra) dataset with the respective differential rotation parameters for spots and magnetic features on each star to produce the brightness and radial magnetic maps shown in Figs. 7.9 and 7.10. We note that the χ^2 achieved for these reconstructed images (χ^2=0.7 for Stokes I and χ^2=1.0 for Stokes V) are essentially the same as the χ^2 for the individual images presented in §7.3. This would indicate that there has been little evolution in the spots or magnetic regions (other than the effect of differential rotation) over the eleven days. In order to show the effect of the differential rotation we also plot the primary radial field map obtained if we do not apply the differential rotation law (top panel of Fig. 7.10). By including the effect of differential rotation the middle panel of Fig. 7.10 shows a higher level of detail. This is especially true at low latitudes where the effects of differential rotation are most noticeable.

Looking back to Fig. 7.2, which shows magnetic maps produced from each five night subset of the data, we find that they contain more low latitude information than the top panel of Fig. 7.10 (no differential rotation) but less than the middle panel Fig. 7.10 (with differential rotation). This is what we would expect, because the effect of differential
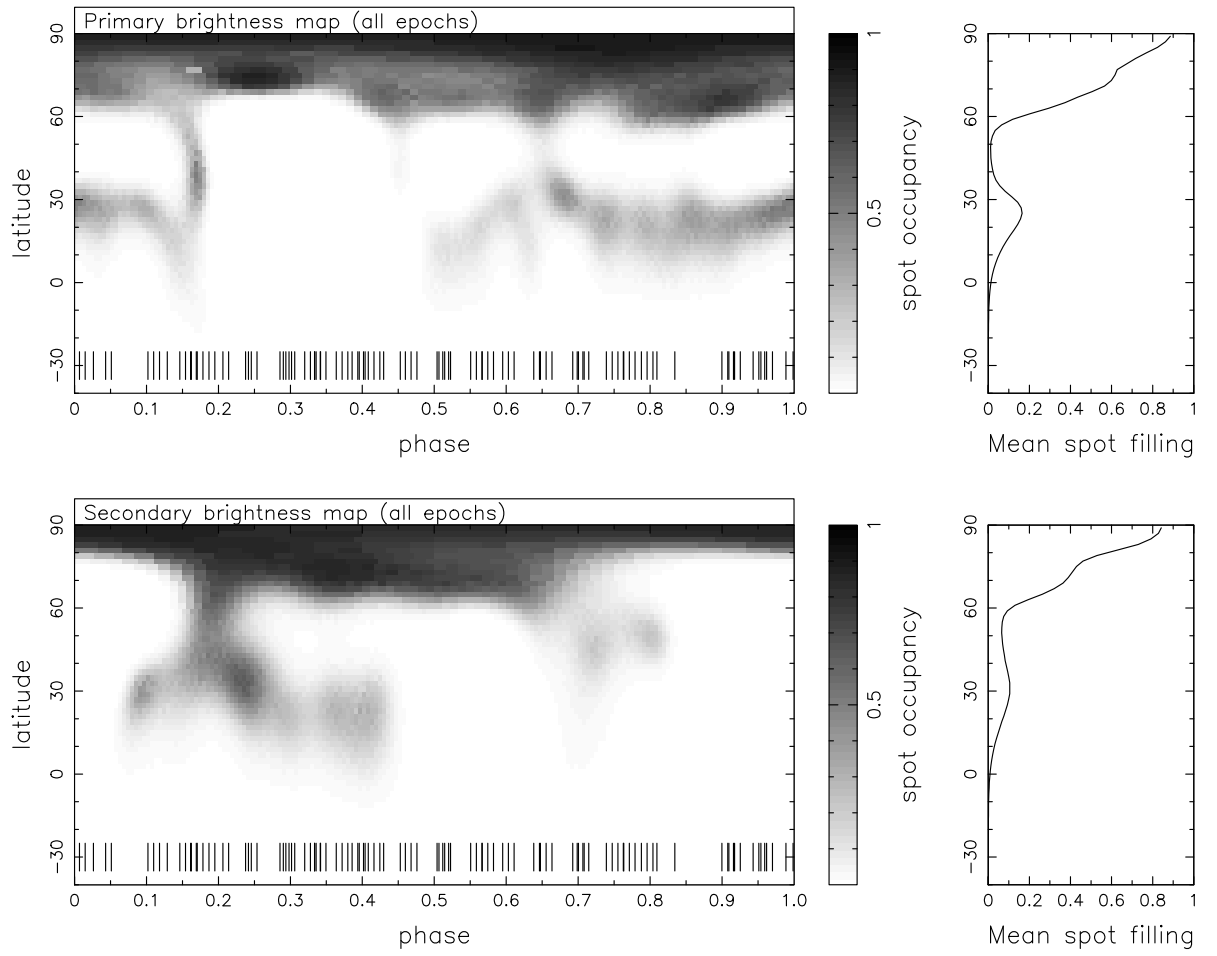
Figure 7.9: Final brightness maps of the primary and secondary stars produced from all eleven nights and using the obtained values of differential rotation.
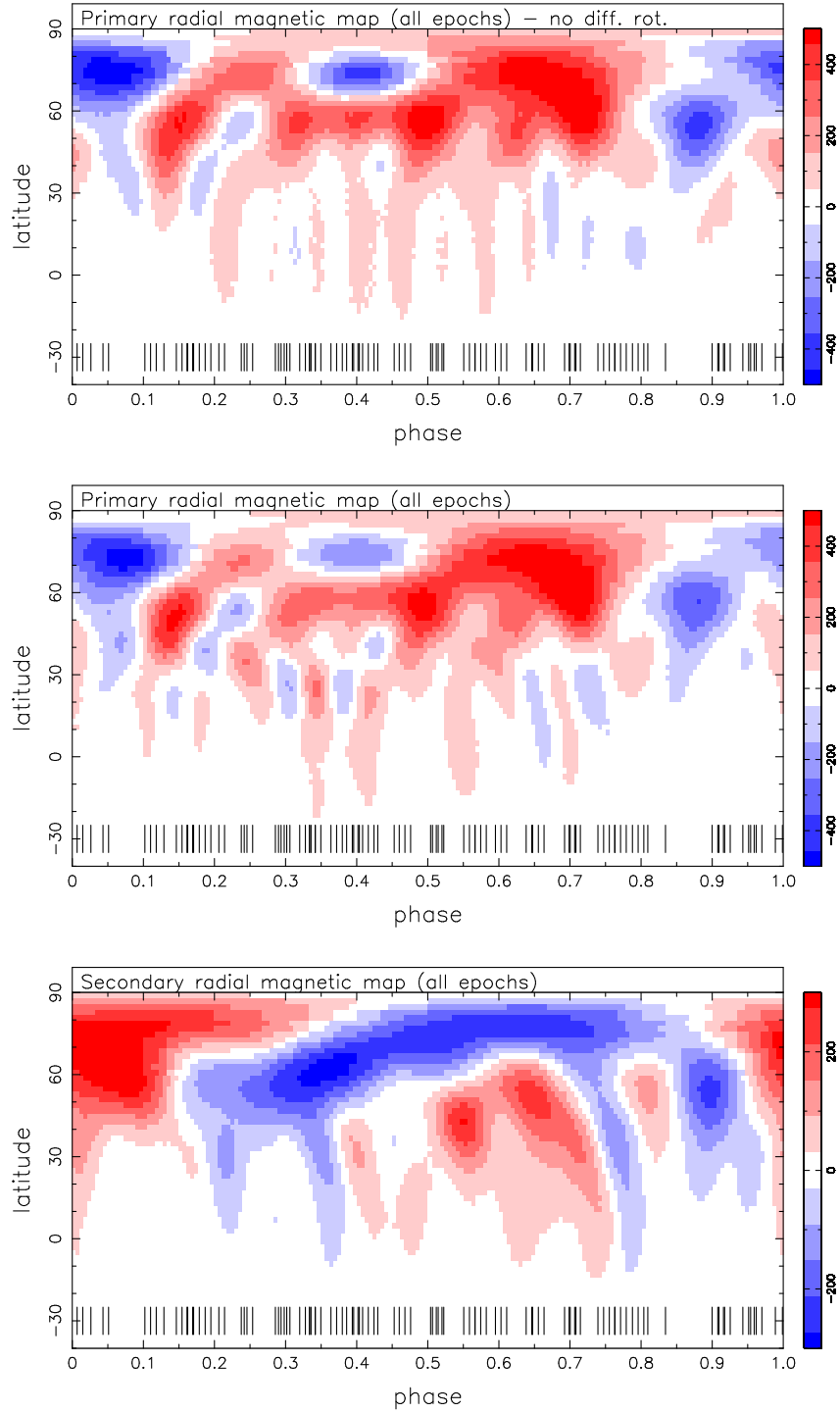
Figure 7.10: Final radial field magnetic maps. The top panel shows the primary radial field map obtained from all eleven nights of observations but without incorporating the measured differential rotation into the imaging process. This should then be compared with the middle panel where the differential rotation was included; note the higher level of detail at low latitudes. The bottom panel shows the radial field map for the secondary star when using the differential rotation parameters.

rotation on only five nights is less than over eleven. Following the same argument we can now explain why the cross-correlation functions (shown in Fig. 7.3) of the magnetic maps gave poor fits at low latitudes. Due to the relatively strong differential rotation, even five nights is sufficient to smear the equator of the primary star by $\Delta\phi = 0.11$ and that of the secondary by $\Delta\phi = 0.07$. Given that these are both larger than a whole resolution element (approximately $\Delta\phi = 0.06$) it is unsurprising that the cross-correlation function fails to follow the $\sin^2$ law at low latitudes. This once again illustrates the advantage of using the sheared image technique.

Despite the improvement in the reconstruction of low latitude features, the maps presented in Fig. 7.10 do not change the conclusions of Chapter 6. It may be interesting to note however, that the small regions of flux, now well reconstructed between phases $\phi = 0.3 - 0.5$ and latitudes 20 and 30°, are in the same location as the gap in the ring of spots seen for primary star in Fig. 7.9. This apparent anti-correlation between the strengths of small magnetic regions and spot features may be an example of how the cooler spot temperatures suppress the contribution to the Stokes V spectra.

7.6.5   Consequences for connecting field lines

In Chapter 6 we discussed the likelihood of field lines from one star connecting with the other. It was found from extrapolating the coronal field of each star separately (using the radial field maps) that the field complexity of the surface radial maps persists out to a significant fraction of the binary separation (7.5 $R_\odot$ or $\simeq$ 5.5 R$_*$, see Table 6.1) and so the interaction between the two fields is also likely to be complex. Now that we know the strength of the differential rotation on both stars, it is possible to speculate on the upper limit of the lifetimes of such binary field lines and so the energy released from the rate of re-connection of the field. Let us consider a field line that is connected from a point on the equator of the facing hemisphere of one star to another on the equator of the facing hemisphere of the other star, a situation sketched in Fig. 7.11. Given that the two stars will be rotating in the same direction, but 180° out of phase, the two equatorial points will start to move away from each other due to differential rotation. The point on the primary star will sweep out a greater angle in the same time due to the stronger differential rotation (as shown in Fig. 7.11).

An interesting timescale often quoted for single stars is the equator-pole laptime.
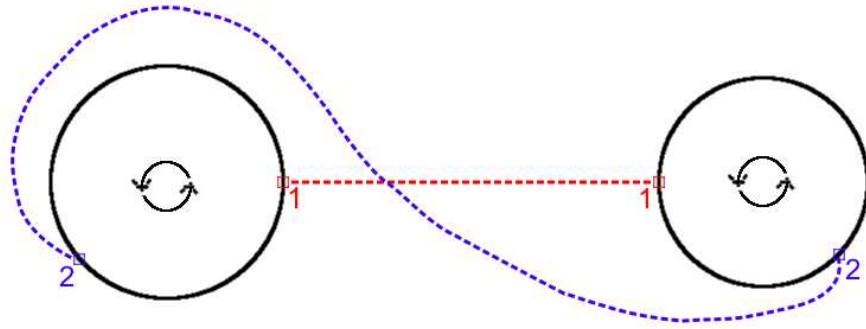
Figure 7.11: A cartoon sketch to show the effect of differential rotation on connecting field lines. The two components (primary - left, secondary - right) of HD 155555 and their separation are plotted to scale. A field line connects the equators of both stars. Initially at '1' the field footpoints are directly facing each other. At '2' we show the location of the footpoints 50 days later when the combined angle swept out by the two footprints is 2π radians.

On this timescale a field line that connects the pole to the equator will have become wound around the star by a full circle (2π rads) and so stores significant magnetic energy. Similarly we can also ask; how long would it take the field points of our connecting field line to sweep out a combined angle of 2π rads? The answer is 50 days (illustrated in Fig. 7.11), which we note is comparable to the equator-pole lap-times of the primary star (44 days) and the secondary star (71 days). Just like the equator-pole laptimes on a single star, the equator-equator field lines connecting the two stars gives us the maximum amount of stress on the field lines. We also note however that in the absence of any force confining such field lines to the equatorial plane the connecting loop will "balloon" up and over the stellar poles above a critical angle (Lynden-Bell & Boily 1994). This would further increase the rate of field reconnection events.

The strong differential rotation provides extra stress on the field that would not be present on evolved binaries such as HR 1099 and IM Peg with their weak differential rotation. We can therefore speculate that the reconnection of these long binary field loops could significantly contribute to the X-ray luminosity of the HD 155555 system and also to the frequency of large flares (see also Ferreira 1998 for a theoretical discussion). The scenario outlined above caused by differential rotation is analogous to the mechanism

thought to produce the so called 'superflares' on classical T Tauri stars. In this case field lines that connect the star with its surrounding disk become stretched due to the fact that the disk is rotating slower than the star (e.g. Montmerle et al. 2000, Fig. 2).

7.7   Conclusions

We have measured the surface rotation properties of both stars in the HD 155555 system. A cross-correlation of the latitude strips of both brightness and magnetic images, produced from two independent datasets, revealed the characteristic signature of differential rotation and confirmed that this can be modelled by a simple solar-like $\sin^2 l$ law. In order to better quantify the strengths of the differential rotation we adapted the sheared-image technique to binary systems. Both stars are found to be synchronously rotating with the binary orbital period, confirming the fact that the system is tidally locked.

Considering only the results from the brightness maps of the surface spot distributions, the primary has an equator-pole lap time of 80 d and the secondary star 162 d. These results show that the strength of differential rotation on both stars is not only non-negligible but of similar magnitude to that found on single, rapidly-rotating stars of the same effective temperature. We used these findings to explore the relative effects of binarity and evolutionary stage on the strength of differential rotation. The large convection-zone depths of the evolved giants in RS CVn systems is more likely to be the cause of their low differential rotation rates than the effects of tidal forces.

Future measurements of differential rotation on the components of HD 155555 are strongly encouraged. It would be very interesting to examine whether temporal changes in the differential rotation rate of the components of HD 155555 are correlated. This may indicate evidence of a joint activity cycle.

CHAPTER 8

Conclusions and future work

The Sun seen setting over Holywell Bay, Cornwall

8.1   Summary of the major findings

The first part of this thesis examined the stellar prominence systems of the young K dwarfs Speedy Mic and AB Dor. We studied the physical properties and locations of prominences around Speedy Mic and compared our findings to other rapidly rotating stars and the Sun. For AB Dor we took preliminary steps towards an understanding of how prominences interact with coronal X-rays and also presented what appears to be the first observation of an erupting stellar prominence.

The second part of the thesis was concerned with the more direct study of stellar magnetic fields using Zeeman Doppler imaging. A binary ZDI code was developed and applied to observations of the pre-main sequence binary system HD 155555. We examined the field topologies of both stars and compared them to those found on other cool stars. Longer term changes in the magnetic field of both stars were examined using a set of observations taken over two years earlier. Finally, we measured the differential rotation of both stars over eleven nights and compared our results to those reported on evolved binary systems and young stars. While the main findings of this thesis were summarised at the end of each chapter, they are also detailed below:

1. The rapidly rotating young dwarf Speedy Mic is found to have a very densely packed prominence system. On average approximately ten prominences are seen as absorption features crossing the rotationally broadened H_α profile per stellar rotation. This level of prominence activity surpasses even that observed on AB Dor.

2. From measuring the heights of the prominences we found that they cluster at twice the height of the co-rotation radius above the stellar surface. This observation implies that prominences on Speedy Mic must be supported by large closed magnetic loops in order to enforce the observed co-rotation and so lends further support to the analogy with solar prominences. This appears to be in conflict with X-ray observations of rapidly rotating stars which indicate that the extent of the corona is confined relatively close to the stellar surface. We note a possible solution to this problem in the formation of closed loops through the connection of open field lines above helmet streamers (as suggested by Jardine & van Ballegooijen 2005).

3. Using exceptionally high signal-to-noise UVES VLT data we show that prominences on Speedy Mic can be detected in all lines of the Balmer series down to at least H_{10}. Furthermore, we show that prominences are clearly present in the CaII H & K lines and are in fact responsible for the rapid changes in these lines observed by Wolter & Schmitt (2005). Using the hydrogen and singly-ionised calcium lines we measure column densities and hence estimate masses for Speedy Mic's prominences. We find that the prominences are rather optically thick ($\tau \simeq 20$) in the H_α line and have masses in the range $0.5 - 2.3 \times 10^{14}$ kg, slightly larger than the masses of giant solar prominences.

4. Further analysis of these data also reveals weak emission from the H_α line outside the stellar rotational profile. From H_α timeseries spectra we show that these trace

sinusoidal loops that coincide with the path of at least one prominence which is observed to transit the stellar disc. This is the first time that a prominence has been seen in both emission and absorption on another star, just as we see prominences and filaments on our Sun. By fitting the width of the emission peak we show that stellar prominences can have a thickness (radial extent) of approximately 2 R_*.

5. The absorption of coronal X-rays by prominence material is investigated on AB Dor. Using the measured column densities of stellar prominences significant absorption (5 - 75 %) could occur if a prominence occulted an EUV-emitting coronal region. We show tentative evidence for a very sharp drop in flux at the phase when a low lying high-latitude prominence crosses the stellar meridian. However, many further observations of such events are required before any firm conclusions can be made.

6. We also present a very unusual event that occurred while a large AB Dor promi-nence was transiting the stellar disc on the 2004 December 31. The prominence suddenly appeared to move to increasingly negative velocities in both the H_α and H_β lines. A maxi-mum velocity in excess of -350 km s^{-1} was observed. This was accompanied by red-shifted absorption at velocities of approximately +250 km s^{-1}. The most likely explanation is that this is the first observation of an erupting stellar prominence. While further analysis of this event is required, it appears to lend additional support to the analogy between stellar prominences and their solar namesakes.

7. The technique of Zeeman Doppler imaging is adapted to model binary star systems. This is found to be relatively important when observing binaries where the com-ponents exhibit similar amplitude Stokes V signatures. Simulations are performed showing that only observing non-conjunction binary phases can lead to a reduction in the overall recovered flux and also to distortion of the maps. Modelling both stars simultaneously enables us to recover maps that are essentially the same as those for single stars, at least for well sampled data.

8. Magnetic maps of both stars in the pre-main sequence binary system HD 155555 are presented. The radial magnetic maps of both stars show a complex magnetic topology with mixed polarities at all latitudes. We also see rings of azimuthal field on both stars, most of which are non-axisymmetric with the stellar rotation axis. By comparing the field strengths and which field component stores the most magnetic energy, we observe changes between our 2004 and 2007 epochs. We find a marked weakening of the field strength of

the secondary star between the 2004 and 2007 epochs. This is accompanied by an apparent shift in the location of magnetic energy from the azimuthal to radial field. We suggest that this could be indicative of a magnetic activity cycle.

9. The image shear method for measuring differential rotation was adapted to the binary case. Differential rotation rate was measured for each component of HD 155555 and compared to the results obtained using a cross-correlation of independent image maps. Both stars are found to have a non-negligible rate of differential rotation. The strengths of differential rotation observed are appropriate for their surface temperatures as they are found to fit well with the results of differential rotation rates on single rapid rotators (Barnes 2005). This leads us to suggest that the observation of weak differential rotation previously observed on the evolved primary stars of RS CVn binaries HR 1099 and IM Peg is a consequence of their large convection zone depths and not the result of binary tidal forces.

10. Using the recovered radial field maps, we extrapolate the coronal field for each star individually - at present ignoring any possible interaction. The secondary star is found to exhibit an extreme tilt ($\simeq 75°$) of its large scale magnetic field relative to its rotation axis for both the 2004 and 2007 epochs. The field complexity that is apparent in the surface maps persists out to a significant fraction of the binary separation. Any interaction between the fields of the two stars is therefore also likely to be complex. We note that a full binary field extrapolation is required to model this. Given that we have measured the differential rotation rate of both stars in the system we can take a first look at what effect this could have on connecting binary field lines. We find that binary field lines that connect the equators of the two stars would experience approximately the same amount of shear as equator-pole connecting field lines on either individual star. This may increase the rate of magnetic reconnection leading to more X-ray flaring events.

8.2   Future work

There are number of possible avenues for future research. I discuss below some of the direct extensions of the work presented in this thesis in addition to more general comments on future directions in the field.

8.2.1 Stellar prominences

Research on stellar prominences often appears to be an after thought of the Doppler imaging process. This is unfortunate because these co-rotating clouds remain one of the only direct tracers of the extent of the closed stellar magnetic field. Future observations (and analysis) are therefore encouraged, particularly those that cover many lines of the Balmer series and the CaII lines. A detailed, and consistent, study of all the prominences observed over the last twenty years of AB Dor observations would also be an interesting project. This would be analogous to recent efforts by Jeffers et al. (2007) to re-analyse all the Doppler images of AB Dor using the latest data reduction and Doppler imaging software. It might be possible to identify year-by-year changes in the numbers, heights and phases where prominences are observed. This may provide clues as to how the large-scale magnetic field is changing with time.

Only a preliminary analysis of the AB Dor prominence eruption event, described in §4.3, has so far been carried out. This very fortunate and unique observation requires more detailed study. In particular it would be useful to consider more about the energetics of the eruption event and attempt to relate it to the emission (presumably from a flare) seen in H_β. However, ultimately the fact that the prominence eruption was not captured (due to lack of sufficient wavelength coverage) in other chromospheric lines, such as CaII H & K, may be the limiting factor. A more complicated model than that presented in §4.3.4 might be able to explain the observed properties of the event more closely.

Future co-incident multi-wavelength observations will be the key to unlocking many of the properties of stellar atmospheres. These programs are inherently difficult to organise and co-ordinate. They are, however, ultimately one of the best ways to understand how different stellar activity phenomena interact. The study of AB Dor using simultaneous optical and X-ray data by Hussain et al. (2007) is a good first step in this direction. Another similar attempt to combine X-ray observations using XMM-Newton and optical spectroscopic data obtained with the VLT was published by Wolter et al. (2008).

8.2.2 (Zeeman) Doppler imaging

We recovered the first magnetic maps of *both* stars of a binary system but have only presented a preliminary analysis of the coronal field extrapolation. A full binary field

extrapolation code is currently being developed (Holzwarth, private communication) and it is hoped that it will soon be ready to be applied to the HD 155555 system. Using the radial field maps of both stars, we will then be able to see which field lines preferentially connect the two rather than looping back on to a region of opposite polarity on the same star. This will hopefully give us a better understanding of the X-ray properties of the binary and the locations of stellar winds.

The binary ZDI code developed here could also be applied to an eclipsing system. This would be interesting as it would potentially allow us to better probe the sizes of magnetic regions on the stellar surface by eclipse mapping. A potentially very promising target for this would be the eclipsing M dwarf binary YY Gem. An eclipsing system would also be a better target for measuring differential rotation. This is because the better known inclination angle of the system reduces a source of uncertainty when calculating differential rotation parameters. Studies of binary systems (such as HD 155555 or YY Gem) give us the opportunity to measure the relative strengths and locations of magnetic energy (e.g. the ratio of radial to azimuthal field) at each epoch. In this regard observing a binary system is very useful as the *relative* field strengths are less affected by changes in the S/N or phase coverage between epochs. Therefore long-term monitoring of one or more eclipsing binary systems to look for activity cycles and secular changes in the strength of differential rotation could prove fruitful. The recent development of the high-throughput spectropolarimeters such as ESPaDOnS and its clone NARVAL help to make such projects viable.

Bibliography

Audard M., Behar E., Güdel M., Raassen A., Porquet D., Mewe R., Foley C., Bromage G., 2001, A&A, 365, L329

Bagnuolo Jr. W. G., Gies D. R., 1991, ApJ, 376, 266

Baliunas S., Donahue R., Soon W., Horne J., Frazer J., Woodard-Eklund L., Bradford M., Rao L., Wilson O., Zhang Q., 1995, ApJ, 438, 269

Barnes J. R., 1999, PhD thesis, University of St Andrews, St Andrews, UK

Barnes J. R., 2005, MNRAS, 364, 137

Barnes J. R., Cameron A. C., Donati J.-F., James D. J., Marsden S. C., Petit P., 2005, MNRAS, 357, L1

Barnes J. R., Collier Cameron A., James D. J., Donati J.-F., 2000, MNRAS, 314, 162

Barnes J. R., Collier Cameron A., James D. J., Donati J.-F., 2001, MNRAS, 324, 231

Barnes J. R., Collier Cameron A., James D. J., Steeghs D., 2001, MNRAS, 326, 1057

Barnes J. R., Collier Cameron A., Unruh Y. C., Donati J. F., Hussain G. A. J., 1998, MNRAS, 299, 904

Bennett N. W. W., Evans D. S., Laing J. D., 1967, MNRAS, 137, 107

Berdyugina S. V., 2005, Living Reviews in Solar Physics, 2, 8

Brickhouse N., Dupree A., 1998, ApJ, 502, 918

Brown B. P., Browning M. K., Brun A. S., Miesch M. S., Nelson N. J., Toomre J., 2007, in American Institute of Physics Conference Series Vol. 948 of American Institute of Physics Conference Series, Strong Dynamo Action in Rapidly Rotating Suns. pp 271–278

Brown S. F., Donati J.-F., Rees D. E., Semel M., 1991, A&A, 250, 463

Byrne P. B., Eibe M. T., Rolleston W. R. J., 1996, A&A, 311, 651

Cameron A. C., 2008, Astron. Nachr., p. 1030

Cameron A. C., et al. 2007, MNRAS, 375, 951

Cameron A. C., Jardine M., Wood K., Donati J.-F., 2003, in EAS Publications Series Stellar prominences and coronal magnetic fields. pp 217–+

Carlsson M., Rutten R. J., Bruls J. H. M. J., Shchukina N. G., 1994, A&A, 288, 860

Carrington R., 1860, MNRAS, 20, 254

Carroll T. A., Kopf M., Ilyin I., Strassmeier K. G., 2007, Astronomische Nachrichten, 328, 1043

Catala C., Donati J.-F., Shkolnik E., Bohlender D., Alecian E., 2007, MNRAS, 374, L42

Chabrier G., Küker M., 2006, A&A, 446, 1027

Charbonneau P., Christensen-Dalsgaard J., Henning R., Larsen R. M., Schou J., Thompson M. J., Tomczyk S., 1999, ApJ, 527, 445

Claret A., 2004, A&A, 424, 919

Collier Cameron A., 1992, in Byrne P. B., Mullan D. J., eds, Surface Inhomogeneities on Late-Type Stars, Proceedings of a colloquium held at Armagh Observatory, Northern Ireland, 24-27 July, 1990. Edited by Patrick B. Byrne and Dermott J. Mullan. Lecture Notes in Physics, Vol. 397. Published by Springer-Verlag, Heidelberg, Germany, 1992., p.33 Modelling Stellar Photospheric Spots Using Spectroscopy (Invited). pp 33–+

Collier Cameron A., 1995, MNRAS, 275, 534

Collier Cameron A., 1996, in Wehlau A., Gray D. F., Rice J., eds, Stellar Surface Structure Vol. 176 of IAU Symposium, Stellar prominences (review). pp 449–+

Collier Cameron A., 1997, MNRAS, 287, 556

Collier Cameron A., Donati J.-F., 2002, MNRAS, 329, L23

Collier Cameron A., Donati J.-F., Semel M., 2002, MNRAS, 330, 699

Collier Cameron A., Duncan D. K., Ehrenfreund P., Foing B. H., Kuntz K. D., Penston M. V., Robinson R. D., Soderblom D. R., 1990, MNRAS, 247, 415

Collier Cameron A., Jeffery C. S., Unruh Y. C., 1992, in Jeffery C. S., Griffin R. E. M., eds, Stellar Chromospheres, Coronae and Winds Photospheric inhomogeneities on cool stars. pp 81–+

Collier Cameron A., Robinson R. D., 1989a, MNRAS, 236, 57

Collier Cameron A., Robinson R. D., 1989b, MNRAS, 238, 657

Collier-Cameron A., Unruh Y. C., 1994, MNRAS, 269, 814

Collier Cameron A., Walter F. M., Vilhu O. e., 1999, MNRAS, 308, 493

Cutispoto G., Kurster M., Pagano I., Rodono M., 1997, Informational Bulletin on Variable Stars, 4419, 1

D'Antona F., Mazzitelli I., 1997, Memorie della Societa Astronomica Italiana, 68, 807

Dempsey R. C., Linsky J. L., Fleming T. A., Schmitt J. H. M. M., 1993, ApJS, 86, 599

Dempsey R. C., Neff J. E., Lim J., 2001, AJ, 122, 332

Donati J. ., Jardine M. M., Petit P., Morin J., Bouvier J., Cameron A. C., Delfosse X., Dintrans B., Dobler W., Dougados C., Ferreira J., Forveille T., Gregory S. G., Harries T., Hussain G. A. J., Menard F., Paletou F., 2007, ArXiv Astrophysics e-prints

Donati J.-F., 1999, MNRAS, 302, 457

Donati J.-F., 2003, in Astronomical Society of the Pacific Conference Series ESPaDOnS: An Echelle SpectroPolarimetric Device for the Observation of Stars at CFHT. pp 41–+

Donati J.-F., Brown S. F., 1997, A&A, 326, 1135

Donati J.-F., Cameron A. C., Semel M., Hussain G. A. J., Petit P., Carter B. D., Marsden S. C., Mengel M., López Ariste A., Jeffers S. V., Rees D. E., 2003, MNRAS, 345, 1145

Donati J.-F., Catala C., Landstreet J. D., Petit P., 2006, in Casini R., Lites B. W., eds, Astronomical Society of the Pacific Conference Series Vol. 358 of Astronomical Society of the Pacific Conference Series, ESPaDOnS: The New Generation Stellar Spectro-Polarimeter. Performances and First Results. pp 362–+

Donati J.-F., Collier Cameron A., 1997, MNRAS, 291, 1

Donati J.-F., Collier Cameron A., Hussain G. A. J., Semel M., 1999, MNRAS, 302, 437

Donati J.-F., Collier Cameron A., Petit P., 2003, MNRAS, 345, 1187

Donati J.-F., Forveille T., Cameron A. C., Barnes J. R., Delfosse X., Jardine M. M., Valenti J. A., 2006, Science, 311, 633

Donati J. F., Jardine M. M., Gregory S. G., Petit P., Paletou F., Bouvier J., Dougados C., Menard F., Cameron A. C., Harries T. J., Hussain G. A. J., Unruh Y., Morin J., Marsden S. C., Manset N., Auriere M., Catala C., Alecian E., 2008, ArXiv e-prints, 802

Donati J.-F., Mengel M., Carter B. D., Marsden S., Collier Cameron A., Wichmann R., 2000, MNRAS, 316, 699

Donati J.-F., Semel M., Carter B. D., Rees D. E., Collier Cameron A., 1997, MNRAS, 291, 658

Donati J.-F. e. a., 2008, MNRAS, In Press

Dupree A., Brickhouse N., Doschek G., Green J., Raymond J., 1993, ApJ, 418, L41

Eibe M. T., 1998, A&A, 337, 757

Engvold O., 1998, in Webb D. F., Schmieder B., Rust D. M., eds, ASP Conf. Ser. 150: IAU Colloq. 167: New Perspectives on Solar Prominences Observations of Filament Structure and Dynamics (Review). pp 23–+

Ferreira J. M., 1998, A&A, 335, 248

Ferreira J. M., 2000, MNRAS, 316, 647

Gänsicke B. T., Hoard D. W., Beuermann K., Sion E. M., Szkody P., 1998, A&A, 338, 933

Gopalswamy N., Hanaoka Y., 1998, ApJ, 498, L179+

Gouttebroze P., Heinzel P., 2002, A&A, 385, 273

Granzer T., Schüssler M., Caligari P., Strassmeier K. G., 2000, A&A, 355, 1087

Gray D. F., 1992, The observation and analysis of stellar photospheres. CUP, University of Camebridge

Güdel M., 2004, A&AR, 12, 71

Güdel M., Audard M., Briggs K., Haberl F., Magee H., Maggio A., Mewe R., Pallavicini R., Pye J., 2001, A&A, 365, L336

Guedel M., Guinan E. F., Skinner S. L., 1997, ApJ, 483, 947

Guinan E. F., Wacker S. W., Baliunas S. L., Loeser J. G., Raymond J. C., 1987, in New Insights in Astrophysics: Eight Years of UV Astronomy with IUE Evidence of large-scale structures in the atmosphere of the active K-dwarf component of V471 Tauri. ESA SP-263, p. 197

Haisch B. M., Linsky J. L., Bornmann P. L., Stencel R. E., Antiochos S. A., Golub L., Vaiana G. S., 1983, ApJ, 267, 280

Hall J. C., Ramsey L., 1992, AJ, 104, 1942

Hatzes A. P., Kürster M., 1999, A&A, 346, 432

Herbst W., Eislöffel J., Mundt R., Scholz A., 2007, in Reipurth B., Jewitt D., Keil K., eds, Protostars and Planets V The Rotation of Young Low-Mass Stars and Brown Dwarfs. pp 297–311

Holzwarth V., 2007, Memorie della Societa Astronomica Italiana, 78, 271

Holzwarth V., Mackay D. H., Jardine M., 2006, MNRAS, 369, 1703

Horne K. D., 1986, PASP, 98, 609

Hussain G., 1999, PhD thesis, University of St Andrews, St Andrews, Scotland

Hussain G., Brickhouse N., Dupree A., Jardine M., van Ballegooijen A., Collier Cameron A., Donati J.-F., Favata F., 2005, ApJ, 621, 999

Hussain G. A. J., Allende Prieto C., Saar S. H., Still M., 2006, MNRAS, 367, 1699

Hussain G. A. J., Donati J.-F., Collier Cameron A., Barnes J. R., 2000, MNRAS, 318, 961

Hussain G. A. J., Jardine M., Donati J.-F., Brickhouse N. S., Dunstone N. J., Wood K., Dupree A. K., Collier Cameron A., Favata F., 2007, MNRAS, 377, 1488

Janson M., Brandner W., Lenzen R., Close L., Nielsen E., Hartung M., Henning T., Bouy H., 2007, A&A, 462, 615

Jardine M., 2004, A&A, 414, L5

Jardine M., 2007, Memorie della Societa Astronomica Italiana, 78, 340

Jardine M., Collier Cameron A., Donati J.-F., 2002, MNRAS, 333, 339

Jardine M., Collier Cameron A., Donati J.-F., Pointer G. R., 2001, MNRAS, 324, 201

Jardine M., Unruh Y., 1999, A&A, 346, 883

Jardine M., van Ballegooijen A. A., 2005, MNRAS, 361, 1173

Jardine M., Wood K., Collier Cameron A., Donati J.-F., Mackay D. H., 2002a, MNRAS, 336, 1364

Jardine M., Wood K., Collier Cameron A., Donati J.-F., Mackay D. H., 2002b, MNRAS, 336, 1364

Jeffers S. V., 2005, MNRAS, 359, 729

Jeffers S. V., Cameron A. C., Barnes J. R., Aufdenberg J. P., 2006, Ap&SS, 304, 371

Jeffers S. V., Donati J.-F., Collier Cameron A., 2007, MNRAS, 375, 567

Jeffries R. D., 1993, MNRAS, 262, 369

Jeffries R. D., Byrne P. B., Doyle J. G., Anders G. J., James D. J., Lanzafame A. C., 1994, MNRAS, 270, 153

Jensen K. A., Swank J. H., Petre R., Guinan E. F., Sion E. M., Shipman H. L., 1986, ApJ, 309, L27

Johns-Krull C. M., Valenti J. A., Hatzes A. P., Kanaan A., 1999, ApJ, 510, L41

Kron G. E., 1947, PASP, 59, 261

Kucera T. A., Andretta V., Poland A. I., 1998, Solar Phys., 183, 107

Kupka F., Piskunov N., Ryabchikova T. A., Stempels H. C., Weiss W. W., 1999, A&AS, 138, 119

Kurucz R., 1993, ATLAS9 Stellar Atmosphere Programs and 2 km/s grid. Kurucz CD-ROM No. 13. Cambridge, Mass.: Smithsonian Astrophysical Observatory, 1993., 13

Leigh C., Cameron A. C., Horne K., Penny A., James D., 2003, MNRAS, 344, 1271

Lister T. A., Collier Cameron A., Hilditch R. W., 2001, MNRAS, 326, 1489

Lockwood G. W., Skiff B. A., Henry G. W., Henry S., Radick R. R., Baliunas S. L., Donahue R. A., Soon W., 2007, ApJS, 171, 260

Lynden-Bell D., Boily C., 1994, MNRAS, 267, 146

Mackay D. H., Jardine M., Cameron A. C., Donati J.-F., Hussain G. A. J., 2004, MNRAS, 354, 737

Maggio A., Pallavicini R., Reale F., Tagliaferri G., 2000, A&A, 356, 627

Makarov V. V., 2003, AJ, 126, 1996

Marino A., Micela G., Peres G., Sciortino S., 2003, A&A, 407, L63

Marsden S. C., Berdyugina S. V., Donati J.-F., Eaton J. A., Williamson M. H., 2007, Astron. Nachr., 328, 1047

Marsden S. C., Donati J.-F., Semel M., Petit P., Carter B. D., 2006, MNRAS, 370, 468

McIvor T., Jardine M., Cameron A. C., Wood K., Donati J.-F., 2003, MNRAS, 345, 601

Mewe R., Raassen A., Drake J., Kaastra J., van der Meer R., Porquet D., 2001, A&A, 368, 888

Mills D., 1994, Technical Report 152, Starlink User Note. Rutherford Appleton Laboratory

Monnier J. D., Zhao M., Pedretti E., Thureau N., Ireland M., Muirhead P., Berger J.-P., Millan-Gabet R., Van Belle G., ten Brummelaar T., McAlister H., Ridgway S., Turner N., Sturmann L., Sturmann J., Berger D., 2007, Sci, 317, 342

Montesinos B., Thomas J. H., Ventura P., Mazzitelli I., 2001, MNRAS, 326, 877

Montmerle T., Grosso N., Tsuboi Y., Koyama K., 2000, ApJ, 532, 1097

Morin J., Donati J.-F., Forveille T., Delfosse X., Dobler W., Petit P., Jardine M. M., Cameron A. C., Albert L., Manset N., Dintrans B., Chabrier G., Valenti J. A., 2008, MNRAS, pp 26–+

Ness J.-U., Güdel M., Schmitt J. H. M. M., Audard M., Telleschi A., 2004, A&A, 427, 667

Noyes R. W., Hartmann L., Baliunas S. L., Duncan D. K., Vaughan A. H., 1984, ApJ, 279, 763

O'Neal D., Neff J. E., Saar S. H., Cuntz M., 2004, AJ, 128, 1802

O'Neal D., Saar S. H., Neff J. E., 1996, ApJ, 463, 766

Parker E. N., 1955, ApJ, 122, 293

Parker E. N., 1993, ApJ, 408, 707

Pasquini L., Cutispoto G., Gratton R., Mayor M., 1991, A&A, 248, 72

Petit P., 2007, ArXiv Astrophysics e-prints

Petit P., Donati J.-F., Oliveira J. M., Aurière M., Bagnulo S., Landstreet J. D., Lignières F., Lüftinger T., Marsden S., Mouillet D., Paletou F., Strasser S., Toqué N., Wade G. A., 2004, MNRAS, 351, 826

Petit P., Donati J.-F., Wade G. A., Landstreet J. D., Bagnulo S., Lüftinger T., Sigut T. A. A., Shorlin S. L. S., Strasser S., Aurière M., Oliveira J. M., 2004, MNRAS, 348, 1175

Piskunov N. E., Kupka F., Ryabchikova T. A., Weiss W. W., Jeffery C. S., 1995, A&AS, 112, 525

Plachinda S. I., Tarasova T. N., 2000, ApJ, 533, 1016

Pollacco D. L., et al. 2006, PASP, 118, 1407

Pont F., Gilliland R. L., Moutou C., Charbonneau D., Bouchy F., Brown T. M., Mayor M., Queloz D., Santos N., Udry S., 2007, A&A, 476, 1347

Radick R. R., Lockwood G. W., Skiff B. A., Baliunas S. L., 1998, ApJS, 118, 239

Radick R. R., Thompson D. T., Lockwood G. W., Duncan D. K., Baggett W. E., 1987, ApJ, 321, 459

Randich S., 2000, in Pallavicini R., Micela G., Sciortino S., eds, Stellar Clusters and Associations: Convection, Rotation, and Dynamos Vol. 198 of Astronomical Society of the Pacific Conference Series, Coronal activity among open cluster stars. pp 401–+

Reiners A., 2006, A&A, 446, 267

Reiners A., Schmitt J. H. M. M., 2003, A&A, 398, 647

Robinson R. D., Collier Cameron A., 1986, Proc. Astron. Soc. Aust., 6, 308

Robinson R. D., Worden S. P., Harvey J. W., 1980, ApJ, 236, L155

Rumph T., Bowyer S., Vennes S., 1994, AJ, 107, 2108

Saar S. H., 1988, ApJ, 324, 441

Saar S. H., 1994, in Rabin D. M., Jefferies J. T., Lindsey C., eds, Infrared Solar Physics Vol. 154 of IAU Symposium, New Infrared Measurements of Magnetic Fields on Cool Stars. pp 493–+

Sanz-Forcada J., Brickhouse N. S., Dupree A. K., 2003, ApJS, 145, 147

Sanz-Forcada J., Maggio A., Micela G., 2003, A&A, 408, 1087

Scharlemann E. T., 1982, ApJ, 253, 298

Scholz A., Eislöffel J., 2004, A&A, 421, 259

Schou J., 1998, ApJ, 505, 390

Schrijver C., Mewe R., van den Oord G., Kaastra J., 1995, A&A, 302, 438

Schrijver C. J., Title A. M., 2001, ApJ, 551, 1099

Schrijver C. J., Zwaan C., 2000, Solar and Stellar Magnetic Activity. Cambridge University Press, New York

Schröder K. P., 1983, A&A, 124, L16

Schüssler M., Solanki S. K., 1992, A&A, 264, L13

Semel M., 1989, A&A, 225, 456

Semel M., Donati J.-F., Rees D. E., 1993, A&A, 278, 231

Sestito P., Randich S., 2005, A&A, 442, 615

Siess L., Dufour E., Forestini M., 2000, A&A, 358, 593

Simkin S., 1974, A&A, 31, 129

Singh K. P., Drake S. A., Gotthelf E. V., White N. E., 1999, ApJ, 512, 874

Skilling J., Bryan R. K., 1984, MNRAS, 211, 111

Skumanich A., 1972, ApJ, 171, 565

Soderblom D. R., Stauffer J. R., 1991, Memorie della Societa Astronomica Italiana, 62, 199

Soderblom D. R., Stauffer J. R., Hudon J. D., Jones B. F., 1993, ApJS, 85, 315

Stauffer J. R., Hartmann L. W., 1987, ApJ, 318, 337

Stauffer J. R., Hartmann L. W., Jones B. F., 1989, ApJ, 346, 160

Steeghs D., Horne K., Marsh T. R., Donati J. F., 1996, MNRAS, 281, 626

Strassmeier K., 1996 Iau symposium 176: Stellar surface structure. Kluwer, pp 289–298

Strassmeier K. G., 1999, A&A, 347, 225

Strassmeier K. G., Hall D. S., Fekel F. C., Scheck M., 1993, A&AS, 100, 173

Strassmeier K. G., Rice J. B., 2000, A&A, 360, 1019

Symington N. H., Harries T. J., Kurosawa R., Naylor T., 2005, MNRAS, 358, 977

Tonry J., Davis M., 1979, AJ, 84, 1511

Unruh Y. C., Collier Cameron A., 1995, MNRAS, 273, 1

Valenti J. A., Johns-Krull C., 2001, in Mathys G., Solanki S. K., Wickramasinghe D. T., eds, Magnetic Fields Across the Hertzsprung-Russell Diagram Vol. 248 of Astronomical Society of the Pacific Conference Series, Magnetic Field Measurements for Cool Stars. pp 179–+

Valenti J. A., Piskunov N., 1996, A&AS, 118, 595

van Ballegooijen A. A., Cartledge N. P., Priest E. R., 1998, ApJ, 501, 866

Vogt S. S., Penrod G. D., 1983, PASP, 95, 565

Watson C. A., Steeghs D., Shahbaz T., Dhillon V. S., 2007, MNRAS, 382, 1105

Wolter U., Robrade J., Schmitt J. H. M. M., Ness J. U., 2008, A&A, 478, L11

Wolter U., Schmitt J. H. M. M., 2005, A&A, 435, L21

Wolter U., Schmitt J. H. M. M., van Wyk F., 2005, A&A, 435, 261

Young P., Dupree A., Wood B., Redfield S., Linsky J., Ake T., Moos H., 2001, ApJ, 555, L121

Zahn J.-P., 1977, A&A, 57, 383

Zeeman P., 1897, Nat, 55, 347